RECTIFIED INERTIAL FORCES ON SPHERICAL PARTICLES IN OSCILLATORY FLUID FLOWS NEAR INTERFACES

BY

SIDDHANSH AGARWAL

DISSERTATION

Submitted in partial fulfillment of the requirements
for the degree of Doctor of Philosophy in Mechanical Engineering
in the Graduate College of the
University of Illinois Urbana-Champaign, 2021

Urbana, Illinois

Doctoral Committee:

Professor Sascha Hilgenfeldt, Chair and Director of Research
Professor Jonathan Freund
Assistant Professor Mattia Gazzola
Assistant Professor Andres Goza

Abstract

Inertial microfluidics has become an indispensable tool in engineering science, materials science, health and medicine, among other fields, to precisely control and manipulate particles, cells and vesicles without the need for charges or chemistry. Despite its ubiquitous prevalence, describing effects of small but finite inertia is a fundamental fluid dynamical problem that has not been solved in full generality. One of the most efficient and powerful ways to exploit inertia in low Reynolds number settings is through the use of oscillatory flows, which can be utilized to exert remarkably consistent and controllable forces on fluid-borne objects over millisecond time scales. Particle manipulation in fast oscillatory flows is now a major tool in lab-on-a-chip processing as well as in diagnostic and biomanufacturing applications. While there are several studies that have successfully exploited inertia in experiments, a theoretical understanding of inertial forces on particles in oscillatory flows, crucial for the systematic design of practical lab-on-a-chip applications, has lagged behind.

Due to the inherent non-linearity of fluid dynamics, a large class of oscillating flows set up by localized oscillating objects gives rise to irreversible steady motion even at low Reynolds number. It has recently been shown that particle transport in such flows leads to differential displacement and efficient sorting of microparticles. In the first part of the dissertation, we describe inertial forces and their effect on particle motion by incorporating the leading order viscous and inviscid effects near localized oscillating interfaces. Resulting in direct predictions for displacement on steady time scales, the model predicts a richer and qualitatively different behavior from that expected from earlier, simplified radiation-force formalisms. Depending on experimental control parameters, the net effect of interfacial oscillation can be either an attraction to or a repulsion from the interface, and particles can be captured at a fixed distance or released. These results are also verified in comparison with experiments.

While this model captures available experimental data well in the low and high frequency limits, it has shortcomings in the intermediate range, important for applications. We revisit the low Reynolds number assumption inherent to the Maxey–Riley (MR) equation, the main theoretical foundation for fluid forces on particles, and find that for particles in flows generated by localized oscillating objects, this assumptions is

easily violated and the nonlinear inertial terms can no longer be neglected. Thus, it is precisely the use of localized oscillations in modern microfluidics that is now pushing the envelope of the MR equation, exposing its limits in predicting the emergence and magnitude of observed significant and persistent forces. Based on insights from both experiments and direct numerical simulations of the full Navier–Stokes equations, we systematically quantify inertial forces on particles in general background flows from first-principles, employing a generalized reciprocal-theorem-based approach. Our formalism can be adapted to manifold flow situations typically encountered in inertial microfluidics.

Because of their paramount importance in the arsenal of modern microfluidics, we specialize our general theory to oscillatory flows. Through a systematic analytical modeling approach we derive, isolate, and understand these inertial forces and find that they naturally emerge from a combination of particle inertia and spatial oscillatory flow variation, and that they can be quantified through a generalization of the Maxey–Riley equation to cases where that theory has been unable to describe observations. Our formalism predicts additional attractive contributions towards oscillating boundaries even for density-matched particles, a previously unexplained experimental phenomenon. The accuracy of the theory is demonstrated against full scale, three-dimensional direct numerical simulations throughout its range.

Having developed a rigorous description of inertial forces on particles in oscillatory flows, the last part of this work focuses on practical utility. The theory is extended to account for the presence of interfaces and arbitrary flows in two dimensions. Using time-scale separation, we derive a system of overdamped ODEs for particle motion on time scales of rectified motion that yields fundamental physical insight and is efficient to compute. We study the transport of finite-sized inertial microparticles under a superposition of streaming and transport flows, focusing on the use of oscillating microbubbles for continuous, high-throughput size or density-based manipulation of microparticles. Our computationally efficient and rigorous model accurately quantifies the magnitude of displacement of particles across streamlines in comparison to experiments. Thus, the proposed formalism offers a systematic and practical approach that augments physical understanding and enables precise model predictions, potentially spurring more compact, reliable, and efficient forms of particle manipulation.

To my parents.

Acknowledgments

This dissertation would not have been possible without the support and guidance that I received from countless people. First and foremost, I would like to express my deepest gratitude to my advisor Professor Sascha Hilgenfeldt, who has been an extraordinary teacher, mentor and guide, affording me a great deal of intellectual and personal independence throughout this journey. I am indebted to him for his role in my personal growth as a researcher—both scientifically and professionally. The numerous, often lengthy, discussions that I have had with him over the past years have played a crucial role in the development of my scientific temperament. I am proud of, and grateful for, my time working with him.

I would like to thank Professor Mattia Gazzola for his initiative and enthusiasm to work together, culminating in a fruitful collaboration. I am grateful to him for guiding me and supporting me in my professional endeavors. I would also like to acknowledge the valuable comments and insightful discussions about my work provided by the other members of my doctoral committee—Professor Jonathan Freund and Professor Andres Goza.

This dissertation would not have been possible without the rigorous foundation in mechanics and applied mathematics that I was provided with through graduate coursework in the MechSE department. I would especially like to thank Professor Moshe Matalon for his excellent course on Asymptotics, and Professor Anil Hirani in the math department for his course on Differential Geometry. These foundational courses have played a crucial role in my intellectual development during my early years as a graduate student at UIUC.

I wish to thank all the people that I have had the pleasure of collaborating with. I would pointedly like to thank Bhargav Rallabandi, whose work this dissertation builds upon. The useful interactions with him, especially during the early years of my PhD, have gone a long way in the success of this work. I am grateful to the current and past members of our research group—Raqeeb Thameem, David Raju, Sangwoo Kim and Partha Das—for fruitful discussions over the years. Special thanks to all my collaborators over the years, for their valuable time and friendship.

I would be remiss if I did not acknowledge the support of the administrative staff of the MechSE department. I would especially like to thank Kathy Smith for her patience and willingness to guide countless

graduate students like me through various stages of graduate school. Thanks to Professor Blake Johnson also—working as a teaching assistant with him has provided me with not only valuable teaching experience but also an opportunity to contribute towards pedagogical course development.

I express my sincere thanks to all my friends—in Champaign-Urbana and beyond—who have been my pillars of support and made life outside of research enjoyable. Heartfelt thanks to a few very close friends of mine—Ayush Khaitan, Amber Shrivastava and Arun Raman—who have been the source of innumerable discussions on life, politics, spirituality and everything in between. Their friendship and support made it easier to persevere through the vicissitudes of graduate school, especially during the tough pandemic year. Finally, I would like to thank my family for their unconditional love, affection and steadfast encouragement. Thank you *Mummy*, for your unwavering faith in me.

Table of Contents

List of Figures

Chapter 1

Introduction

1.1 Inertial Microfluidics

Microfluidics often entails precise control and manipulation of microparticle motion in low Reynolds number settings. The most common application is in the experimental quantification and characterization of the flow itself through the use of tracer particles. Other applications include trapping, sorting or segregation of fluid-borne objects based on their physical properties, e.g., size, density, deformability, electrical conductivity etc., where precise positional control and force actuation is desired. Despite the prevalence of small Reynolds numbers on the microscale, inertia has only recently been recognized as an important player in microfluidics applications. Describing effects of small but finite inertia is a fundamental fluid dynamical problem that has not been solved in full generality [70, 93, 147]. Several of these inertial effects have been utilized in microfluidic devices for practical lab-on-a-chip applications. These nonlinear inertial effects are predominantly studied in two contexts: (i) secondary or rectified flows due to fluid inertia, e.g., Dean flows [45], acoustic streaming [88, 118, 140], etc., and (ii) migration of finite-sized particles due to inertial lift forces [47, 170]. While the emergence of second order flows as a consequence of finite fluid inertia in low Reynolds number settings has been well-studied over the last few decades, both experimentally and theoretically, there has been no systematic investigation of the physical mechanisms underlying the migration of particles due to inertial lift forces.

Modern microfluidic devices routinely utilize inertial lift forces on particles to manipulate them without the need for complicated pre-processing such as fluorescence tagging, electric charges or chemical concentration gradients. The applications of these techniques range from centrifuges on a chip to trap cancer cells from blood in vortical flows [99, 155] to sheathless high-throughput flow cytometry to seggregate particles from a buffer in order to image and count rare blood cells [39, 74]. In all these predominantly experimental, empirical studies, steady shear flow gradients are utilized in order to exert persistent lift forces on particles. However, there are no systematic predictive theories that can inform the intelligent design of inertial microfluidic devices.

1.2 Particle manipulation using oscillatory flows

Inertial forces on finite-sized objects (of radius a_p) have been discussed extensively in two main contexts: (i) the inertial migration of particles due to steady shear flow gradients as mentioned earlier [47, 170], where the inertial migration force scales differentially near the wall compared to the bulk (a_p^6 vs a_p^4) resulting in equilibrium positions; and (ii) in acoustofluidics, where the particle is exposed to the oscillatory flow in acoustic waves and the radiation force due to scattering of sound waves scales much more favorably with particle size (as a_p^3), see e.g., [146]. Oscillatory flows are, by far, one of the most efficient ways to induce significant inertial forces on particles over extremely short time-scales, with remarkable control and precision. They have, thus, become an important and indispensable tool in the arsenal of modern microfluidics.

More recently, a new field of microfluidics applications has been discussed that is concerned with particles in incompressible flows near localized oscillating interfaces. Perhaps the simplest class of these flows is set up by cylindrical or spherical bubbles of radius a_b that oscillate with a small amplitude $\epsilon a_b, \epsilon \ll 1$. Particles near such bubbles often get attracted towards the interface [35, 124, 143], while in other situations differential repulsion has been noted [160, 167–169]. Related work concerns acoustic interactions between bubble-driven microswimmers [9]. More generally, localized oscillating interfaces, such as bubbles, may give rise to steady streaming, driven by non-zero Reynolds stresses due to the inertia of the fluid oscillation [72, 90, 91, 142]. Recent studies have shown how microbubbles positioned at walls of the microfluidic device can be used, with a great degree of success, in several practical applications such as particle trapping [94, 97, 143, 167], size-selective particle sorting [160, 162, 167, 168], microfluidic mixing [8, 89, 169], and shear force actuation [100].

In many of these cases, attraction of the particle towards the oscillating interface has been attributed semi-quantitatively to the "Secondary Radiation Force (SRF)" on a spherical particle in the far field of a radial standing acoustic wave [18, 42, 68]. This effect has been discussed in a variety of scenarios, (cf. [34, 67]), but there has been no attempt, to our knowledge, to systematically include force contributions beyond SRF, or generalize this concept to include repulsive forces. In the context of particles near oscillating interfaces, the unmodified use of SRF is not appropriate, as the particle is not in a standing acoustic far field, but is exposed to an incompressible oscillatory flow that is strongly influenced by the nearby interfacial geometry as well as by viscous effects. Therefore, though the above-mentioned setups have been successfully employed in applications, their design has to a large extent been empirically driven, due to an absence of a theory connecting the spatially varying, unsteady background flow field description to the inertial forces experienced by the particle immersed in such a flow.

It is somewhat surprising that relatively little is known about the motion of microparticles in the general

case of unsteady, spatially non-uniform flows (cf. [93]). Recent work [73] has shown that the effect of finite particle inertia can be accounted for by a regular asymptotic expansion in the particle Reynolds number in the case of a steady, unidirectional Poiseuille flow. On the other hand, for Saffman-like lift forces, one must employ a singular perturbation expansion in Reynolds number [145]. Both these effects have very different physical origins, and scale differently with Reynolds number. This situation is further complicated by the presence of boundaries [70, 73] and the introduction of unsteadiness [56, 92] and/or spatially non-uniform flows, for which no systematic theory exists. Many microfluidic applications rely on vortical or unsteady flow actuation parts, in addition to an imposed transport flow, in order to manipulate microparticles; a fundamental understanding of inertial forces is crucial for the design of practical applications.

In the context of oscillatory flows, numerous publications [48, 49, 119, 148] have described the inertial force on a particle in an acoustic setting, but they do not capture the effect of a nearby interface and/or assume a very specific form of the spatial variation of the background flow field. Conversely, other works attribute the motion of the particle to a steady streaming flow generated by a nearby oscillating body/interface whereas, in general, the particle experiences both the drag due to a steady streaming (and transport) flow, and rectified inertial forces due to oscillations. To our knowledge, this general setting has so far never been investigated; we seek to illuminate its properties with analytical modeling in this dissertation.

1.3 Organization of the dissertation

The dissertation can be broadly divided as follows: In Chapter 2, we derive a model for inertial forces on particles in incompressible oscillatory flows near interfaces. Heuristically superposing leading order viscous and inviscid force contributions near such interfaces, we efficiently bridge the acoustofluidic and microfluidic approaches, accurately capturing particle dynamics in the limit of high frequencies. Resulting in direct predictions for particle motion on rectified timescales, the model predicts a richer and qualitatively different behavior from that expected from simplified radiation-force formalisms: Depending on experimental control parameters, the net effect of interfacial oscillation can be either an attraction to or a repulsion from the interface, and particles can be captured at a fixed distance or released. These results are also verified in comparison with experiments.

In Chapter 3, we recognize that the model has shortcomings in the intermediate frequency range, where viscous effects become important. We revisit the assumptions inherent to the Maxey–Riley equation, the main theoretical foundation for fluid forces on particles, and find that for particles in flows generated by localized oscillating objects, these assumptions are easily violated. We develop a systematic, first-principles

formalism for inertial forces on the particle immersed in a generic unsteady background flow, using a generalized reciprocal-theorem-based approach. The advantage of this formalism is that it can adapted to manifold flow situations typically encountered in inertial microfluidics. The next two chapters are devoted to specializing this formalism for inertial forces on particles in oscillatory flows.

In Chapters 4 and 5, through a combination of theory and high-resolution simulations we derive, isolate, and understand inertial forces acting on spherical particles. We find that these forces emerge from a combination of particle inertia and spatial oscillatory flow variation, and that they can be quantitatively predicted through a generalization of the Maxey–Riley equation to cases where that theory has been unable to describe observations. The analysis explains particle manipulation in fast oscillatory flows, a major tool in lab-on-a-chip processing, diagnostics, analysis, and biomanufacturing applications.

Having developed a rigorous description of inertial forces on particles in oscillatory flows, Chapter 6 focuses on practical applications. The theory is extended to account for the presence of interfaces and arbitrary flows in two dimensions. Using time-scale separation we derive a system of over-damped ODEs for the motion of the particle on time scales of rectified motion. These provide fundamental physical insight into the lift forces acting on particles in more complicated flows and, furthermore, are computationally inexpensive to solve. We study the transport of finite-sized inertial microparticles under a superposition of streaming and Poiseuille flows, focusing on the use of microbubbles for continuous high-throughput size or density dependent manipulation of microparticles. Our computationally efficient and rigorous model accurately quantifies the magnitude of displacement of particles across streamlines in comparison to experiments. It also suggests novel design strategies for precise manipulation of particles in continuous flow situations, potentially opening up new avenues for more compact and reliable particle manipulation strategies, such as marker-less flow cytometry for biomedical applications.

1.4 Key Accomplishments

The key accomplishments of the research are organized into separate publications—each represents both a set of related technical ideas as well as a key step in furthering the understanding of inertial forces on particles.

- **Generalized formalism for inertial forces on particles** [5, 6]: We develop here, for the first time, a rigorous, first-principles formalism for inertial forces on a spherical particle in *any* background time-dependent flow, that varies on scales much larger than the particle size, and that can be adapted to a rich set of scenarios, applications, and flow types. Our reciprocal-theorem-based approach employs a

Laplace transform to compute the forces and it can accommodate a wide variety of flow field descriptions. This includes any time-dependent (or independent) background flow as well as modifications to include the effect of walls or boundaries, such as for particles in a finite-sized channel flow. The flexibility that the formalism offers translates to a manifold reduction in computational effort. Thus, this work represents a significant advancement in the fundamental understanding of how inertial effects cause fluid-borne objects to behave irreversibly even in laminar, low Reynolds number flows.

- **An unrecognized flow curvature induced inertial force in microfluidics** [6]: We show here that a specialization of our generalized formalism for inertial forces on particles to oscillatory flows directly results in a previously unrecognized, strongly relevant inertial force acting even on neutrally buoyant particles entrained in oscillatory flows. We find that this novel force stems from an interplay of particle inertia, flow gradients, and flow curvature; it accounts for many previously unexplained experimental observations. Oscillatory flows have become an important and indispensable tool in the arsenal of modern microfluidics and offer the most controlled way to induce significant inertial effects at the microscale over short time scales. Our general and closed expression of the inertial force, thus, provides a result of immediate practical utility in experimental design. This potentially opens up new avenues for exerting precise and consistent control on particles in biomedical applications, where density contrasts are small.

- **Equation of motion for the particle** [4–6]: We systematically derive the equation of motion for a spherical particle in a given general, time-dependent background flow that generalizes the Maxey–Riley equation, the main theoretical foundation for describing particle dynamics, to include inertial effects. Validated against large-scale direct numerical simulations, this equation captures particle dynamics accurately and is applicable to a wide variety of flow situations and can be extended to multiple dimensions. We also resolve a long-standing question about the form of the added mass term in the original Maxey–Riley formalism: We find that a systematic derivation of inertial forces results in additional contributions stemming from the slip velocity and background flow gradients, which specialize to the well-known Auton et al. [11] correction in the potential flow (or high-frequency) limit; these forces can also be substantially larger owing to, e.g., viscous streaming around the particle.

- **Bridging the acoustofluidic and inertial microfluidic approaches** [4, 5]: We demonstrate that our Maxey–Riley like general approach reduces to well-known radiation forces in acoustofluidics when the particle is in the bulk, i.e., at large distances from any interface, thus bridging the two fields. We also shed light on the disagreement in literature pertaining to the direction of acoustofluidic radiation forces

on particles in standing-wave fields: Different well-established theories make conflicting predictions about the force direction. This forms the first such reported connection between these disparate approaches.

- **Particle manipulation in two dimensional microbubble streaming flows** [7]: We quantify the behavior of finite-sized inertial microparticles transported near an oscillating bubble interface, where the flow field is a superposition of streaming and transport flows. This allows for a fast, size or density-based manipulation of microparticles. In order to achieve fast displacement of particles across fluid streamlines over millisecond time scales, significant lift forces on particles are required. We argue that such a net displacement—whether attractive towards or repulsive from the bubble—is a consequence of the particle experiencing significant radial "kicks" when it is near the bubble interface. We incorporate important effects on particle motion due to proximity to an interface and, using time-scale separation, derive a system of over-damped ODEs for the motion of particle on time scales of rectified motion. Resulting in accurate quantification of particle displacements observed in experiments, we show that our systematic formalism is successful across parameters, whereas other theories fail to account for most of these effects, grossly under-predicting the extent of displacement observed in experiments. Our model also suggests new strategies for density or size-based manipulation of particles in microfluidics.

Chapter 2

Inertial forces on particles in the high-frequency limit

In this chapter[1], we present a model that generalizes a Maxey–Riley like equation for particle motion in oscillatory flows in the high-frequency limit, incorporating important viscous and inviscid effects near oscillating interfaces and efficiently bridging the acoustofluidic and microfluidic approaches. Due to the inherent nonlinearity of fluid dynamics, a large class of oscillating flows gives rise to rectified effects of steady motion. It has recently been shown that particle transport in such flows leads to differential displacement and efficient sorting of microparticles. Resulting in direct predictions for particle motion on slower time scales, the model predicts a richer and qualitatively different behavior from that expected from simplified radiation-force formalisms: depending on experimental control parameters, the net effect of interfacial oscillation can be either an attraction to or a repulsion from the interface, and particles can be captured at a fixed distance or released. These results are verified in comparison with experiments.

2.1 Introduction

Despite the prevalence of small Reynolds numbers, inertia has recently been acknowledged as an important player in microfluidics applications. Inertia has been discussed extensively in two main contexts: the inertial migration of particles due to steady shear flow gradients [47, 170], and acoustofluidics, where the particle is exposed to the oscillatory flow in acoustofluidic waves, see e.g [146]. While acoustofluidic forces are used in applications and well-understood in the inviscid limit for particles in isolation [30], different theories with contradictory predictions about the magnitude and direction of forces have been proposed when viscous effects become important [148][48].

More recently, a third complex of microfluidics applications has been discussed that is concerned with particles in incompressible flows near oscillating interfaces. Perhaps the simplest class of these flows is set up by cylindrical or spherical bubbles of radius a_b that oscillate with a small amplitude $\epsilon a_b, \epsilon \ll 1$. Particles near such bubbles often get attracted towards the interface [35, 124, 143], while in other situations differential

[1] This chapter is adapted from Agarwal et al. [4]

repulsion has been noted [160, 167–169]. Related work concerns acoustic interactions between bubble-driven microswimmers [9]. In many of these cases, attractive forces have been attributed semi-quantitatively to the "Secondary Radiation Force (SRF)" on a spherical particle in the far field of a radial standing acoustic wave [18, 42, 68]. This effect has been discussed in a variety of scenarios, (cf.[34, 67]), but there has been no attempt, to the authors' knowledge, to systematically include force contributions beyond SRF, or unify this concept with that of repulsive forces. In the context of particles near oscillating interfaces, the unmodified use of SRF may not be appropriate, as the particle is not in a standing acoustic far field, but is exposed to an incompressible oscillatory flow that is strongly influenced by the nearby interfacial geometry as well as by viscous effects.

Numerous publications [48, 49, 119, 148] have described the force on a particle in an acoustic setting, but they do not capture the effect of a nearby interface and/or assume a very specific form of the background flow field. In the spirit of previous work [161], the present work incorporates the aforementioned effects in the context of a Maxey–Riley-like formalism [103], aiming for a flexible tool to efficiently predict particle motion in a variety of oscillating flows. Section 2.2 generalizes a previous approach of time-scale separation to incorporate important density-dependent and inertial effects. In section 2.3 we discuss the predicted impact of the effects on particle manipulation (attraction or repulsion). Section 2.4 compares the results with a specific set of experimental data and elucidates previously unexplained phenomena for particles near interfaces. In section 2.5 it is pointed out that, even far from interfaces, the present formalism agrees with, and sheds light on, inviscid and viscous versions of acoustofluidic forces. Conclusions are presented in section 2.6.

2.2 Particle equation of motion near an interface

In order to address the issues alluded to above, a new approach was proposed by Thameem et al. [161] where the motion of a particle near an oscillating interface is modeled by a modified version of the Maxey–Riley equation [103], which is an ODE for motion of a rigid sphere (radius a_p, density ρ_p) of mass $m_p = (4/3)\pi\rho_p a_p^3$ placed in a general incompressible, known background flow field $\mathbf{u}(\mathbf{r}, t)$ (present without the particle). The current chapter aims at incorporating additional effects into this Maxey–Riley approach and derive the rectified particle motion on time scales longer than the oscillation period for a wide variety of scenarios, in order to assess the qualitative and quantitative impact on the particle position dependent on parameters like density contrast, particle size, or driving frequency. Despite the wider scope, we aim to maintain the character of an explicit equation of motion for the position of the particle center $\mathbf{r}_p(t)$, in which the known

flow field $\mathbf{u}$, together with its derivatives, is instantaneously evaluated at $\mathbf{r}_p(t)$. In particular, this excludes non-local or history effects. This approach necessitates additional approximations, but yields a versatile equation that can be readily applied to a multitude of situations and yields straightforward ODE solutions for particle trajectories.

Following [83], we will decompose the hydrodynamic force into inviscid and viscous contributions $\mathbf{F}^H = \mathbf{F}_i^H + \mathbf{F}_v^H$ and discuss additional effects that modify these terms in the case of our interest.

2.2.1 Correction terms and approximations

The original derivation of Maxey and Riley [103] is valid for a spherical particle of radius a_p with small inertia; specifically, (i) the particle Reynolds number based on a typical *difference* velocity between particle speed and background flow must be small, and (ii) the background flow must satisfy the small Stokes number condition $a_p^2 U_0/(\nu L_0) \ll 1$, where U_0 and L_0 are the velocity and gradient scales of $\mathbf{u}$, and ν the kinematic viscosity. In specializing the problem to periodic flows induced by the oscillation with angular frequency ω of an interfaces with finite curvature scale (e.g. a bubble of radius a_b), we identify $L_0 = a_b$ and $U_0 = \epsilon a_b \omega$, so that the latter condition can be written as $\epsilon\lambda \ll 1$, where we define the inertial parameter $\lambda = \frac{1}{3}\frac{a_p^2\omega}{\nu}$ [161]. A third, natural condition is (iii) assuming the particle to be small compared to the scale of the interface, i.e., $a_p/a_b \ll 1$.

A consequence of the oscillatory nature of the flows is that time averages of first-order forces in ϵ will vanish, while second-order rectified terms will persist as steady effects. In particular, $\mathcal{O}(\epsilon^2)$ inertial effects are not necessarily negligible (for appreciable Reynolds number of the primary oscillating flow), so that an original approximation from [103] neglecting second-order terms in $\mathbf{F}_i^H$ involving the perturbation flow induced by the presence of the particle is not generally valid. In [83], the effect of such terms was worked out; in addition to the terms of advective inertia already present in the Maxey-Riley equation, and using $m_f = m_p \rho_f/\rho_p$, this yields

$$\mathbf{F}_i^H \approx -\frac{1}{2} m_f \left(\frac{d\mathbf{v}_p}{dt} - \frac{D\mathbf{u}}{Dt} \right) + m_f \frac{D\mathbf{u}}{Dt} + \frac{1}{3} m_f a_p^2 \nabla\mathbf{u} : \nabla\left(\nabla\mathbf{u}\right) , \tag{2.1}$$

where the last term on the right-hand side represents the second-order effect of the perturbation flow. This term will turn out to be of considerable, and sometimes dominant, size for small distances between the particle and the oscillating interface, which is the main interest of this study. A term proportional to $\nabla^2\mathbf{u}$ has been neglected, as the primary oscillatory flow (of appreciable Reynolds number) is nearly irrotational, so that $\nabla^2\mathbf{u}$ is negligible.

The proximity of the interface also introduces important modifications in the viscous part of the force, as was previously shown in [161]. It is well known that the viscous hydrodynamic force on a sphere depends on the distance to the interface, interpolating between the usual Stokes drag far away and a lubrication expression nearby [28]. In [161], the forces were only appreciable at very small separation distance, so that the expression was always dominated by lubrication drag. However, in the present chapter we will be concerned with both small and large separation distances; therefore, we acknowledge in the model that the action of the viscous lubrication term in the oscillatory flow is confined to separation distances less than the Stokes boundary layer thickness $\delta_S = \sqrt{2\nu/\omega}$. This confinement has been described in various oscillating-flow lubrication problems with both no-slip and stress-free interfaces [38, 41, 55]. For an interface of characteristic radius of curvature a_b, we identify the center of curvature with the origin (see Fig. 2.1) and combine the Stokes and lubrication expressions [161], so that

$$\mathbf{F}_v^H \approx -6\pi\nu\rho_f a_p \left[\frac{d\mathbf{r}_p}{dt} - \mathbf{u} + H\left(\frac{h(\mathbf{r}_p,t)}{\delta_S}\right) \frac{a_p \left(\frac{d\mathbf{r}_p}{dt} \cdot \mathbf{e}_r - \frac{\partial r_b}{\partial t} \right)}{n_B h(\mathbf{r}_p,t)} \mathbf{e}_r \right] \tag{2.2}$$

where $r_b(\theta,t)$ is the radial position of the point on the oscillating interface nearest the particle and $h(\mathbf{r}_p,t) = \mathbf{r}_p \cdot \mathbf{e}_r - r_b - a_p$ used in the lubrication term is the separation distance between the surfaces of particle and interface (cf. Fig 2.1). The integer n_B depends on the boundary condition at the interface: $n_B = 1$ for no-slip, and $n_B = 4$ for no-stress (the case pursued for oscillating bubbles in this work). The decay of the lubrication force outside the boundary layer is modeled by the exponential $H(z) = \exp(-z)$, consistent with the literature [41, 50, 55]. Expression (2.2) neglects Faxén-term contributions proportional to $\nabla^2\mathbf{u}$, consistent with the above approximations. We also assume that there is negligible feedback on $r_b(\theta,t)$ from the particle's presence (small capillary numbers due to particle motion, cf. [98])

Both (2.1) and (2.2) also omit contributions from the Basset-Boussinesq history force. These are known to be negligible in a number of relevant situations [37, 101, 108]. For the current case of harmonic oscillatory flows, the history integral becomes an explicit expression if (a) transients have died out and (b) the leading-order oscillatory motion of the particle is harmonic translation in bulk. For this particular case, the history term reduces to well-established correction terms in (2.1) and (2.2) [44, 81] of order $\lambda^{-1/2}$, which are negligible in the limits of both large and small viscous effects. While assumption (a) is sustainable, we focus here on forces on particles not in bulk, but near an interface, so that we omit these terms altogether and defer a discussion to Section 2.5, where we evaluate forces at large distance from the interface.

Another effect of order $\lambda^{-1/2}$ is the Saffman lift for particles traversing shear gradients, considered e.g. in Chong et al. [37]; in the present chapter, we will exclusively deal with particles moving parallel to the

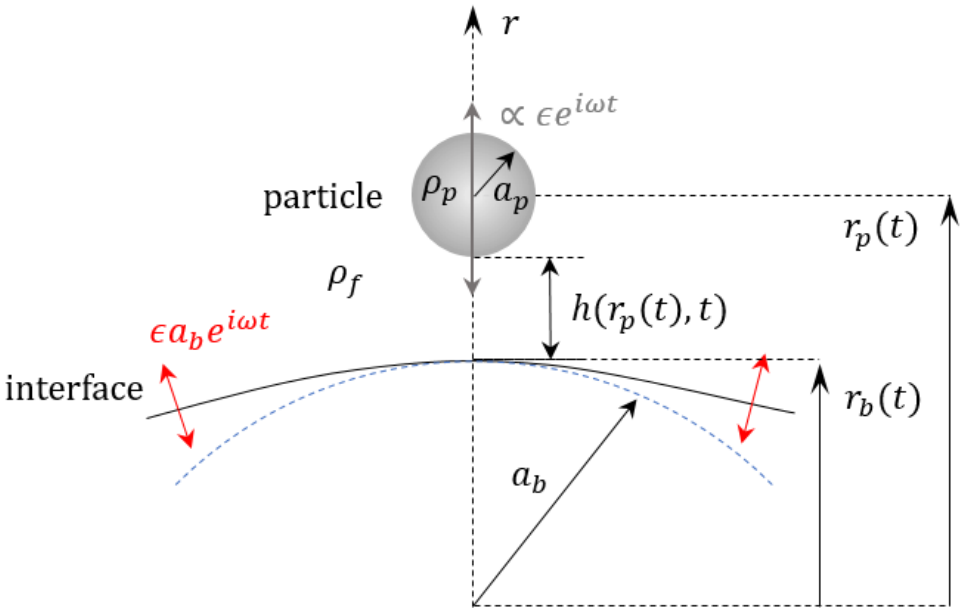

Figure 2.1: Problem set-up and nomenclature for a spherical particle of radius a_p near an oscillating interface (curvature length scale a_b).

flow field, and thus omit this term. In summary, we shall use

$$\begin{aligned}\mathbf{F}^H \approx &-6\pi\nu\rho_f a_p\left[\left(\frac{d\mathbf{r}_p}{dt}-\mathbf{u}\right)+H\left(\frac{h}{\delta_S}\right)\frac{a_p\left(\frac{d\mathbf{r}_p}{dt}\cdot\mathbf{e}_r-\frac{\partial r_b}{\partial t}\right)}{n_B h(\mathbf{r}_p,t)}\mathbf{e}_r\right]\\ &-\frac{1}{2}m_f\left(\frac{d^2\mathbf{r}_p}{dt^2}-\frac{D\mathbf{u}}{Dt}\right)+m_f\frac{D\mathbf{u}}{Dt}+\frac{1}{3}m_f a_p^2\nabla\mathbf{u}:\nabla\left(\nabla\mathbf{u}\right)\end{aligned} \tag{2.3}$$

as our approximation for the force governing particle motion near an interface. Defining dimensionless variables $\tilde{\mathbf{r}}_p=\mathbf{r}_p/a_b$, $\tilde{t}=\omega t$, and $\tilde{\mathbf{u}}=\mathbf{u}/U_0$, we use (2.3) to obtain an ordinary differential equation that describes a wide variety of oscillatory particle dynamics,

$$\begin{aligned}&\lambda\left(\hat{\kappa}+1\right)\frac{d^2\tilde{\mathbf{r}}_p}{d\tilde{t}^2}+\left(\mathbf{I}+H\left(\frac{\tilde{h}}{\tilde{\delta}}\right)\frac{\gamma\mathbf{e}_r\mathbf{e}_r}{\tilde{h}(\tilde{\mathbf{r}}_p,t)}\right)\cdot\frac{d\tilde{\mathbf{r}}_p}{d\tilde{t}}\\ &=\epsilon\left[\lambda\left(\frac{\partial\tilde{\mathbf{u}}}{\partial\tilde{t}}+\epsilon\tilde{\mathbf{u}}\cdot\tilde{\nabla}\tilde{\mathbf{u}}\right)+\frac{2}{9}\epsilon\lambda n_B^2\gamma^2\tilde{\nabla}\tilde{\mathbf{u}}:\tilde{\nabla}\left(\tilde{\nabla}\tilde{\mathbf{u}}\right)+\tilde{\mathbf{u}}+H\left(\frac{\tilde{h}}{\tilde{\delta}}\right)\frac{\gamma}{\tilde{h}(\tilde{\mathbf{r}}_p,\tilde{t})}\frac{\partial\tilde{r}_b}{\partial\tilde{t}}\mathbf{e}_r\right]_{\tilde{\mathbf{r}}_p}\end{aligned} \tag{2.4}$$

where we have introduced $\gamma\equiv a_p/(n_B a_b)\ll 1$ and $\tilde{\delta}=\delta_S/a_b$, and the density contrast $\hat{\kappa}=\frac{2}{3}\left(\frac{\rho_p}{\rho_f}-1\right)$, while $\tilde{h}(\tilde{\mathbf{r}}_p,t)=\tilde{r}_p-\tilde{r}_b-n_B\gamma$ is the dimensionless particle-interface separation distance. Our discussion goes beyond [161] because (2.4) contains additional correction terms and because we will not restrict ourselves to $\hat{\kappa}=0$. Thus, the dynamics of the particle $\tilde{\mathbf{r}}_p(\tilde{t})$ depend on moments of the undisturbed background

fluid velocity at the particle center, the motion of the bubble interface, and the independent dimensionless parameters ϵ, γ, $\hat{\kappa}$, $\tilde{\delta}$ and n_B; we note that λ is related to these by $\lambda = 2/(3n_B^2\gamma^2\tilde{\delta}^2)$.

2.2.2 Time-scale separation and the radial problem

The most extensive set of quantitative experimental data available for comparison (see section 2.4) concerns an interface with almost purely radial oscillations. Thus, we project (2.4) onto the radial direction and obtain a simpler equation using the radial velocity $\tilde{u}$. Such a purely radial oscillation does not give rise to any steady streaming flow [91], so that the non-trivial rectification effects of particle motion studied here can be studied in isolation from streaming transport, which in more general flows would be a further consequence of the oscillations. We do allow for an externally imposed steady Lagrangian component of flow $\epsilon\tilde{u}_L$ in addition to the oscillatory $\tilde{u}_{osc}$, so that $\tilde{u} = \tilde{u}_{osc}(r,\tau) + \epsilon\tilde{u}_L(r) = \tilde{u}_0(r)e^{i\tilde{t}} + \epsilon\tilde{u}_L(r)$, where $\tilde{u}_0(r)$ is the spatial dependence of the oscillatory part. The factor ϵ anticipates the relative scaling of these flows. We make analytical progress using time scale separation, introducing the slow time scale $\tilde{T} = \epsilon^2\tilde{t}$ and expanding (2.4) to second order in ϵ, seeking a solution as

$$\tilde{r}_p(\tilde{t},\tilde{T}) = \tilde{r}_{p_0}(\tilde{t},\tilde{T}) + \epsilon\tilde{r}_{p_1}(\tilde{t},\tilde{T}) + \epsilon^2\tilde{r}_{p_2}(\tilde{t},\tilde{T}) + ... \tag{2.5}$$

The procedure follows [161] closely, taking into account the additional terms, extracting a leading-order equation for $\tilde{r}_{p_0}$ dependent on the slow scale T only (the scale t is averaged out). In the following, we will drop all tildes for clarity. We project (2.4) onto the radial direction to obtain a second order nonlinear ODE for the particle position,

$$\begin{aligned}\lambda\left(\hat{\kappa}+1\right)\frac{d^2r_p}{dt^2} + \left[1 + H\left(\frac{X-\epsilon\Delta R(t)}{\delta}\right)\frac{\gamma}{X-\epsilon\Delta R(t)}\right]\frac{dr_p}{dt} \\ = \epsilon\Bigg[\lambda\left(\frac{\partial u}{\partial t} + \epsilon u\frac{\partial u}{\partial r}\right) + \frac{2}{9}\epsilon\lambda n_B^2\gamma^2\left(\frac{2u}{r_p^2}\left(\frac{\partial u}{\partial r} - \frac{u}{r_p}\right) + \frac{\partial u}{\partial r}\frac{\partial^2 u}{\partial r^2}\right) \\ + u + H\left(\frac{X-\epsilon\Delta R(t)}{\delta}\right)\frac{\gamma\dot{\Delta R}}{X-\epsilon\Delta R(t)}\Bigg]_{r_p},\end{aligned} \tag{2.6}$$

subject to initial conditions:

$$r_p(0) = r_{p_i}, \tag{2.7a}$$

$$\left.\frac{dr_p}{dt}\right|_{t=0} = \epsilon V_i, \tag{2.7b}$$

where $r_b = 1 + \epsilon\Delta R(t)$, $u_b = \frac{1}{\epsilon}\frac{dr_b}{dt} = \dot{\Delta R}$, $X = r_p - 1 - n_B\gamma$ is the gap between particle and mean position of the interface and $H(z) = \exp[-z]$ enforces a decay of the lubrication drag on the order of boundary

layer thickness distance away from the interface. Additionally, we decompose $u = u_{osc}(r,t) + \epsilon u_L$ which is appropriate for radial oscillatory flows with a slow steady component. Assuming all parameters are $O(1)$ and $\epsilon \ll 1$, we introduce a "slow time" $T = \epsilon^2 t$, in addition to the "fast time" t. Using the following transformations

$$r_p(t) \mapsto r_p(t,T), \tag{2.8a}$$

$$\frac{d}{dt} \mapsto \frac{\partial}{\partial t} + \epsilon^2 \frac{\partial}{\partial T}, \tag{2.8b}$$

$$\frac{d^2}{dt^2} \mapsto \frac{\partial^2}{\partial t^2} + 2\epsilon^2 \frac{\partial^2}{\partial t \partial T} + \epsilon^4 \frac{\partial^2}{\partial T^2}, \tag{2.8c}$$

we seek a perturbation solution in the general form: $r_p(t,T) = r_{p_0}(t,T) + \epsilon r_{p_1}(t,T) + \epsilon^2 r_{p_2}(t,T) + \dots$ and separate orders of ϵ. At $O(1)$, the equation is:

$$\lambda\left(\hat{\kappa}+1\right)\frac{\partial^2 r_{p_0}}{\partial t^2} + \left[1 + H_0\frac{\gamma}{h_0}\right]\frac{\partial r_{p_0}}{\partial t} = 0 \tag{2.9}$$

with ICs,

$$r_{p_0}(0,0) = r_{p_i}, \tag{2.10a}$$

$$\left.\frac{\partial r_{p_0}}{\partial t}\right|_{(0,0)} = 0 \tag{2.10b}$$

where we have written $h_0 \equiv X_0 = r_{p_0} - 1 - n_B\gamma$ and also expanded $H(h/\delta) = H(h_0/\delta) + (\epsilon/\delta)\left(r_{p_1} - \Delta R\right) H'(h_0/\delta) + \cdots \equiv H_0 + (\epsilon/\delta)\left(r_{p_1} - \Delta R\right) H_0' + \dots$. Equation (2.9) just means that $O(1)$ changes in particle position only occur over the slow time scale T or, in other words, $r_{p_0}(t,T) = r_{p_0}(T)$ with $r_{p_0}(0) = r_{p_i}$.

Going to $O(\epsilon)$, one obtains:

$$\lambda\left(\hat{\kappa}+1\right)\frac{\partial^2 r_{p_1}}{\partial t^2} + \left(1 + H_0\frac{\gamma}{h_0}\right)\frac{\partial r_{p_1}}{\partial t} = \left[\lambda\frac{\partial u_{osc}}{\partial t} + u_{osc} + H_0\frac{\gamma}{h_0}\dot{\Delta R}\right]_{r_{p_0}}. \tag{2.11}$$

Letting $u_{osc}(r,t) = u(r)e^{it}$, $\Delta R = -ie^{it}$ and $\dot{\Delta R} = e^{it}$, the ensuing linear ODE is solved explicitly by

$$r_{p_1}(t,T) = -i\left(u(r_{p_0}) + w(r_{p_0})\right)e^{it} + A_1(T)\left(1 - e^{-\frac{h_0 + H_0\gamma}{\lambda(\hat{\kappa}+1)h_0}t}\right) + B_1(T), \tag{2.12}$$

where,

$$w = -\frac{\gamma H_0\left(u-1\right) + iu\hat{\kappa}\lambda h_0}{h_0 + \gamma H_0 + i(\hat{\kappa}+1)\lambda h_0}, \tag{2.13}$$

is the oscillatory slip velocity. The general solution $r_{p_1}(t,T)$ satisfies the initial conditions if

$$A_1(0) = \frac{\lambda(\hat{\kappa}+1)h_0}{h_0+\gamma H_0}\left(V_i - u(r_{p_0}) - w(r_{p_0})\right)_{T=0}, \tag{2.14a}$$

$$B_1(0) = i\left(u(r_{p_0}) + w(r_{p_0})\right)_{T=0}. \tag{2.14b}$$

For $|\hat{\kappa}| \ll 1$, transients decay on a scale of $t = O(\lambda)$, corresponding to $O(\lambda/(2\pi)) \lesssim 10$ oscillation cycles for the typical experimental parameters in section 2.4. We note that this time corresponds to $T = O(\epsilon^2\lambda) \ll \epsilon\lambda \ll 1$ (small Stokes number), making transients negligible on the slow time scales of interest. The oscillatory part of r_{p_1} can be, more generally, written as

$$\bar{r}_{p_1} = -i\left(u(r_{p_0}) + w(r_{p_0})\right)e^{it} = \int \left(u_{osc}(r_{p_0}) + w_{osc}(r_{p_0})\right)dt\,. \tag{2.15}$$

With both initial conditions satisfied and ignoring transients, the equation at $O(\epsilon^2)$ after some rearrangement, reads

$$\begin{aligned}
&\lambda(\hat{\kappa}+1)\frac{\partial^2 r_{p_2}}{\partial t^2} + \left(1+H_0\frac{\gamma}{h_0}\right)\frac{\partial r_{p_2}}{\partial t} + \left(1+H_0\frac{\gamma}{h_0}\right)\frac{\partial r_{p_0}}{\partial T} \\
&= \Bigg[u_L + \bar{r}_{p_1}\frac{\partial}{\partial r}\left(\lambda\frac{\partial u_{osc}}{\partial r} + u_{osc}\right) + \frac{2}{9}\lambda n_B^2\gamma^2\left(\frac{2u_{osc}}{r^2}\left(\frac{\partial u_{osc}}{\partial r} - \frac{u_{osc}}{r}\right) + \frac{\partial u_{osc}}{\partial r}\frac{\partial^2 u_{osc}}{\partial r^2}\right) \\
&\quad + \frac{\gamma}{h_0}\left(\frac{H_0}{h_0} - \frac{H_0'}{\delta}\right)\frac{\partial}{\partial t}\left(\frac{(\Delta R - \bar{r}_{p_1})^2}{2}\right) + \lambda\left(u_{osc}\frac{\partial u_{osc}}{\partial r}\right)\Bigg]_{r_{p_0}}.
\end{aligned} \tag{2.16}$$

The slow time (t independent) dynamics are obtained by performing a time average of (2.16) over a fast time oscillation cycle. As a consequence, only terms involving slow time (T) and products of first order fast time (t) quantities survive and the resulting time-averaged equation reduces to the following explicitly

computable form,

$$\begin{aligned}\left(1+H_0\frac{\gamma}{h_0}\right)\frac{\partial r_{p_0}}{\partial T} =& u_L(r_{p_0}) + \left\langle\left(\int w_{osc}(r_{p_0})dt\right)\frac{\partial}{\partial r}\left(\lambda\frac{\partial u_{osc}}{\partial t}+u_{osc}\right)\right\rangle_{r_{p_0}} \\ &+\frac{2}{9}\lambda n_B^2\gamma^2\left\langle\frac{2u_{osc}}{r^2}\left(\frac{\partial u_{osc}}{\partial r}-\frac{u_{osc}}{r}\right)+\frac{\partial u_{osc}}{\partial r}\frac{\partial^2 u_{osc}}{\partial r^2}\right\rangle_{r_{p_0}} \\ &+\frac{\gamma}{h_0}\left(\frac{H_0}{h_0}-\frac{H_0'}{\delta}\right)\overbrace{\frac{\partial}{\partial t}\left\langle\frac{(\Delta R-\bar{r}_{p_1})^2}{2}\right\rangle}^{\text{identically 0}} \\ &+\lambda\overbrace{\frac{\partial}{\partial t}\left\langle\left(\int u_{osc}(r_{p_0})dt\right)\frac{\partial u_{osc}}{\partial r}\right\rangle}^{\text{identically 0}} \\ &+\overbrace{\left\langle\left(\int u_{osc}(r_{p_0})dt\right)\frac{\partial u_{osc}}{\partial r}\right\rangle}^{\text{Fluid Stokes drift = 0 for monopole}} \quad . \end{aligned} \tag{2.17}$$

The non-zero time averages on the RHS of the above equation can be conveniently computed using complex variables and after making appropriate substitutions, the resulting equation is an overdamped (first order in time) ODE for the particle position representing a quasi-steady force balance involving only the instantaneous undisturbed flow field:

$$\begin{aligned} -F_D &= F_R + F_\rho + F_{i,2} \equiv F_\lambda\,, \quad \text{where} \\ F_D &= \left(u_L - \frac{h_0+H_0\gamma}{h_0}\frac{dr_{p_0}}{dT}\right), \\ F_R &= \left(H_0\gamma\lambda\frac{(-1+u_0(r_{p_0}))\,u_0'(r_{p_0})}{2}\frac{h_0(\hat{\kappa}+2)+H_0\gamma}{(h_0+H_0\gamma)^2+h_0^2\lambda^2(\hat{\kappa}+1)^2}\right), \\ F_\rho &= \left(\hat{\kappa}\lambda\frac{u_0(r_{p_0})u_0'(r_{p_0})}{2}h_0\frac{h_0\left(\lambda^2(\hat{\kappa}+1)-1\right)-H_0\gamma}{(h_0+H_0\gamma)^2+h_0^2\lambda^2(\hat{\kappa}+1)^2}\right), \\ F_{i,2} &= \left(\frac{1}{9}\lambda n_B^2\gamma^2\left(\frac{2u_0(r_{p_0})}{r_{p_0}^2}\left(u_0'(r_{p_0})-\frac{u_0(r_{p_0})}{r_{p_0}}\right)+u_0'(r_{p_0})u_0''(r_{p_0})\right)\right). \end{aligned} \tag{2.18}$$

Every non-dimensional force term can be made dimensional by multiplying with the Stokes drag scale $\mathcal{F}_S \equiv 6\pi\nu\rho_f a_p\epsilon^2 a_b\omega$.

In (2.18), $h_0 = r_{p0} - 1 - n_B\gamma$ is the average of the separation distance h over an oscillation cycle, $H_0 = H(h_0/\delta)$, and all the flow quantities are evaluated at the particle position. F_D is the drag force acting on the particle, whereas F_R results from inertial rectification terms independent of $\hat{\kappa}$ and repels the particle from the interface if u_0 decays with r (as is physically reasonable for most flow fields). While these two contributions have been explained in a previous study [161], the last two terms are novel and add attractive forces to the scenario. The force F_ρ is proportional to the density contrast ($\hat{\kappa}$) and particle inertia (λ)

parameters; it is attractive for $\hat{\kappa} > 0$ and $\lambda \gtrsim 1$. This term decays more slowly with r near the interface compared to the inertial rectification term and typically overwhelms it at distances $h_0 \geq \gamma$. The last term, $F_{i,2}$, represents the inviscid correction of [83] (last term in (2.1)), which always attracts the particle towards the interface regardless of $\hat{\kappa}$, but decays more strongly with r since it depends on higher-order derivatives of the flow field.

Having completed the time-scale separation, we verify that the $r_{p_0}(T)$ dynamics resulting from (2.18) agrees with the full unsteady numerical solution of (2.4) for a range of parameter combinations (λ, $\hat{\kappa}$ and γ). Anticipating comparison to an experimental situation where a bubble oscillates in a spherical breathing mode, we set $u_0(r) = 1/r^2$, $n_B = 4$ and solve both equations, first assuming $u_L = 0$. Figure 2.2 illustrates this agreement for two representative cases, showing repulsion for light particles in Figure 2.2a and attraction towards a fixed-point distance for density matched particles in Figure 2.2b. The existence of fixed points for r_{p_0} can be assessed by evaluating the net inertial force F_λ. Figure 2.2c graphs F_λ for the two representative cases, showing that the first is unconditionally repulsive ($F_\lambda > 0$ for all r) while the second has a stable fixed point at some surface-to-surface distance h_s, where $dr_{p_0}/dT = 0$.

We can estimate the magnitude of h_s by expanding F_λ for $\lambda \gg 1$, $\gamma \ll 1$, and $|\hat{\kappa}| \ll 1$ (the situation reflecting the most common range of experimental parameters modeled here) and obtain

$$h_s \approx \frac{(2\gamma)^{3/2}}{(32\gamma^2 + \hat{\kappa})^{1/2}\lambda}\,. \tag{2.19}$$

For approximately density-matched particles this further simplifies to the estimate $h_s \sim \gamma^{1/2}/(4\sqrt{2}\lambda)$. Thus, for typical parameters in oscillator experiments (where often $\lambda \gg 1$) the equilibrium distance is expected to be extremely small compared with the interface scale, and typically even compared with the particle scale. This shows (i) that the inclusion of a lubrication force term is important to explain particle behavior near an equilibrium point and (ii) that it should be experimentally feasible to stably position particles at extraordinarily close distances to the interface.

2.3 Parameter dependence of the forces

Since (2.18) is a first-order ODE, it is easily integrated numerically for many parameter combinations to construct a phase diagram in order to predict the behavior of a particle executing oscillatory motion in a radial flow field (with $u_L = 0$). One expects any such flow field to be dominated by the lowest-order oscillation mode—therefore, as in the above example, we will fix the flow to the monopolar field $u_0 = 1/r^2$ (induced by a spherical bubble in breathing mode, so that $n_B = 4$). The practically relevant question is then

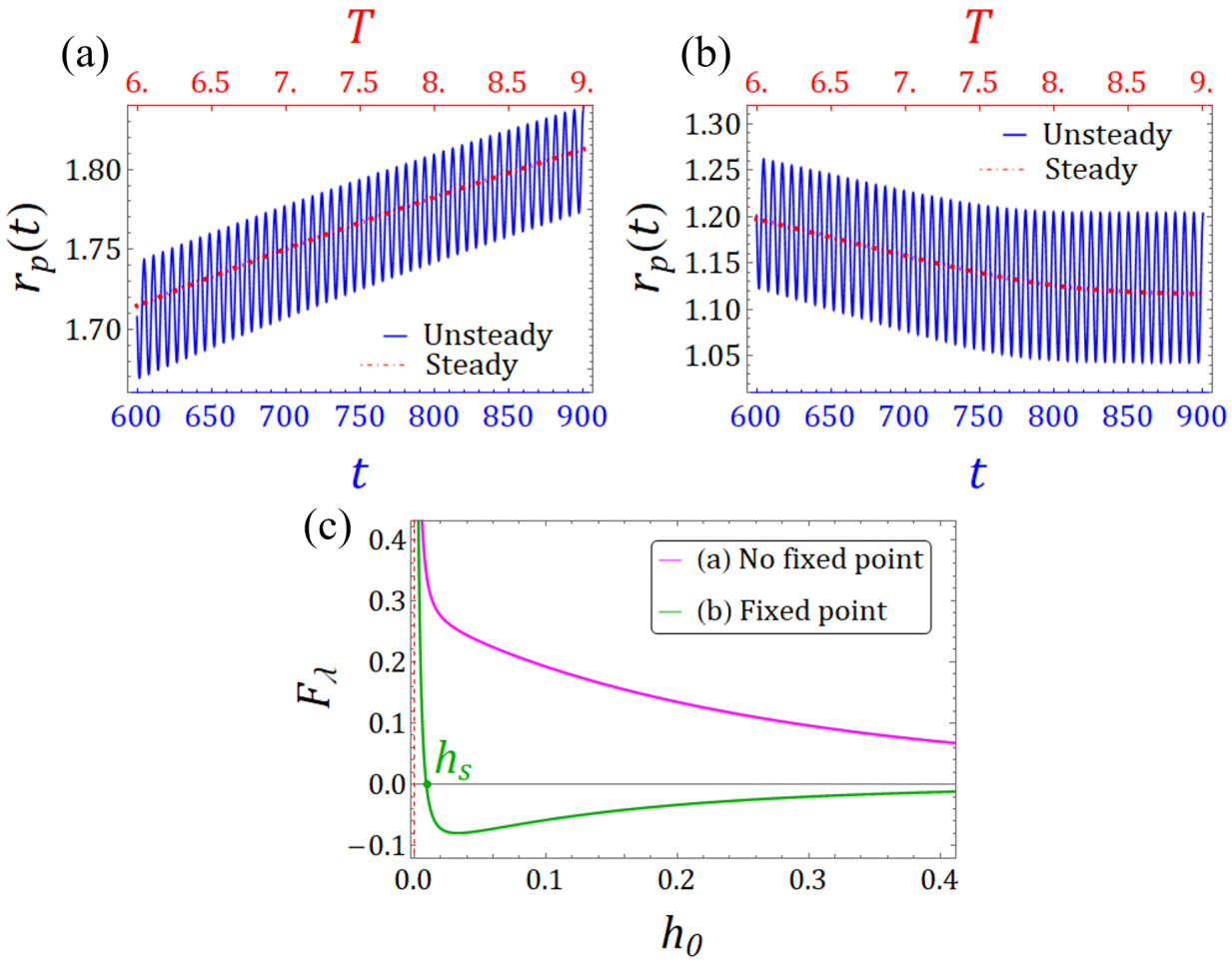

Figure 2.2: Comparison of slow-time (steady, Eq.(2.18)) and oscillatory (unsteady, Eq.(2.4)) numerical solution for $\epsilon = 0.1$, $\gamma = 0.026$, $r_p(0) = 1.36$ and $r_p'(0) = \epsilon u_0(r_p(0), 0) = 0.054$ (with $u_L = 0$, $n_B = 4$): (a) $\hat{\kappa} = -0.06$ (particle lighter than fluid), $\lambda = 10$; (b) $\hat{\kappa} = 0$ (density matched), $\lambda = 10$; (c) Total steady force on the particle as a function of interface separation, showing no fixed points for the repulsive case (a) and a stable fixed point for the attractive case (b).

whether there is attraction to or repulsion away from the interface depending on parameters. As explained above, the physical distinction is between cases where there are no fixed points (F_λ is always positive, and thus repulsive) and cases where a stable fixed point exists (cf. Fig. 2.2c), with the force being attractive for $h > h_s$. By continuity, there will be a range of parameters in between these cases where two fixed points (one stable, one unstable) exist so that $F_\lambda < 0$ for a finite range $h_s < h < h_u$ while still $F_\lambda(r \to \infty) > 0$. It can be shown, however, that this regime of a finite range of attraction is small and always closely adjacent to the critical points where $h_s = h_u = h_c$. The latter condition of the double fixed point requires the simultaneous fulfillment of

$$F_\lambda(h_c) = 0\,, \qquad F'_\lambda(h_c) = 0\,. \tag{2.20}$$

In the following phase diagrams, we choose our axes as the easiest parameters to change independently in experiment: particle size (i.e., γ) and density contrast (i.e., $\hat{\kappa}$). The relative importance of viscosity on the particle is quantified by the dimensionless boundary layer thickness $\delta = \sqrt{\frac{2\nu}{a_b^2\omega}}$. We first determine a phase diagram for fixed δ: Finding pairs of (γ, $\hat{\kappa}$) values that solve (2.20) yields the red curves in Fig. 2.3a and 2.3b, which show that two separate regions of net repulsion exist (for $\hat{\kappa}$ and γ both small or both large), separated by a contiguous region of attraction. We quantify the behavior in the attractive and repulsive regions differently: In Fig. 2.3a, we show the separation distance h_s at the stable fixed point position. Note that these values tend to be very small (small fractions of the oscillator radius a_b, and for realistic parameters often in the sub-micron range). By contrast, for the repulsive region Fig. 2.3b shows the time (in slow time units $1/(\epsilon^2\omega)$) required for a particle initially touching the interface to traverse its own diameter $2a_p$. This is a time that may be relevant in experiments in which particles are supposed to be separated by size. As the phase plot shows, these times quickly become very small even a short distance away from the phase boundary between attraction and repulsion. In summary, the forces exerted on the particles effect their displacement quickly and efficiently. Figure 2.3c demonstrates that this scenario does not qualitatively depend on the exact magnitude of viscous effects (changing δ). Even for much larger $\delta \gtrsim 1$, this statement is valid, although the boundaries between attraction and repulsion get pushed to regions of γ and $\hat{\kappa}$ that are either impractical (too large density difference leads to rapid precipitation or creaming of even very small particles) or violate conditions such as $\gamma \ll 1$.

Further analysis shows that the almost horizontal phase boundaries in Figs. 2.3 for small γ are dominated by a sign change of F_ρ, which, to leading approximation for $|\hat{\kappa}| \ll 1$, is given by the condition $\lambda = 1$, translating into $\gamma = (3/32)^{1/2}\delta$. The horizontal dot-dashed lines in Fig. 2.3c demonstrate the accuracy of this approximation. The other boundary in the phase diagram results from balancing the leading order terms of F_ρ and $F_{i,2}$ for $\lambda \gg 1$ and $h_s \ll 1$, so that the radial coordinate is $r_s \approx 1 + 4\gamma$. This obtains

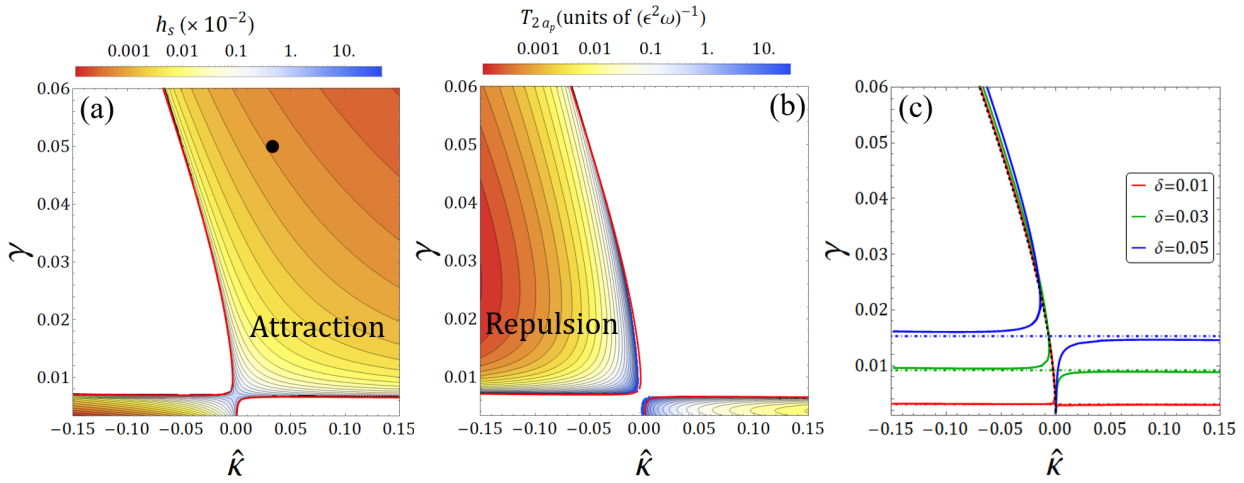

Figure 2.3: Phase diagrams of particle behavior as a function of γ and $\hat{\kappa}$; (a), (b) have fixed $\delta = 0.022$. (a) Attractive case: contours indicate the fixed-point equilibrium distance h_s between particle and interface; the red line is the boundary for existence of fixed points from (2.20). The black dot identifies the experimental parameters of section 2.4. (b) Repulsive case: contours indicate the time T_{2a_p} for a particle near touching the interface to traverse a distance $2a_p$. (c) Boundary between the attractive and repulsive cases for different δ. The dot-dashed and dashed lines give the analytical predictions based on the sign change of F_ρ and the balancing of the terms F_ρ and $F_{i,2}$, respectively (see the text for more details).

a boundary governed by $\hat{\kappa}/(\hat{\kappa}+1) = 32\gamma^2/(1+4\gamma)^2$ independent of δ, which the dashed line in Fig. 2.3c proves to be an accurate prediction, almost indistinguishable from the numerically determined boundary for small δ.

2.4 Particles near an Interface: Comparison with experiment

In a recent study [35], a series of experiments were performed that approximate closely the simple scenario quantified in the previous section: A near-spherical microbubble ($a_b = 150\,\mu$m) was placed at the wall of a microfluidic chamber, and spherical polystyrene beads ($a_p = 30\,\mu$m, $\rho_p = 1050$ kg/m^3) were transported near the bubble by an imposed channel flow (water, $\rho_f = 1000$ kg/m^3), cf. Fig. 2.4a. When the bubble was driven by a Piezo transducer ($f = 20 - 36$ kHz), it responded by nearly exclusively volumetric, small-amplitude oscillations (typically $\epsilon < 0.01$); this purely radial dynamics was intentionally set up to suppress streaming effects. Beyond a threshold ($\epsilon > \epsilon_c$), particles sufficiently close to the bubble were caught and transported to a stationary position very close to the bubble interface (Fig. 2.4b), from which they could be released by lowering ϵ below ϵ_c. We are grateful to Prof. Lee and her group for making the data set from this experiment available to us.

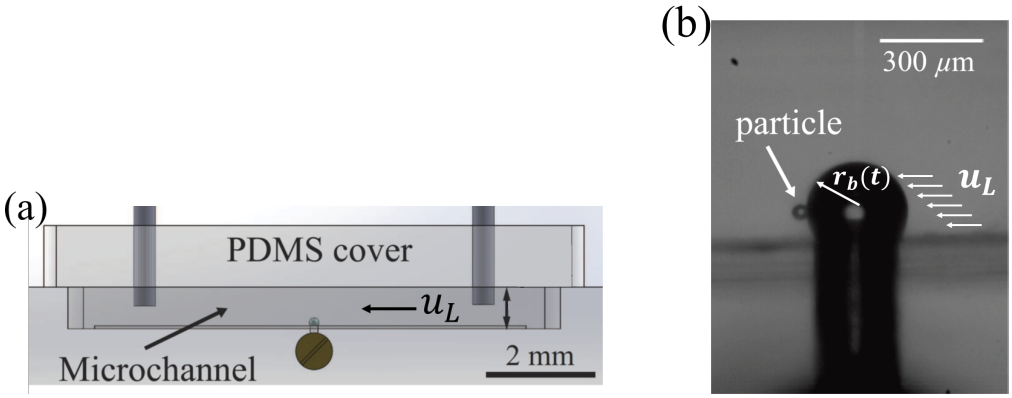

Figure 2.4: Experimental setup (figure modified from [35]); (a) a spherical bubble is exposed to the microchannel flow u_L and driven to volumetric oscillations by a piezoelectric transducer; (b) a spherical particle is captured at a close distance to the bubble interface.

2.4.1 Polystyrene particle trapping/release

The channel flow past the bubble induces a steady flow component u_L around the bubble, exerting a drag on the particle, which by itself would transport the particle away from the bubble. It is the net attractive force from the rectified oscillatory flow that successfully counteracts the drag. Assessing the parameters for a typical experimental situation ($f = 29\,\mathrm{kHz}$ results in $\lambda \approx 55$, while $\hat{\kappa} \approx 0.033$ and $\gamma \approx 0.05$, and thus $\delta \approx 0.022$), we find that, as expected, these parameter values lie well within the attractive regime predicted by the phase diagram from equation (2.18) for $u_L = 0$ as shown by the black dot in Figure 2.3a. To model this experimental scenario, we need to incorporate u_L in (2.18), the flow field induced by the channel flow. A strong enough u_L, or small enough ϵ, will move the boundary of the corresponding phase diagram such that an attractive scenario becomes repulsive to the particle.

2.4.2 Theory results

We model the flow field u_L as a low-Re steady flow flowing around the bubble in the downstream (x) direction, obeying no-slip boundary conditions at the channel wall and no-stress at the bubble surface. The particle will be located at a height y_p above the wall and the flow must asymptote to the channel Poiseuille flow speed u_c in the downstream direction, $u_L(x \to \infty, y = y_p) = u_c$. From the rectangular channel dimensions, and the flow rate given in [35], a Poiseuille solution is constructed (cf. [113, 158]) and the dimensional U_c at height $y_p a_b$ is obtained. Since the steady part of the flow field is defined as $\epsilon \tilde{u}_L(r)$ (see section 2.2B), this translates to $u_c = U_c/(\epsilon^2 a_b \omega)$; for the experiments on the release of particles we model here, the particle is situated $\approx 75\mu$m away from the wall, and the asymptotic speed is $U_c \approx 7.5$mm/s. Knowing u_c, the flow u_L is then constructed by taking into account the no-slip boundary condition at the wall exactly while the no-stress

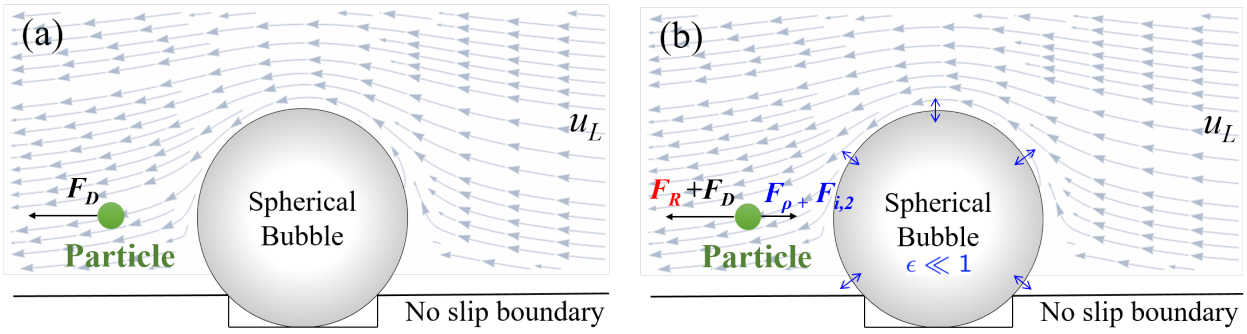

Figure 2.5: (a) Computed flow field u_L around the quiescent bubble, indicating the drag F_D on the particle; (b) with volumetric bubble oscillations, the Force balance from (2.18) determines particle position.

condition at the bubble interface is satisfied approximately using singularity flow results from the literature [19, 20, 77, 110]. Omitting some details, u_L is obtained analytically as a sum of Stokeslet, a stresslet, and their corresponding image systems along with a background linear shear flow that approximates the Poiseuille flow well near the wall (cf. Fig. 2.5). The height of the captured particle in experiment coincides closely with the location of the bubble equator (note the bubble is situated in a recessed pit), so that the drag force F_D acts under a small angle to the radial direction. The force is projected onto the r-direction accordingly to balance it with those force components induced by the oscillatory flow. All force terms in the slow-time equation (2.18) are now evaluated and plotted in Fig. 2.6a for the aforementioned experimental parameter values as a function of distance. The sum $F_\lambda + u_L$ is shown in Fig. 2.6c, and zeroes of this function mark equilibrium points with zero particle velocity. The repulsive force F_R leads, as expected, to the formation of a stable equilibrium at h_s, and the presence of F_D induces an unstable equilibrium at $h_u > h_s$. The value of h_s is insensitive to parameter changes within the range of experiments and translates to a sub-micron gap between bubble and particle at equilibrium, consistent with video material. Contrast this situation with a force balance that only contains the drag F_D and the acoustic far-field secondary radiation force approximation [18, 42, 68]

$$F_{SR} = -\frac{\lambda}{r^5}\left(\frac{\hat{\kappa}}{\hat{\kappa}+1}\right) \tag{2.21}$$

(Figs. 2.6b and 2.6d), as suggested in previous approaches [35, 143]: while the attractive force values are of similar magnitude, there is no stable equilibrium at any finite distance from the bubble. The particle would be driven to contact with the bubble, contradicting the experiments.

The existence of a net attractive force for the range of gap $h_s < h < h_u$ explains the experiments that capture particles approaching the bubble sufficiently closely. While the minimum approach distance for capture was not quantified, the video data indicates that this distance is on the order of a few 10 μm,

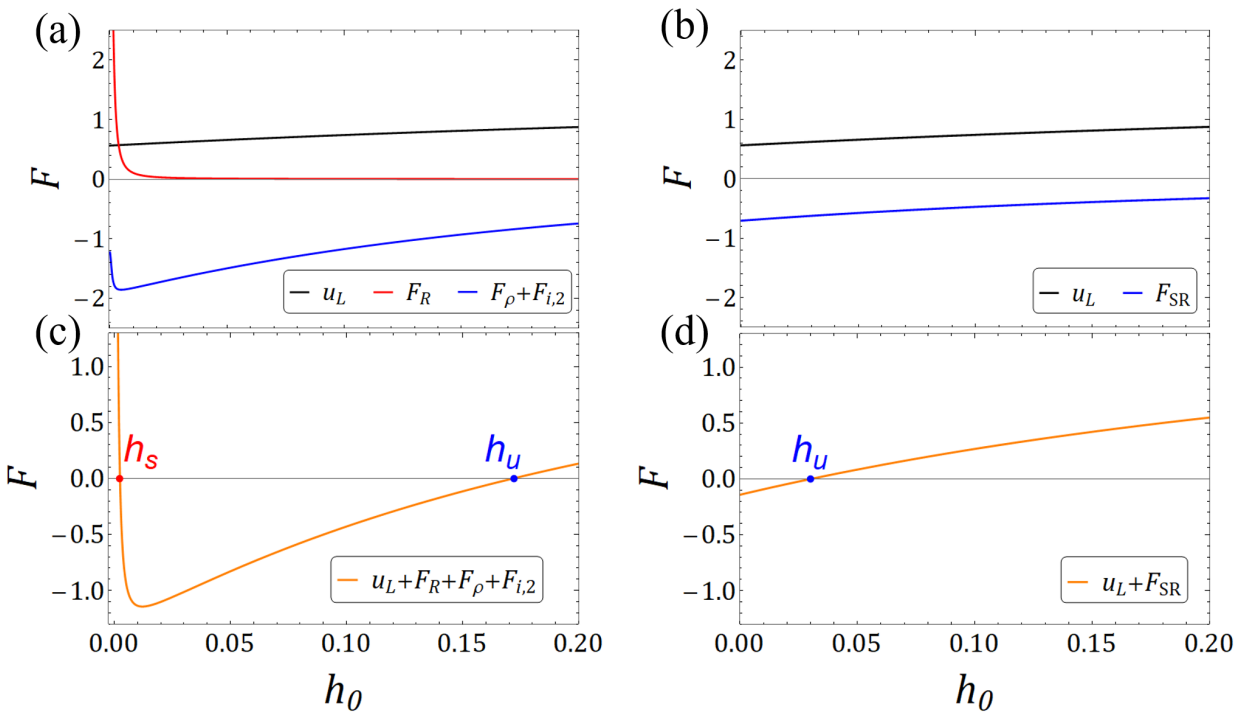

Figure 2.6: Force contributions for $\lambda = 55$, $\gamma = 0.05$, $\hat{\kappa} = 0.033$ corresponding to the experiments with $\epsilon = 0.012$. Radial distances are normalized by $a_b = 150\,\mu$m; the dashed red line at $r_p = 1.2$ indicates contact between particle and bubble. (a) Forces from (2.18); (b) F_{SR} and Drag force; (c) sum of forces in (a) showing two fixed points at r_s and r_u; (d) Sum of forces in (b) resulting in only one unstable fixed point.

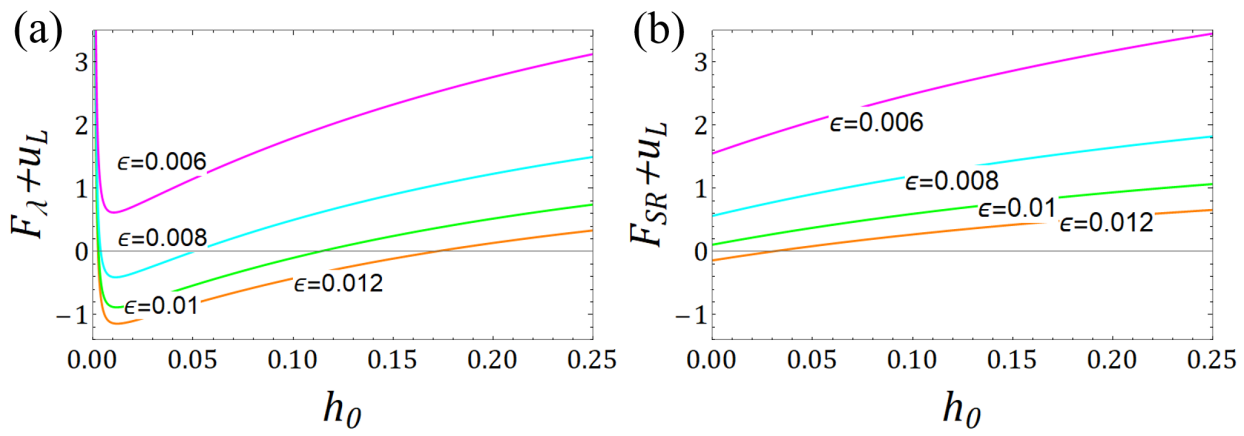

Figure 2.7: Particle release. (a) Sum of forces from (2.18): as ϵ is decreased, the stable fixed point is lost at a finite distance from bubble surface ($\epsilon_c \approx 0.007$ in agreement with experiment); (b) Sum of F_{SR} and F_D: the unstable fixed point is lost at the bubble surface, and ϵ_c does not agree with the measured value.

consistent with Fig. 2.6c. The particle was released from the trapping when the bubble oscillation amplitude fell below $\epsilon_c \approx 0.006$ in experiment. This is easily tested within the model: the force balance suggested by [35] is plotted in Fig. 2.6c for different values of ϵ. The stable and unstable fixed points approach as ϵ is decreased and merge (at the analog of the phase boundary in Fig. 2.3a) when $\epsilon = \epsilon_c \approx 0.007$, in good agreement with the observed value. Unlike in Fig. 2.6d, which again depicts the balance of F_D and F_{SR} only, our model shows that the equilibrium point is lost at a finite distance from the bubble surface as ϵ is decreased—dimensionally, the particle-bubble distance is still very small at this point, $h_0 \approx 1.5\,\mu$m. It should be noted that the magnitude of the modeled attractive force is significantly altered by the presence of the higher-order term $F_{i,2}$ for particles with these experimental parameters. Without it, the agreement with experiment would not be quantitative. The successful modeling for this particular $f = 29\,$kHz case translates directly to the other frequencies in the experimental range, as the dependence of ϵ_c on f in both experiment and theory is consistent with $\epsilon_c \propto 1/f$ [35]. This behavior can be deduced from the dominant balance of u_L and F_ρ, taking into account the scaling of u_L and λ with ϵ and $\omega = 2\pi f$.

2.5 Particles at large distances: Connection to Acoustofluidics

The equations developed in Section 2.2 prove accurate both very close to the interface as well as at moderate distances and incorporates both viscous and inviscid effects. When the particle is at a large distance from the interface, the situation becomes analogous to SRF in acoustofluidics [30], where the particle is exposed to the oscillatory flow in a standing or traveling wave without a material boundary nearby. We note that there exist many well-established results in the inviscid limit of acoustofluidics, while in the opposite limit

of strong viscous effects the recent literature gives contradictory results even for the direction of the force in certain situations [44, 48, 148].

The motivation for the present section is twofold: (i) we demonstrate that the Maxey–Riley like approach outlined in this chapter reduces to well-known results in acoustofluidics in the large distance limit and thus bridges the fields of acoustofluidics and inertial microfluidics; (ii) we will shed light on the debate on the direction of viscous acoustofluidic forces. For definiteness, we shall compare the force on a particle in a spherical monopolar flow field (the $r \to \infty$ limit of the previous section) with that on a particle in a standing wave field. These results are expected to be equivalent except for effects of compressibility contrast between particle and fluid in the acoustofluidic case [30], resulting in monopole scattering, which cannot occur in our analysis of a rigid particle in incompressible flow. Since the particle is far away from boundaries, it becomes appropriate to include the viscous corrections mentioned in section 2.2.A, which can be derived from the Basset–Boussinesq history force for translational oscillation in bulk. These corrections depend on the the viscous boundary layer thickness δ or, equivalently, its ratio to particle size $\delta_p = \delta/(n_B\gamma) = \sqrt{\frac{2}{3\lambda}}$. Explicitly, the hydrodynamic force (2.3) on the particle, in this far-field limit, becomes

$$\mathbf{F}^H \approx -6\pi\nu\rho_f a_p \left[\left(\frac{d\mathbf{r}_p}{dt} - \mathbf{u}\right)\left(1 + \frac{1}{\delta_p}\right)\right] - \left(\frac{1}{2} + \frac{9}{4}\delta_p\right) m_f \left(\frac{d\mathbf{v}_p}{dt} - \frac{D\mathbf{u}}{Dt}\right) + m_f \frac{D\mathbf{u}}{Dt} \tag{2.22}$$

Appropriate to the $r \to \infty$ limit, we have omitted the lubrication term and the higher-order inviscid correction. Note that the δ_p correction terms are of sub-leading order for either $\delta_p \ll 1$ or $\delta_p \gg 1$. The corrections are understood to be applied to the oscillatory terms of the particle and fluid velocities (for which a δ_p is defined), but not to the slow-time parts. As before, we render (2.22) dimensionless and perform time scale separation; the projection on the radial direction is natural in this limit (the radial axis connects the oscillator and the particle). The resulting slow-time equation is

$$\frac{dr_{p0}}{dT} = \hat{\kappa}\frac{u_0(r_{p0})u_0'(r_{p0})}{3\delta_p^2}\left(\frac{(1+3\delta_p/2)\,(\hat{\kappa}+1+3\delta_p/2) - \left(3\delta_p^2/2\,(1+1/\delta_p)\right)^2}{(\hat{\kappa}+1+3\delta_p/2)^2 + \left(3\delta_p^2/2\,(1+1/\delta_p)\right)^2}\right). \tag{2.23}$$

Here, we have made use of the relation $\lambda = 2/(3\delta_p^2)$ to obtain a particle speed explicitly dependent on $\hat{\kappa}$ and δ_p. Interpreting the right-hand side as an effective far-field force F_f and normalizing by the secondary radiation force F_{SR} from (2.21), we obtain

$$\frac{F_f}{F_{SR}} = (\hat{\kappa}+1)\left(\frac{(1+3\delta_p/2)\,(\hat{\kappa}+1+3\delta_p/2) - \left(3\delta_p^2/2\,(1+1/\delta_p)\right)^2}{(\hat{\kappa}+1+3\delta_p/2)^2 + \left(3\delta_p^2/2\,(1+1/\delta_p)\right)^2}\right) \tag{2.24}$$

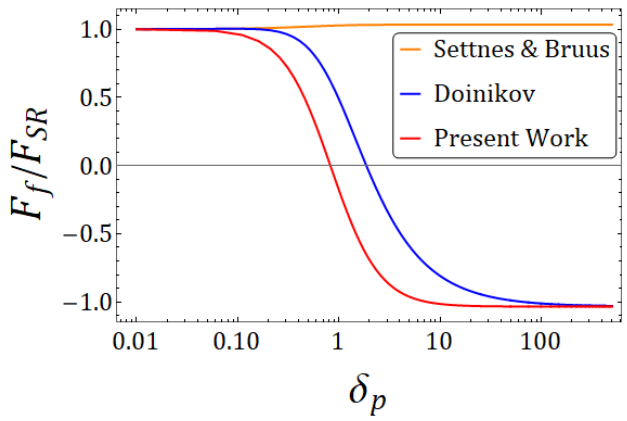

Figure 2.8: Normalized force on a particle for large distances from the oscillation source, graphed as a function of $\delta_p = \sqrt{2\nu/(a_p^2\omega)}$ for $\hat{\kappa} = 0.033$ (corresponding to a polystytrene particle in water). The present work (Eq.(2.24)) predicts a sign change of the force as viscous effects become important, in agreement with Doinikov [48] and in contradiction to Settnes and Bruus [148].

This ratio is depicted in Fig. 2.8; it asymptotes to 1 for $\delta_p \to 0$ independent of $\hat{\kappa}$, as expected, and shows a dramatic reversal of sign around $\delta_p \sim 1$. The asymptote at large δ_p depends on $\hat{\kappa}$, but approaches -1 for $|\hat{\kappa}| \ll 1$.

Also shown in Fig. 2.8 are two results from the acoustofluidics literature that both computed the contributions of monopole and dipole scattering from a spherical particle in a standing-wave field under the large sound wavelength assumption ($\lambda_w \gg a_p$) for arbitrary δ_p. Only the dipole part of those solutions is plotted, as effects of compressibility contrast are not present in the current situation. While [48] predicts a sign reversal like our approach, more recently [148], using a simplified formalism, have argued that this result is unphysical. The qualitative agreement of our independent Maxey-Riley like approach with Doinikov [48] is obvious and can be further quantified: in the two limits, we obtain from (2.24),

$$F_{\delta_p \to 0} = F_{SR}\left[1 + \frac{3}{2}\left(\frac{\hat{\kappa}}{\hat{\kappa}+1}\right)\delta_p + O\left(\delta_p\right)^2\right] \tag{2.25a}$$

$$F_{\delta_p \to \infty} = -F_{SR}\left[(\hat{\kappa}+1) + O\left(\frac{1}{\delta_p}\right)^2\right] \tag{2.25b}$$

The explicitly shown orders are in exact agreement with [48]. The approximations in our formalism do not simultaneously and systematically expand the viscous and inviscid force contributions, and fail to pick up the $O(\delta_p^{-1})$ in the viscous limit. The theory of [148] omits several viscous effects, primarily because of the assumption of a potential flow in the far-field of the particle. While appropriate for the oscillatory flow, this assumption is inconsistent with the secondary (steady) flow, whose inertia is negligible and as a result does not have an inviscid far-field, i.e. viscous stresses are comparable with the fluid pressure [44, 48].

In addition, [148] implicitly assume that (i) the disturbance flow due to particle translation is weak, by neglecting self-interaction terms, and (ii) the disturbance flow due to the straining of the background flow is negligible. All of these assumptions are associated with viscous effects that are systematically accounted for in the work of [48] and [44], and that are approximated by our current theory.

2.6 Conclusions

A generalized model for inertial forces on particles in incompressible oscillatory flows was derived that takes into account the effect of an interface at any distance and approximates important viscous effects (δ_p values). Time scale separation of the oscillatory Maxey-Riley-like equation allows for a fast, simple calculation of forces leading to a formalism that provides simple predictions for the rectified migration of particles relative to a background flow field that is previously computed or measured and is an explicit input to the computation. Note that this steady particle displacement is different from any steady streaming displacement of the fluid elements—while there was no streaming in the particular (monopolar) flow fields quantified here, its presence does not affect the conclusions.

The parameter dependence of forces shows that even the simplest oscillatory flow fields can have both attractive and repulsive effects on particles depending on their relative density, their size relative to the interface scale and relative to the boundary layer thickness, as well as on the separation distance from the interface. Attraction eventually positions the particle at a stable equilibrium point that in many cases is much closer to the interface than any of the imposed scales of the problem. This makes the approach well-suited for accumulating, concentrating, and accurate positioning of objects in microfluidic flow set-ups, including biological cells. For the latter, the finite stand-off distance from the interface furthermore prevents harmful exposure of the cells to a body of gas.

The regions of attraction and repulsion in the phase diagrams are governed primarily by the density-dependent inertial force F_ρ, which is a generalization of F_{SR} in acoustofluidics, showing a richer dependence on parameters and particle position. The δ-dependence of the phase diagram also shows that a judicious choice of parameters allows for a transition from attractive to repulsive behavior or vice versa not only by changing the drag from an externally imposed flow or the amplitude of oscillation, but also by changing the frequency of driving, which is usually the easiest to effect. Release of particles from capture thus becomes predictable and selectively tunable. We also demonstrate that near the interface there are always significant force contributions independent of density contrast, unlike what would be inferred from F_{SR} alone.

While the formalism opens up new possibilities for manipulation of microparticles very close to interfaces,

it is also applicable to particles at larger distance from the oscillating object. Then our approach agrees in both the viscous and inviscid limits with forces in acoustofluidic standing-wave fields, bridging inertial-force research in the acoustofluidic and microfluidic fields.

It should also be noted that the forces exerted on particles in the flow from oscillating interfaces can be considerably stronger—whether attractive or repulsive—than those in other inertial microfluidics (either shear-induced migration or acoustofluidics). Any (dimensional) inertial force in this context can be written as $\mathcal{F} \sim \rho U^2 a_p^2 f(\hat{\kappa}) g(a_p/L_u)$, where U^2 is a scale of squared flow velocity and g is a dimensionless function of particle size and characteristic flow length scale L_u. In inertial shear migration [47], U^2 is simply the square of the steady transport speed u_L, while in a channel of height H, $g = (a_p/H)^2$ or, near the wall of the channel, $g = (a_p/H)^4$; the $\hat{\kappa}$ dependence is weak in this case. For the radiation force $\mathcal{F}_{SR}$ of acoustofluidics, $U^2 = \langle u_w^2 \rangle$ with the oscillating fluid velocity in the wave u_w; furthermore, $g = a_p/\lambda_w$, using the wavelength λ_w, and (focusing on dipolar scattering) $f = \hat{\kappa}$. In the current work, we can write the dimensional rectification forces $\mathcal{F}_R$, $\mathcal{F}_\rho$, and $\mathcal{F}_{i,2}$ using $U^2 = \langle (\epsilon a_b \omega)^2 u_{osc}^2 \rangle$ and $g = a_p/a_b$. $\mathcal{F}_\rho$, as an analog of $\mathcal{F}_{SR}$, shares the proportionality $f = \hat{\kappa}$, while the other contributions are approximately or exactly $\hat{\kappa}$-independent. Compared with shear migration, the forces described here scale more favorably with a_p and are larger because of the smaller scale $a_b < H$. The oscillatory velocity scale can easily exceed either typical transport speeds or fluid speeds in acoustic waves (also, $a_b < \lambda_w$ in many cases for practical parameters).

Furthermore, a different oscillation behavior of the interface (different $u_0(r)$) will give rise to different positional dependence of the forces, opening more versatile options for the capture and manipulation of particle position. The interface does not need to be a bubble—oscillating membranes or solid objects on the microscale (cf. [1, 95]) are other possibilities. Exploiting these advantages should lead to exciting applications for a variety of tasks in microfluidics—from trapping and concentrating, to controlled release, to simultaneous size segregation and transport. The latter task involves generalizing the current theory to higher-dimensional flows, which will be described in Chapter 6.

Chapter 3

Generalized formalism for inertial forces on particles

In the previous chapter, we modeled inertial forces on particles by an ad hoc superposition of the leading-order viscous and inviscid effects [83]. While this approximation works well in the high-frequency (large λ) limit, it has shortcomings in the intermediate frequency range, i.e., when $\lambda \sim \mathcal{O}(1)$, arguably, the operational regime for a large majority of practical microfluidic lab-on-a-chip applications. In this chapter[1], we systematically derive the formal $\mathcal{O}(\mathrm{Re}_p)$ inertial force on the particle in *any* general time-dependent background flow that varies on scales much larger than the particle size. Subsequently, this formalism is specialized to the case of oscillatory background flows, due to their paramount significance in modern microfluidics. The next two chapters are devoted to obtaining closed-form results that are valid across the entire operational viscous-to-inviscid spectrum of λ. For neutrally buoyant particles, we find a previously unrecognized flow-curvature induced inertial force that is generically present in a large class of microfluidic systems, independent of particle-fluid compressibility or density contrasts. We also find additional density-contrast dependent inertial force terms, not present in existing formalisms, that are not small effects but can be quite significant, thus generalizing important slip-velocity dependent inertial forces on non-neutrally buoyant particles in oscillatory flows.

3.1 Introduction

Describing the motion of particles immersed in a given background flow is a fundamental fluid dynamics problem that has evaded a general solution. Most analytical attempts work under the assumption of reversible unsteady Stokes flows, i.e., inertial effects that break the symmetry of such flows are completely neglected. The main theoretical foundation for describing forces on particles was laid by the work of Maxey and Riley [103] (MR), introduced almost 40 years ago, and still represents the state-of-the-art. In their detailed and systematic derivation they clearly stated the pertinent assumptions and elucidated several intricate theoretical concepts—exposing and rectifying some of the omissions and errors of previous ad hoc,

[1] This chapter is adapted from Agarwal et al. [5, 6]

semi-empirical studies on the equation of motion of a rigid sphere. As a result, the final equation has been used extensively in the last forty years.

While successful in many practical applications, they made several assumptions in the derivation of the creeping flow equation and laid out the severity of its limitations. One of its most glaring shortcomings was pointed out by Leal [82], concerning its incompatibility with the experimentally observed phenomenon of lateral migration of particles due to lift forces, which are a consequence of inertial effects. Subsequent work has aimed at the development of equations valid at finite Reynolds numbers, however, these are specialized to individual applications and no general and practically useful formalism exists to systematically account for these effects in general flows. Modern microfluidics, through its use of inertia to reliably manipulate fluid-borne objects, is further pushing the envelope of the MR equation, exposing its inability to explain many experimental observations.

The derivation of MR makes two important assumptions. In particular, it is valid for spherical particles of radius a_p with small inertia; specifically, (i) the particle Reynolds number based on a typical *difference* velocity between particle speed and background flow must be small, and (ii) the background flow gradients must be small compared to viscous momentum diffusion (or $\epsilon\lambda << 1$); so that the disturbance flow satisfies the unsteady Stokes equation. In many typical inertial microfluidic applications involving particle sorting or trapping, the second assumption typically breaks down, e.g., near a localized oscillating interface since, for many practically relevant cases, $\mathrm{Re}_p \sim \epsilon\lambda \sim \mathcal{O}(1)$. The high-frequency inviscid limit of $\lambda \gg 1$ was treated in the previous chapter by augmenting the force contribution with the additional higher order term derived in [83], however, one needs a more systematic way to include viscous effects.

We first sketch a brief outline of our formalism: Incorporating the inertial terms in the equation of motion is done through a regular perturbation expansion. The application of a generalized reciprocal theorem (cf. [93]) formally yields the $\mathcal{O}(\mathrm{Re}_p)$ inertial force as a volume integral over the entire domain without needing to actually compute the flow field at that order. To evaluate this volume integral one does, however, need as input the leading order disturbance flow (unsteady Stokes flow) explicitly. Analytical progress is made by Taylor expanding the background flow around the particle centre and expressing the leading order unsteady Stokes disturbance flow in terms of known background flow quantities and general mobility tensors for spherical, rigid objects. For example, one can exploit the spherical symmetry for an oscillating sphere immersed in a quiescent flow to obtain closed-form solutions, (cf. the classical Landau-Lifshitz solution for the disturbance flow field around an oscillating solid sphere [81]). Finally, the volume integral involves taking products of Laplace-transformed quantities and is executed analytically. We thus systematically obtain expressions for the $\mathcal{O}(\mathrm{Re}_p)$ force on a rigid particle and its equation of motion.

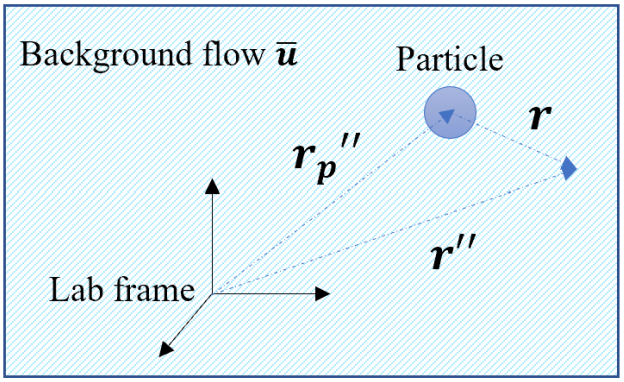

Figure 3.1: Caricature of coordinate system used. Quantities with double primes, such as $\mathbf{r}''$, are in the fixed reference frame of the lab, while quantities without the primes, such as $\mathbf{r}$, are in the moving reference frame located at the particle center.

3.2 Theoretical Formalism

In order to systematically account for the inertial forces on a sphere of radius a_p centered at $\mathbf{r}_p$ moving with with velocity $\mathbf{u}_p$ (neglecting effects of rotation) and exposed to a known (lab-frame) background undisturbed flow $\bar{\mathbf{u}}$, we begin with the non-dimensionalized Navier–Stokes equation for the flow around a rigid sphere [103]:

$$\nabla^2 \boldsymbol{u}'' - \nabla p'' = 3\lambda \frac{\partial(\mathbf{u}'' + \mathbf{u}_p)}{\partial t} + \mathrm{Re}_p \left[\boldsymbol{u}'' \cdot \nabla \boldsymbol{u}''\right], \tag{3.1a}$$

$$\boldsymbol{\nabla} \cdot \boldsymbol{u}'' = 0, \tag{3.1b}$$

$$\boldsymbol{u}'' = 0 \quad \text{on } r'' = 1, \tag{3.1c}$$

$$\boldsymbol{u}'' = \overline{\boldsymbol{u}} - \boldsymbol{u}_p \quad \text{as } r'' \to \infty. \tag{3.1d}$$

where we non-dimensionalize velocities by U^*, lengths by a_p, pressure by $\mu U^*/a_p$ and time by $1/\omega$, and express them in particle-fixed coordinates (lower case represents non-dimensional quantities everywhere). Here, $\mathrm{Re}_p = U^* a_p/\nu$ is the non-dimensional particle Reynolds number and we have used the following relation between the absolute and relative frames of reference: $(\partial \mathbf{u}/\partial t)_a = (\partial \mathbf{u}/\partial t)_r - \mathbf{u}_p \cdot \nabla \mathbf{u}$. The parameter λ is, generally, a measure of the timescale of unsteadiness relative to the vorticity diffusion timescale (a_p^2/ν); it specializes to the expression defined in the preceding chapter for oscillatory flows. We introduce the disturbance velocity and pressure fields $\mathbf{u} = \mathbf{u}'' - \overline{\mathbf{u}} + \mathbf{u}_p$ and $p = p'' - \overline{p}$ such that the fluid velocity in the laboratory frame is given by $\mathbf{v} = \mathbf{u} + \overline{\mathbf{u}}$ (see Fig. 3.1).

We generally split the Navier–Stokes equations that govern the flow field into an undisturbed flow $\boldsymbol{w}^{(0)} = \bar{\mathbf{u}} - \mathbf{u}_p$ and a disturbance flow $\boldsymbol{w}^{(1)}$ (we adopt the same notation as [103]). Then, in a particle-centered

(moving) coordinate system, we have

$$\nabla^2 \boldsymbol{w}^{(0)} - \nabla p^{(0)} = 3\lambda \frac{\partial \boldsymbol{w}^{(0)}}{\partial t} + \mathrm{Re}_p \left(\boldsymbol{w}^{(0)} \cdot \nabla \boldsymbol{w}^{(0)} \right), \tag{3.2a}$$

$$\nabla^2 \boldsymbol{w}^{(1)} - \nabla p^{(1)} = 3\lambda \frac{\partial \boldsymbol{w}^{(1)}}{\partial t} + \mathrm{Re}_p \left[(\bar{\mathbf{u}} - \mathbf{u}_p) \cdot \nabla \boldsymbol{w}^{(1)} + \boldsymbol{w}^{(1)} \cdot \nabla \bar{\mathbf{u}} + \boldsymbol{w}^{(1)} \cdot \nabla \boldsymbol{w}^{(1)} \right], \tag{3.2b}$$

$$\boldsymbol{\nabla} \cdot \boldsymbol{w}^{(0)} = 0, \quad \boldsymbol{\nabla} \cdot \boldsymbol{w}^{(1)} = 0, \tag{3.2c}$$

$$\boldsymbol{w}^{(1)} = \mathbf{u}_p - \bar{\mathbf{u}} \quad \text{on } r = 1 \quad \text{and} \quad \boldsymbol{w}^{(1)} = 0 \quad \text{as } r \to \infty, \tag{3.2d}$$

where $\mathrm{Re}_p = U^* a_p / \nu$ is the particle Reynolds number. Quantities in these equations are non-dimensionalized by scaling velocities with U^*, lengths with a_p, pressure with $\mu U^*/a_p$, and time by ω^{-1}.

The force contribution from the undisturbed flow is $\mathbf{F}^{(0)} = (F_S/6\pi) \oint_S \mathbf{n} \cdot \boldsymbol{\sigma}^{(0)} dS$, like in the original Maxey–Riley (MR) formalism [103], where $\boldsymbol{\sigma}^{(0)} = -p^{(0)}\mathbf{I} + \nabla \boldsymbol{w}^{(0)} + \left(\nabla \boldsymbol{w}^{(0)}\right)^T$ is the stress tensor associated with the undisturbed flow field $\boldsymbol{w}^{(0)}$, and $F_S/6\pi = \nu \rho a_p U^*$ is the Stokes drag scale. The force contribution at the disturbance flow order is given by $\mathbf{F}^{(1)} = (F_S/6\pi) \oint_S \mathbf{n} \cdot \boldsymbol{\sigma}^{(1)} dS$, where $\boldsymbol{\sigma}^{(1)} = -p^{(1)}\mathbf{I} + \nabla \boldsymbol{w}^{(1)} + \left(\nabla \boldsymbol{w}^{(1)}\right)^T$ is the stress tensor associated with the disturbance flow field $\boldsymbol{w}^{(1)}$. The corresponding (dimensional) equation of motion for the particle then reads

$$m_p \frac{d\mathbf{U}_p}{dt} = \mathbf{F}^{(0)} + \mathbf{F}^{(1)}. \tag{3.3}$$

Note that everything up to this point is exact and no assumptions have been made. MR [103] make the unsteady Stokes flow approximation in (3.2) by setting $\mathrm{Re}_p = 0$, and compute $\mathbf{F}^{(1)}$ without explicitly evaluating the disturbance flow, using a symmetry relation. While this assumption is plausible in many traditional microfluidic flow situations, recent advances in, e.g., fast oscillatory particle manipulation can give rise to large disturbance flow gradients so that the inertial terms on the RHS of (3.2b) are not necessarily negligible compared to the viscous diffusion term (typically $\mathrm{Re}_p \sim \mathcal{O}(1)$).

3.2.1 Small Re_p expansion

In order to make analytical progress, following [43, 70, 73], we expand $\boldsymbol{w}^{(1)}$, $p^{(1)}$, $\mathbf{r}_p$, $\mathbf{u}_p$ and $\boldsymbol{\sigma}^{(1)}$ (and consequently $\mathbf{F}^{(1)}$) in a regular asymptotic expansion for small Re_p,

$$\boldsymbol{w}^{(1)} = \boldsymbol{w}_0^{(1)} + \mathrm{Re}_p\, \boldsymbol{w}_1^{(1)} + \dots, \tag{3.4a}$$

$$p^{(1)} = p_0^{(1)} + \mathrm{Re}_p\, p_1^{(1)} + \dots, \tag{3.4b}$$

$$\mathbf{r}_p = \mathbf{r}_{p_0} + \mathrm{Re}_p\, \mathbf{r}_{p_1} + \dots, \tag{3.4c}$$

$$\mathbf{u}_p = \mathbf{u}_{p_0} + \mathrm{Re}_p\, \mathbf{u}_{p_1} + \dots, \tag{3.4d}$$

$$\boldsymbol{\sigma}^{(1)} = \boldsymbol{\sigma}_0^{(1)} + \mathrm{Re}_p\, \boldsymbol{\sigma}_1^{(1)} + \dots, \tag{3.4e}$$

$$\mathbf{F}^{(1)} = \mathbf{F}_0^{(1)} + \mathrm{Re}_p\, \mathbf{F}_1^{(1)} + \dots. \tag{3.4f}$$

The leading-order equations for $(\boldsymbol{w}_0^{(1)}, p_0^{(1)})$ are unsteady Stokes,

$$\nabla^2 \boldsymbol{w}_0^{(1)} - \nabla p_0^{(1)} = 3\lambda \frac{\partial \boldsymbol{w}_0^{(1)}}{\partial t}, \tag{3.5a}$$

$$\boldsymbol{\nabla} \cdot \boldsymbol{w}_0^{(1)} = 0, \tag{3.5b}$$

$$\boldsymbol{w}_0^{(1)} = \mathbf{u}_{p_0} - \bar{\mathbf{u}} \quad \text{on } \mathbf{r} = 1, \tag{3.5c}$$

$$\boldsymbol{w}_0^{(1)} = 0 \quad \text{as } \mathbf{r} \to \infty. \tag{3.5d}$$

We note that in the original derivation of MR [103], a symmetry relation was used at this order to compute $\mathbf{F}_0^{(1)}$ without explicitly solving for $\boldsymbol{w}_0^{(1)}$. However, since we are interested in computing the force contribution at $\mathcal{O}(\mathrm{Re}_p)$, we need an explicit solution for the leading-order disturbance flow $\boldsymbol{w}_0^{(1)}$. To obtain explicit results, we expand the background flow field $\bar{\mathbf{u}}$ around the leading-order particle position $\mathbf{r}_{p_0}$ into spatial moments of alternating symmetry,

$$\bar{\mathbf{u}} = \bar{\mathbf{u}}|_{\mathbf{r}_{p_0}} + \mathbf{r} \cdot \mathbf{E} + \mathbf{r}\mathbf{r} : \mathbf{G} + \dots, \tag{3.6}$$

where $\mathbf{E} = (a_p/L_\Gamma)\nabla\bar{\mathbf{u}}|_{\mathbf{r}_{p_0}}$ and $\mathbf{G} = \frac{1}{2}(a_p^2/L_\kappa^2)\nabla\nabla\bar{\mathbf{u}}|_{\mathbf{r}_{p_0}}$ with gradient L_Γ and curvature L_κ length scales. This approximation is valid as long as the background flow varies on scales much larger than the particle size, i.e., $a_p \ll \min(L_\Gamma, L_\kappa, \dots)$. As a consequence of (3.6), the boundary condition (3.5c) is also expanded around $\mathbf{r}_{p_0}$, so that in the particle fixed coordinate system

$$\boldsymbol{w}_0^{(1)} = \mathbf{u}_{p_0} - \bar{\mathbf{u}} = \mathbf{u}_{p_0} - \bar{\mathbf{u}}|_{\mathbf{r}_{p_0}} - \mathbf{r} \cdot \mathbf{E} - \mathbf{r}\mathbf{r} : \mathbf{G} + \dots \quad \text{on} \quad \mathbf{r} = 1\,, \tag{3.7}$$

where we have retained the first three terms in the background flow velocity expansion. Owing to the linearity of the leading order unsteady Stokes equation, the solution can generally be expressed as [81, 132]

$$\boldsymbol{w}_0^{(1)} = \boldsymbol{\mathcal{M}}_D \cdot \mathbf{u}_s - \boldsymbol{\mathcal{M}}_Q \cdot (\mathbf{r} \cdot \mathbf{E}) - \boldsymbol{\mathcal{M}}_O \cdot (\mathbf{rr} : \mathbf{G}) + \ldots, \tag{3.8}$$

where $\boldsymbol{\mathcal{M}}_{D,Q,O}(r, \lambda)$ are spatially dependent mobility tensors. For oscillatory flows, they depend on the Stokes number λ, while for other flows they may have a more complicated dependence on relevant parameters. More explicit forms of these tensors will be given in Section 3.3.1.

With the leading-order disturbance flow field known, the equations at $\mathcal{O}(\mathrm{Re}_p)$ are as follows:

$$\nabla^2 \boldsymbol{w}_1^{(1)} - \nabla p_1^{(1)} = \nabla \cdot \boldsymbol{\sigma}_1^{(1)} = 3\lambda \frac{\partial \boldsymbol{w}_1^{(1)}}{\partial t} + \mathbf{f}_0, \tag{3.9a}$$

$$\boldsymbol{\nabla} \cdot \boldsymbol{w}_1^{(1)} = 0, \tag{3.9b}$$

$$\boldsymbol{w}_1^{(1)} = \mathbf{u}_{p_1} \quad \text{on } \mathbf{r} = 1, \tag{3.9c}$$

$$\boldsymbol{w}_1^{(1)} = 0 \quad \text{as } \mathbf{r} \to \infty\,, \tag{3.9d}$$

where $\mathbf{f}_0 = \boldsymbol{w}^{(0)} \cdot \nabla \boldsymbol{w}_0^{(1)} + \boldsymbol{w}_0^{(1)} \cdot \nabla \boldsymbol{w}^{(0)} + \boldsymbol{w}_0^{(1)} \cdot \nabla \boldsymbol{w}_0^{(1)}$ is the (explicitly known) leading-order nonlinear forcing of the disturbance flow. In order to compute the force at this order, we employ a reciprocal relation in the Laplace domain since the problem is time-dependent and, for oscillatory flows, the Laplace transform is explicitly obtained.

3.2.2 Reciprocal theorem and test flow

As shown in Fig. 3.2, a known test flow (denoted by primed quantities such as $\mathbf{u}'$) is chosen around a sphere executing a time-dependent motion $u'(t)\,\mathbf{e}$ such that it satisfies the following unsteady Stokes equation:

$$\nabla^2 \mathbf{u}' - \nabla p' = \nabla \cdot \boldsymbol{\sigma}' = 3\lambda \frac{\partial \mathbf{u}'}{\partial t}, \tag{3.10a}$$

$$\boldsymbol{\nabla} \cdot \mathbf{u}' = 0, \tag{3.10b}$$

$$\mathbf{u}' = u'(t)\,\mathbf{e} \quad \text{on } \mathbf{r} = 1, \tag{3.10c}$$

$$\mathbf{u}' = 0 \quad \text{as } \mathbf{r} \to \infty, \tag{3.10d}$$

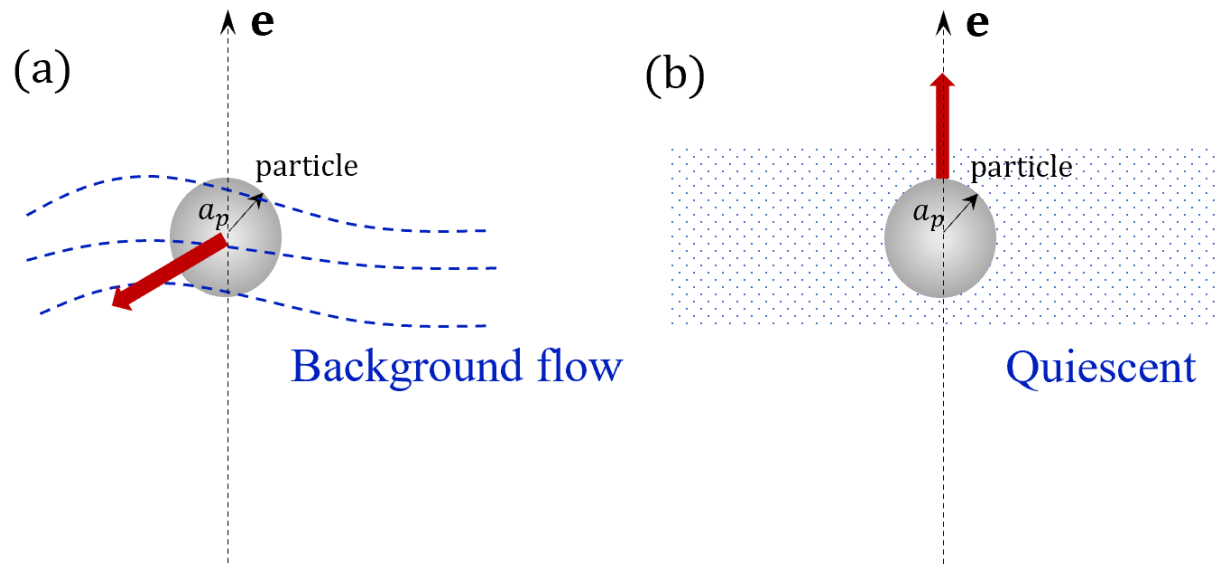

Figure 3.2: (a) Spherical particle immersed in a general time-dependent background flow. The unit vector $\mathbf{e}$ coincides with the direction in which the force is desired; (b) Model problem of a sphere in a quiescent fluid executing time-dependent motion $u'(t)$ in the direction of the unit vector $\mathbf{e}$.

where the unit vector $\mathbf{e}$ is chosen to coincide with the direction in which the force on the particle is desired. The solution to this problem is of the same form as (3.8), but with only the first term, i.e.,

$$\mathbf{u}' = u'(t)\boldsymbol{\mathcal{M}}_D \cdot \mathbf{e}\,. \tag{3.11}$$

Denoting Laplace transformed quantities by hats (e.g., $\hat{\mathbf{u}}$), one can write down the following symmetry relation using the divergence theorem (cf. [73, 93, 103]):

$$\oint_S (\hat{\boldsymbol{w}}_1^{(1)} \cdot \hat{\boldsymbol{\sigma}}' - \hat{\mathbf{u}}' \cdot \hat{\boldsymbol{\sigma}}_1^{(1)}) \cdot \mathbf{m}\, dS = \int_V \left[\nabla \cdot (\hat{\boldsymbol{w}}_1^{(1)} \cdot \hat{\boldsymbol{\sigma}}') - \nabla \cdot (\hat{\mathbf{u}}' \cdot \hat{\boldsymbol{\sigma}}_1^{(1)})\right] dV, \tag{3.12}$$

where $\mathbf{m}$ is the outward unit normal vector to the surface (pointing inward over the sphere surface), and $\hat{\boldsymbol{\sigma}} = \nabla\hat{\mathbf{u}} + (\nabla\hat{\mathbf{u}})^T - \hat{p}\mathbf{I}$. Substituting boundary conditions from (3.9) and (3.10), and setting the volume equal to the fluid-filled domain, we obtain

$$\begin{aligned}
&\hat{\mathbf{u}}_{p_1}^{(1)} \cdot \int_{S_p} (\hat{\boldsymbol{\sigma}}' \cdot \mathbf{m}) dS - \hat{u}'\mathbf{e} \cdot \int_{S_p} (\hat{\boldsymbol{\sigma}}_1^{(1)} \cdot \mathbf{m}) dS + \int_{S_\infty} (\hat{\boldsymbol{w}}_1^{(1)} \cdot \hat{\boldsymbol{\sigma}}') \cdot \mathbf{m} dS - \int_{S_\infty} (\hat{\mathbf{u}}' \cdot \hat{\boldsymbol{\sigma}}_1^{(1)}) \cdot \mathbf{m} dS \\
&= \int_V \left[\hat{\boldsymbol{w}}_1^{(1)} \cdot (\nabla \cdot \hat{\boldsymbol{\sigma}}') - \hat{\mathbf{u}}' \cdot (\nabla \cdot \hat{\boldsymbol{\sigma}}_1^{(1)}) + \nabla\hat{\boldsymbol{w}}_1^{(1)} : \hat{\boldsymbol{\sigma}}' - \nabla\hat{\mathbf{u}}' : \hat{\boldsymbol{\sigma}}_1^{(1)}\right] dV\,.
\end{aligned} \tag{3.13}$$

The third term on the LHS is 0 since the viscous test flow stress tensor decays to zero at infinity. Similarly, the integral in the fourth term vanishes in the far field if viscous stresses dominate inertial terms, and also in the case of inviscid irrotational flows (see [93, 157]). The third and fourth terms on the RHS also go to zero, owing to incompressibilty and symmetry of the stress tensor, explicated in the following:

$$\begin{aligned}&\nabla\hat{\boldsymbol{w}}_1^{(1)} : \hat{\boldsymbol{\sigma}}' - \nabla\hat{\mathbf{u}}' : \hat{\boldsymbol{\sigma}}_1^{(1)} \\ &= \nabla\hat{\boldsymbol{w}}_1^{(1)} : (\nabla\hat{\mathbf{u}}' + (\nabla\hat{\mathbf{u}}')^T) - \hat{p}'\nabla\cdot\hat{\boldsymbol{w}}_1^{(1)} - \nabla\hat{\mathbf{u}}' : (\nabla\hat{\boldsymbol{w}}_1^{(1)} + (\nabla\hat{\boldsymbol{w}}_1^{(1)})^T) - \hat{p}^{(1)}\nabla\cdot\hat{\mathbf{u}}' = 0\,. \end{aligned} \tag{3.14}$$

The divergence of the hatted stress tensors in the remaining two terms of the RHS can be obtained by taking the Laplace transforms of (3.9) and (3.10) and using the property $\widehat{f'(t)} = s\widehat{f(t)} - f(0)$, so that

$$\nabla\cdot\hat{\boldsymbol{\sigma}}' = \bar{\lambda}s\hat{\mathbf{u}}' - \mathbf{u}'(0), \tag{3.15a}$$

$$\nabla\cdot\hat{\boldsymbol{\sigma}}_1^{(1)} = \bar{\lambda}s\hat{\boldsymbol{w}}_1^{(1)} - \boldsymbol{w}_1^{(1)}(0) + \hat{\mathbf{f}}_0\,. \tag{3.15b}$$

Now, the force on the sphere at this order is given by $\mathbf{F}_1^{(1)} = \int_{S_p}(\boldsymbol{\sigma}_1^{(1)}\cdot\mathbf{n})dS = -\int_{S_p}(\boldsymbol{\sigma}_1^{(1)}\cdot\mathbf{m})dS$, since $\mathbf{m}$ points inwards while $\mathbf{n}$ points outwards on the surface of the sphere. Assuming both flows start from rest, we have (cf. [93])

$$\hat{u}'\mathbf{e}\cdot\frac{\hat{\mathbf{F}}_1^{(1)}}{F_S/(6\pi)} = \hat{\mathbf{u}}_{p_1}\cdot\int_{S_p}(\hat{\boldsymbol{\sigma}}'\cdot\mathbf{n})dS - \int_V \hat{\mathbf{u}}'\cdot\hat{\mathbf{f}}_0 dV + \mathcal{O}(\mathrm{Re}_p^2)\,. \tag{3.16}$$

Adding the force contribution from the previous order, the net force on the particle due to its disturbance flow reads

$$\begin{aligned}\hat{u}'\mathbf{e}\cdot\frac{\hat{\mathbf{F}}^{(1)}}{F_S/(6\pi)} &= \hat{u}'\mathbf{e}\cdot\left(\hat{\mathbf{F}}_0^{(1)} + \mathrm{Re}_p\,\hat{\mathbf{F}}_1^{(1)}\right) + \mathcal{O}(\mathrm{Re}_p^2) \\ &= \int_{S_p}\left(\hat{\mathbf{u}}_{p_0} - \hat{\bar{\mathbf{u}}} + \mathrm{Re}_p\,\hat{\mathbf{u}}_{p_1}\right)\cdot(\hat{\boldsymbol{\sigma}}'\cdot\mathbf{n})dS - \mathrm{Re}_p\int_V \hat{\mathbf{u}}'\cdot\hat{\mathbf{f}}_0 dV + \mathcal{O}(\mathrm{Re}_p^2) \qquad (3.17a)\\ \implies \mathbf{e}\cdot\mathbf{F}^{(1)} &= \frac{F_S}{6\pi}\mathcal{L}^{-1}\left\{\int_{S_p}\frac{\left(\hat{\mathbf{u}}_p - \hat{\bar{\mathbf{u}}}\right)}{\hat{u}'}\cdot(\hat{\boldsymbol{\sigma}}'\cdot\mathbf{n})dS - \frac{1}{\hat{u}'}\mathrm{Re}_p\int_V\hat{\mathbf{u}}'\cdot\hat{\mathbf{f}}_0 dV\right\} + \mathcal{O}(\mathrm{Re}_p^2), \qquad (3.17b)\end{aligned}$$

where we have used $\mathbf{u}_p = \mathbf{u}_{p_0} + \mathrm{Re}_p\, \mathbf{u}_{p_1} + \mathcal{O}(\mathrm{Re}_p^2)$, and $\mathcal{L}^{-1}$ denotes the inverse Laplace transform. Therefore, in summary, the equation of motion in the direction $\mathbf{e}$ reads,

$$m_p \frac{dU_p}{dt} = F_0^{(0)} + F_0^{(1)} + \mathrm{Re}_p(F_1^{(0)} + F_1^{(1)}) + \mathcal{O}(\mathrm{Re}_p^2), \tag{3.18a}$$

$$F_0^{(0)} = \frac{F_S}{6\pi} \int_V (3\lambda \partial_t \bar{\mathbf{u}}) \cdot \mathbf{e} dV, \tag{3.18b}$$

$$F_0^{(1)} = \frac{F_S}{6\pi} \mathcal{L}^{-1} \left\{ \int_{S_p} \frac{(\hat{\mathbf{u}}_p - \hat{\bar{\mathbf{u}}})}{\hat{u}'} \cdot (\hat{\boldsymbol{\sigma}}' \cdot \mathbf{n}) dS \right\}, \tag{3.18c}$$

$$F_1^{(0)} = \frac{F_S}{6\pi} \int_V (\bar{\mathbf{u}} \cdot \nabla \bar{\mathbf{u}}) \cdot \mathbf{e} dV, \tag{3.18d}$$

$$F_1^{(1)} = -\frac{F_S}{6\pi} \mathcal{L}^{-1} \left\{ \frac{1}{\hat{u}'} \int_V \hat{\mathbf{u}}' \cdot \hat{\mathbf{f}}_0 dV \right\}, \tag{3.18e}$$

The first term on the RHS of (3.17b) is denoted as $F_0^{(1)}$ (and is the same as that obtained by MR), while the second term represents the $\mathcal{O}(\mathrm{Re}_p)$ inertial force and is denoted as $F_1^{(1)}$. We note that no assumptions about the time or spatial dependence of the background flow have been made so far, and the formalism is entirely general. In the next section, we will specialize to oscillatory flows.

3.3 Evaluation of the inertial force

In this section, we will explicitly evaluate the volume integral in (3.17b) representing the $\mathcal{O}(\mathrm{Re}_p)$ inertial force due to the disturbance flow. This requires obtaining $\mathbf{f}_0$ from the leading-order disturbance flow field $\boldsymbol{w}_0^{(1)}$. In the following, we obtain explicit closed-form solutions for particles in oscillatory flows with spherical symmetry.

3.3.1 Solution to the unsteady Stokes equation for the disturbance flow

We already remarked that, given the background flow field expansion in uniform, linear, and quadratic parts around the particle, $\boldsymbol{w}_0^{(1)}$ is formally obtained as the linear combination (3.8). For harmonically oscillating, axisymmetric background flows (i.e., $\bar{\mathbf{u}}(\mathbf{r}) = \{\bar{u}_r, \bar{u}_\theta, 0\}$ in the spherical particle coordinate system, with all components $\propto e^{it}$), general explicit expressions can be derived for the mobility tensors $\boldsymbol{\mathcal{M}}_{D,Q,O}$, ensuring no-slip boundary conditions on the sphere order-by-order. A procedure obtaining $\boldsymbol{\mathcal{M}}_D$ is described in Landau–Lifshitz [81]; the other tensors are determined analogously. Using components in spherical coordinates, they

read

$$\boldsymbol{\mathcal{M}}_D = \begin{bmatrix} \frac{2a(r)}{r^2} & 0 & 0 \\ 0 & \frac{a'(r)}{r} & 0 \\ 0 & 0 & 0 \end{bmatrix}, \quad \boldsymbol{\mathcal{M}}_Q = \begin{bmatrix} \frac{b(r)}{r^3} & 0 & 0 \\ 0 & \frac{b'(r)}{3r^2} & 0 \\ 0 & 0 & 0 \end{bmatrix}, \quad \boldsymbol{\mathcal{M}}_O = \begin{bmatrix} \frac{-32c(r)}{3r^4} & 0 & 0 \\ 0 & \frac{8c'(r)}{3r^3} & 0 \\ 0 & 0 & 0 \end{bmatrix}, \tag{3.19}$$

where

$$a(r) = \frac{1}{2\beta^2 r}\left[\beta^2 - 3i\beta + 3 - 3e^{-i\beta(r-1)}\left(1 + i\beta r\right)\right], \tag{3.20a}$$

$$b(r) = \frac{1}{\beta^2(\beta - i)r^2}\left[\beta(-15 + \beta(\beta - 6i)) + 15i + 5e^{-i\beta(r-1)}(\beta r(3 + i\beta r) - 3i)\right], \tag{3.20b}$$

$$c(r) = \frac{-3(105 + \beta(\beta(-45 + \beta(\beta - 10i)) + 105i)) + 21e^{-i\beta(r-1)}(15 + \beta r(-\beta r(6 + i\beta r) + 15i))}{32\beta^2(-3 + \beta(\beta - 3i))r^3}, \tag{3.20c}$$

and $\beta = \sqrt{-ia_p^2/(\nu/\omega)} = \sqrt{-3i\lambda}$ is the complex oscillatory boundary layer thickness. We emphasize that these expressions are the same for arbitrary axisymmetric oscillatory $\bar{\mathbf{u}}$. Accordingly, only the expansion coefficients $\mathbf{u}_s$, $\mathbf{E}$, and $\mathbf{G}$ contain information about the particular flow.

Similarly, the solution to the unsteady test flow is obtained directly as

$$\mathbf{u}' = \boldsymbol{\mathcal{M}}_D \cdot \begin{bmatrix} \cos\theta \\ -\sin\theta \\ 0 \end{bmatrix} e^{it}. \tag{3.21}$$

It is understood everywhere that physical quantities are obtained by taking real parts of these complex functions.

3.3.2 Execution of the volume integral

In order to compute the volume integral in (3.17b), we first note that only certain products in $\mathbf{f}_0$ are non-vanishing when the angular integration over θ is performed. In particular, due to alternating symmetry of terms in the background flow field expansion (3.6), and consequently in the leading order disturbance flow (3.8), only products of adjacent terms survive. This is because, in the Taylor expansion of the background flow field, the first and third terms are symmetric ($\mathbf{u}(-\mathbf{r}) = \mathbf{u}(\mathbf{r})$) while the second one is anti-symmetric ($\mathbf{u}(-\mathbf{r}) = -\mathbf{u}(\mathbf{r})$). For example, the first term in $\mathbf{f}_0$ reads

$$\boldsymbol{w}^{(0)} \cdot \nabla \boldsymbol{w}_0^{(1)} = (-\mathbf{u}_s + \mathbf{r} \cdot \mathbf{E} + \mathbf{rr} : \mathbf{G}) \cdot \nabla \left(\boldsymbol{\mathcal{M}}_D \cdot \mathbf{u}_s - \boldsymbol{\mathcal{M}}_Q \cdot (\mathbf{r} \cdot \mathbf{E}) - \boldsymbol{\mathcal{M}}_O \cdot (\mathbf{rr} : \mathbf{G})\right), \tag{3.22}$$

and the only terms that survive the angular integration are the symmetric ones (after a contraction with the symmetric test flow $\mathbf{u}'$), i.e.,

$$(-\mathbf{u}_s + \mathbf{rr} : \mathbf{G}) \cdot \nabla \left(-\boldsymbol{\mathcal{M}}_Q \cdot (\mathbf{r} \cdot \mathbf{E})\right) + (\mathbf{r} \cdot \mathbf{E}) \cdot \nabla \left(\boldsymbol{\mathcal{M}}_D \cdot \mathbf{u}_s - \boldsymbol{\mathcal{M}}_O \cdot (\mathbf{rr} : \mathbf{G})\right) . \tag{3.23}$$

All of the above quantities are explicitly known for oscillatory flows and the evaluation of the volume integration is straightforward. In the following chapter, we will quantify the leading-order inertial force contribution for neutrally buoyant particles, while the subsequent chapter will deal with inertial effects associated with a finite density contrast.

3.4 Discussion

The theoretical formalism described in detail in Section 3.2 can be generalized to any background flow situation one may typically encounter in inertial microfluidics, including particles in a finite-sized channel flow. We have specialized this general theory to oscillatory flows in Section 3.3 for three reasons: (i) oscillatory flows have become an important and indispensable tool in the arsenal of modern microfluidics; (ii) oscillatory flows are the most controlled way to induce significant inertial effects at the microscale; (iii) for oscillatory flows, we arrive at general and closed expressions of the inertial force in the subsequent chapters, which provide a result of immediate practical utility in experimental design. This was only possible by systematically extending the MR equation to capture the dominant, and sometimes the only, inertial forces resulting from flow gradients, curvature, etc. in a generic background flow.

In our specialization we did not include an inertia-dominated outer region. However, we note that inertial force contributions from an outer region are most often negligible in practical applications. For general unsteady flows, this holds when the characteristic unsteady time scale is much shorter than the convective time scale [93]. Dominant convective inertia on the microfluidic scale in most cases requires unrealistically high flow speeds or driving pressures. The specific criteria relevant to oscillatory flows will be discussed in the subsequent chapters. Moreover, in steady flows of realistic speed at the microscale, the inertial outer region "wake" is at a distance that far exceeds the characteristic channel dimensions of a microfluidic set-up (cf. [73]), and is thus also irrelevant for the particle motion.

That said, there is no principal obstacle to incorporating an inner-outer region matching formalism into our theory (cf. [157]). Our reciprocal-theorem-based approach employs a Laplace transform to compute the $\mathcal{O}(\mathrm{Re}_p)$ inertial force and can accommodate a wide variety of flow field descriptions. This includes any time-dependent background flow as well as modifications to include the effect of walls or boundaries, such

as for particles in a finite-sized channel flow. In these cases, the evaluation of the volume integral (3.17b) might involve complicated integrals over temporal and/or spatial domains, and will not typically yield a closed analytical result, unlike for oscillatory flows.

3.5 Conclusions

Our systematic first-principles approach is general and can be adapted to a rich set of scenarios, applications, and flow types. For example, the theoretical formalism developed here is general enough to cover forces such as Faxen's law and Secondary Radiation force, which naturally emerge from the reciprocal-theorem-based approach. In order to obtain Saffman lift, our formalism needs to be augmented with contributions from the outer region (see Ref. [157] for a comprehensive discussion), which our formalism allows for. We have systematically augmented the foundations of the Maxey–Riley theory to rigorously derive all the dominant inertial forces on a rigid, spherical particle—consistent with a first-principle solution of the Navier-Stokes equations—in *any* background time-dependent flow, that varies on scales much larger than the particle size. This includes any time-dependent (or independent) background flow as well as modifications to include the effect of walls or boundaries, such as for particles in a finite-sized channel flow. This flexibility that the formalism offers ultimately translates to a significant reduction in computational costs, as we will see in the following chapters.

Chapter 4

Inertial force on neutrally-buoyant particles

In this chapter[1], through a combination of theory and high-resolution simulations, we derive, isolate, and understand a previously unrecognized, strong force acting on particles in inertial microfluidic settings. The analysis applies especially to particle manipulation in fast oscillatory flows, a major tool in lab-on-a-chip processing as well as in diagnostic and biomanufacturing applications. Our approach systematically extends the Maxey–Riley equation, the main theoretical foundation for quantifying fluid forces on particles, to account for unexplained observations related to localized flow curvature and irreversible motion at low Reynolds number.

Modern inertial microfluidics routinely employs oscillatory flows around localized solid features or microbubbles for controlled, specific manipulation of particles, droplets and cells. It is shown that theories of inertial effects that have been state of the art for decades miss major contributions and strongly underestimate forces on small suspended objects in a range of practically relevant conditions. An analytical approach is presented that derives a complete set of inertial forces and quantifies them in closed form as easy-to-use equations of motion, spanning the entire range from viscous to inviscid flows. The theory predicts additional attractive contributions towards oscillating boundaries even for density-matched particles, a previously unexplained experimental observation. The accuracy of the theory is demonstrated against full scale, three-dimensional direct numerical simulations throughout its range.

4.1 Introduction

Describing effects of small but finite inertia on suspended particles is a fundamental fluid dynamical problem that has never been solved in full generality [46, 52, 70, 73, 93, 147]. Modern microfluidics has turned this academic problem into a practical challenge through the use of high-frequency ($\omega \sim$ kHz–MHz) oscillatory flows, perhaps the most efficient way to take advantage of inertial effects at low Reynolds numbers, to precisely manipulate particles, cells and vesicles without the need for charges or chemistry [97, 143, 162].

[1] This chapter is adapted from Agarwal et al. [6]

The systematic theoretical understanding of flow forces on particles has so far hinged on the pioneering work of Maxey and Riley (MR in the following) [103], introduced almost 40 years ago and encompassing a number of specialized approaches [54, 108, 111] including acoustic secondary radiation forces (SRF) that have been invoked to rationalize observed attractive forces towards localized features in oscillatory flows [34, 40, 67, 143, 151]. However, recent experimental [35] and theoretical [4] advances have shown that the classical MR theory falls significantly short of explaining the magnitude of attraction. We demonstrate here theoretically and computationally that previously unrecognized, significant forces act towards oscillating boundaries, even on neutrally buoyant particles, stemming from the interplay of particle inertia, flow gradients, and flow curvature. These forces cannot be understood quantitatively or qualitatively by MR (or SRF), and instead naturally emerge from a systematic generalization of MR, paving the way for enhanced and novel inertial microfluidic applications of great potential benefit in biomanufacturing, health, and medicine.

Oscillatory microfluidics is usually set up by or past a localized object (e.g. a microbubble or a no-slip solid [96, 143]), resulting in spatially non-uniform flows characterized by strong variations on gradient L_Γ and curvature L_κ length scales. Such flows exert remarkably consistent and controllable forces on particles, and have been employed with great success for guidance, separation, aggregation, and sorting [34, 124, 146, 160, 162, 166, 167]. Nonetheless, it is precisely this use of localized oscillations in modern microfluidics that is now pushing the envelope of the MR equation, exposing its limits in predicting the emergence and magnitude of observed significant and persistent forces. Here we provide a thorough revision of its theoretical foundations, but first, in light of the importance of this work for applications, we state a major practical outcome: in any oscillatory background flow field $\bar{\mathbf{U}}$ associated with a localized object, a density-matched (ρ) spherical particle of radius a_p experiences an attractive force towards the object. The component of this force along the object-to-particle connector $\mathbf{e}$ takes the explicit form

$$F_{\Gamma\kappa} = m_f \left\langle a_p^2 \nabla\bar{\mathbf{U}} : \nabla\nabla\bar{\mathbf{U}} \right\rangle \mathcal{F}(\lambda) \cdot \mathbf{e}\,, \tag{4.1}$$

where $m_f = 4\pi\rho a_p^3/3$ is the displaced fluid mass and the inner product represents the interaction of flow gradients and curvatures. Force (4.1) is steady, resulting from a time average $\langle\cdot\rangle$. The effect of oscillation frequency is quantified by the universal, analytically derived function $\mathcal{F}$ of the Stokes number λ. For harmonic oscillatory flows, $\lambda \equiv a_p^2\omega/(3\nu)$ and to excellent approximation $\mathcal{F}(\lambda)$ reads

$$\mathcal{F}(\lambda) = \frac{1}{3} + \frac{9}{16}\sqrt{\frac{3}{2\lambda}}, \tag{4.2}$$

valid over *the entire range* from the viscous $\lambda \ll 1$ to the inviscid $\lambda \gg 1$ limits. In practice, (4.1) moves a

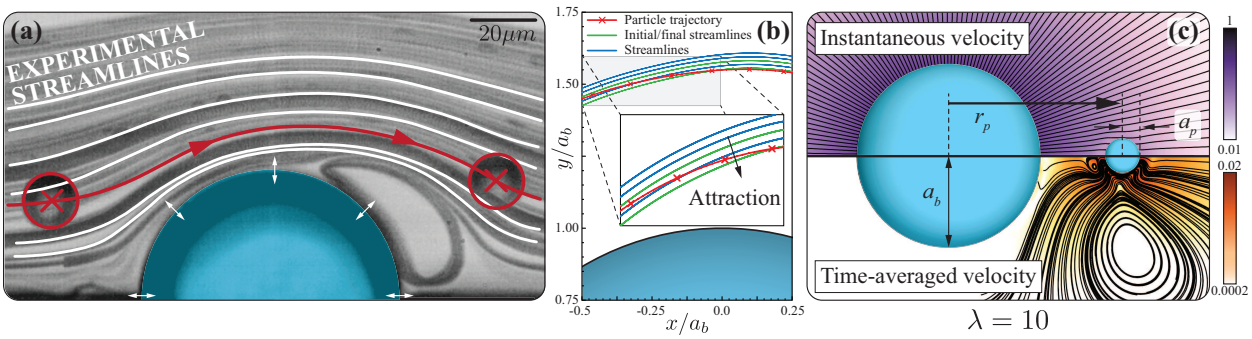

Figure 4.1: Particle attraction to oscillating bubbles. (a) A polystyrene particle ($a_p = 10\mu m$, $\lambda \approx 4$) is transported past an oscillating microbubble ($a_b = 40\mu$m, $\omega/(2\pi) = 20$kHz). (b) Close-up of the experimental trajectory (red) of a neutrally buoyant particle intersecting streamlines (blue), indicating a net attraction towards the bubble over fast time scales of a few ms, unexplained by existing theories: Inertial particle migration due to shear gradients [46, 47, 170] is far slower; the secondary radiation force of acoustofluidics [18, 30, 42, 68, 146] is proportional to the particle-fluid density contrast and thus vanishes here; an ad hoc theory for nearly inviscid flows ($\lambda \gg 1$) from [4] predicts an attraction much too weak to explain observations. A detailed discussion of this particular experiment in the context of our analysis is postponed to Chapter 6. (c) Simulation of the prototypical problem: a particle exposed to the flow of a bubble oscillating in volume mode at relative amplitude ϵ. Top figure: instantaneous streamlines (color bar is flow speed in units of U^*); bottom figure: time-averaged streamlines (color bar is steady flow speed in units of ϵU^*).

particle against its Stokes mobility along a radial coordinate measuring distance r_p from the localized object, so that the steady equation of motion becomes simply

$$\frac{dr_p}{dt} = \frac{F_{\Gamma\kappa}}{6\pi a_p \nu \rho}\,, \tag{4.3}$$

with ν the kinematic viscosity of the fluid. For generic flows, $F_{\Gamma\kappa} < 0$, since the amplitude of $\bar{\mathbf{U}}$ decays with distance from the oscillating object, indicating attraction. If an additional steady flow component is present, (4.3) quantifies the deviation between particle and fluid motion.

The above equations completely describe the particle dynamics and stem from a specialization of the rigorous, general formalism developed in Chapter 3 to respond to discrepancies observed experimentally. Indeed, as illustrated in Fig. 4.1ab, when neutrally buoyant particles of moderate λ approach the surface of oscillating bubbles (cf. [160, 162, 168, 169]), we find evidence of significant radial attractive forces, even at a considerable distance from the bubble. This observation is in direct contradiction to existing theories such as SRF [4, 18, 30, 34, 35, 42, 47, 67, 68, 124, 143, 146, 170], which either predict no attraction at all or a much too weak effect (see caption of Fig. 4.1 and Chapter 6 for more details).

Our goal here is to develop a unifying theory that explains observations, accounts for particle inertia, and seamlessly spans the full viscous-to-inviscid operational flow spectrum. Accordingly, we revisit MR [103] and systematically account for all leading-order terms in particle Reynolds number $\mathrm{Re}_p = a_p U^*/\nu$, with U^*

the velocity scale of the background flow. We then reveal their effect through a specially constructed case: a bubble of radius a_b oscillating in pure volume (breathing) mode, with a spherical, neutrally buoyant particle placed at an initial center-to-center distance $r_p(0)$. This scenario induces no rectified (streaming) flow in the absence of the particle [91], and therefore allows for the precise evaluation of the newly considered disturbance flow effects introduced by the particle itself. The analysis is complemented by direct numerical simulations (DNS) that provide first-principle solutions of flow field and particle displacement. Figure 4.1c (upper half) shows that the computed oscillatory flow component closely resembles the background flow even in the presence of the particle, while time-averaging over an oscillation cycle (bottom half) reveals the much richer secondary steady disturbance flow induced by the particle.

Like MR, we wish to describe the hydrodynamic forces on a particle centered at $\mathbf{r}_p$ using only information from the given undisturbed background flow $\bar{\mathbf{U}}$. In the following, we reiterate the important steps of our general formalism described in the preceding chapter. We fix a (moving) coordinate system at $\mathbf{r}_p$ and non-dimensionalize lengths by a_p, times by ω^{-1}, and velocities by U^* (using lowercase letters for non-dimensional velocities). A spherical particle exposed to a known (lab-frame) background flow $\bar{\mathbf{u}}$ and moving with velocity $\mathbf{u}_p$ (neglecting effects of rotation) then experiences the effects of the undisturbed flow $\boldsymbol{w}^{(0)} = \bar{\mathbf{u}} - \mathbf{u}_p$ and a disturbance flow $\boldsymbol{w}^{(1)}$. Following [103], the latter obeys

$$\begin{aligned} \nabla^2 \boldsymbol{w}^{(1)} - \nabla p^{(1)} &= 3\lambda \frac{\partial \boldsymbol{w}^{(1)}}{\partial t} + \mathrm{Re}_p \, \mathbf{f}, \quad \text{where} \\ \mathbf{f} &= \boldsymbol{w}^{(0)} \cdot \nabla \boldsymbol{w}^{(1)} + \boldsymbol{w}^{(1)} \cdot \nabla \boldsymbol{w}^{(0)} + \boldsymbol{w}^{(1)} \cdot \nabla \boldsymbol{w}^{(1)} \end{aligned} \tag{4.4}$$

with boundary conditions $\boldsymbol{w}^{(1)} = \mathbf{u}_p - \bar{\mathbf{u}}$ on $r = 1$, and $\boldsymbol{w}^{(1)} = 0$ as $r \to \infty$. This equation is exact and does not rely on small Re_p. To obtain explicit results, we use two expansions: one, like MR, expands the background flow around the particle position into spatial moments of alternating symmetry:

$$\bar{\mathbf{u}} = \bar{\mathbf{u}}|_{\mathbf{r}_p} + \mathbf{r} \cdot \mathbf{E} + \mathbf{r}\mathbf{r} : \mathbf{G} + \ldots, \tag{4.5}$$

where $\mathbf{E} = (a_p/L_\Gamma)\nabla\bar{\mathbf{u}}|_{\mathbf{r}_p}$ and $\mathbf{G} = \frac{1}{2}(a_p^2/L_\kappa^2)\nabla\nabla\bar{\mathbf{u}}|_{\mathbf{r}_p}$ capture the background flow shear gradients and curvatures, whose scales are, in practice, much larger than a_p, justifying (4.5).

The other cornerstone of our theory is a regular perturbation expansion of all variables in (4.4), using subscripts for orders of Re_p , e.g., $\boldsymbol{w}^{(1)} = \boldsymbol{w}_0^{(1)} + \mathrm{Re}_p \, \boldsymbol{w}_1^{(1)} + \mathcal{O}(\mathrm{Re}_p^2)$. In contrast to MR, this retains a term $\mathrm{Re}_p \, \mathbf{f}_0$ in (4.4), where $\mathbf{f}_0 = \boldsymbol{w}^{(0)} \cdot \nabla \boldsymbol{w}_0^{(1)} + \boldsymbol{w}_0^{(1)} \cdot \nabla \boldsymbol{w}^{(0)} + \boldsymbol{w}_0^{(1)} \cdot \nabla \boldsymbol{w}_0^{(1)}$ is the leading-order nonlinear forcing of the disturbance flow. Note also that $w_0^{(1)}$ is purely oscillatory, while $w_1^{(1)}$ has a non-zero time-average,

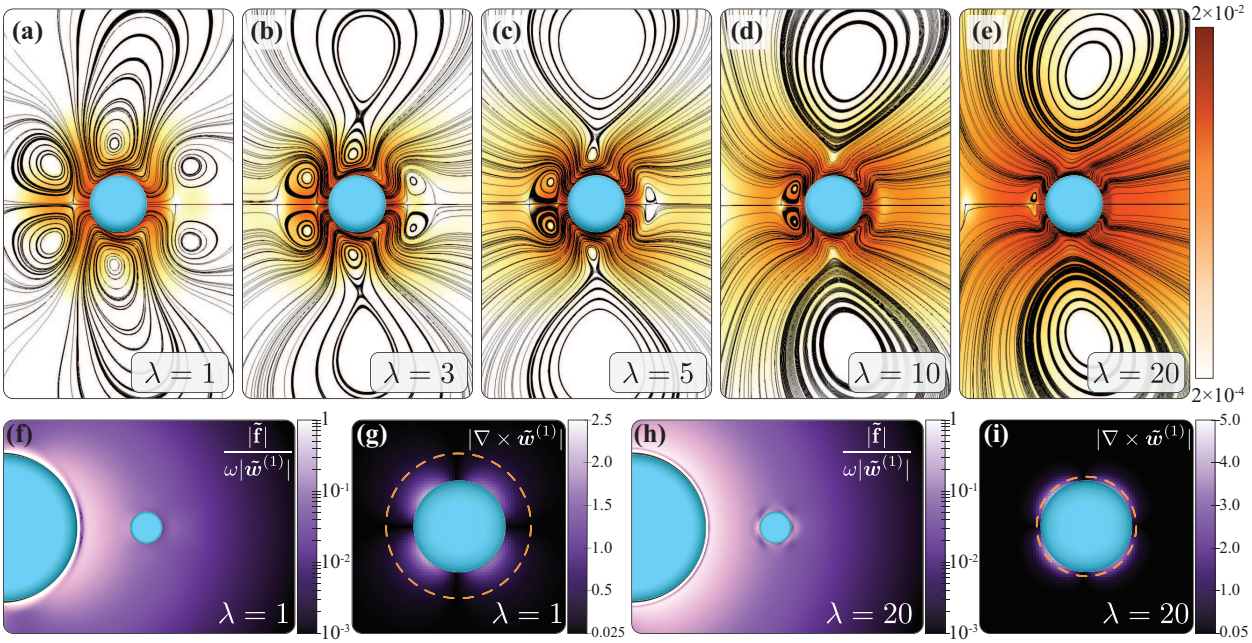

Figure 4.2: Flow field simulation results. (a-e) Streamlines of the steady flow $\langle \boldsymbol{w} \rangle = \langle \boldsymbol{w}^{(1)} \rangle$ (Stokes streamfunction isolines) for different λ; color bar is velocity magnitude in units of ϵU^*; (f,h) The magnitude of Fourier-transformed quantities (indicated by tildes) evaluated at the driving frequency ω demonstrates that the flow field has no outer, inertia-dominated region. The ratio between oscillatory disturbance flow advective force $\tilde{\mathbf{f}}(\omega)$ and the Fourier component of the unsteady inertia $\partial \boldsymbol{w}^{(1)}/\partial t$ remains small away from the bubble. (g,i) The Fourier component of vorticity at ω is confined to the oscillatory Stokes layer thickness δ_S (orange-dashed circle) around the particle.

exemplified by the flow in Fig. 4.1c (bottom).

Forces on the particle, as integrals of the fluid stress tensor over the particle surface S_p, are also expanded in this fashion. Application of a reciprocal theorem [93] formally yields the inertial force components as volume integrals over the entire fluid domain without the need to explicitly compute the flow field at that order. The reciprocal theorem employs a known test flow $\mathbf{u}' = u'(t)\mathbf{e}$ in a chosen direction $\mathbf{e}$. The component of the equation of particle motion in that direction, to $\mathcal{O}(\mathrm{Re}_p)$, is then

$$m_p \frac{dU_p}{dt} = F_0^{(0)} + F_0^{(1)} + \mathrm{Re}_p(F_1^{(0)} + F_1^{(1)}) + \mathcal{O}(\mathrm{Re}_p^2), \tag{4.6a}$$

$$F_0^{(0)} = \frac{F_S}{6\pi}\int_V (3\lambda\partial_t\bar{\mathbf{u}})\cdot\mathbf{e}dV, \tag{4.6b}$$

$$F_0^{(1)} = \frac{F_S}{6\pi}\mathcal{L}^{-1}\left\{\int_{S_p}\frac{(\hat{\mathbf{u}}_p - \hat{\bar{\mathbf{u}}})}{\hat{u}'}\cdot(\hat{\boldsymbol{\sigma}}'\cdot\mathbf{n})dS\right\}, \tag{4.6c}$$

$$F_1^{(0)} = \frac{F_S}{6\pi}\int_V (\bar{\mathbf{u}}\cdot\nabla\bar{\mathbf{u}})\cdot\mathbf{e}dV, \tag{4.6d}$$

$$F_1^{(1)} = -\frac{F_S}{6\pi}\mathcal{L}^{-1}\left\{\frac{1}{\hat{u}'}\int_V \hat{\mathbf{u}}'\cdot\hat{\mathbf{f}}_0 dV\right\}, \tag{4.6e}$$

where $\boldsymbol{\sigma}'$ is the stress tensor of the test flow, hats denote Laplace transforms, and $\mathcal{L}^{-1}$ their inverse. All dimensional forces have the common Stokes drag scale $F_S/6\pi = \nu\rho a_p U^*$. Equations (4.6b) and (4.6d) are forces exerted by the background flow, while (4.6c) and (4.6e) stem from the disturbance flow. The original MR equation contains $F_0^{(0)}$ and $F_0^{(1)}$, but only part of $F_1^{(0)}$, while $F_1^{(1)}$ is an entirely new term due to particle inertia. We shall show that these unrecognized contributions are not small corrections, but are dominant in relevant applications, particularly the inertial disturbance force $F_1^{(1)}$.

4.2 Evaluation of the inertial force

4.2.1 General solutions and the Reciprocal Theorem

The leading-order oscillatory disturbance flow field $\boldsymbol{w}_0^{(1)}$ is obtained by inserting (4.5) into the leading order of (4.4) and can be formally expressed as a series solution [81, 132]

$$\boldsymbol{w}_0^{(1)} = \boldsymbol{\mathcal{M}}_D\cdot\mathbf{u}_s - \boldsymbol{\mathcal{M}}_Q\cdot(\mathbf{r}\cdot\mathbf{E}) - \boldsymbol{\mathcal{M}}_O\cdot(\mathbf{rr}:\mathbf{G}) + \ldots, \tag{4.7}$$

where $\mathbf{u}_s = \mathbf{u}_{p_0} - \bar{\mathbf{u}}|_{\mathbf{r}_{p_0}}$ is the slip velocity and $\boldsymbol{\mathcal{M}}_{D,Q,O}(\mathbf{r},\lambda)$ are spatially dependent mobility tensors independent of the particular background flow—Section 3.3.1 gives explicit expressions in the case of harmonic oscillatory flows, though the formalism applies for general flows. All information about the specific back-

ground flow is contained in the constant quantities $\mathbf{u}_s$, $\mathbf{E}$, and $\mathbf{G}$. The $\mathcal{O}(\mathrm{Re}_p)$ flow field $\boldsymbol{w}_1^{(1)}$ does not need to be computed explicitly; instead, we use a reciprocal theorem. Denoting Laplace-transformed quantities by hats, application of the divergence theorem results in the following symmetry relation:

$$\oint_S (\hat{\boldsymbol{w}}_1^{(1)} \cdot \hat{\boldsymbol{\sigma}}' - \hat{\mathbf{u}}' \cdot \hat{\boldsymbol{\sigma}}_1^{(1)}) \cdot \mathbf{m}\, dS = \int_V \left[\nabla \cdot (\hat{\boldsymbol{w}}_1^{(1)} \cdot \hat{\boldsymbol{\sigma}}') - \nabla \cdot (\hat{\mathbf{u}}' \cdot \hat{\boldsymbol{\sigma}}_1^{(1)})\right] dV. \tag{4.8}$$

As shown in Chapter 3, the above expression yields the $\mathcal{O}(\mathrm{Re}_p)$ force on the particle captured by (4.6e). We note that the computation of the volume integral simplifies considerably: the integrand is proportional to $\mathbf{f}_0$, in which only certain products are non-vanishing when the angular integration around the particle is performed. For instance, the first term in $\mathbf{f}_0$ is $(\bar{\boldsymbol{u}} - \mathbf{u}_{p_0}) \cdot \nabla \boldsymbol{w}_0^{(1)} = (-\mathbf{u}_s + \mathbf{r} \cdot \mathbf{E} + \mathbf{rr} : \mathbf{G}) \cdot \nabla (\boldsymbol{\mathcal{M}}_D \cdot \mathbf{u}_s - \boldsymbol{\mathcal{M}}_Q \cdot (\mathbf{r} \cdot \mathbf{E}) - \boldsymbol{\mathcal{M}}_O \cdot (\mathbf{rr} : \mathbf{G}))$. Due to the alternating symmetry of terms in the background flow and consequently $\boldsymbol{w}_0^{(1)}$, only products of adjacent terms survive integration, while e.g. a term involving $\mathbf{u}_s \cdot \nabla (\boldsymbol{\mathcal{M}}_D \cdot \mathbf{u}_s)$ vanishes after volume integration. Furthermore, in this chapter we restrict ourselves to the case of neutrally buoyant particles and consequently the slip velocity is $\mathbf{u}_s = 0$. In summary, only the following terms in $\mathbf{f}_0$ have non-trivial contributions to the volume integral:

$$\begin{aligned}
\mathbf{f}_0 = &- (\mathbf{rr} : \mathbf{G}) \cdot \nabla (\boldsymbol{\mathcal{M}}_Q \cdot (\mathbf{r} \cdot \mathbf{E})) - (\mathbf{r} \cdot \mathbf{E}) \cdot \nabla (\boldsymbol{\mathcal{M}}_O \cdot (\mathbf{rr} : \mathbf{G})) \\
&- (\boldsymbol{\mathcal{M}}_Q \cdot (\mathbf{r} \cdot \mathbf{E})) \cdot \nabla (\mathbf{rr} : \mathbf{G}) - (\boldsymbol{\mathcal{M}}_O \cdot (\mathbf{rr} : \mathbf{G})) \cdot \nabla (\mathbf{r} \cdot \mathbf{E}) \\
&+ (\boldsymbol{\mathcal{M}}_Q \cdot (\mathbf{r} \cdot \mathbf{E})) \cdot \nabla (\boldsymbol{\mathcal{M}}_O \cdot (\mathbf{rr} : \mathbf{G})) + (\boldsymbol{\mathcal{M}}_O \cdot (\mathbf{rr} : \mathbf{G})) \cdot \nabla (\boldsymbol{\mathcal{M}}_Q \cdot (\mathbf{r} \cdot \mathbf{E}))\,.
\end{aligned} \tag{4.9}$$

All information about the background flow field is contained in the constant tensors $\mathbf{E}$ and $\mathbf{G}$, which are evaluated at the particle position. If the particle is farther away from the surface of the oscillating object exciting the flow than the Stokes layer thickness δ_S, it is exposed to a pure potential flow; this will be the case in the overwhelming majority of realistic scenarios. For potential flows it can be shown that all non-zero terms of (4.9) are proportional to $\mathbf{E} : \mathbf{G}$. Choosing a test flow in direction $\mathbf{e}$, one obtains a surprisingly compact result for the $\mathbf{e}$-component of the $\mathcal{O}(\mathrm{Re}_p)$ inertial force:

$$\left\langle \frac{F_1^{(1)}}{F_S} \right\rangle = -\frac{1}{6\pi} \left\langle \mathcal{L}^{-1} \left\{ \frac{1}{\hat{u}'} \int_V \hat{\mathbf{u}}' \cdot \hat{\mathbf{f}}_0 dV \right\} \right\rangle = \frac{4}{9} \langle \mathbf{E} : \mathbf{G} \rangle \cdot \mathbf{e}\, \mathcal{F}_1^{(1)}(\lambda)\,. \tag{4.10}$$

We have here applied the required Laplace transforms as well as a time average to extract the steady part of the force. Performing the volume integral leaves a universal dimensionless function $\mathcal{F}(\lambda)$, whose contributions

stem from $\boldsymbol{\mathcal{M}}_{D,Q,O}$. Explicitly, this function reads

$$
\begin{aligned}
\mathcal{F}_1^{(1)}(\lambda) = \Bigg[& 2\pi\Bigg(-796500\bar{\lambda}^{3/2} - 336636\bar{\lambda}^{5/2} + 34005\bar{\lambda}^{7/2} + 59790\bar{\lambda}^{9/2} + 3312\bar{\lambda}^{11/2} + 568\bar{\lambda}^{6} \\
& + 14078\bar{\lambda}^{5} + 97470\bar{\lambda}^{4} - 109920\bar{\lambda}^{3} - 646137\bar{\lambda}^{2} - 648594\bar{\lambda} - 322056\sqrt{\bar{\lambda}} - 76545\Bigg) \\
& + e^{(1-i)\sqrt{\bar{\lambda}}}\pi\bar{\lambda}^{5/2}\Bigg(9\Bigg(\pi(4410+2033i) - 28176e^{(1+i)\sqrt{\bar{\lambda}}}\mathrm{Ei}\left(-2\sqrt{\bar{\lambda}}\right) + e^{(2+2i)\sqrt{\bar{\lambda}}}(5600-12600i)\mathrm{Ei}\left((-3-i)\sqrt{\bar{\lambda}}\right) \\
& - (2033+4410i)e^{2i\sqrt{\bar{\lambda}}}\mathrm{Ei}\left((-1-i)\sqrt{\bar{\lambda}}\right) + e^{2\sqrt{\bar{\lambda}}}(5600+12600i)\mathrm{Ei}\left((-3+i)\sqrt{\bar{\lambda}}\right) - (2033-4410i)\mathrm{Ei}\left((-1+i)\sqrt{\bar{\lambda}}\right) \\
& + e^{(2+2i)\sqrt{\bar{\lambda}}}(12600+5600i)\pi + e^{2i\sqrt{\bar{\lambda}}}(4410-2033i)\pi + e^{2\sqrt{\bar{\lambda}}}(12600-5600i)\pi\Bigg)\bar{\lambda}^{3/2} + 6\Bigg(\pi(4195+3982i) \\
& - 28080e^{(1+i)\sqrt{\bar{\lambda}}}\mathrm{Ei}\left(-2\sqrt{\bar{\lambda}}\right) - (3982+4195i)e^{2i\sqrt{\bar{\lambda}}}\mathrm{Ei}\left((-1-i)\sqrt{\bar{\lambda}}\right) - (3982-4195i)\mathrm{Ei}\left((-1+i)\sqrt{\bar{\lambda}}\right) \\
& + e^{2i\sqrt{\bar{\lambda}}}(4195-3982i)\pi\Bigg)\bar{\lambda}^{5/2} + 4\Bigg(\pi(241+1714i) + 720e^{(1+i)\sqrt{\bar{\lambda}}}\mathrm{Ei}\left(-2\sqrt{\bar{\lambda}}\right) - (1714+241i)e^{2i\sqrt{\bar{\lambda}}}\mathrm{Ei}\left((-1-i)\sqrt{\bar{\lambda}}\right) \\
& - (1714-241i)\mathrm{Ei}\left((-1+i)\sqrt{\bar{\lambda}}\right) + e^{2i\sqrt{\bar{\lambda}}}(241-1714i)\pi\Bigg)\bar{\lambda}^{7/2} - (120+120i)\Bigg(\pi\left(-i+e^{2i\sqrt{\bar{\lambda}}}\right) - ie^{2i\sqrt{\bar{\lambda}}}\mathrm{Ei}\left((-1-i)\sqrt{\bar{\lambda}}\right) \\
& + \mathrm{Ei}\left((-1+i)\sqrt{\bar{\lambda}}\right)\Bigg)\bar{\lambda}^{9/2} - (4+4i)\Bigg(\pi\left(e^{2i\sqrt{\bar{\lambda}}}(248+127i) + (-127-248i)\right) + e^{2i\sqrt{\bar{\lambda}}}(127-248i)\mathrm{Ei}\left((-1-i)\sqrt{\bar{\lambda}}\right) \\
& + (248-127i)\mathrm{Ei}\left((-1+i)\sqrt{\bar{\lambda}}\right)\Bigg)\bar{\lambda}^{4} - (6+6i)\Bigg(e^{2i\sqrt{\bar{\lambda}}}\pi(567+2134i) + e^{(1+i)\sqrt{\bar{\lambda}}}(736-736i)\mathrm{Ei}\left(-2\sqrt{\bar{\lambda}}\right) \\
& + e^{2i\sqrt{\bar{\lambda}}}(2134-567i)\mathrm{Ei}\left((-1-i)\sqrt{\bar{\lambda}}\right) + (567-2134i)\mathrm{Ei}\left((-1+i)\sqrt{\bar{\lambda}}\right) + (-2134-567i)\pi\Bigg)\bar{\lambda}^{3} \\
& + \Bigg(\pi(39033+25089i) - 381504e^{(1+i)\sqrt{\bar{\lambda}}}\mathrm{Ei}\left(-2\sqrt{\bar{\lambda}}\right) - (25089+39033i)e^{2i\sqrt{\bar{\lambda}}}\mathrm{Ei}\left((-1-i)\sqrt{\bar{\lambda}}\right) \\
& - (25089-39033i)\mathrm{Ei}\left((-1+i)\sqrt{\bar{\lambda}}\right) + e^{2i\sqrt{\bar{\lambda}}}(39033-25089i)\pi\Bigg)\bar{\lambda}^{2} + (315+315i)\Bigg(e^{(2+2i)\sqrt{\bar{\lambda}}}\pi(420+60i) \\
& - (96-96i)e^{(1+i)\sqrt{\bar{\lambda}}}\mathrm{Ei}\left(-2\sqrt{\bar{\lambda}}\right) + e^{(2+2i)\sqrt{\bar{\lambda}}}(60-420i)\mathrm{Ei}\left((-3-i)\sqrt{\bar{\lambda}}\right) - (49+28i)e^{2i\sqrt{\bar{\lambda}}}\mathrm{Ei}\left((-1-i)\sqrt{\bar{\lambda}}\right) \\
& + e^{2\sqrt{\bar{\lambda}}}(420-60i)\mathrm{Ei}\left((-3+i)\sqrt{\bar{\lambda}}\right) + (28+49i)\mathrm{Ei}\left((-1+i)\sqrt{\bar{\lambda}}\right) - (60+420i)e^{2\sqrt{\bar{\lambda}}}\pi + (49-28i)\pi \\
& + e^{2i\sqrt{\bar{\lambda}}}(28-49i)\pi\Bigg)\bar{\lambda} + 15120e^{\sqrt{\bar{\lambda}}}\Bigg(-5ie^{\sqrt{\bar{\lambda}}}\pi + 5ie^{(1+2i)\sqrt{\bar{\lambda}}}\pi + 5e^{(1+2i)\sqrt{\bar{\lambda}}}\mathrm{Ei}\left((-3-i)\sqrt{\bar{\lambda}}\right) + 5e^{\sqrt{\bar{\lambda}}}\mathrm{Ei}\left((-3+i)\sqrt{\bar{\lambda}}\right) \\
& - e^{i\sqrt{\bar{\lambda}}}\mathrm{Ei}\left(-2\sqrt{\bar{\lambda}}\right)\Bigg) + 945\Bigg(7\pi + 7e^{2i\sqrt{\bar{\lambda}}}\pi - 160ie^{2\sqrt{\bar{\lambda}}}\pi + 160ie^{(2+2i)\sqrt{\bar{\lambda}}}\pi + 160e^{(2+2i)\sqrt{\bar{\lambda}}}\mathrm{Ei}\left((-3-i)\sqrt{\bar{\lambda}}\right) \\
& + 160e^{2\sqrt{\bar{\lambda}}}\mathrm{Ei}\left((-3+i)\sqrt{\bar{\lambda}}\right) - 48e^{(1+i)\sqrt{\bar{\lambda}}}\mathrm{Ei}\left(-2\sqrt{\bar{\lambda}}\right) - 7ie^{2i\sqrt{\bar{\lambda}}}\mathrm{Ei}\left((-1-i)\sqrt{\bar{\lambda}}\right) + 7i\mathrm{Ei}\left((-1+i)\sqrt{\bar{\lambda}}\right)\Bigg)\sqrt{\bar{\lambda}}\Bigg)\Bigg] \Bigg/ \\
& \left[15120\sqrt{\bar{\lambda}}\left(84\bar{\lambda}^{3/2} + 32\bar{\lambda}^{5/2} + 8\bar{\lambda}^{3} + 64\bar{\lambda}^{2} + 72\bar{\lambda} + 36\sqrt{\bar{\lambda}} + 9\right)\right].
\end{aligned}
$$

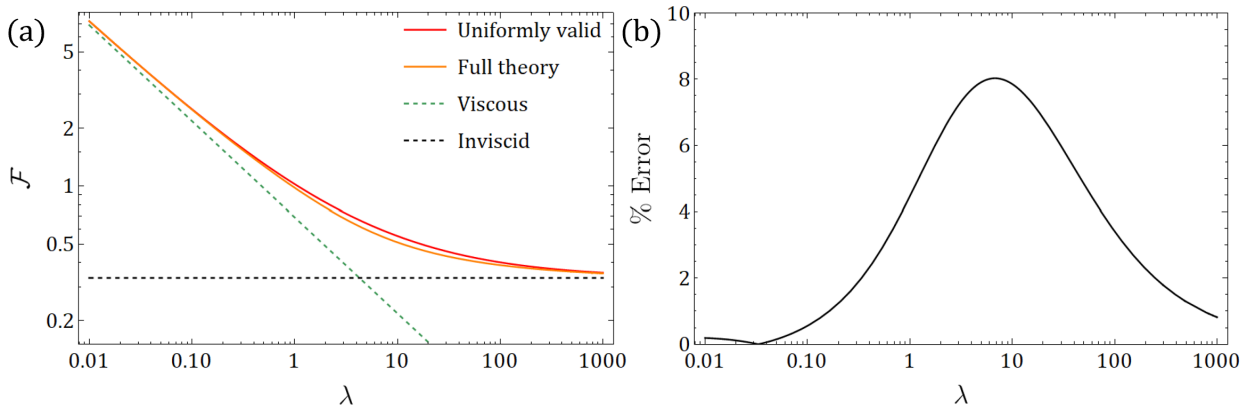

Figure 4.3: (a) Logarithmic plot of the overall inertial force magnitude $\mathcal{F}(\lambda)$: the uniformly valid expression (red) closely tracks the full solution (orange) while the inviscid theory (gray dashed) severely underestimates the inertial force even for moderately large λ. (b) The magnitude of the percentage error between the uniformly valid and full solutions is small throughout the entire range of λ, with a maximum error of $\sim 8\%$ where the two limits blend, as one would expect.

Here $\bar{\lambda} = (3/2)\lambda$ and Ei is the exponential integral function.

4.2.2 Accuracy of the uniformly valid expression for $\mathcal{F}$

While the explicit functional form (4.11) of $\mathcal{F}_1^{(1)}(\lambda)$ is rather lengthy, we show below that this expression is approximated to great accuracy by two simple terms. We Taylor expand in both the viscously dominated limit ($\lambda \to 0$) and the inviscid limit ($\lambda \to \infty$) to obtain

$$\mathcal{F}^v = \frac{9}{16}\sqrt{\frac{3}{2\lambda}} + \mathcal{O}(1), \quad \mathcal{F}^i = \frac{1}{3} + \mathcal{O}(1/\sqrt{\lambda}). \tag{4.12}$$

We construct a uniformly valid solution by simply adding the two leading order results, yielding $\mathcal{F}(\lambda) = \frac{1}{3} + \frac{9}{16}\sqrt{\frac{3}{2\lambda}}$. In Fig. 4.3(a), we plot the uniformly valid $\mathcal{F}$ (red curve) and the full theory represented by Eq. (4.11) (orange), along with the viscous and inviscid limits denoted by dashed lines. Figure 4.3(b) shows that the relative error between the red and orange curves is small ($\lesssim 8\%$) for all λ, even those far smaller or larger than practically relevant values.

We stress again here that the result is universal for any oscillatory potential flow; for the prototypical case of the volumetrically oscillating bubble, $\langle \mathbf{E} : \mathbf{G} \rangle \cdot \mathbf{e}_r = -9/r_p^7$.

4.2.3 Net inertial force

The time-averaged force contribution from the background flow at $\mathcal{O}(\mathrm{Re}_p)$ is of the same form as (4.10), except that $\mathcal{F}(\lambda)$ is replaced by the simple constant $\mathcal{F}_1^{(0)} = \frac{1}{5}$ [139]. The two contributions $F_1^{(1)}$ and $F_1^{(0)}$

can thus be simply added. Transforming back to dimensional variables, we obtain the net time-averaged force on the particle as

$$\mathbf{F}_{\Gamma\kappa} = m_f a_p^2 \left\langle \nabla\bar{\mathbf{U}} : \nabla\nabla\bar{\mathbf{U}} \right\rangle \mathcal{F}(\lambda), \tag{4.13}$$

where $\mathcal{F} = \mathcal{F}_1^{(1)} + \mathcal{F}_1^{(0)}$ and $m_f = 4\pi\rho a_p^3/3$, as noted earlier. This time-averaged inertial force on the particle is derived for a background flow that is symmetric about an axis $\mathbf{e}$ passing through the center of the particle.

It was remarked above that the simple form of (4.13) is a consequence of the background flow being potential. This can be backed up by symmetry arguments and dimensional analysis for an arbitrary oscillatory background flow that has a harmonic scalar potential, $\bar{\mathbf{U}} = \nabla\bar{\varphi}$ with $\nabla^2\bar{\varphi} = 0$. Such a flow is in fact generic since the background flow vorticity decays exponentially outside the Stokes boundary layer of the compact object driving the background flow. We are interested in a time-averaged force on the particle that is (i) quadratic in the oscillation amplitude and (ii) involves contractions of the flow gradient $\nabla\bar{\mathbf{U}} = \nabla\nabla\bar{\varphi}$ and the flow curvature tensor $\nabla\nabla\bar{\mathbf{U}} = \nabla\nabla\nabla\bar{\varphi}$. The only dimensionless parameter in the problem not already specified by $\bar{\mathbf{U}}$ is the Stokes number λ. Collecting the above statements, the only way to construct the time-averaged force (a vector) from the higher rank tensors $\nabla\nabla\bar{\varphi}$ and $\nabla\nabla\nabla\bar{\varphi}$ is by their contraction $\nabla\nabla\bar{\varphi} : \nabla\nabla\nabla\bar{\varphi}$. All other combinations are either of insufficient tensor rank or are identically zero (since $\nabla^2\bar{\varphi} = 0$). See [44] for similar arguments for flows without curvature. Including the correct dimensions, the time averaged force for any oscillatory potential background flow thus has the form

$$\mathbf{F}_{\Gamma\kappa} = m_f a_p^2 \left\langle \nabla\nabla\bar{\varphi} : \nabla\nabla\nabla\bar{\varphi} \right\rangle \mathcal{F}(\lambda)\,. \tag{4.14}$$

Note that although the background flow is irrotational, the disturbance flow has a finite vorticity within the Stokes layer around the particle. Under this general setting there is no requirement of axisymmetry of the background flow, so (4.13) as well as (4.1) apply to the generic case of an oscillatory potential flow background, and with the same universal function $\mathcal{F}(\lambda)$.

4.3 Results

The outlined formalism is entirely general for arbitrary background flows and provides analytical expressions for the new forces $F_1^{(0)}$ and $F_1^{(1)}$. The former straightforwardly reads

$$\frac{F_1^{(0)}}{F_S} = \frac{4}{9}\left(\mathbf{E} : \mathbf{G}\right) \cdot \mathbf{e}\, \mathcal{F}_1^{(0)}\,, \tag{4.15}$$

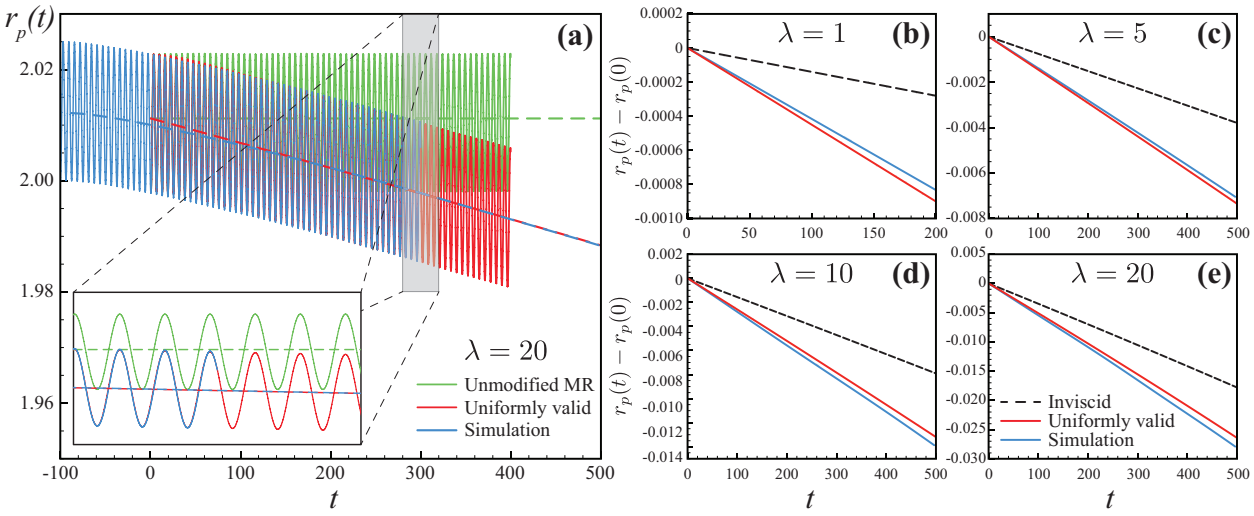

Figure 4.4: Comparison of theoretical (red) and simulated (blue) particle dynamics (radial displacements). (a) Full unsteady dynamics (solid lines) from DNS and theory Eq. (4.17) and time-averaged dynamics (dashed lines; theory uses Eq. (4.19) with (4.2)). The classical MR equation solutions (green) fail to even qualitatively capture the particle attraction to the bubble. (b-e) Steady dynamics from the uniformly valid asymptotic theory agrees with DNS for the entire range of λ values. Dashed lines show the inviscid-limit theory, demonstrating significant quantitative discrepancies even for the largest λ.

where $\mathcal{F}_1^{(0)} = 1/5$ [139]. The force $F_1^{(1)}$, by contrast, is generally composed of various contributions involving the expansion coefficients of (4.5), cf. Chapters 3 and 5. However, it simplifies greatly in oscillatory background flows that are potential: this condition is fulfilled in almost all cases, requiring only that the distance h_p between the particle and object surfaces is greater than the Stokes boundary layer thickness $\delta_S = \sqrt{2\nu/\omega}$, which simplifies to the easily satisfied condition $\lambda \gtrsim (a_p/h_p)^2$. Then, the only way to construct a force vector from a contraction of the higher rank tensors $\mathbf{E}$ and $\mathbf{G}$ is $\mathbf{E} : \mathbf{G}$ (cf. [44, 115]). If furthermore the particle is neutrally buoyant, the slip velocity $\mathbf{u}_s$ vanishes and we obtain

$$\frac{F_1^{(1)}}{F_S} = \frac{4}{9} (\mathbf{E} : \mathbf{G}) \cdot \mathbf{e} \, \mathcal{F}_1^{(1)}(\lambda) \,, \tag{4.16}$$

where the function $\mathcal{F}_1^{(1)}(\lambda)$ was determined analytically and is universal, i.e., valid for arbitrary flow fields. While both (4.15) and (4.16) need non-zero gradient and curvature terms of the background flow, $\mathcal{F}_1^{(1)}(\lambda)$ captures the nonlinear effect of inertia of the leading order unsteady disturbance flow $\boldsymbol{w}_0^{(1)}$ on the particle. For micron-size particles where $\lambda \sim 1$, $\mathcal{F}_1^{(1)}$ is considerably larger than $\mathcal{F}_1^{(0)}$, so that (4.16) is the dominant effect in practical microfluidic applications. The sum of both contributions (4.15) and (4.16) results in the dimensional force (4.1), before time-averaging.

4.3.1 Oscillatory equation of motion in radial flow

We now turn to the prototypical oscillatory flow example of Fig. 4.1c. This flow field's unique scale is the bubble radius ($L_\Gamma = L_\kappa = a_b$). With an oscillation amplitude of ϵa_b ($\epsilon \ll 1$ in practical situations) the velocity scale is $U^* = \epsilon a_b \omega$, and we anticipate the relevant rectified (time-averaged) force to lead to irreversible particle motion proportional to ϵ^2 (cf. [4]). It is advantageous to change the length scale to a_b here, introducing $\alpha \equiv a_p/a_b$, and to change the coordinate origin to the bubble center, so that the background flow has only one component $\bar{u} = \sin t/r^2$ in the direction $\mathbf{e} = \mathbf{e}_r$. For the special case of the bubble executing pure breathing oscillations with the radial flow field $\bar{u} = \sin t/r^2$, it is straightforward to compute $\mathbf{E} : \mathbf{G} \cdot \mathbf{e}_r = -18 \sin^2 t/r_p^7$, where $r_p(t)$ is the instantaneous particle position. Using (4.6), (4.15), (4.16), and noting $\alpha \,\mathrm{Re}_p = 3\epsilon\lambda$, the non-dimensional equation of motion for $r_p(t)$ of a neutrally buoyant particle explicitly reads:

$$\begin{aligned}\lambda \frac{d^2 r_p}{dt^2} &= \epsilon\lambda \left(\frac{\cos t}{r_p^2} - 2\epsilon \frac{\sin^2 t}{r_p^5} \right) - \frac{2\lambda}{3} \epsilon^2 \alpha^2 \frac{18 \sin^2 t}{r_p^7} \mathcal{F}^{(0)} \\ &+ \left[\frac{\sin t}{r_p^2} - \frac{dr_p}{dt} \right] - \left[\frac{2\lambda}{3} \epsilon^2 \alpha^2 \frac{(18 \sin^2 t)}{r_p^7} \mathcal{F}_1^{(1)} \lambda) \right], \end{aligned} \tag{4.17}$$

where the first line on the RHS represents contributions from $F_0^{(0)}$ and $F_1^{(0)}$, while the first and second terms in square parentheses represent $F_0^{(1)}$ and $F_1^{(1)}$, respectively. Note that, for neutrally buoyant particles, the time-periodic character of the flow precludes memory terms that would otherwise emerge from the inverse Laplace transforms [15, 93, 103].

4.3.2 Time scale separation and time averaging

Assuming $\epsilon \ll 1$, we introduce the slow time $T = \epsilon^2 t$, in addition to the fast time t. Using the following transformations

$$r_p(t) \mapsto r_p(t, T), \tag{4.18a}$$

$$\frac{d}{dt} \mapsto \frac{\partial}{\partial t} + \epsilon^2 \frac{\partial}{\partial T}, \tag{4.18b}$$

$$\frac{d^2}{dt^2} \mapsto \frac{\partial^2}{\partial t^2} + 2\epsilon^2 \frac{\partial^2}{\partial t \partial T} + \epsilon^4 \frac{\partial^2}{\partial T^2}, \tag{4.18c}$$

we seek a perturbation solution in ϵ of the general form $r_p(t, T) = r_p(T) + \epsilon \breve{r}_p(t, T) + \epsilon^2 \breve{\breve{r}}_p(t, T) + \ldots$, and separate orders in (4.17). The procedure is outlined in [4] and results in a leading-order equation for $r_p(T)$ given by (4.19), dependent on the slow time scale only (the scale t being averaged out). Higher-order corrections to the irreversible, rectified particle motion only occur at $\mathcal{O}(\epsilon^4)$.

Our ultimate goal is to predict the rectified trajectory of the particle after time-averaging over the fast oscillatory time scale, to provide practically useful guidance for precision applications. Time scale separation using the *slow time* $T = \epsilon^2 t$ analogous to Section 2.2.2 (see also [4]) obtains the leading order equation for the rectified particle motion $r_p(T)$

$$\frac{dr_p}{dT} = -\frac{6}{r_p^7}\alpha^2\lambda\mathcal{F}(\lambda)\,, \tag{4.19}$$

where $\mathcal{F}(\lambda) = \mathcal{F}_1^{(1)}(\lambda) + \mathcal{F}_1^{(0)}$. (4.19) is readily solved analytically and is analogous to the result (4.3). Indeed, while the analytical form of the universal function $\mathcal{F}_1^{(1)}$ is complicated (see Section 4.2.2), we Taylor expanded in both the viscous limit ($\lambda \to 0$) and the inviscid limit ($\lambda \to \infty$) to obtain (4.12).

The simple sum of these leading terms yields the uniformly valid expression (4.2) for the total dimensionless force $\mathcal{F}(\lambda)$ on the particle. Note that our derivation is based fundamentally on the presence of both viscous and inertial effects, so that even $\mathcal{F}^v$ is a finite-inertia force. Its $\lambda^{-1/2}$ scaling for small λ is reminiscent of Saffman's lift force [145], but is obtained without decomposing the domain into viscous and inertial regions. Remarkably, the opposite limit $\mathcal{F}^i$ exactly asymptotes to the result obtained from the purely inviscid (high-frequency limit) formalism of Chapter 2 (also [4]) as $\lambda \to \infty$.

4.3.3 Comparison with Direct Numerical Simulations

We now demonstrate that (4.2) is accurate over the entire range of Stokes numbers by comparing our theory with independent, large-scale, 3D numerical simulations[2], previously validated in a variety of streaming scenarios. Please see Bhosale et al. [17], Gazzola et al. [59], Parthasarathy et al. [125] for details on the simulations. Fig. 4.2a-e illustrate the rich time-averaged flow $\langle \boldsymbol{w} \rangle$ at different λ, while Fig. 4.2g,i exemplify the expected confinement of vorticity around the particle. The simulations also serve to justify our omission of an inertia-dominated outer region (Fig. 4.2f,h). In Fig. 4.4a, we compare analytical and simulated particle trajectories on both the oscillatory and slow time scales. The classical MR equation fails to capture any of the attraction observed in DNS, while the present theory is in excellent agreement both for the instantaneous motion and the rectified drift of the particle. Moreover, it succeeds over the entire range of λ values, cf. Fig. 4.4b-e. In the figure we also see that the inviscid formalism of Chapter 2 (dashed lines) gives a much too weak attraction, particularly for practically relevant $\lambda \sim 1$. This is an intuitive outcome of taking viscosity into account, as the Stokes boundary layer (cf. Fig. 4.2g,i) effectively increases particle size, so that forces scaling with particle size (cf. (4.1)) become larger. Figure 4.4 also illustrates the great benefit of the analytical theory (4.19), as individual DNS incur large computational costs of up to $\sim$ 100,000 core-hours

[2]Simulations performed by Gazzola group

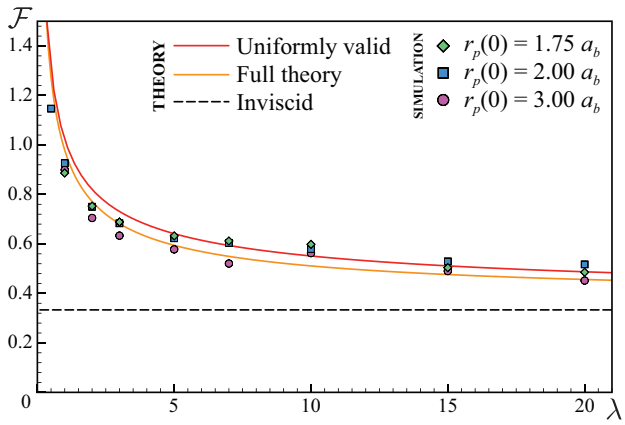

Figure 4.5: Comparison of the overall inertial force magnitude $\mathcal{F}$ in theory (lines) and simulation (symbols), for various λ and initial particle positions $r_p(0)$. The uniformly valid expression (red) is extremely close to the full solution (orange) and in excellent agreement with all DNS data, while the inviscid theory (black dashed) severely underestimates the forces.

on the Stampede2 supercomputer.

Figure 4.5 summarizes the comparison between theory and simulations: Time-averaged DNS trajectories (beyond an initial transient) for different values of λ were fitted to (4.19) to determine the dimensionless force $\mathcal{F}$. Our analytical predictions are in quantitative agreement with DNS across the range of λ, exhibiting an average error of $\approx 7\%$. This remaining discrepancy is attributed to effects of the narrowing distance between particle and bubble interface, which modifies the integration volume in (4.6e) and also compromises the assumption of purely radial flow at the bubble interface, due to the particle disturbance flow.

4.4 Discussion

The data presented above demonstrate that particle motion can be described quantitatively by the novel forcing terms of (4.15) and (4.16). It is furthermore important to show that other hydrodynamic force contributions will not alter or overwhelm the effects described here.

4.4.1 Comparison with other hydrodynamic forces

We have investigated the case of radially symmetric flow specifically because it isolates the novel inertial forces reported here as the only effect, allowing us to assess the accuracy of the theory. In more general flow situations, other forces will compete with $F_{\Gamma\kappa}$, and we estimate their relative magnitude here to show that in many practical scenarios they will not overwhelm the newly identified contribution. If the particle density ρ_p does not match ρ, a density contrast force [4] is induced, generalizing acoustofluidic secondary radiation forces. This force is included within our general formalism, but in order for it to exceed $F_{\Gamma\kappa}$, the density

contrast needs to fulfill $\rho_p/\rho - 1 \gtrsim 3(a_p/r_p)^2(1 + 2/\sqrt{\lambda})$. Appreciable forces only act when $r_p \gtrsim a_b$ and if λ is not very small; thus, $\rho_p/\rho - 1 \gtrsim 0.3$ for typical geometries characterized by $\alpha \lesssim 0.2$. In most microfluidic, and certainly in biomedical applications, the density contrast is far less: even at 5% density difference (e.g. for polystyrene particles), $F_{\Gamma\kappa}$ is 5-30 times stronger than the density contrast force for $0.5 < \lambda < 5$. Other forces result from steady flows: oscillation of an a_b-sized object will generically induce steady streaming flow at speed $\sim \epsilon^2 a_b U^*$, and it may have transverse gradients of scale a_b (in addition to radial gradients). This situation induces a Saffman lift force L_S [145] for particles with finite slip velocity V_s, again because of density mismatch [4, 93]. Augmenting our theory with an outer-flow inertial region [157] would reproduce this force. L_S and $F_{\Gamma\kappa}$ are of equal magnitude if $V_s \sim 5\alpha^2(4.1 + 2\sqrt{\lambda})U^*$. In realistic settings, V_s would need to exceed U^*, implying that the steady flow would overwhelm the oscillatory motion, defeating the purpose of oscillatory-flow microfluidics. Lastly, flows with finite $\nabla^2\bar{\mathbf{U}}$ give rise to Faxén terms in added mass and drag. However, the oscillatory flows discussed here are (almost) potential flows as shown above, so that the leading order effect of Faxén terms comes from steady flow curvature and provides only an $\mathcal{O}(\alpha^2)$ correction to the steady-flow Stokes drag.

4.4.2 Absence of outer-flow inertia

Often, the evaluation of forces on particles in a flow is complicated by the transition between a viscous-dominated inner flow volume (near the particle) and an inertia-dominated outer volume, necessitating an asymptotic matching of the two limits (such as for the Oseen [93] and Saffman [145] problems). The present formalism, however, only employs an inner-solution expansion and still obtains accurate predictions (see also [73], where it is shown that such an expansion is successful even up to $Re_p \sim 10$). This behavior can be rationalized by invoking the analysis of Lovalenti and Brady [93] who showed that an outer region is not present when the characteristic unsteady time scale ω^{-1} is shorter than the convective inertial time scale $\nu/(U^* w^{(0)})^2$, where $w^{(0)}$ is the dimensionless velocity scale of the fluid as measured in the particle reference frame. For density matched particles $w^{(0)} = \mathcal{O}(\alpha)$, so that this criterion reduces to $\epsilon^2\lambda \ll 1$, requiring the oscillation amplitude of the flow to be smaller than $\delta_S\alpha^{-1}$, which is easily satisfied in most experimental situations. More directly, the Lovalenti-Brady criterion relies on the magnitude of oscillatory inertia in the disturbance flow $\partial \boldsymbol{w}^{(1)}/\partial t$ being much larger than that of the advective term $\mathbf{f}$. DNS verifies that this relation holds for the entire range of λ treated here (see Fig. 4.2f,h). In flows that do not satisfy this condition, our theory can be applied to both inner and outer region, with matching expansions in particle Reynolds number. As a separate effect, outer flow inertia due to the slow (steady) motion of the particle will be present, but only results in $O(\epsilon)$ corrections to the Stokes drag.

4.5 Conclusions

We thus conclude that the novel inertial force terms described here are not a small correction, but the dominant effect in many commonplace oscillating microfluidics applications, in particular for nearly density matched particles, the most relevant case in medicine and health contexts, where biological materials are primary targets. These forces are ubiquitous in viscous flows with finite inertial effects from oscillatory driving, they stem from flow gradients and curvatures, they are attractive towards the oscillating object under mild assumptions, and they are much stronger than inviscid forces. They lead to significant displacements of cell-sized particles ($1-10\mu m$) over ms time scales, making them a promising tool for precision manipulation strategies. Further, our analysis shows that a surprisingly simple expression accurately predicts particle motion, as quantitatively confirmed against first-principle, large-scale direct numerical simulations. The theory highlights the immense reduction in computational effort between DNS and an explicit analytical theory, and as a generalization of the Maxey–Riley formalism is applicable to a wide variety of flow situations.

Chapter 5

Inertial force on non-neutrally buoyant particles

The previous chapter dealt with background flow curvature induced $\mathcal{O}(\mathrm{Re}_p)$ forces on neutrally buoyant inertial particles, that we showed can be significant and often dominate other forces in oscillatory microfluidic application. In this chapter[1], we will quantify additional inertial lift forces on particles emanating from a finite density-contrast with the surrounding fluid. As a consequence of this density-contrast, the difference of velocities between the particle and the fluid evaluated at the particle position is non-vanishing, resulting in a force prediction that stems from the interaction of background flow gradients, particle-fluid slip velocity and particle inertia. The forces described here are not a small correction, but an important effect, in particular for nearly density matched cell-sized particles in biomicrofluidics, where they can be used for fast displacement and separation. We also establish a connection to acoustofluidics: Our formalism rigorously generalizes the secondary radiation force—typically encountered in acoustofluidics—to include viscous effects. These results are verified in comparison to direct numerical simulations.

5.1 Introduction

There have been a number of studies over the past few decades on deriving an equation of motion for particles, droplets or bubbles in manifold situations, where a semi-empirical equation of motion is used—from the earliest results going back to Basset [15] to the empirical data obtained a couple of decades ago (see [108] for a brief history). It was only in the seminal work by Maxey and Riley [103] (MR) that a rigorous and systematic approach to including forces on particles was offered, albeit strictly in the limit of vanishing inertial effects. While this work has been the state-of-the-art for over the past 40 years, recent advances, e.g., in oscillatory microfluidics, have recognized the importance of particle inertia in order to efficiently manipulating particles in a high-throughput fashion; the Maxey–Riley equation fails to explain these observations. Theoretical development of the field, in general, has lagged experimental advances; consequently, many ad hoc assumptions have been made to understand these effects. Thus, our motivation

[1] This chapter is adapted from Agarwal et al. [5]

for studying the effects of finite particle inertia is two-fold. First, there is a lack of basic understanding of the forces acting on a particle immersed in a general unsteady background flow. Second, a plethora of applications in inertial microfluidics exploit particle inertia and a fundamental understanding of inertial forces can open up new avenues for ultra-fast, high-throughput particle manipulation.

The MR equation does not predict any net force on neutrally buoyant particles; while in the previous chapter we showed that there can be significant inertial forces on such particles which are completely missed by MR, in this chapter we further show that MR misses important contributions even for particles with a finite density contrast which emanate from an interplay between the particle's slip velocity and flow gradients. Written in dimensional form (ignoring gravity and Faxen terms), the MR equation reads explicitly:

$$m_p \frac{d\mathbf{U}_p}{dt} = m_f \frac{D\mathbf{U}}{Dt} - \frac{1}{2} m_f \frac{d}{dt}\left(\mathbf{U}_p - \mathbf{U}\right) - 6\pi\nu\rho_f a_p \left(\mathbf{U}_p - \mathbf{U}\right) - 6\pi\nu\rho_f a_p^2 \int_0^t \frac{d/d\tau\left(\mathbf{U}_p - \mathbf{U}\right)}{(\pi\nu(t-\tau))^{1/2}} d\tau, \tag{5.1}$$

where the first term on the RHS is acceleration following the fluid element, the second term is the added-mass force, the third term is the usual Stokes drag and the last term is the Basset history term. As noted in the previous chapter, (5.1) predicts no net deviation of a neutrally buoyant particle from the fluid trajectory since the slip velocity $\mathbf{U}_p - \mathbf{U} = 0$. Consequently, all terms except the first term on the RHS vanish. We previously showed how MR missed important force contributions that depend on the flow curvature, both at the background flow and the disturbance flow orders. Here, we further point out important contributions due to a finite density contrast.

The equation of motion derived by MR differed from previous versions in the form of the fluid acceleration term, i.e., $m_f \frac{D\mathbf{U}}{Dt}$ instead of $m_f \frac{d\mathbf{U}}{dt}$ following the particle—the values of the two derivatives can differ substantially when the Reynolds number is not small. A similar question arises over the form of the added mass term in (5.1): Auton et al. [11] showed that for potential flows this is incorrect and should instead be $\frac{1}{2} m_f \left(\frac{d\mathbf{U}_p}{dt} - \frac{D\mathbf{U}}{Dt}\right)$. Again, in the limit of the low Reynolds number approximation used by MR in deriving the disturbance flow field force, these two expressions are identical. However, for flows distinguished by non-zero inertial effects, the difference between the two expressions can be quite significant. In the following, we will show that a systematic inclusion of the $\mathcal{O}(\mathrm{Re}_p)$ force through a regular perturbation expansion leads to additional contributions due to the slip velocity. These specialize to the Auton [11] correction in the potential flow limit, but can also be substantially larger when viscous effects are important e.g., due to the presence of viscous streaming around the particle in the case of oscillatory flows. We will also show how our formalism generalizes the far-field acoustofluidic secondary radiation force on particles in inviscid flows to include viscous effects, thus bridging the two fields.

5.2 Inertial forces due to slip velocity

The evaluation of the $\mathcal{O}(\mathrm{Re}_p)$ force proceeds analogous to the reciprocal-theorem-based procedure outlined in the previous chapter. In particular, to compute the volume integral in (3.17b), as noted previously, only certain products in $\mathbf{f}_0$ are non-vanishing when the angular integration over θ is performed due to alternating symmetry of terms in the background flow field Taylor expansion (3.6). Consequently, in the leading order disturbance flow (3.8), only products of adjacent terms survive. For example, the first term in $\mathbf{f}_0$ reads

$$\boldsymbol{w}^{(0)} \cdot \nabla \boldsymbol{w}_0^{(1)} = (-\mathbf{u}_s + \mathbf{r}\cdot\mathbf{E} + \mathbf{rr} : \mathbf{G}) \cdot \nabla \left(\boldsymbol{\mathcal{M}}_D \cdot \mathbf{u}_s - \boldsymbol{\mathcal{M}}_Q \cdot (\mathbf{r}\cdot\mathbf{E}) - \boldsymbol{\mathcal{M}}_O \cdot (\mathbf{rr} : \mathbf{G})\right), \tag{5.2}$$

and the only terms that survive the angular integration are the symmetric ones (after a contraction with the symmetric test flow $\mathbf{u}'$), i.e.,

$$(-\mathbf{u}_s + \mathbf{rr} : \mathbf{G}) \cdot \nabla \left(-\boldsymbol{\mathcal{M}}_Q \cdot (\mathbf{r}\cdot\mathbf{E})\right) + (\mathbf{r}\cdot\mathbf{E}) \cdot \nabla \left(\boldsymbol{\mathcal{M}}_D \cdot \mathbf{u}_s - \boldsymbol{\mathcal{M}}_O \cdot (\mathbf{rr} : \mathbf{G})\right). \tag{5.3}$$

In this chapter, we evaluate the inertial force due to a finite slip velocity $\mathbf{u}_s$ for a non-neutrally buoyant particle. Only the following terms in $\mathbf{f}_0$ have non-trivial contributions to the volume integral:

$$\begin{aligned}\mathbf{f}_0 =& \mathbf{u}_s \cdot \nabla \left(\boldsymbol{\mathcal{M}}_Q \cdot (\mathbf{r}\cdot\mathbf{E})\right) + (\mathbf{r}\cdot\mathbf{E}) \cdot \nabla \left(\boldsymbol{\mathcal{M}}_D \cdot \mathbf{u}_s\right) \\ &+ (\boldsymbol{\mathcal{M}}_D \cdot \mathbf{u}_s) \cdot \nabla (\mathbf{r}\cdot\mathbf{E}) \\ &- (\boldsymbol{\mathcal{M}}_D \cdot \mathbf{u}_s) \cdot \nabla \left(\boldsymbol{\mathcal{M}}_Q \cdot (\mathbf{r}\cdot\mathbf{E})\right) - (\boldsymbol{\mathcal{M}}_Q \cdot (\mathbf{r}\cdot\mathbf{E})) \cdot \nabla \left(\boldsymbol{\mathcal{M}}_D \cdot \mathbf{u}_s\right).\end{aligned} \tag{5.4}$$

The flow field information is contained in $\mathbf{u}_s$ and $\mathbf{E}$, which are both evaluated at the particle position. As before, we make the potential flow approximation for the background flow and assume, without loss of generality, that all temporal dependences are proportional to $e^{i\tau}$. The slip velocity, in general, can then be decomposed into an in-phase and an out-of-phase component with respect to the background flow such that, $\mathbf{u}_s(\mathbf{r}_p, \tau) = \mathbf{u}_s^I(\mathbf{r}_p)\exp(i\tau)\tau + \mathbf{u}_s^O(\mathbf{r}_p) i \exp(i\tau)$, where $\mathbf{u}_s^I$ and $\mathbf{u}_s^O$ are the in-phase and out-of-phase potential flow spatial dependences evaluated at the particle position $\mathbf{r}_p$. The $\mathcal{O}(\mathrm{Re}_p)$ inertial force will have products involving $\mathbf{u}_s^I$ and $\mathbf{u}_s^O$ with $\mathbf{E}$, which is purely in-phase. In order to isolate contributions from the in-phase and out-of-phase slip velocity components and taking advantage of the potential flow nature of the background flow, the inertial force can be suggestively cast into the form:

$$\left\langle \frac{F_1^{(1)}}{F_S/6\pi} \right\rangle = -\left\langle \mathcal{L}^{-1}\left\{ \frac{1}{\hat{u}'} \int_V \hat{\mathbf{u}}' \cdot \hat{\mathbf{f}}_0 dV \right\} \right\rangle = \langle \mathbf{u}_s \cdot \mathbf{E} \rangle \cdot \mathbf{e}\, \mathcal{G}_1'(\lambda) + \langle \partial_t \mathbf{u}_s \cdot \mathbf{E} \rangle \cdot \mathbf{e}\, \mathcal{G}_2'(\lambda) \tag{5.5}$$

where the first term is the in-phase contribution while the second term is the out-of-phase contribution and the $\mathcal{G}_i'(\lambda)$'s are the explicit outcomes of the volume integration evaluation. More generally, in dimensional terms, these force contributions are rewritten as

$$\begin{aligned}\mathrm{Re}_p\, F_1^{(1)} =&\rho_f a_p^2 {U^*}^2 \left(\mathbf{u}_s \cdot \mathbf{E} \cdot \mathbf{e}\, \mathcal{G}_1'(\lambda) + \partial_\tau \mathbf{u}_s \cdot \mathbf{E} \cdot \mathbf{e}\, \mathcal{G}_2'(\lambda)\right) \\ =&m_f \left[(\mathbf{U}_p - \mathbf{U}) \cdot \nabla \mathbf{U}\right] \cdot \mathbf{e}\, \mathcal{G}_1(\lambda) + m_f \left[\partial_t (\mathbf{U}_p - \mathbf{U}) \cdot \nabla \mathbf{U}\right] \cdot \mathbf{e}\, \frac{\mathcal{G}_2(\lambda)}{\omega}\end{aligned} \tag{5.6}$$

where, without loss of generality for oscillatory flows, we remove the time-averaging operation. Here, $\mathcal{G}_i(\lambda) = \mathcal{G}_i'(\lambda)/(4\pi/3)$.

5.2.1 Evaluation of $\mathcal{G}_1$ and $\mathcal{G}_2$

We obtain an explicit but rather lengthy expression from the volume integration in (5.5) for the in-phase inertial force component for oscillatory flows:

$$\begin{aligned}\mathcal{G}_1 =&e^{-i\sqrt{\bar\lambda}}\Bigg[225e^{3\sqrt{\bar\lambda}}\bar\lambda^{3/2}\Bigg(e^{2i\sqrt{\bar\lambda}}\left((3+2i)\sqrt{\bar\lambda}+2i\right)\left(\mathrm{Ei}\left((-3-i)\sqrt{\bar\lambda}\right)+i\pi\right) \\ &-\left(2+(2+3i)\sqrt{\bar\lambda}\right)\left(\pi+i\mathrm{Ei}\left((-3+i)\sqrt{\bar\lambda}\right)\right)\Bigg) \\ &+48e^{(2+i)\sqrt{\bar\lambda}}\left(2\bar\lambda+12\sqrt{\bar\lambda}+11\right)\bar\lambda^{5/2}\mathrm{Ei}\left(-2\sqrt{\bar\lambda}\right) \\ &-e^{\sqrt{\bar\lambda}}\left(2\sqrt{\bar\lambda}+3\right)\bar\lambda^2\Bigg(e^{2i\sqrt{\bar\lambda}}\left(2\left(\sqrt{\bar\lambda}+(2+i)\right)\sqrt{\bar\lambda}\left(2\bar\lambda+(3+3i)\sqrt{\bar\lambda}+(3+6i)\right)+15i\right) \\ &\left(\pi-i\mathrm{Ei}\left((-1-i)\sqrt{\bar\lambda}\right)\right) \\ &+\left(2\left(\sqrt{\bar\lambda}+(2-i)\right)\sqrt{\bar\lambda}\left(2\bar\lambda+(3-3i)\sqrt{\bar\lambda}+(3-6i)\right)-15i\right)\left(\pi+i\mathrm{Ei}\left((-1+i)\sqrt{\bar\lambda}\right)\right)\Bigg) \\ &+e^{i\sqrt{\bar\lambda}}\left(302\bar\lambda^{3/2}+144\bar\lambda^{5/2}+12\bar\lambda^{7/2}+8\bar\lambda^4-8\bar\lambda^3+36\bar\lambda^2-598\bar\lambda-512\sqrt{\bar\lambda}-189\right)\Bigg] \\ &\Big/\left(160\left(2\bar\lambda^{3/2}+2\bar\lambda+\sqrt{\bar\lambda}\right)\right),\end{aligned} \tag{5.7}$$

where $\bar\lambda = 3\lambda/2$ and Ei is the exponential integral function. Analogous to $\mathcal{F}$ in Chapter 4, an excellent uniformly valid solution can be constructed by simply adding the leading orders of the small and large λ Taylor expansions of $\mathcal{G}_1$. We Taylor expand in both the viscously dominated limit ($\lambda \to 0$) and the inviscid limit ($\lambda \to \infty$) to obtain

$$\mathcal{G}_1^v = -\frac{63}{80}\sqrt{\frac{3}{2\lambda}} + \mathcal{O}(1), \quad \mathcal{G}_1^i = -\frac{1}{2} + \mathcal{O}(1/\sqrt{\lambda}). \tag{5.8}$$

Adding these two results in the following expression:

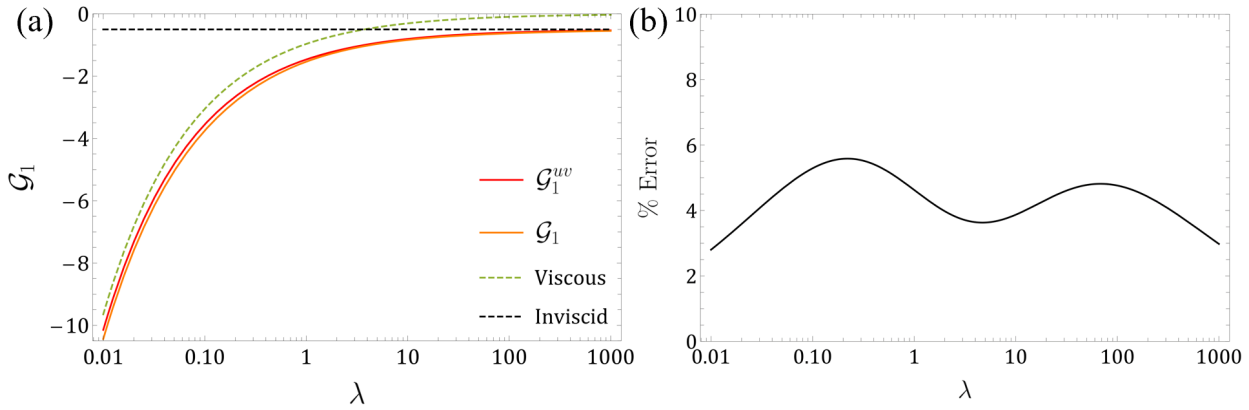

Figure 5.1: Plot of the overall inertial force magnitude $\mathcal{G}_1$: the uniformly valid expression (red) closely tracks the full solution (orange) for $\mathcal{G}_1$. (b) The magnitude of the percentage error between the uniformly valid and full solutions is small throughout the entire range of λ, with a maximum error of $\sim 6\%$

$$\mathcal{G}_1^{uv}(\lambda) \approx -\left(\frac{1}{2} + \frac{63}{80}\sqrt{\frac{3}{2\lambda}}\right). \tag{5.9}$$

This is an excellent approximation to the full (5.7), as illustrated in Fig. 5.1: The simple two-term expression agrees well quantitatively over the entire range of the parameter λ with a maximum error of $\sim 6\%$.

The expression for the out-of-phase component $\mathcal{G}_2$ is similarly explicit but lengthy:

$$\begin{aligned}
\mathcal{G}_2 =& e^{-i\sqrt{\bar\lambda}}\sqrt{\bar\lambda}\Big[-240e^{(2+i)\sqrt{\bar\lambda}}\left(2\bar\lambda^{3/2}+6\bar\lambda+6\sqrt{\bar\lambda}+3\right)\bar\lambda^{3/2}\mathrm{Ei}\left(-2\sqrt{\bar\lambda}\right) \\
&+225e^{3\sqrt{\bar\lambda}}\bar\lambda^{3/2}\Big(\left(3+(3+2i)\sqrt{\bar\lambda}\right)\left(\mathrm{Ei}\left((-3+i)\sqrt{\bar\lambda}\right)-i\pi\right) \\
&+e^{2i\sqrt{\bar\lambda}}\left((2+3i)\sqrt{\bar\lambda}+3i\right)\left(\pi-i\mathrm{Ei}\left((-3-i)\sqrt{\bar\lambda}\right)\right)\Big) \\
&+e^{\sqrt{\bar\lambda}}\left(2\sqrt{\bar\lambda}+3\right)\bar\lambda^2\Big(\left((10+14i)\bar\lambda^{3/2}+4i\bar\lambda^2+(30+12i)\bar\lambda+30\sqrt{\bar\lambda}+15\right) \\
&\left(\pi+i\mathrm{Ei}\left((-1+i)\sqrt{\bar\lambda}\right)\right) \\
&+e^{2i\sqrt{\bar\lambda}}\left(15-2i\left(\sqrt{\bar\lambda}+(2+i)\right)\sqrt{\bar\lambda}\left(2\bar\lambda+(3+3i)\sqrt{\bar\lambda}+(3+6i)\right)\right)\left(\pi-i\mathrm{Ei}\left((-1-i)\sqrt{\bar\lambda}\right)\right)\Big) \\
&-e^{i\sqrt{\bar\lambda}}\left(42\bar\lambda^{3/2}+340\bar\lambda^{5/2}+60\bar\lambda^{7/2}+8\bar\lambda^4+128\bar\lambda^3+666\bar\lambda^2-288\bar\lambda+54\sqrt{\bar\lambda}+45\right)\Big] \\
&\Big/\left(240\left(2\bar\lambda^{3/2}+2\bar\lambda+\sqrt{\bar\lambda}\right)\right)
\end{aligned} \tag{5.10}$$

However, a Taylor expansion in the viscous and inviscid limits respectively results in

$$\mathcal{G}_2^v = \frac{3}{16}\sqrt{\frac{3}{2\lambda}} + \mathcal{O}(1), \quad \mathcal{G}_2^i = -\frac{57}{40}\sqrt{\frac{3}{2\lambda}} + \mathcal{O}(1/\lambda). \tag{5.11}$$

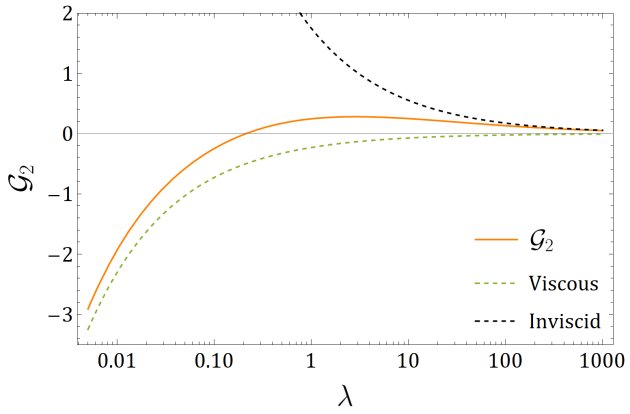

Figure 5.2: Plot of the overall inertial force magnitude $\mathcal{G}_2$: the approximation (red) is shown against the full solution (orange) for $\mathcal{G}_2$. (b) The magnitude of the percentage error between approximation and full solutions over the entire range of λ is shown

Both the leading order large and small λ limits, thus, have a $\mathcal{O}(1/\sqrt{\lambda})$ scaling with different prefactors. $\mathcal{G}_2$ is subdominant to $\mathcal{G}_1$ when $\lambda \gtrsim 1$ and it decays to zero in the potential flow ($\lambda \to \infty$) limit. An approximation cannot be constructed by simply adding the two terms; we use the full expression (5.10), noting that the contribution from this term is a small correction compared to $\mathcal{G}_1$.

5.2.2 The Auton correction to MR

The first term on the RHS of (5.5), involving $\mathcal{G}_1$, modifies the added-mass term at $\mathcal{O}(\mathrm{Re}_p^0)$ in the original derivation of MR [103] and results in the well-known Auton correction [11] in the inviscid ($\lambda \to \infty$) limit, modifying $\frac{d\mathbf{U}}{dt}$ to $\frac{D\mathbf{U}}{Dt}$, shown below explicitly:

$$
\begin{aligned}
&-\frac{1}{2}m_f\frac{d}{dt}\left[\mathbf{U}_p-\mathbf{U}\right]\cdot\mathbf{e}+m_f\left[(\mathbf{U}_p-\mathbf{U})\cdot\nabla\mathbf{U}\right]\cdot\mathbf{e}\,\mathcal{G}_1(\lambda)\\
&=-\frac{1}{2}m_f\left[\frac{d}{dt}\mathbf{U}_p-\frac{\partial\mathbf{U}}{\partial t}-\mathbf{U}_p\cdot\nabla\mathbf{U}\right]\cdot\mathbf{e}-\left(\frac{1}{2}+\frac{63}{80}\sqrt{\frac{3}{2\lambda}}\right)m_f\left[(\mathbf{U}_p-\mathbf{U})\cdot\nabla\mathbf{U}\right]\cdot\mathbf{e}\\
&=-\frac{1}{2}m_f\left[\frac{d}{dt}\mathbf{U}_p-\frac{D}{Dt}\mathbf{U}\right]\cdot\mathbf{e}-\frac{63}{80}\sqrt{\frac{3}{2\lambda}}m_f\left[(\mathbf{U}_p-\mathbf{U})\cdot\nabla\mathbf{U}\right]\cdot\mathbf{e}\,.
\end{aligned}
\tag{5.12}
$$

where we use the simple two-term approximation (5.9) for $\mathcal{G}_1$. Thus, unlike previous studies which heuristically modify the derivative in the added mass term, our approach shows that a rigorous derivation of the $\mathcal{O}(\mathrm{Re}_p)$ inertial forces results in the modification of the added mass term. Furthermore, virtually all practically relevant oscillatory flows involve small to moderate values of the parameter λ. Therefore, the contribution from the second term of (5.12)—capturing the effect of viscous streaming around the particle—results in the inertial force being quite large due to the $1/\sqrt{\lambda}$ scaling, reminiscent of Saffman lift [145].

We note that the second term in (5.5), involving $\mathcal{G}_2$, arises due to the out-of-phase component of the slip velocity and thus characterises diffusion of vorticity from the particle—it decays to 0 as $\lambda \to \infty$. This term is, physically, analogous to the Basset-Boussinesq history force and contributes when $\lambda \sim \mathcal{O}(1)$.

5.3 Equation of motion for the particle

In summary, after including all the $\mathcal{O}(\mathrm{Re}_p)$ force terms, the dimensional equation of motion for a rigid spherical particle immersed in an oscillatory background flow field $\mathbf{U}$ reads

$$\begin{aligned} m_p \frac{d\mathbf{U}_p}{dt} =& m_f \frac{D\mathbf{U}}{Dt} - \frac{1}{2} m_f \frac{d}{dt}\left[\mathbf{U}_p - \mathbf{U}\right] - 6\pi\rho_f \nu a_p \left[\mathbf{U}_p(t) - \mathbf{U}(\mathbf{r}_p(t), t)\right] \\ & - 6\pi^{1/2}\nu^{1/2} a_p^2 \rho_f \int_{-\infty}^{t} \frac{d/d\tau \left[\mathbf{U}_p(t) - \mathbf{U}(\mathbf{r}_p(t), t)\right]}{\sqrt{t-\tau}} d\tau \\ & + m_f \left[(\mathbf{U}_p - \mathbf{U}) \cdot \nabla \mathbf{U}\right] \mathcal{G}_1(\lambda) + m_f \left[\partial_t (\mathbf{U}_p - \mathbf{U}) \cdot \nabla \mathbf{U}\right] \frac{\mathcal{G}_2(\lambda)}{\omega} + m_f a_p^2 \nabla \mathbf{U} : \nabla\left(\nabla \mathbf{U}\right) \mathcal{F} \end{aligned} \tag{5.13}$$

It is well-known that the Basset history integral poses a special challenge (cf. [107, 134, 163]): Its evaluation is often computationally intensive since one has to numerical solve an integro-differential equation. However, for oscillatory flows it can be evaluated explicitly—reducing to a simple ODE—and results in sub-dominant corrections to the Stokes drag and Added mass forces (cf. [44, 81]), i.e.,

$$\begin{aligned} 6\pi^{1/2}\nu^{1/2} a_p^2 \rho_f \int_{-\infty}^{t} \frac{d/d\tau \left[\mathbf{U}_p(t) - \mathbf{U}(\mathbf{r}_p(t), t)\right]}{\sqrt{t-\tau}} d\tau = & \frac{1}{2} m_f \frac{d}{dt}\left[\mathbf{U}_p(t) - \mathbf{U}(\mathbf{r}_p(t), t)\right] \left(3\sqrt{\frac{3}{2\lambda}}\right) \\ & + 6\pi\rho_f \nu a_p \left[\mathbf{U}_p(t) - \mathbf{U}(\mathbf{r}_p(t), t)\right] \left(\sqrt{\frac{3\lambda}{2}}\right). \end{aligned} \tag{5.14}$$

We note that these corrections apply only if the velocity difference between the particle and the fluid is oscillatory, i.e. $(\mathbf{U}_p(t) - \mathbf{U}(\mathbf{X}_p(t), t)) \propto e^{it}$. Therefore, (5.13) cannot be easily used to describe the unsteady particle dynamics with rectified motion due to the difficulty in evaluating the history term. The following subsection will deal with how one can easily evaluate the non-local integral and obtain a rigorous and easy to use equation of motion for the particle.

5.3.1 Time-scale separation: Rectified equation of motion

Equation (5.13) describes the unsteady particle dynamics where the history integral becomes explicit only for particles executing purely oscillatory motion. In more general settings, where there is superposition of *slower* rectified or transport fluid flows—with a clear separation of scales from the *fast* oscillatory motion—

it becomes advantageous to employ the method of multiple scales. This separation of scales allows for an explicit, analytical evaluation of the history integral and results in a simple over-damped equation of motion for the particle that captures the dynamics accurately. The $\mathcal{O}(\mathrm{Re}_p)$ inertial forces derived previously due to the fast oscillatory motion result in an additional rectified lift force on the particle.

In order to separate time scales, we first specialize (5.13) to oscillatory flows established by a localized oscillating source with curvature scale a_b, amplitude ϵa_b and angular frequency ω. We, thus, non-dimensionalize with a_b, $\epsilon a_b \omega$ and $1/\omega$ as the characteristic length, velocity and time scales. The resulting non-dimensional unsteady equation of motion reads:

$$\begin{aligned}\lambda\left(\hat{\kappa}+1\right)\frac{d^2\mathbf{r}_p}{dt^2} =&\epsilon\lambda\frac{\partial\mathbf{u}}{\partial t}+\frac{2\lambda}{3}\epsilon^2\mathbf{u}\cdot\nabla\mathbf{u}-\frac{\lambda}{3}\epsilon^2\lambda\mathbf{U}_p\cdot\nabla\mathbf{u}+\sqrt{\frac{3\lambda}{\pi}}\int_{-\infty}^{t}\frac{d/d\tau\left[d\mathbf{r}_p(\tau)/d\tau-\epsilon\mathbf{u}(\mathbf{r}_p(\tau),\tau)\right]}{\sqrt{t-\tau}}d\tau\\ &-\left(\frac{d\mathbf{r}_p}{dt}-\epsilon\mathbf{u}\right)+\frac{2\lambda}{3}\epsilon\,\mathcal{G}_1\left(\frac{d\mathbf{r}_p}{dt}-\epsilon\mathbf{u}\right)\cdot\nabla\mathbf{u}+\frac{2\lambda}{3}\epsilon\,\mathcal{G}_2\partial_t\left(\frac{d\mathbf{r}_p}{dt}-\epsilon\mathbf{u}\right)\cdot\nabla\mathbf{u}\\ &+\frac{2\lambda}{3}\epsilon^2\alpha^2\,\mathcal{F}\nabla\mathbf{u}:\nabla\nabla\mathbf{u},\end{aligned} \tag{5.15}$$

where $\hat{\kappa}=2/3\left(\frac{\rho_p}{\rho_f}-1\right)$, $\lambda=\frac{a_p^2\omega}{3\nu}$, $\alpha=a_p/a_b$ and $\frac{d\mathbf{r}_p}{dt}=\epsilon\mathbf{u}_p$.

Assuming all parameters are $O(1)$ and $\epsilon\ll 1$, we introduce a "slow time" $T=\epsilon^2 t$, in addition to the "fast time" t. Using the following transformations previously defined in Section 2.2.2,

$$r_p(t)\mapsto r_p(t,T), \tag{5.16a}$$

$$\frac{d}{dt}\mapsto\frac{\partial}{\partial t}+\epsilon^2\frac{\partial}{\partial T}, \tag{5.16b}$$

$$\frac{d^2}{dt^2}\mapsto\frac{\partial^2}{\partial t^2}+2\epsilon^2\frac{\partial^2}{\partial t\partial T}+\epsilon^4\frac{\partial^2}{\partial T^2}, \tag{5.16c}$$

we seek a perturbation solution in the general form: $r_p(t,T)=r_{p_0}(t,T)+\epsilon r_{p_1}(t,T)+\epsilon^2 r_{p_2}(t,T)+\ldots$. Projecting onto the radial direction, we separate orders of ϵ in the following.

We first comment on the contribution due to the history term. Owing to the clear separation of time-scales we obtain:

$$\begin{aligned}\int_{-\infty}^{t}\frac{d/d\tau\left[dr_p(\tau)/d\tau-\epsilon u(r_p(\tau),\tau)\right]}{\sqrt{t-\tau}}d\tau=&\int_{-\infty}^{t}\frac{\frac{\partial^2}{\partial\tau^2}\left(r_{p_0}(T)+\epsilon r_{p_1}(\tau,T)\right)-\epsilon\partial_\tau(u_{osc}+\epsilon r_{p_1}\partial_r u_{osc})}{\sqrt{t-\tau}}d\tau\\ =&\epsilon\int_{-\infty}^{t}\frac{\partial_\tau^2 r_{p_1}(\tau)-\partial_\tau(u_{osc})}{\sqrt{t-\tau}}d\tau\end{aligned} \tag{5.17}$$

The contribution due to the $\mathcal{O}(\epsilon^2)$ nonlinear forcing term $\partial_\tau(\epsilon r_{p_1}\partial_r u_{osc})$ is identically zero for oscillatory flows. Additionally, the effect on the steady flow component is higher-order in ϵ and is, therefore, negligible. Thus, the main contributions due to the history integral appear as sub-dominant corrections to the Stokes drag and Added mass terms, given by (5.14), at the oscillatory flow order, i.e., at $\mathcal{O}(\epsilon)$.

We now proceed with the formal separation of timescales. At $O(1)$, the equation is:

$$\lambda\left(\hat{\kappa}+1\right)\frac{\partial^2 r_{p_0}}{\partial t^2}+\frac{\partial r_{p_0}}{\partial t}=0 \tag{5.18}$$

This equation is trivially satisfied if $r_{p_0}=r_{p_0}(T)$; thus, the leading order particle position r_{p_0} depends only on the slow-time T. At $O(\epsilon)$, we obtain the following after explicitly evaluating the history integral:

$$\lambda\left(\hat{\kappa}+d\right)\frac{\partial^2 r_{p_1}}{\partial t^2}+c\frac{\partial r_{p_1}}{\partial t}=\left\{\lambda d\frac{\partial u_{osc}}{\partial t}+cu_{osc}\right\}_{r_{p_0}}, \tag{5.19}$$

where $c=\left(1+\sqrt{\frac{3\lambda}{2}}\right)$ and $d=\left(1+\sqrt{\frac{3}{2\lambda}}\right)$ encode the Basset force contributions to the Stokes drag and Added mass forces respectively. Assuming $u_{osc}=u_0(r)e^{it}$ and ignoring transients, the solution at $O(\epsilon)$ is given by

$$r_{p_1}=\int\left(u_{osc}+w_{osc}\right)dt \tag{5.20a}$$

$$w_{osc}=-\frac{iU_0\lambda\hat{\kappa}}{c+i\lambda(\hat{\kappa}+d)}e^{it} \tag{5.20b}$$

With the $\mathcal{O}(\epsilon)$ oscillatory particle dynamics explicitly known, we obtain at $O(\epsilon^2)$, after time averaging:

$$\begin{aligned}\frac{dr_{p_0}}{dT}=&\lambda\left\langle r_{p_1}\frac{\partial}{\partial r}\frac{\partial u_{osc}}{\partial t}\right\rangle+\left\langle r_{p_1}\frac{\partial u_{osc}}{\partial r}\right\rangle+\frac{2\lambda}{3}\left\langle u_{osc}\frac{\partial u_{osc}}{\partial r}\right\rangle+\frac{\lambda}{3}\left\langle\frac{\partial r_{p_1}}{\partial t}\frac{\partial u_{osc}}{\partial r}\right\rangle\\&+\frac{2\lambda}{3}\mathcal{G}_1\left\langle\left(\frac{\partial r_{p_1}}{\partial t}-u_{osc}\right)\frac{\partial u_{osc}}{\partial r}\right\rangle+\frac{2\lambda}{3}\mathcal{G}_2\left\langle\partial_t\left(\frac{\partial r_{p_1}}{\partial t}-u_{osc}\right)\frac{\partial u_{osc}}{\partial r}\right\rangle\\&+\frac{2\lambda}{3}\alpha^2\left\langle\nabla\mathbf{u}:\nabla\nabla\mathbf{u}\right\rangle\cdot\mathbf{e}\mathcal{F}\\=&\left\langle\left(\int w_{osc}dt\right)\frac{\partial u_{osc}}{\partial r}\right\rangle-\frac{2\lambda}{3}\left\langle w_{osc}\frac{\partial u_{osc}}{\partial r}\right\rangle\\&+\frac{2\lambda}{3}\mathcal{G}_1\left\langle w_{osc}\frac{\partial u_{osc}}{\partial r}\right\rangle+\frac{2\lambda}{3}\mathcal{G}_2\left\langle\partial_t w_{osc}\frac{\partial u_{osc}}{\partial r}\right\rangle+\frac{2\lambda}{3}\alpha^2\left\langle\nabla\mathbf{u}:\nabla\nabla\mathbf{u}\right\rangle\cdot\mathbf{e}\mathcal{F}.\end{aligned} \tag{5.21}$$

Inserting (5.20), the evaluation of these time-averages is straightforward; the leading order overdamped equation for radial particle motion reads:

$$\frac{dr_{p_0}}{dT}=F_{SR}\mathcal{G}(\lambda)+\frac{2\lambda}{3}\alpha^2\mathcal{F}\left\langle\nabla\mathbf{u}:\nabla\nabla\mathbf{u}\right\rangle\cdot\mathbf{e}, \tag{5.22}$$

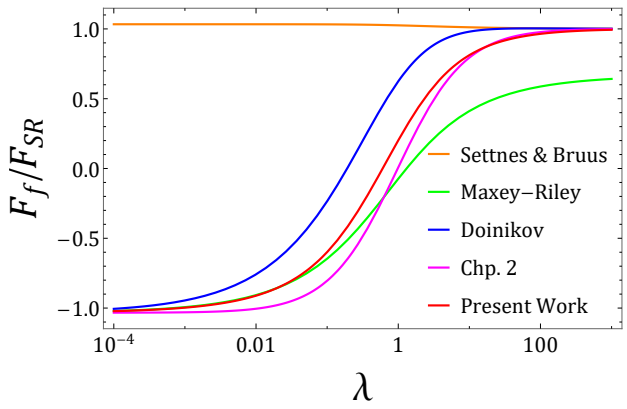

Figure 5.3: Normalized force on a particle for large distances from the oscillation source, graphed as a function of λ for $\hat{\kappa} = 0.033$ (corresponding to a polystytrene particle in water). The present work (Eq. (5.23)) improves upon the force from Chapter 2 (Eq.(2.24)), in agreement with Doinikov [48] and in contradiction to both Settnes and Bruus [148] and Maxey and Riley [103].

where $F_{SR} = \frac{\hat{\kappa}\lambda}{(\hat{\kappa}+1)} \frac{u_0(r_{p_0})u_0'(r_{p_0})}{2}$ is the acoustofluidic Secondary Radiation force, $\mathcal{F}(\lambda) \approx \frac{1}{3} + \frac{9}{16}\sqrt{\frac{3}{2\lambda}}$ and

$$\mathcal{G}(\lambda) = \left(\frac{(\hat{\kappa}+1)(2(1-\mathcal{G}_1)(d+\hat{\kappa})\lambda^2 + c\sqrt{6\lambda}\mathcal{G}_2 - 3c^2)}{3(c^2 + (d+\hat{\kappa})^2\lambda^2)} \right) = \frac{F_f}{F_{SR}}. \tag{5.23}$$

Here, $\hat{\kappa} = \frac{2}{3}(\frac{\rho_p}{\rho_f} - 1)$. Written in this form, it is easy to see that $\mathcal{G}$ is the deviation the of the far-field inviscid F_{SR} when viscous effects are accounted for.

5.3.2 Particles at large distances: Connection to Acoustofluidics Revisited

When the particle is far-away from the oscillating source, i.e. $r_{p_0} \gg 1$, the first term of (5.22) is the dominant contribution to the force on the particle and generalizes the acoustofluidic secondary radiation force (F_{SR}) to include viscous effects. In Chapter 2, we heuristically combined the leading-order inviscid and viscous effects to obtain a prediction for the force on a particle far away from the oscillating source. Our simplified formalism agreed exactly with the much more complicated calculations of Doinikov [48] in both the viscously-dominated ($\lambda \to 0$) and the inviscid limits ($\lambda \to \infty$) while quantitative discrepancies remained in the intermediate regime. In Fig. 5.3, we reproduce the data from Fig. 2.8, graphing it as a function of λ, along with normalized force predictions from Maxey–Riley [103] and Eq. (5.23) (Present Work). The Maxey–Riley formalism complete misses the inviscid limit ($\lambda \to \infty$) and this discrepancy can be directly attributed to having the incorrect form of the fluid acceleration in the added mass term—the modification due to Auton et al. [11]. The formalism of Settnes and Bruus [148] misses the opposite viscous limit ($\lambda \to 0$), as noted previously in Chapter 2. Our current formalism, on the other hand, improves upon the predictions

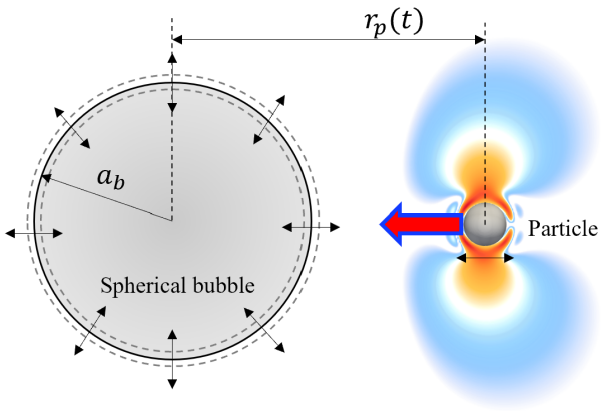

Figure 5.4: The prototypical situation of a particle in an oscillatory flow actuated by a spherically oscillating bubble, resulting in rectified motion, e.g., towards the bubble interface. The time-averaged disturbance flow around the particle is visualized, showing that viscous streaming plays an important role.

from Chapter 2 in the intermediate λ regime. We note that both our theoretical formalism and Doinikov [48] make analytical predictions by employing approximate spatial expansions which are different in their character and therefore, not expected to match exactly. Future work involving numerical solutions of the full Navier–Stokes equations can, perhaps, shed more light on this topic.

In the next section, we specialize (5.22) to the simplest case of a volumetrically oscillating background flow—a situations commonly found in many practical microfluidic setups involving acoustically excited microbubbles—and compare our results with direct numerical simulations.

5.4 Case study: Monopolar background flow field

Equation (5.22) is generally valid for any 1D radial flow with a spatial variation. Here, we specialize to a solid sphere immersed in a spherically monopolar background oscillatory flow, so that $u_0(r) = 1/r^2$. This kind of flow is produced, e.g., by volumetrically oscillating spherical bubbles and is commonly exploited to actuate forces on particles in oscillatory microfluidics. Inserting into (5.22), the time-averaged equation of motion reads (we drop the subscript 0):

$$\frac{dr_p}{dT} = -\frac{\hat{\kappa}\lambda}{r_p^5(\hat{\kappa}+1)}\mathcal{G}(\lambda) - \frac{6}{r_p^7}\alpha^2\lambda\mathcal{F}(\lambda), \tag{5.24}$$

where $-\frac{\hat{\kappa}\lambda}{r_p^5(\hat{\kappa}+1)} = F_{SR}$ and r_p is in units of radius of the oscillating source. We know from the previous chapter that the second term involving $\mathcal{F}$ is always negative, indicating attraction towards the source; however, the sign of the first term depends on $\hat{\kappa}$ as well as on $\mathcal{G}$ (see Fig. 5.3). It is apparent that the magnitude of these two terms depends not only on the parameters such as λ and $\hat{\kappa}$ but also on the radial

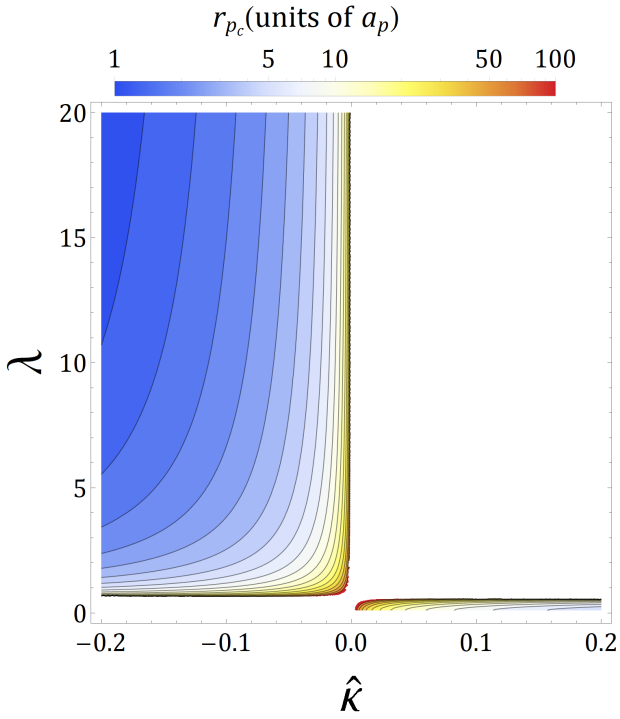

Figure 5.5: Plot showing contours of the critical radial extent r_{p_c} graphed as a function of λ and $\hat{\kappa}$. The isolines indicating values of the trapping extent range from infinite extent at $\hat{\kappa} = 0$ to a particle radius.

distance from the oscillating source—the second, attractive term decays much more strongly with distance in comparison to the first term—resulting in an interesting interplay between the radial distance r_p and the various parameters. In the following, we explore the question of radial equilibrium positions predicted by this simple model.

5.4.1 Equilibrium position

In order to find the critical points of (5.24), we set $\frac{dr_p}{dT} = 0$ and solve for r_p to obtain the critical radial position as

$$r_{p_c} = \sqrt{-\frac{(\hat{\kappa}+1)\mathcal{F}(\lambda)}{\hat{\kappa}\mathcal{G}(\lambda)}}, \tag{5.25}$$

where r_{p_c} is the critical point in units of the particle size. In most practically relevant situations, $\lambda \gtrsim \mathcal{O}(1)$ so that that $\mathcal{G} > 0$, as illustrated in Fig. 5.3. Furthermore, one obtains a real root—an unstable equilibrium position—from (5.25) if the particle is lighter than the surrounding medium ($\hat{\kappa} < 0$). Thus, for lighter particles and $\lambda \gtrsim \mathcal{O}(1)$ this model predicts a critical radial distance (in units of particle radius a_p) below which the particle is attracted towards the oscillating source.

Figure 5.5 plots the iso-lines of (5.25) as a function of the parameters λ and $\hat{\kappa}$. These contours describe

the trapping range of a volumetrically oscillating spherical object: For neutrally buoyant or heavier particles with $\lambda \gtrsim 1$ there is always an attraction towards the source (the extent diverges as $r_{p_c} = \sqrt{\frac{-2}{\hat{\kappa}}}$ when $\lambda \gg 1$), while for lighter particles there is a finite cut-off distance beyond which the particle gets repelled from the oscillating object. Conversely, when $\lambda \sim \mathcal{O}(1)$ the deviation $\mathcal{G}$ of the density-contrast proportional force from F_{SR} due to viscous effects is quite significant and the force changes sign. It predicts repulsion even for heavier particles, however, the λ has to be quite small—this regime is typically inaccessible in practical applications. Thus, r_{p_c} is an important quantity for practical design considerations in many microfluidic setups that make use of e.g., an acoustically excited micro-bubble to selectively trap particles (cf. Chen et al. [35]).

We have not accounted for effects due to a nearby interface in this analysis. In Chapter 2, we found the existence of a stable fixed point, that occurs when the particle is in extremely close proximity to the boundary. This stable equilibrium is consequence of the repulsive lubrication force balancing the attractive force which is dominated by $F_{\Gamma\kappa}$ at short distances. As long as $|\hat{\kappa}| \ll 1$, which is the case in an overwhelming majority of practical applications, the conclusions of Eq. (2.19) are not affected by the findings here. Thus, the stable equilibrium distance is expected to be extremely small compared to the interface scale, and typically even compared with the particle scale.

5.4.2 Comparison with Direct Numerical Simulations

In this subsection, we demonstrate that our formalism is accurate over the entire range of Stokes numbers by comparing our theory with independent, first-principles numerical simulations[2] of the full Navier–Stokes equations, previously validated in a variety of streaming scenarios (see Refs. [17, 59, 125] for simulation details). We noted earlier in Section 5.3 that computing the unsteady particle dynamics entails evaluating the non-local Basset memory integral, which is computationally expensive and not as straight-forward. Instead, a consistent scale separation of (5.15) yielded a simple-to-use and rigorous time-averaged equation of particle motion (5.22). Consequently, in Fig. 5.6(a-d) we compare the analytical and simulated particle trajectories on the slow time scales. The classical MR equation (green dashed lines) fails to capture most of the attraction observed in DNS. Likewise, the inviscid theory of Chapter 2 (black dashed lines) also misses important force contributions and underestimates the attraction, particularly for practically relevant $\lambda \sim \mathcal{O}(1)$. On the other hand, the present theory is in excellent agreement for the rectified drift of the particle, succeeding over the entire range of λ values considered. Figure 5.6 also illustrates the great benefit of the analytical theory (5.24), as individual DNS incur large computational costs.

[2]Simulations performed by Gazzola group

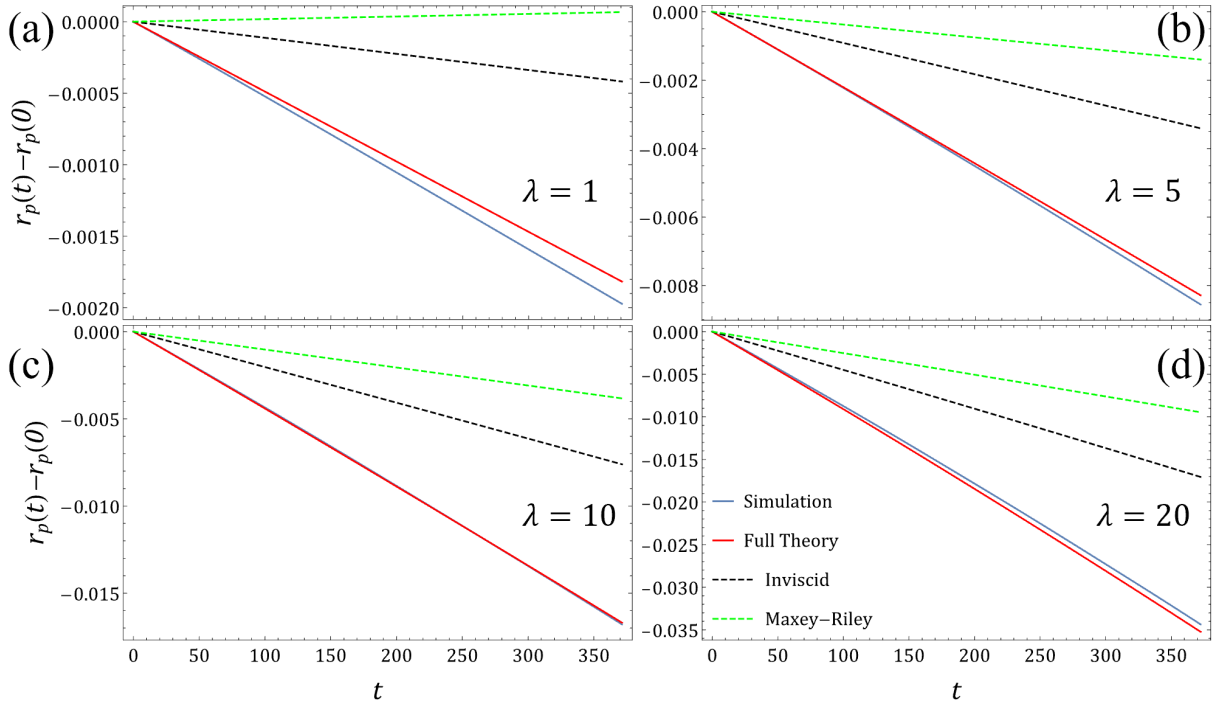

Figure 5.6: Comparison of theoretical (red) and simulated (blue) particle dynamics (radial displacements) for $\hat{\kappa} = 0.033$. (a-d) Time-averaged dynamics from the full theory uses Eq. (5.24) (with the full expressions for $\mathcal{G}$ and $\mathcal{F}$) agrees with DNS for the entire range of λ values. The classical MR equation solutions (green dashed) fail to even qualitatively capture the particle attraction to the bubble for $\lambda = 1$, grossly underestimating the attractive force. The inviscid formalism of Chapter 2 (black dashed) similarly fails quantitatively, demonstrating significant quantitative discrepancies even for the largest λ.

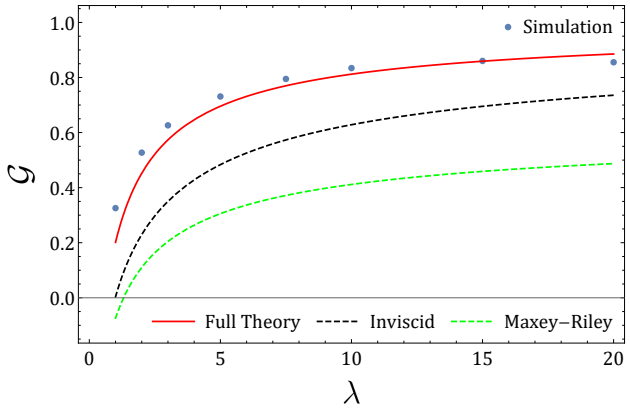

Figure 5.7: Comparison of the overall inertial force magnitude $\mathcal{G}$ in theory (lines) and simulation (filled circles), for $\hat{\kappa} = 0.033$, $\alpha = 0.2$, $\epsilon = 0.05$ and various λ values. The full expression (red) is in excellent agreement with all DNS data, while both the inviscid (black dashed) and Maxey–Riley formalisms (green dashed) severely underestimate the forces.

Figure 5.7 summarizes the comparison between theory and simulations: Using the full expression for $\mathcal{F}$, time-averaged DNS trajectories (beyond an initial transient) for different values of λ were fitted to (5.24) to determine the dimensionless force $\mathcal{G}$. Our analytical predictions are in quantitative agreement with DNS across the range of λ, exhibiting an average error of $\approx 5 - 10\%$.

5.5 Discussion

The results presented above show that particle motion can be described quantitatively by the inertial forcing terms obtained here and in the previous chapter. We noted in the previous chapter that there is often the complication of a transition between a viscous-dominated inner flow volume (near the particle) and an inertia-dominated outer volume, necessitating an asymptotic matching of the two limits (such as for the Oseen [93] and Saffman [145] problems). Our formalism, however, only employs an inner-solution expansion and still obtains accurate predictions; this behavior was rationalized by invoking the analysis of Lovalenti and Brady [93] who showed that an outer region is not present when the magnitude of oscillatory inertia in the disturbance flow $\partial \boldsymbol{w}^{(1)}/\partial t$ is much larger than that of the advective term $\mathbf{f}$, i.e., the characteristic unsteady time scale ω^{-1} is shorter than the convective inertial time scale $\nu/(U^* w^{(0)})^2$, where $w^{(0)}$ is the dimensionless velocity scale of the fluid as measured in the particle reference frame. For the case of non-neutrally buoyant particles $w^{(0)} = \mathcal{O}(\hat{\kappa})$, so that the criterion becomes $\epsilon^2 \lambda \ll \min(\alpha^2/\hat{\kappa}^2, 1)$. As long as $|\hat{\kappa}| \ll 1$, this is easily satisfied in most experimental situations. An interesting point to note is that the condition $\epsilon^2 \lambda \ll \alpha^2/\hat{\kappa}^2$ can be rewritten as $\epsilon \ll \delta_S/(a_b \hat{\kappa})$, i.e., it is independent of the particle length scale. This is a consequence of the fact that first term of the background flow field expansion is evaluated at the particle position and

contains no information about the particle length scale.

In Fig. 5.7, we illustrated how our formalism, in agreement with DNS, predicts a much stronger inertial force compared to both Maxey and Riley [103] and the inviscid formalisms. For particles typically encountered e.g., in microfluidic applications involving biological cells, the density difference is typically around 5%, while the geometric parameter $\alpha \lesssim 0.2$ and $\lambda \gtrsim 1$. A practically useful metric to quantify the effect of the inertial force actuated on the particle by a localized oscillating source is the timescale for radial displacement by about a particle diameter. In most particle manipulation strategies, $r_p \gtrsim a_b$ and on solving (5.24) with these nominal parameter values, we find that our formalism predicts a timescale of $\sim$ 10ms compared to $\sim$ 50ms predicted by the inviscid formalism, translating to much more efficient design strategies to, e.g., sort particles based on size or density. The MR formalism, on the other hand, results in a particle diameter displacement timescale prediction of $\sim$ 500ms, which is off by more than an order of magnitude and completely misses important effects.

As noted in the previous chapter, the major contribution is due to $F_{\Gamma\kappa}$ for these prototypical particles at distances $r_p \gtrsim a_b$. However, since $F_{\Gamma\kappa}$ decays much more strongly with the distance from the source, the density contrast dependent force can become comparable in magnitude, resulting in, e.g., unstable equilibrium positions for particles with $\hat{\kappa} < 0$. Thus, present work suggests new avenues for particle trapping/sorting relying on density contrast; some of these ideas will be explored in the next chapter.

5.6 Conclusions

While the inertial force contribution of Chapter 5 is entirely new, we have shown that the terms derived in the present chapter are, nevertheless, important and sometimes overwhelming corrections to the density-contrast dependent terms already present in the original MR formalism. We thus conclude that the inertial forces described here are not a small correction, but an important effect in many customary microfluidic settings, in particular for nearly density matched cell-sized particles—the most relevant case in medicine and health contexts—where biological materials are primary targets. Present work systematically accounts for finite inertial forces in viscous flows that result from the interaction of the density-contrast dependent slip velocity with flow gradients. We have shown rigorously that the well-known Auton et al. [11] modification to MR for particles in potential flows naturally emerges from the generalized reciprocal-theorem-based theoretical formalism, showcasing its versatility and power for modeling inertial forces on particles in oscillatory microfluidics.

We have, furthermore, established a connection to forces on spherical particles in acoustofluidics: Our

formalism generalizes the far-field secondary radiation force on particles in inviscid flows to include crucial viscous effects that emerge from an interplay between particle inertia and oscillatory boundary layer. Our first-principles analysis shows that a simple ODE accurately predicts particle motion, confirmed against independent direct numerical simulations. This generalization of the Maxey–Riley formalism is applicable to manifold flow situations.

Chapter 6

Particle manipulation in two-dimensional streaming flows

Previous chapters have systematically quantified the dominant $\mathcal{O}(\mathrm{Re}_p)$ inertial force on a spherical particle arising due to nonlinear interactions of spatial gradients (and gradients of gradients, etc.) of a "fast" background oscillatory flow field with particle inertia. In many microfluidics applications, these flows are driven by acoustically-excited vibrating bubbles (radius a_b) oscillating with an amplitude ϵa_b, where $\epsilon \ll 1$. Additionally, in these situations one must also consider steady streaming flows generated by the bubble oscillations and/or transport flows that deliver particles to the site of force actuation, i.e. the bubble. In this chapter[1], we will develop a rigorous description of forces acting on particles exposed to such flows generated by oscillating interfaces, aiming to arrive at a computationally efficient yet rigorous system of overdamped ODEs for particle motion on steady time scales in two dimensional streaming flows. In order to achieve this, however, one must account for the presence of a nearby interface in addition to the rectified lift forces due to the primary oscillatory driving and transport due to second-order flows.

In order to make quantitative comparisons with typical microfluidic setups, we model the presence of the interface through an augmented drag force that captures the short range lubrication dominated interaction between the particle and the bubble, consistent with Chapter 2. A rigorous separation of time scales in two dimensions yields a time-averaged system of equations for particle motion that accurately predicts particle displacements across streamlines in comparison to experiments. Our theory also suggests new particle manipulation strategies using oscillating bubbles are force actuators, e.g., marker-less flow cytometry based on particle size or density, important for biomicrofluidics.

6.1 Introduction

There have been numerous experimental studies that have observed attraction of particles to localized oscillating interfaces [14, 34, 35, 40, 100, 124, 136, 143, 172, 173]. These experiments span various lab-on-a-chip applications from size-dependent particle sorting and manipulation to precise control of the swimming

[1] This chapter is adapted from Agarwal et al. [7]

path of biological microorganisms like *C. elegans*, all of which operate by actuating forces through oscillatory flows generated by acoustically-excited vibrating bubbles. All of these studies rely on empirical design approaches, without offering a rigorous fundamental explanation for the lift forces acting on particles.

If a theoretical explanation for the attraction is offered, it relies on the formula for secondary radiation forces (SRF) of acoustic theory (cf. [34, 136, 143, 172]), present for explicitly density-mismatched particles. One of these experimental studies ([35]) is designed for the quantitative measurement of attractive forces (by specifically avoiding the excitation of streaming flows that would compromise measurement accuracy). It was found that SRF significantly underestimated the observed attraction (by about a factor of 2), and the SRF formula was modified by an ad hoc factor to conform to observations. In Chapter 2, (also, [4]), we showed that (i) SRF can be derived from the classical MR equation as a well-defined limit, but that (ii) it indeed severely underpredicts the observed forces (by a factor of about 2) as well as the range of particle trapping (by almost 3 bubble lengths). Trapping efficiency is thus severely underestimated; accurate estimates of these forces could mean the difference between being able to attract and sort sickle cells and bacteria, which differ in shape and size, from healthy red blood cells.

The theory of Chapter 2 introduced, ad hoc, an element of inviscid theory to rationalize the discrepancy. It was only in the following three chapters that we systematically augment the foundations of the Maxey–Riley theory to rigorously derive all inertial forces, consistent with a first-principle solution of the Navier-Stokes equations around particles. Crucially, it encompasses all λ, i.e., the entire viscous-to-inviscid operational flow spectrum. The results of Chapter 2 are likewise put on a rigorous footing as the $\lambda \to \infty$ limit of this work.

In most of the above-mentioned experiments, bubble oscillations generate streaming flow fields, whose presence complicates a theoretical description further. A rigorous modeling on a par with the formalism presented in this dissertation requires elements: (a) the particle approaches the oscillating interface quite closely, necessitating the incorporation of boundary effects; (b) the background flow field is a superposition of a channel transport flow and a complicated bubble oscillation combining volume and shape modes (cf. [140]), thus requiring extension of the theory to two dimensions.

In the following, we will carefully incorporate these additional elements and quantitatively compare theory predictions with experimental data. As argued in Chapter 2, we augment the drag force on the particle with an additional lubrication drag that acts only when the separation between the particle and the interface is $\mathcal{O}(\delta_S)$. We also detail modifications to the inertial forces derived in the previous chapters. We then extend the time scale separation of the particle equation of motion to two dimensions, arriving at a system of ODEs for the leading order particle motion on the slow time scale. The resulting equations predict

particle displacements in quantitative agreement with experiments, in contrast to other theories, and also suggest new particle sorting strategies.

6.2 Incorporating effects of boundary

A plethora of real-world particle laden flows involve motion near an interface, e.g., flow of a suspension through a pipe or particles transported near acoustically-excited bubbles. The classical work on quantifying the effect of a nearby interface on particle motion concerns the slow motion of a particle near the boundary—in the Stokes flow limit—obtaining a closed form expression in the large particle-boundary separation limit ($h \gg a_p$) [28]. These results were generalized to include the effects of inertia and flow curvature on the interface in many subsequent studies. Other studies have taken into account particle-particle and particle-wall interactions.

Recently, a general theory was developed for the force on a rigid spherical particle suspended in a general background flow in the vicinity of a large obstacle and a closed-form uniformly-valid expression for the force on the particle in a direction normal to the surface of the obstacle was derived [141]. In particular, the normal force on the particle due to the presence of an interface augments the instantaneous Stokes drag on the particle as follows:

$$\mathbf{F}_D = -6\pi\rho_f\nu a_p \left[\mathbf{U}_p(t) - \mathbf{U}(\mathbf{r}_p(t),t) + \frac{a_p\left(\mathbf{U}_p(t)-\mathbf{U}_b(t)\right)\cdot\mathbf{e}_r}{n_B h(\mathbf{r}_p,t)}\mathbf{e}_r\right], \tag{6.1}$$

where $\mathbf{U}_b$ is the interfacial velocity, $n_B = 4$ (1) for a no-stress (no-slip) surface and h is the instantaneous minimum surface-to-surface distance between the particle and the boundary. This expression is valid in the Stokes quasi-steady limit; the introduction of oscillatory unsteadiness, in general, results in a much weaker effect ($\propto 1/h^3$) due to the boundary when the particle is far-away ($h \gg \delta_S$) [57], but interpolates to the above expression in the small-separation lubrication limit ($h \ll \delta_S$). In this work, we consider only leading-order corrections due to the interface and neglect these higher-order effects. Therefore, in order to construct a uniformly-valid expression for the drag force on the particle, the decay of the lubrication force outside the boundary layer is modeled by the exponential $H(z) = \exp(-z)$, as described in Chapter 2. In summary, the drag force on a particle oscillating near an interface reads:

$$\mathbf{F}_D = -6\pi\rho_f\nu a_p \left[\mathbf{U}_p(t) - \mathbf{U}(\mathbf{r}_p(t),t) + H\left(\frac{h(\mathbf{r}_p,t)}{\delta_S}\right)\frac{a_p\left(\mathbf{U}_p(t)-\mathbf{U}_b(t)\right)\cdot\mathbf{e}_r}{n_B h(\mathbf{r}_p,t)}\mathbf{e}_r\right]. \tag{6.2}$$

Another consequence of the boundary is that the flow field near the interface is no longer potential and

viscous effects begin to dominate [140]. The inertial force correction derived in Chapter 5 for non-neutrally buoyant particles depends on the oscillatory slip velocity which gets explicitly modified by the increased lubrication drag near the interface (cf. Eq. (2.13))—capturing the leading order effect due to the interface. However, incorporating such an effect explicitly in the density-contrast independent inertial force $F_{\Gamma\kappa}$ derived in Chapter 4 is more cumbersome. The magnitude and sign of this force depends, crucially, on the flow curvature and gradient. The presence of an interface modifies the leading order disturbance flow in a way that the flow becomes 'slower' on the side closer to the interface—viewed in a reference frame moving with the particle centre—as the particle approaches the boundary. Thus, the magnitude of the flow gradient (and curvature) across the particle weakens and ultimately flips; the attraction due to $F_{\Gamma\kappa}$ is expected to diminish greatly. Additionally, the assumption of the primary oscillatory background flow being potential breaks down and one cannot directly use the expression developed in Chapter 4. Instead, analogous to the decay of the lubrication force outside the boundary layer, we modify $F_{\Gamma\kappa}$ so that it decays to 0 inside the boundary layer. In summary, we multiply $1 - H\left(\frac{h(\mathbf{r}_p,t)}{\delta_S}\right)$ to the inertial force due to the background flow curvature $F_{\Gamma\kappa}$.

6.3 Multiple scale analysis for the 2D equation of particle motion

A meaningful comparison to experiments requires prediction of particle trajectories in the presence of, often complicated, streaming or transport flows. This necessitates obtaining an equation of motion for the particle in two dimensions, incorporating all the inertial forces we have derived. As pointed out in Chapter 5, while one can attempt to solve the full unsteady equation of motion for the particle, the evaluation of the history integral is computationally expensive and not as straight forward. One can, however, exploit the separation of time scales between the fast oscillatory scale and the much slower steady time scale. Using the method of multiple scales we derive an overdamped equation of motion for the particle on rectified time scales, which is computationally efficient to compute and also yields physical insight into the mechanism of the action of dominant lift forces.

We first display the dimensional equation of motion for the particle, after incorporating all the inertial

force terms and the modifications of the previous section:

$$
\begin{aligned}
m_p\frac{d\mathbf{U}_p}{dt} =& m_f\frac{D\mathbf{U}}{Dt} - \frac{1}{2}m_f\frac{d}{dt}\left[\mathbf{U}_p - \mathbf{U}\right] - 6\pi^{1/2}\nu^{1/2}a_p^2\rho_f\int_{-\infty}^{t}\frac{d/d\tau\left[\mathbf{U}_p(\tau)-\mathbf{U}(\mathbf{r}_p(\tau),\tau)\right]}{\sqrt{t-\tau}}d\tau \\
&- 6\pi\rho_f\nu a_p\left[\mathbf{U}_p(t) - \mathbf{U}(\mathbf{r}_p(t),t) + H\left(\frac{h(\mathbf{r}_p,t)}{\delta_S}\right)\frac{a_p\left(\mathbf{U}_p(t)\cdot\mathbf{e}_r - \frac{\partial r_b}{\partial t}\right)}{n_B h(\mathbf{r}_p,t)}\mathbf{e}_r\right] \\
&+ m_f\left[(\mathbf{U}_p-\mathbf{U})\cdot\nabla\mathbf{U}\right]\mathcal{G}_1(\lambda) + m_f\left[\partial_t(\mathbf{U}_p-\mathbf{U})\cdot\nabla\mathbf{U}\right]\frac{\mathcal{G}_2(\lambda)}{\omega} \\
&+ m_f a_p^2\nabla\mathbf{U}:\nabla\left(\nabla\mathbf{U}\right)\mathcal{F}(1-H)
\end{aligned}
\tag{6.3}
$$

We specialize to the case of streaming flows generated by acoustic excitation of a cylindrical bubble (cf. [140, 169]) with radius a_b, oscillating with an amplitude ϵa_b, and an angular frequency of ω. Thus, we non-dimensionalize (6.3) with a_b, $\epsilon a\omega$ and ω^{-1} as the characteristic length, velocity and time scales, respectively, to obtain:

$$
\begin{aligned}
&\lambda\left(\hat{\kappa}+1\right)\frac{d^2\mathbf{r}_p}{dt^2} + \left(\boldsymbol{\mathcal{I}} + H\gamma\frac{\mathbf{n}_b}{h(\mathbf{r}_p)}\mathbf{n}_b\right)\cdot\frac{d\mathbf{r}_p}{dt} + \sqrt{\frac{3\lambda}{\pi}}\int_{-\infty}^{t}\frac{d/d\tau\left[d\mathbf{r}_p(\tau)/d\tau - \epsilon\mathbf{u}(\mathbf{r}_p(t),t)\right]}{\sqrt{t-\tau}}d\tau \\
&\quad= \epsilon\Bigg[\lambda\frac{\partial\mathbf{u}}{\partial t} + \frac{2\lambda}{3}\epsilon\mathbf{u}\cdot\nabla\mathbf{u} + \frac{\lambda}{3}\frac{d\mathbf{r}_p}{dt}\cdot\nabla\mathbf{u} + \mathbf{u} + H\gamma\frac{\mathbf{n}_b\cdot\mathbf{u}_b}{h(\mathbf{r}_p)}\mathbf{n}_b \\
&\quad+ \frac{2\lambda}{3}\mathcal{G}_1\left(\frac{d\mathbf{r}_p}{dt} - \epsilon\mathbf{u}\right)\cdot\nabla\mathbf{u} + \frac{2\lambda}{3}\mathcal{G}_2\partial_t\left(\frac{d\mathbf{r}_p}{dt} - \epsilon\mathbf{u}\right)\cdot\nabla\mathbf{u} \\
&\quad+ \frac{2\lambda}{3}\epsilon\alpha^2\nabla\mathbf{u}:\nabla\left(\nabla\mathbf{u}\right)\mathcal{F}(1-H)\Bigg]_{\mathbf{r}_p}.
\end{aligned}
\tag{6.4}
$$

Here $\gamma = a_p/4a_b$. We formally Taylor expand particle position in 2D polar coordinates as:

$$
\begin{aligned}
\mathbf{r}_p =& \mathbf{r}_{p_0} + \epsilon\mathbf{r}_{p_1} + \epsilon^2\mathbf{r}_{p_2} + .. \\
=& r_{p_0}\mathbf{e}_r(\theta_0) + \epsilon\left(r_{p_1}\mathbf{e}_r(\theta_0) + r_{p_0}\theta_1\mathbf{e}_\theta(\theta_0)\right) + \epsilon^2\left((r_{p_2} - r_{p_0}\theta_2)\mathbf{e}_r(\theta_0) + r_{p_1}\theta_1\mathbf{e}_\theta(\theta_0)\right) + \mathcal{O}(\epsilon^2).
\end{aligned}
\tag{6.5}
$$

The bubble surface can, in general, have shape modes that are defined as: $r_b(\theta) = 1 + \epsilon\Delta R(\theta)$, where $\Delta R(\theta)$ captures the angular dependence of the bubble interface. The normal $\mathbf{n}_b$ to the interface at any angle θ_n is computed by taking the gradient of the surface functional $S(X_b(\theta_n)) = r - r_b(\theta_n)$, so that:

$$
\begin{aligned}
\mathbf{n}_b(\theta_n) &= \left.\frac{\nabla(r-r_b)}{|\nabla(r-r_b)|}\right|_{X_b} = \frac{1}{\sqrt{1+\frac{\epsilon^2\Delta R'^2}{(1+\epsilon\Delta R)^2}}}\mathbf{e}_r(\theta_n) - \epsilon\frac{\Delta R'}{(1+\epsilon\Delta R)\sqrt{1+\frac{\epsilon^2\Delta R'^2}{(1+\epsilon\Delta R)^2}}}\mathbf{e}_\theta(\theta_n) \\
&= \mathbf{e}_r(\theta_n) - \epsilon\Delta R'\mathbf{e}_\theta(\theta_n) + \mathcal{O}(\epsilon^2).
\end{aligned}
\tag{6.6}
$$

Now, the kinematic condition connecting the bubble surface to the particle centre reads:

$$r_b(\theta_n)\mathbf{e}_r(\theta_n) + (h+\alpha)\mathbf{n}_b(\theta_n) = \mathbf{r}_p \tag{6.7}$$

Inserting the small ϵ Taylor expansions of $h = h_0 + \epsilon h_1 + \mathcal{O}(\epsilon^2)$ and $\theta_n = \theta_{n_0} + \epsilon\theta_{n_1} + \mathcal{O}(\epsilon^2)$ and separating orders, one obtains at $O(1)$ and $O(\epsilon^2)$, respectively

$$h_0 = r_{p_0} - 1 - \alpha, \tag{6.8a}$$

$$r_{p_1}\mathbf{e}_r(\theta_0) + r_{p_0}\theta_{p_1}\mathbf{e}_\theta(\theta_0) = \Delta R(\theta_{p_0})\mathbf{e}_r(\theta_{p_0}) + \theta_{n_1}\mathbf{e}_\theta(\theta_{p_0}) + h_1\mathbf{e}_r(\theta_{p_0}) - (h_0+\alpha)(\theta_{n_1} - \Delta R')\mathbf{e}_\theta(\theta_{p_0}) \tag{6.8b}$$

Therefore,

$$h_0 = r_{p_0} - 1 - \alpha, \qquad h_1 = r_{p_1} - \Delta R, \tag{6.9a}$$

$$\theta_{n_0} = \theta_{p_0}, \qquad \theta_{n_1} = \theta_{p_1} + (1 - 1/r_{p_0})\,\Delta R', \tag{6.9b}$$

which are evaluated at θ_{p_0}. Consistent to $O(\epsilon)$, the normal vector may now be expressed as:

$$\begin{aligned}\mathbf{n}_b &= \mathbf{e}_r(\theta_0) + \epsilon(\theta_{n_1} - \Delta R')\mathbf{e}_\theta(\theta_0) = \mathbf{e}_r(\theta_0) + \epsilon\left(\theta_{p_1} - \frac{\Delta R'}{r_{p_0}}\right)\mathbf{e}_\theta(\theta_0) \\ &= \mathbf{e}_r(\theta_0) + \epsilon\theta_{n_{b_1}}\mathbf{e}_\theta(\theta_0)\end{aligned} \tag{6.10}$$

Thus, we can now compute the projected interface velocity and the gap between particle-bubble interfaces as follows:

$$\begin{aligned}(\mathbf{n}_b\cdot\mathbf{u}_b)\mathbf{n}_b(\theta_n) &= \left(\dot{\Delta R}(\theta_0) + \epsilon\theta_{n_1}\dot{\Delta R'}(\theta_0)\right)\left(\mathbf{e}_r(\theta_0) + \epsilon\theta_{n_{b_1}}\mathbf{e}_\theta(\theta_0)\right) \\ h(\mathbf{r}_p) &= h(\mathbf{r}_{p_0}) + \epsilon h_1(\mathbf{r}_{p_0}) = h_0 + \epsilon(r_{p_1} - \Delta R)\end{aligned} \tag{6.11}$$

We now proceed with the standard technique of multiple scale analysis by introducing a slow time $T = \epsilon^2\tau$ along with the fast time τ; analogous to Section 2.2.2, we separate time scales by making the following substitutions:

$$\begin{aligned}\mathbf{r}_p(\tau) &\to \mathbf{r}_p(\tau, T) \\ \frac{d}{d\tau} &\to \frac{\partial}{\partial\tau} + \epsilon^2\frac{\partial}{\partial T} \\ \frac{d^2}{d\tau^2} &\to \frac{\partial^2}{\partial\tau^2} + 2\epsilon^2\frac{\partial^2}{\partial\tau\partial T} + \epsilon^4\frac{\partial^2}{\partial T^2}\end{aligned}$$

For streaming flows, the background flow field may, in general, be decomposed as: $\mathbf{u} = \mathbf{u_{osc}} + \epsilon\mathbf{u_E}$ [140].

We Taylor expand (6.4) formally, to obtain at $\mathcal{O}(1)$:

$$\lambda\hat{\mu}\frac{\partial^2\mathbf{r}_{p_0}}{\partial\tau^2}+\left(1+H\gamma\frac{\mathbf{e}_r}{h_0}\mathbf{e}_r\cdot\right)\frac{\partial\mathbf{r}_{p_0}}{\partial\tau}=0 \tag{6.12}$$

This just means that $\mathbf{r}_{p_0}(\tau,T)=\mathbf{r}_{p_0}(T)$—we know that $\mathcal{O}(1)$ changes happen over slow time T. We have also neglected contributions from the history term since it has an extremely weak effect on the steady velocities.

At $\mathcal{O}(\epsilon)$, we can explicitly evaluate the Basset-Boussinesq history integral to obtain:

$$\lambda(\hat{\kappa}+d)\frac{\partial^2\mathbf{r}_{p_1}}{\partial\tau^2}+\left(c+H\gamma\frac{\mathbf{e}_r}{h_0}\mathbf{e}_r\cdot\right)\frac{\partial\mathbf{r}_{p_1}}{\partial\tau}=\left\{\left(d\lambda\frac{\partial\mathbf{u}_{osc}}{\partial\tau}+c\mathbf{u}_{osc}\right)+H\gamma\frac{\dot{\Delta R}}{h_0}\mathbf{e}_r\right\}_{\mathbf{r}_{p_0}}, \tag{6.13}$$

where, like in Chapter 5, $c=1+\sqrt{3\lambda/2}$ and $d=1+\sqrt{3/(2\lambda)}$ encode the corrections to the Stokes Drag and Added Mass terms, respectively, due to the history integral. The oscillatory component-wise parts of the $\mathcal{O}(\epsilon)$ solution can be generally written as:

$$r_{p_1}(\tau)=\int(w_{1_{osc}}+u_{osc})d\tau \tag{6.14}$$

$$r_{p_0}\theta_{p_1}(\tau)=\int(w_{2_{osc}}+v_{osc})d\tau \tag{6.15}$$

where,

$$\begin{aligned}w_{1_{osc}}&=-\frac{H\gamma(u_{osc}-\dot{\Delta R})+i\hat{\kappa}h_0\lambda u_{osc}}{ch_0+H\gamma+i\lambda(\hat{\kappa}+d)h_0},\\ w_{2_{osc}}&=-\frac{i\hat{\kappa}\lambda v_{osc}}{c+i\lambda(\hat{\kappa}+d)},\end{aligned} \tag{6.16}$$

are the oscillatory slip velocities in the radial and azimuthal directions respectively, analogous to (2.13).

At $\mathcal{O}(\epsilon^2)$, omitting terms that are not products of first order quantities since their time average will

vanish, we have:

$$
\begin{aligned}
&\left(1+\gamma\frac{\mathbf{e}_r}{h_0}\mathbf{e}_r\cdot\right)\frac{\partial\mathbf{r}_{p_0}}{\partial T}+H\frac{\gamma}{h_0}\left(\theta_{n_{b_1}}(\mathbf{e}_r\mathbf{e}_\theta+\mathbf{e}_\theta\mathbf{e}_r)-\frac{h_1}{h_0}\mathbf{e}_r\mathbf{e}_r\right)\cdot\frac{\partial\mathbf{r}_{p_1}}{\partial\tau}\\
&\quad=\Bigg\{\mathbf{u}_E+\mathbf{r}_{p_1}\cdot\nabla\left(\lambda\frac{\partial\mathbf{u}_{osc}}{\partial\tau}+\mathbf{u}_{osc}\right)+\frac{2\lambda}{3}\mathbf{u}_{osc}\cdot\nabla\mathbf{u}_{osc}+\frac{\lambda}{3}\frac{d\mathbf{r}_{p_1}}{d\tau}\cdot\nabla\mathbf{u}_{osc}\\
&\qquad+\frac{2\lambda}{3}\mathcal{G}_1\left(\mathbf{w}_{osc}\cdot\nabla\mathbf{u}_{osc}\right)+\frac{2\lambda}{3}\mathcal{G}_2\left(\partial_t\mathbf{w}_{osc}\cdot\nabla\mathbf{u}_{osc}\right)\\
&\qquad+\frac{2\lambda}{3}(4\gamma)^2\left(\nabla\mathbf{u}:\nabla\nabla\mathbf{u}\right)\mathcal{F}(1-H)\\
&\qquad+\frac{\gamma}{h_0}\theta_{n_{b_1}}\dot{\Delta R}\mathbf{e}_\theta+\frac{\gamma}{h_0}\theta_{n_1}\dot{\Delta R'}\mathbf{e}_r-\frac{\gamma\dot{\Delta R}h_1}{h_0^2}\mathbf{e}_r\Bigg\}_{\mathbf{r}_{p_0}}\\
&\quad=\Bigg\{\mathbf{u}_L+\lambda\frac{\partial}{\partial\tau}\left(\mathbf{r}_{p_1}\cdot\nabla\mathbf{u}_{osc}\right)+\left(\int\mathbf{w}_{osc}d\tau\right)\cdot\nabla\mathbf{u}_{osc}\\
&\qquad+\frac{2\lambda}{3}(\mathcal{G}_1-1)\left(\mathbf{w}_{osc}\cdot\nabla\mathbf{u}_{osc}\right)+\frac{2\lambda}{3}\mathcal{G}_2\left(\partial_t\mathbf{w}_{osc}\cdot\nabla\mathbf{u}_{osc}\right)\\
&\qquad+\frac{2\lambda}{3}(4\gamma)^2\left(\nabla\mathbf{u}:\nabla\nabla\mathbf{u}\right)(1-H)\mathcal{F}\\
&\qquad+\frac{\gamma}{h_0}\theta_{n_{b_1}}\dot{\Delta R}\mathbf{e}_\theta+\frac{\gamma}{h_0}\theta_{n_1}\dot{\Delta R'}\mathbf{e}_r-\frac{\gamma\dot{\Delta R}h_1}{h_0^2}\mathbf{e}_r\Bigg\}_{\mathbf{r}_{p_0}}
\end{aligned}
\tag{6.17}
$$

where we use the relation between Lagrangian and Eulerian velocities: $\mathbf{u}_L=\mathbf{u}_E+\left(\int\mathbf{u}_{osc}d\tau\right)\cdot\nabla\mathbf{u}_{osc}$. The equation of particle motion at this order is over-damped, i.e., the flow at the rectified scale is Stokes-like. Consequently, the exponential cutoff function H is not appropriate in the uniformly valid drag force expression at the slow time scale. We now split the above equation into its 'r' and 'θ' components (we drop

quantities that vanish when time-averaged):

$$\begin{aligned}\left(1+\frac{\gamma}{h_0}\right)\frac{\partial r_{p_0}}{\partial T} =& \Bigg\{u_L + \left\langle \left(\int w_{1_{osc}} d\tau\right)\frac{\partial u_{osc}}{\partial r} + \left(\int w_{2_{osc}} d\tau\right)\frac{\partial v_{osc}}{\partial r}\right\rangle \\ &+ \frac{2\lambda}{3}(\mathcal{G}_1 - 1)\left\langle w_{1_{osc}}\frac{\partial u_{osc}}{\partial r} + w_{2_{osc}}\frac{\partial v_{osc}}{\partial r}\right\rangle \\ &+ \frac{2\lambda}{3}\mathcal{G}_2\left\langle \partial_t w_{1_{osc}}\frac{\partial u_{osc}}{\partial r} + \partial_t w_{2_{osc}}\frac{\partial v_{osc}}{\partial r}\right\rangle \\ &+ \frac{2\lambda}{3}(4\gamma)^2\left\langle \nabla\mathbf{u} : \nabla\nabla\mathbf{u}\right\rangle \cdot \mathbf{e}_r \mathcal{F}(1-H)\Bigg\}_{\mathbf{r}_{p_0}}, \end{aligned} \tag{6.18a}$$

$$\begin{aligned} r_{p_0}\frac{\partial \theta_{p_0}}{\partial T} =& \Bigg\{v_L + \left\langle \left(\int w_{1_{osc}} d\tau\right)\frac{\partial v_{osc}}{\partial r} - \left(\int w_{2_{osc}} d\tau\right)\frac{\partial u_{osc}}{\partial r}\right\rangle \\ &+ \frac{2\lambda}{3}(\mathcal{G}_1 - 1)\left\langle w_{1_{osc}}\frac{\partial v_{osc}}{\partial r} - w_{2_{osc}}\frac{\partial u_{osc}}{\partial r}\right\rangle \\ &+ \frac{2\lambda}{3}\mathcal{G}_2\left\langle \partial_t w_{1_{osc}}\frac{\partial v_{osc}}{\partial r} - \partial_t w_{2_{osc}}\frac{\partial u_{osc}}{\partial r}\right\rangle \\ &+ \frac{2\lambda}{3}(4\gamma)^2\left\langle \nabla\mathbf{u} : \nabla\nabla\mathbf{u}\right\rangle \cdot \mathbf{e}_\theta \mathcal{F}(1-H) \\ &+ \frac{H\gamma}{h_0 r_{p_0}}\left\langle \left(\frac{\partial r_{p_1}}{\partial \tau} - \dot{\Delta R}\right)\left(\Delta R' - r_{p_0}\theta_{p_1}\right)\right\rangle\Bigg\}_{\mathbf{r}_{p_0}}. \end{aligned} \tag{6.18b}$$

We have, thus, derived a system of overdamped time-averaged ODEs for the leading order particle position (r_{p_0}, θ_{p_0}), in a cylindrical coordinate system centered at the oscillating source. In the following section, we will validate the predictions of particle displacement across streamlines predicted by these equations with experimental data.

6.4 Two-dimensional microbubble streaming

In most particle trapping/sorting applications with oscillating interfaces encountered in microfluidics, particles are transported to the site of force actuation where they not only experience hydrodynamic lift forces but the situation is also complicated by the presence of steady streaming and/or transport flows. Previous chapters generalized time-averaged forces on particles in spatially varying radial bulk flows to include effects of viscous streaming around the particle, whereas the flow field as well as the forces on particles in oscillatory microfluidic applications are generally, (1) not purely radial and (2) strongly influenced by proximity to the oscillating interface driving the flow. In the previous section, we extended the time-averaging formalism of Chapter 2 to two dimensions (provided that the transport and steady streaming flows can be modeled analytically) and incorporated the leading-order interfacial effect on the forces acting on the particle. In the following subsections, we will make quantitative comparisons of (6.18) with experimental data.

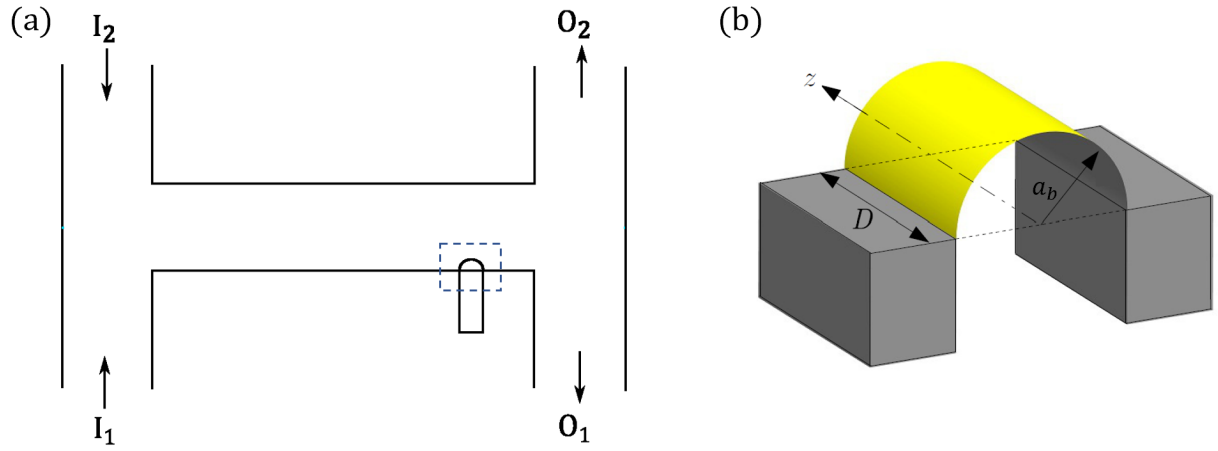

Figure 6.1: (a) Schematic of the device for microparticle sorting, showing inlets and outlets and a cylindrical microbubble located in the main channel (marked by a dashed box). Solution containing microparticles is sent through I_1 while a pure solution enters through I_2. The outlets O_1 and O_1 are left open to the atmosphere. The geometry of the cylindrical bubble (inside the dashed box) is illustrated in (b) (Figures modified from [138])

6.4.1 Experimental setup for particle sorting

A typical experimental setup for microfluidic particle sorting is illustrated in Fig. 6.1, showing the locations of inlets and outlets of the microchannel and the sessile microbubble. An admixture of fluid containing spherical particles is introduced through the inlet I_1, while fluid without any particles is infused through I_2. The bubble radius is $a_b = 40\mu m$, and the distance of the bubble center to the opposite channel wall is typically $250\mu m$, while the particle radii range from $2.5\mu m$ to $10\mu m$—much smaller than the bubble or channel dimensions.

A piezoelectric transducer is attached to the microfluidic device that drives a periodic pressure variation at a driving angular frequency ω in the trapped air bubble. Since the bubble is pinned to the microchannel surface, this causes its surface to oscillate in multiple shape and a dominant 'breathing' mode. A single amplitude ϵa_b is defined in relation to the monopolar mode, taking into account the multiple oscillation modes. The surface of the bubble is a 'no-stress' boundary while the surrounding channel walls form a 'no-slip' boundary. Previous work (cf. [138, 140, 169]) analytically described the two-dimensional streaming flow field generated by this setup through asymptotic theory, showing excellent quantitative agreement with experimental observations across the entire spectrum of frequencies.

The particles are sent through an imposed transport flow through the main channel; the presence of a directional transport flow greatly alters the overall shape of the steady vortex streaming near the bubble. For small-amplitude oscillations of the bubble (ϵ = Amplitude/$a_b << 1$), the flow field can be decomposed

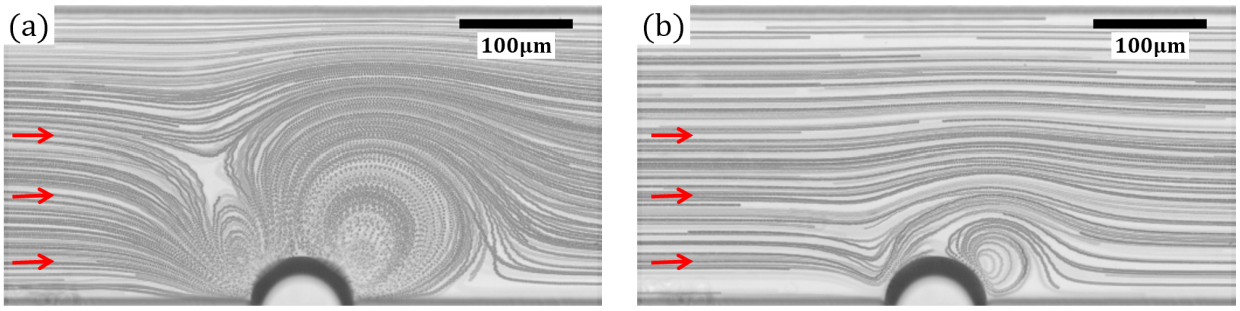

Figure 6.2: Streaklines of bubble streaming with an imposed transport flow (red arrows indicate direction of net flow) through the channel for (a) 'low' s shows an upstream vortex near the bubble. On the other hand, flows with (b) 'high' s are qualitatively different and do not have an upstream vortex.

into oscillatory and steady streaming/transport components that are $\mathcal{O}(\epsilon)$ apart from each other. Thus, the full flow field can be described by a superposition of the two and was modeled analytically in previous work by Rallabandi et al. [140]. The overall shape of the flow field is dictated by the relative strengths of the imposed Poiseuille and streaming flows, quantified by the following parameter,

$$s = \frac{\bar{U}_p}{U_{max}}, \tag{6.19}$$

where $\bar{U}_p = Q/HD$ is the average Poiseuille velocity, Q is the flow rate of the fluid through the channel, and U_{max} is the maximum streaming speed which occurs at the bubble surface. While previous studies have considered flows with 'low' values of the parameter s, typically accompanied with the presence of an upstream vortex near the bubble surface as shown in Fig. 6.2(a), in this Chapter we will quantify displacements of particles in 'high' s flows, i.e. situations with no upstream vortex as displayed in Fig. 6.2(b). The presence of an upstream vortex results in funneling of incoming particles to extremely close distances to the bubble interface, where they experience size-dependent differential repulsive forces that prevent penetration with the surface. Previous studies [160, 162] have exploited this short-range lubrication dominated repulsion to efficiently sort particles based on their size in a high-throughput manner. This displacement of particles in such a flow configuration was previously explained by a geometric exclusion mechanism [160]. On the other hand, when there is no upstream vortex the particles don't get as close to the interface and they experience longer range hydrodynamic inertial lift forces—in addition to the short-ranged lubrication dominated repulsive forces—resulting in a much more complex interaction with both the bubble and the flow generated by it.

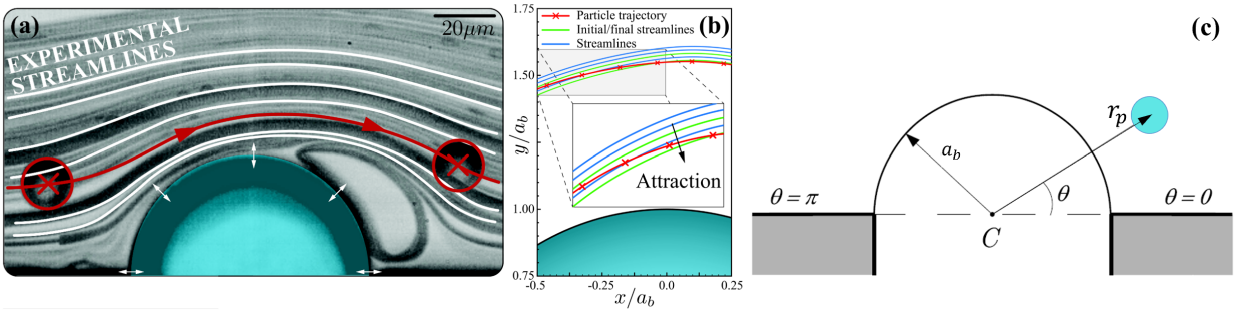

Figure 6.3: (a) A polystyrene particle ($a_p = 10\mu m$, $\lambda \approx 4$) is transported past an oscillating microbubble ($a_b = 40\mu$m, $\omega/(2\pi) = 20$kHz). (b) Close-up of the experimental trajectory (red) of a neutrally buoyant particle intersecting streamlines (blue), indicating a net attraction towards the bubble over fast time scales of a few ms. (c) Coordinate system used for theory computations.

6.4.2 Lift forces on particles transported close to the interface

In a typical sorting experiment, spherical micro-particles of various sizes are transported close to the oscillating interface. Because of the compressed nature of the fluid streamlines close to the interface due to steady streaming, a small displacement of the particle across streamlines is amplified as it leaves the vicinity of the bubble. While this is a desirable outcome in terms of practical applications, it requires a fundamental understanding of the inertial lift forces acting on the particle since a small displacement relative to fluid streamlines near the interface can result in a large net deviation of the particle trajectory. In this section, we will use the knowledge built upon in the previous chapters to understand and describe a prototypical situation of particle manipulation using micro-bubble streaming, that both validates our formalism and also illustrates its practical utility.

We revisit the experimental trajectory shown in Fig. 4.1 of Chapter 4. Figure 6.3(a) exemplifies (in red) a stroboscopic trajectory of a spherical particle transported past an oscillating cylindrical bubble, pinned to the channel wall as shown in the sorting setup described in Fig. 6.1. These experiments are conducted at 20kHz and the fluid used is either pure water in one case ($\delta = \sqrt{2\nu/\omega}/a_b = 0.095$) or a 24% glycerol water solution ($\delta = 0.130$) with dissolved Sodium Polytungstate to vary fluid density (using Sodium Polytungstate does not change the viscosity of the fluid). Particles with radius $a_p \leq 1\mu m$ behave passively due to their small size and therefore are used as proxies for fluid streamlines, marked as white trajectories in Fig. 6.3(a). A constant inlet flow rate of 3μL/min is established through the channel inlets and the input voltage of the piezo-transducer is varied to change the value of s parameter. While previous work focused on low 's' values, here we describe experiments with large 's'; this eliminates the presence of the upstream vortex, as previously noted. Another important parameter of interest is the closest approach distance of the particle trajectory to bubble surface h_{min}. The lift forces experienced by the particle strongly depend on this distance and can

result in qualitatively different outcomes, e.g., attraction vs. repulsion.

We refrained from presenting a direct comparison to theory in the previous chapters, because a rigorous modeling on a par with the formalism we present requires additional elements: (a) the background flow field in experiment is a superposition of a channel transport flow and a flow field resulting from a complicated bubble oscillation combining volume and shape modes (cf. [140]); (b) by nature of this background flow, the particle's trajectory approaches the bubble quite closely, necessitating the incorporation of boundary effects, i.e., taking into account the location of the bubble surface as a fluid boundary. In the previous subsections, we carefully incorporated the additional effects of flow field complexity and boundaries, further generalizing the theory in a systematic way. Thus, we can now use Eqs. (6.18) to make quantitative predictions, combining the flow field approximation of Rallabandi et al. [140], the repulsive lubrication drag force of Section 6.2 (the leading boundary effect), the extension of the time-scale separation formalism to 2D in Section 6.3, and the rigorous inertial force computations of the Chapters 4 and 5.

We model this situation using polar coordinates (r, θ), shown in Fig. 6.3(c), since variations along the z-direction are small in the experiments; we could more generally extend this approach to include 3D effects as well. The extension of the 1D radial formalism to 2D was conceptually straightforward, as described in Section 6.3. Omitting all the arduous details, the resulting overdamped equations (6.18) can be formally rewritten as

$$\begin{aligned}\left(1+\frac{\gamma}{h_0}\right)\frac{dr_{p_0}}{dT} &= u_L + \langle f_1(t)g_1(t)\rangle_{\mathbf{r}_{p_0}} \\ r_{p_0}\frac{d\theta_{p_0}}{dT} &= v_L + \langle f_2(t)g_2(t)\rangle_{\mathbf{r}_{p_0}}\end{aligned} \tag{6.20}$$

where $\langle\cdot\rangle$ indicates time averaging over the fast time-scale t and the quantities inside are products of two first-order oscillatory velocities (and their gradients, gradients of gradients etc.). These are, in general, complicated but known functions of background oscillatory flow velocities evaluated at the leading order particle position $\mathbf{r}_{p_0}$ and the time-averaging integral over a fast time period can be executed analytically. u_L and v_L are the known background Lagrangian steady streaming flow velocities that differ from their Eulerian counterparts by the Stokes drift, and in general incorporate streaming flow [140]. The prefactor containing h_0—the leading order mean distance between the particle and bubble surfaces—enforces the geometric exclusion condition of Thameem et al. [160].

For bubble oscillations dominated by a monopolar "breathing" mode, a natural consequence due to the continuity equation is that the oscillatory flow component perpendicular to the interface (u_{osc}) is much greater than the tangential one (v_{osc}). Therefore, since $f_1 g_1 \sim \mathcal{O}(u_{osc}^2)$ and $f_2 g_2 \sim \mathcal{O}(u_{osc} v_{osc})$ to leading order, the major contribution of these forces, in most cases, is in the radial direction. Intuitively, this means

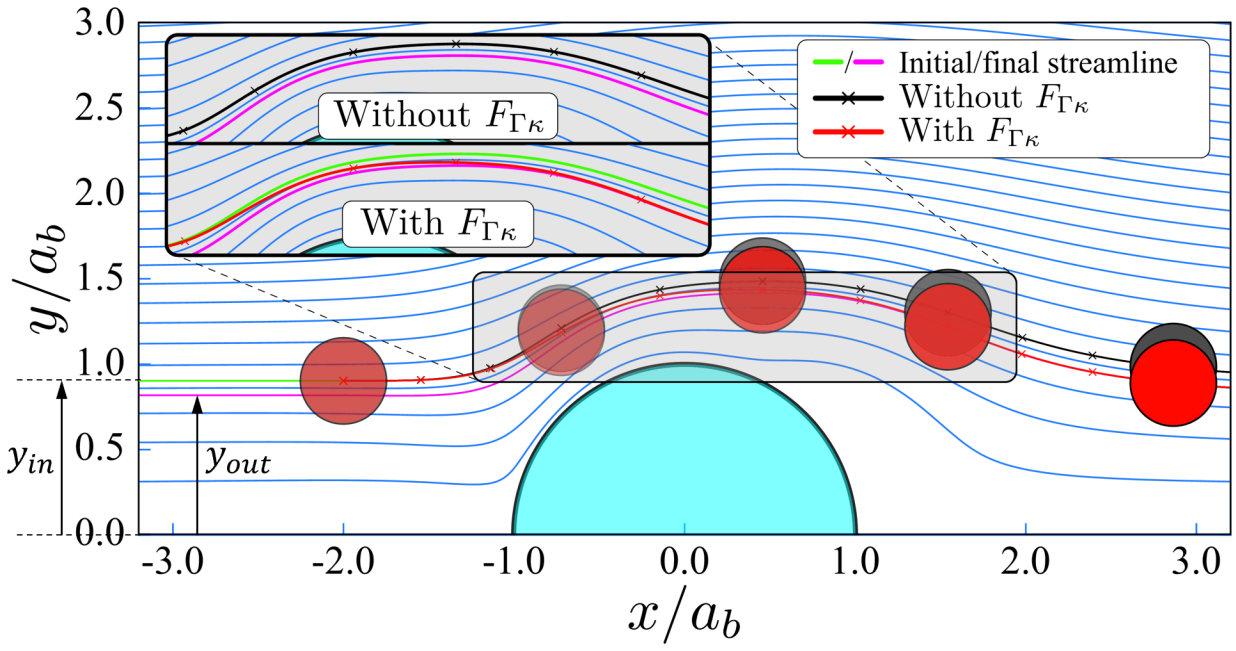

Figure 6.4: An exemplary particle trajectory computed using Eq. (6.18) for the inertial forces combined with the streaming and transport flow fields around a cylindrical bubble shows a displacement downwards (attraction to the bubble, inset) consistent with the experimental observation of Fig. 6.3(b) (red line and red symbols). A computation without the newly introduced inertial force yields no significant displacement (black line and gray symbols). The parameters reflect those of the experiment in Fig. 6.3(b), and the final displacement of the particle where it leaves the field of view is $\sim 3.4\mu m$.

that the particle experiences radial "kicks" due to the 'r' equation while the 'θ' equation merely advects it along fluid streamlines.

6.4.3 Comparison with experiments

The trajectory plotted in Fig. 6.3(b) was obtained experimentally by tracking a neutrally buoyant particle of radius $10\mu m$ transported past an oscillating cylindrical microbubble of radius $a_b = 40\mu$m. The particle experiences an attractive force towards the bubble leading to a sizeable displacement across fluid streamlines (towards the bottom channel wall) that is a substantial fraction of the particle size. This observation is in direct contradiction to existing theories like acoustic radiation forces [18, 30, 34, 35, 42, 47, 67, 68, 124, 143, 146, 170], which depend crucially on contrasts of density or compressibility between the particle and its surrounding fluid and, thus, predict no attraction at all or a much too weak effect.

We numerically integrate Eqs. (6.18) and plot the resultant trajectory for a neutrally buoyant particle ($a_p = 10\mu m$, $\lambda = 4$) in Fig. 6.4, providing as input the background flow field computed using the theory developed by Rallabandi et al. [140]. Particle advection under this given flow field and initial conditions are computed numerically using a fourth order Runge–Kutta scheme. The ensuing trajectory, incorporating

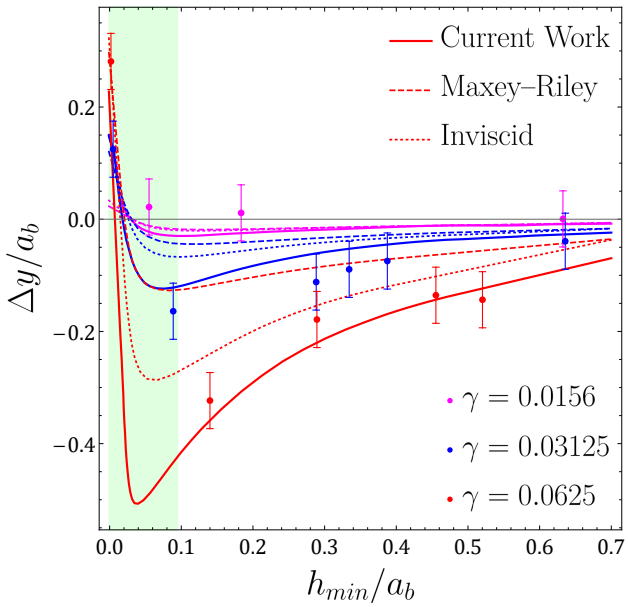

Figure 6.5: Measured particle displacements $\Delta y/a_b$ plotted as a function of the minimum gap between the particle and bubble interfaces h_{min}/a_b, for heavier particles with $\hat{\kappa} = 0.033$ and three different particle sizes ($2.5\mu m$, $5\mu m$, $10\mu m$). Theory predictions from current work (represented by solid curves) are in close agreement with the experimental data points (represented by solid dots). Both the MR and inviscid formalisms miss important effects. Experiments have large uncertainties in measurements indicated by the error bars. The filled light green rectangle indicates the oscillatory boundary layer region ($\delta_S/a_b = 0.095$), where lubrication forces dominate. See [137] for experimental details.

all the elements of the theory, shows a net attraction towards the bubble, in agreement with experimental observations. This effective attraction towards the interface is a consequence of the density-contrast independent force $F_{\Gamma\kappa}$, which was quantified in Chapter 4. On the other hand, an analogous computation without including $F_{\Gamma\kappa}$—equivalent to using the original Maxey–Riley formalism with a modified lubrication drag (cf. [162])—shows no net displacement. We note that a point-by-point comparison of trajectories with experiment is unfeasible primarily because of limitations in modeling the flow field, whose amplitudes and phases are not easy to measure with great accuracy.

In order to make more quantitative comparisons with experimental data, the most relevant quantity, perhaps, is the eventual particle displacement. In the field of vision displayed in Fig. 6.4, the particle enters on a fluid streamline 'y_{in}' and exits on a different streamline 'y_{out}' due to the action of lift forces. The practical outcome of the force actuation due to the bubble, which we seek to predict using our two dimensional time-averaged theory, is $\Delta y = y_{out} - y_{in}$. A positive value of Δy indicates net repulsion while a negative value indicates a net attraction towards the oscillating interface. It is primarily a function of the particle size ratio α, density mismatch $\hat{\kappa}$, particle inertia λ and the distance of closest approach to the bubble surface h_{min}.

Thus, motivated by a systematic study of these forces, experimental observations of multiple trajectories are made that span a range of initial particle heights 'y_{in}', measured vertically from the bottom wall, which translate to different values of h_{min}. If the particle gets very close to the bubble interface, or in other words $h_{min} \lesssim \mathcal{O}(\delta_S)$, short-range repulsive lubrication interactions overwhelm other forces and the net effect on the particle is repulsion, consistent with observations from earlier work [160, 162]. Conversely, particles that are far away—at distances $h_{min} \gtrsim \mathcal{O}(a_b)$—see no major displacement. It is only when $\mathcal{O}(\delta_S) \lesssim h_{min} \lesssim \mathcal{O}(a_b)$ that inertial forces dominate and result in a net downward displacement, i.e., attraction towards the bubble in these experiments.

Figure 6.5 graphs the experimentally obtained net particle displacements Δy as a function of the minimum surface-to-surface gap h_{min} for three different particle sizes: $2.5\mu m$ (magenta), $5\mu m$ (blue) and $10\mu m$ (red). The particles are slightly heavier than the fluid ($\hat{\kappa} = 0.033$). Each data point represents an individual experimental particle trajectory that was post-processed to extract the net displacement [137]. The bubble radius is $a_b = 40\mu m$ and all experiments are conducted at a frequency $\omega/2\pi = 20$kHz, so that $\delta_S/a_b = 0.095$. The filled light green region in Fig. 6.5 indicates when the particle is inside the boundary layer region, where viscous effects dominate. In these experiments, the λ ranges between $0.3-4.5$. For the largest 10μm particles, a maximum net downward displacement of around 20μm (or about a particle diameter) is observed which is quite sizeable for inertial microfluidics. On the other end of the spectrum, 2.5μm particles are essentially passive tracers (unless they get too close to the interface). The experimental data (graphed as points) have large uncertainties in measurements for two reasons: (i) the particle sizes are known only to an accuracy of about $\sim \pm 0.3\mu$m; and (ii) the wavelength of the incident light is $\sim 0.7\mu$m which is close to the observed particle displacements in some cases, resulting in uncertainties due to optical resolution. Owing to these limitations in accurately quantifying net particle displacements, we choose these experiments performed with slightly heavier particles as our validation case. This is a situation where the net particle displacements are reasonably large and meaningful quantitative comparisons are, therefore, feasible.

The solid curves in Fig. 6.5 are predictions from theory obtained after numerically solving the system of ODEs (6.18); these show excellent agreement with experimentally obtained data points (indicated by solid circles). The inviscid theory of Chapter 2 misses important effects for 5μm and 10μm particles where $\lambda \sim \mathcal{O}(1)$, while the original MR formalism is off by almost an order of magnitude, in some cases. The most dramatic effect of this can be seen for 10μm particles when $h_{min} \sim \mathcal{O}(\delta_S)$. These observations cannot be explained by previous theories—both MR and inviscid theory—while current work carefully incorporates important inertial and boundary effects, and is in close quantitative agreement with experiments. It, thus, generalizes previous work [162], accurately predicting repulsion for particles that get extremely close to the

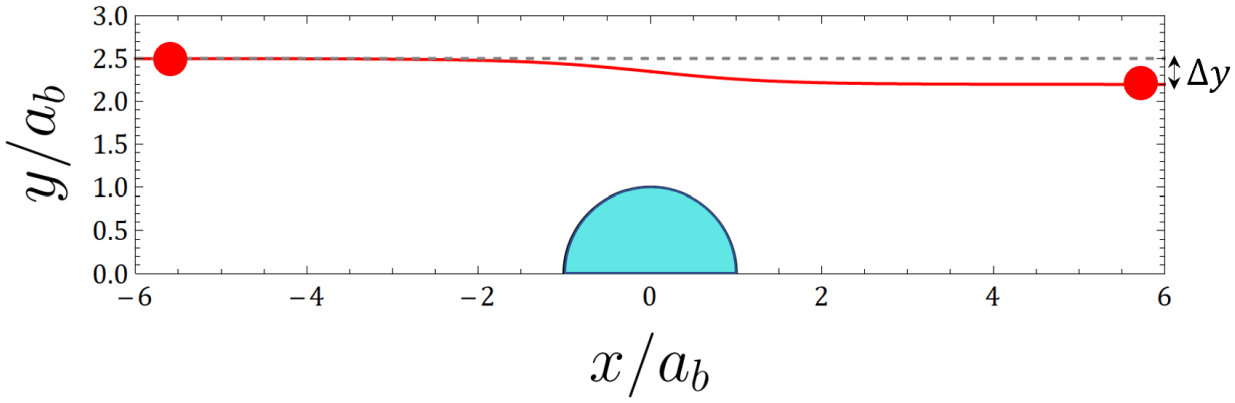

Figure 6.6: A simplified view of force actuation by the bubble (light blue semicircle) on the particle (red) transported past it considers vertical displacements only due to inertial forces, while particle advection in the horizontal direction is driven by the imposed transport flow of relative strength s. The overall effect of the force actuator (bubble) on the particle in this micro-channel setup is quantified by the net vertical displacement Δy.

bubble boundary, to span the entire range of particle-bubble separations and parameters.

In many practical setups involving high 's', one is interested in regime of intermediate distances from the bubble boundary, i.e., the particle does not get as close to the interface. Consequently, the short-range lubrication repulsion can be neglected and the dominant inertial forces on the particle are the radial $F_{\Gamma\kappa}$ and F_f, quantified in Chapters 4 and 5. One can analytically estimate the magnitude of the displacement in the vertical direction for particles transported past the bubble in a micro-channel by constructing a simple minimal model. The prototypical situation is illustrated in Fig. 6.6: We assume that the particle is transported in the x-direction by the imposed Poiseuille flow of relative strength s while displacements in the y-direction occur only due to the action of (radial) inertial forces. We, thus, project (5.22) onto Cartesian coordinates, centered around the bubble. For flows near oscillating cylindrical bubbles dominated by a monopolar mode ($u_0(r) = 1/r$), we obtain the following system of equations:

$$\frac{dx}{dt} = \epsilon^2 s, \quad \frac{dy}{dt} = -\frac{4}{3}\epsilon^2\alpha^2\lambda\mathcal{F}\frac{y}{(x^2+y^2)^3} - \epsilon^2\lambda\frac{\hat{\kappa}}{2(1+\hat{\kappa})}\mathcal{G}\frac{y}{(x^2+y^2)^2} \tag{6.21}$$

where x and y are the time dependent particle horizontal and vertical positions in the channel respectively. The solution in the x-direction is trivial and reads: $x(t) = x_0 + \epsilon^2 st$, where x_0 is the initial horizontal particle position from the bubble centre. Thus, the time it takes for the particle to get transported from $-x_0$ to $+x_0$ (symmetric transport past the bubble) is given by $t = -2x_0/\epsilon^2 s$. We further make the assumption of small vertical deviations and Taylor expand y around the initial (non-dimensional) particle height y_0. In practical settings, the channel length is much larger than the bubble size, so we take the limit $x_0 \to -\infty$.

Combining all these approximations and solving for $y(t)$, we obtain a closed form expression for the leading order vertical particle displacement:

$$\Delta y = y_{final} - y_0 = -\frac{\pi\lambda}{2sy_0^2}\left(\frac{\alpha^2\mathcal{F}}{y_0^2} + \frac{\hat{\kappa}\mathcal{G}}{2(1+\hat{\kappa})}\right). \tag{6.22}$$

This is the practical outcome of the inertial force actuation by the bubble. In practical settings, both terms in (6.22) have similar contributions in magnitude to the eventual displacement. As an example, for prototypical parameter values such for the 10μm particles from Fig. 6.5: $\hat{\kappa} = 0.033$, $a_p = 10\mu$m, $a_b = 40\mu$m, $\omega/(2\pi) = 20$kHz, $\delta_S/a_b = 0.095$ and $s = 0.35$, (6.22) predicts a displacement of $\Delta y \sim -0.35$ which is very close to the experimental value. We note that in assuming only a monopolar mode of bubble oscillation, this simple analytical approximation ignores many details of the setup, e.g., the flow field complexity due to other steady streaming modes and complicated lubrication dominated short-range interactions between the particle and bubble. Therefore, an exact match with the full numerical solutions of (6.18) is not expected. However, this provides a simple criterion for improved design strategies to build practical microfluidic devices based on a fundamental understanding of the inertial forces.

In the following section, we will focus on analyzing applications of microbubble streaming; our theory suggests potential design strategies for practical microfluidic lab-on-a-chip devices.

6.5 Practical Application: Continuous size or density-based particle focusing

We focus here on understanding the application of acoustically excited microbubbles in continuous sorting microfluidic devices. While previous work suggested a lubrication dominated mechanism for size-dependent sorting in the presence of an upstream vortex ('low s'), here we study high-throughput differential size or density-based focusing of particles through differential inertial forces. Any sorting device utilizing steady flows must entail a deviation between particle trajectories from nominal fluid trajectories. In experiments described in the previous section, this deviation depends, crucially, on both the size of the particle as well as its density. It was also found that magnitude of the attraction towards or repulsion from the interface depends strongly on the distance of closest approach and the time spent near the interface. Thus, the ultimate fate of the particle can be precisely tuned by varying the relative strength between streaming and Poiseuille flow (the 's' parameter). Important for practical applications, the sensitivity of the sorter to different particle sizes or densities is, thus, tunable and its continuous nature allows particles to be sorted

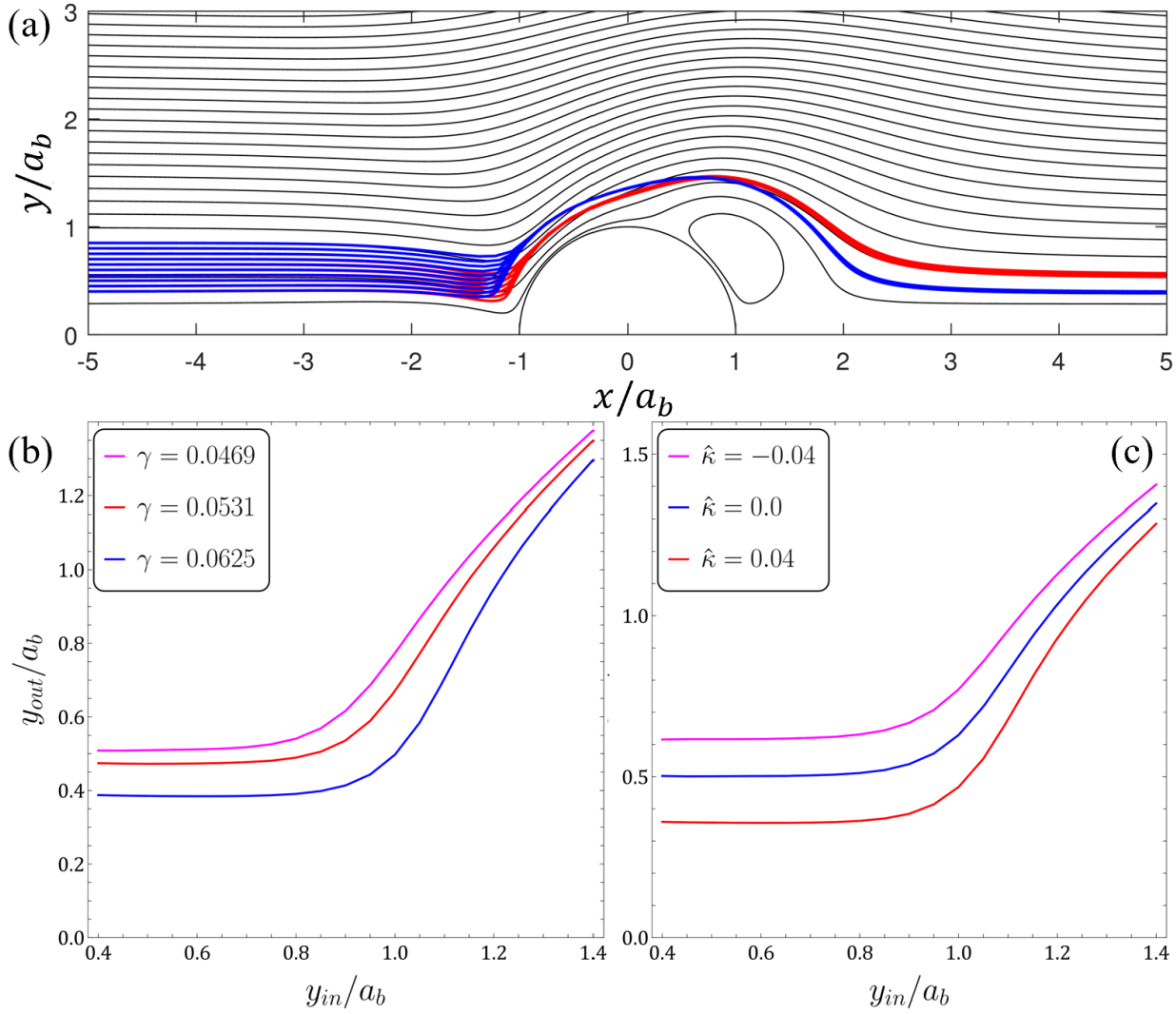

Figure 6.7: Microbubble streaming as an actuator for high-throughput flow focusing: (a) Exemplary trajectories obtained from numerically integrating (6.18) for two different sized particles: 10μm (blue) and 5μm (red), showcasing focusing of initially dispersed trajectories onto distinct exit streamlines. (b) Size-based sorting: Particles with three different sizes are focused onto three distinct final streamlines (y_{out}) for a range of initial heights (y_{in}). (c) Density-based sorting: Particles with three different densities are focused onto three distinct final streamlines (y_{out}) for a range of initial heights (y_{in}).

at much higher throughputs compared with conventional inertial focusing techniques.

In Fig. 6.7(a), we display exemplary particle trajectories of two intrinsically different kinds of particles, obtained after numerically integrating (6.18). The initial heights of the particle trajectories span a sizeable fraction of the channel but are finally focused onto two distinct final streamlines. For a fixed background flow field (here $s = 0.25$), the precise location of the final trajectory depends on the size and the density of the particles. Indeed, Figs. 6.7(b,c) quantify the height of the exit streamlines (y_{out}) as a function of the entry height (y_{in}) for size or density-based high throughput sorting. In both cases, particles entering up to an initial height $y_{in} \sim a_b$ are squeezed into the geometric-exclusion zone near the bubble where they get bundled onto the same streamline. As they exit the vicinity of the interface, they experience hydrodynamic lift forces and are focused onto disparate final heights. Thus, as the particles traverse around the bubble, they experience radial "kick" that displace them from their current streamline, whose magnitude depends on the intrinsic size and/or density of the particles. This "marker-less" continuous sorting is highly relevant for biological materials, such as cells or vesicles where cell viability is an important consideration. Therefore, a fundamental understanding of these inertial forces can open up new avenues for flow cytometry.

6.6 Conclusions

We have systematically extended the rigorous theory developed in previous chapters to account for the presence of interfaces and arbitrary flows in two dimensions. The effect of an oscillating interface is modeled through an augmented drag force on the particle, accurate to leading order. Using time-scale separation, we derive a system of overdamped ODEs for particle motion on time scales of rectified motion that yields fundamental physical insight and is efficient to compute. We study the transport of finite-sized inertial microparticles under a superposition of streaming and transport flows, focusing on the use of oscillating microbubbles for continuous, high-throughput size or density-based manipulation of microparticles. Our computationally efficient and rigorous model accurately quantifies the magnitude of displacement of particles across streamlines in comparison to experiments. Based on a fundamental understanding of inertial forces, we also propose a simple, analytical design criterion that can strategically guide the development of future lab-on-a-chip devices.

As a practical application of the first-principles theory developed in this work, we have, furthermore, demonstrated here that steady streaming flows driven by acoustically excited microbubbles can be used effectively for the continuous size or density-based fast focusing of particles. By superimposing the streaming flow with a pressure-driven Poiseuille flow through the channel carrying microparticles, we have designed a

continuous size-sensitive focusing device. Contrary to other devices exploiting inertial effects, the bundling onto distinct streamlines occurs over $\mathcal{O}(1)$ ms time scales, without the use of any active feedback. We have described a hydrodynamic basis for the observed focusing, which generally accounts for the effect of long-range hydrodynamic forces on particle migration, advancing the field of inertial microfluidics toward a more general understanding of particle dynamics in microfluidic flows. Thus, the proposed formalism offers a systematic and practical approach that augments physical understanding and enables precise model predictions, potentially spurring more compact, reliable and efficient forms of particle manipulation.

Chapter 7

Conclusions

In this dissertation, we have rigorously quantified inertial forces on particles exposed to general background flows, with gradients that vary on scales much larger than the particle size, through a systematic and general modeling approach. Due to their immediate importance in modern microfluidics, we specialized our theory to oscillatory flows, resulting in inertial force predictions that naturally emerge from a combination of particle inertia and spatial oscillatory flow variation.

7.1 Summary of research

In the first part of this work, we focused on deriving a generalized model for inertial forces on particles in incompressible oscillatory flows near interfaces. Heuristically superposing leading order viscous and inviscid force contributions near such interfaces, we efficiently bridged the acoustofluidic and microfluidic approaches, accurately capturing particle dynamics in the limit of high frequencies. Resulting in direct predictions for particle motion on slower timescales, the model predicted a richer and qualitatively different behavior from that expected from simplified radiation-force formalisms: Depending on experimental control parameters, the net effect of interfacial oscillation can be either an attraction to or a repulsion from the interface, and particles can be captured at a fixed distance or released. These results were also verified in comparison with experiments.

We then recognized that while this model captures available experimental data well in the low and high frequency limits, it had shortcomings in the intermediate range, important for application. We found that the assumptions inherent to the Maxey–Riley equation, the main theoretical foundation for fluid forces on particles, were easily violated for particles in flows generated by localized oscillating objects. Based on insights from both experiments and direct numerical simulations of the full Navier–Stokes equations, we subsequently quantified inertial forces on particles immersed in general background flows from first-principles, employing a generalized reciprocal-theorem-based approach. The advantage of this formalism is that it can be adapted to most flow situations typically encountered in inertial microfluidics.

The next part of this body of work was devoted to specializing the general theory to oscillatory flows, owing to their importance in modern microfluidics. We found that these inertial forces naturally emerge from a combination of particle inertia and spatial oscillatory flow variation, and that they can be quantified through a generalization of the Maxey–Riley equation to cases where that theory has been unable to describe observations. We reported a new kind of generically present attractive inertial force that does not rely on any density or compressibility contrasts, but rather results from flow curvature—suggesting several exciting biomedical applications ranging from in situ self-assembly to marker-less flow cytometry.

Having developed a rigorous description of inertial forces on particles in oscillatory flows, the last part of this dissertation focused on practical applications, advancing important ideas and techniques that are useful in understanding and modeling experimentally observed particle displacements in general streaming flows. The theory was extended to account for the presence of interfaces and arbitrary flows in two dimensions. Using time-scale separation, we derived a system of equations for particle motion on the steady time scale. This yielded fundamental physical insight and was, moreover, extremely efficient to compute. Finally, we studied the transport of finite-sized inertial microparticles under a superposition of streaming and transport flows, focusing on the use of oscillating microbubbles for continuous, high-throughput size or density-based manipulation of microparticles. Our computationally efficient and rigorous model accurately quantified the magnitude of displacement of particles across streamlines in comparison to experiment. It also suggested novel design strategies for precise manipulation of particles in continuous flow situations, potentially opening up new avenues for marker-less flow cytometry in biomedical applications. Thus, the rewards that our approach offers are threefold: (i) a fundamental understanding of inertial forces; (ii) sizable savings in terms of computation time; and (iii) accessibility for practical applications.

7.2 Ongoing and future work

7.2.1 Inertial forces on non-spherical or deformable particles

We have developed a generalized formalism for inertial forces on fluid-borne spherical particles in arbitrary background flows. Many applications in microfluidics, however, entail soft biological objects such as cells, vesicles or microorganisms that not only deviate from spherical geometry but also have deformable interfaces, e.g., red blood cells are dumbbell-shaped in profile and their membranes are known to be deformable in response to shear stresses during circulation, facilitating their efficient passage through microvessels [36]. Thus, many biological materials are not rigid spheres but soft, deformable non-spherical bodies with boundary conditions that are neither perfectly no-slip nor no-stress. Relatively little is known about the behavior

of such objects in microfluidic flows—even in the limit of Stokes flow—and modeling even any one of these above-mentioned effects in isolation is potentially challenging.

As we noted in this work, small spherical particles when introduced into a non-uniform unsteady flow are transported irreversibly due to inertial forces. Small non-spherical particles, even when inertial effects are negligible, display a rich orientation dynamics and their particle velocity is a function of both of its orientation as well as the local flow gradients [69, 102]. The zero Reynolds number motion of a small, rigid ellipsoid exposed to simple shear flow is described, in the absence of rotary motion, by the classical solution of Jeffery [76], who showed that the particle will traverse any one of an infinite family of periodic closed orbits. This degeneracy is lifted by fluid and particle inertia. Einarsson et al. [52] showed that, for neutrally buoyant spheroids, inertial effects determine the stabilities of the orbital dynamics at infinitesimal shear Reynolds numbers. Subramanian and Koch [159] solved the problem for rod-shaped particles in the slender-body approximation, using a reciprocal-theorem-based approach similar to ours. The effect of unsteadiness, however, remains an open question to be investigated—both experimentally and theoretically. In principle, our formalism could be extended to allow for the evaluation of forces on arbitrary geometries and deformable interfaces, however, the resulting integrals may not admit analytical solutions. Nevertheless, asymptotic theory for small deviations from a spherical geometry might yield physical insight, for small-amplitude oscillatory flows. We anticipate that time scale separation will, even in this complicated but practically relevant situation, result in simplified overdamped equations of motion for both translation and rotation.

7.2.2 Rotational Inertia

In this dissertation, we have neglected the effects of rotation while deriving the inertial forces on spherical particles. Recent advancements in the field of microfluidics have seen the increased use of electric or magnetic field gradients, in concert with inertial effects, to exert another degree of active positional control in order to manipulate particles [10, 121]. Recently, the spontaneous spinning of a dielectric sphere in a uniform DC electric field, first described over a century ago by Quincke [135], has gathered renewed interest, due to its applications in the field of suspensions. A zoo of experiments have revealed interesting effects, ranging from collective motion to observations of attractive forces between particles resulting in chain formation, and to even Lorenz chaos [131, 133]. Until now, none of the models of the Quincke rotation have systematically taken into account the inertia of the particle. Rotational oscillations—even for spherical particles—will have associated non-trivial inertial effects that might break the symmetry of Stokes flow in interesting ways, leading to irreversible motion. Rotational inertia, thus, provides another knob to tune the behavior of

fluid-borne objects, and is largely unexplored so far. Our formalism allows for the inclusion of these effects, albeit closed-form results may be challenging to obtain. Ultimately, the goal is to formalize a comprehensive predictive theory that guides the design of practical applications.

7.2.3 Aggregation of particles at micro/nano scales

One of the grand challenges in the field of micro/bio-manufacturing is to make selective aggregates of particles, through accurate valence control, and force them to stick together or form controllable aggregates. Bottom-up manufacturing through manipulation of individual particles has enormous potential as a way to make novel biomaterials with tunable properties. It is a task for which microfluidics is especially suited for, owing to a variety of available avenues for precise control of particles. This is somewhat surprisingly hard to achieve due to how strong short-range repulsive lubrication forces are in the micro-scale regime. Additionally, the phenomenon of aggregation of particles involves additional physics, such as surface chemistry, and depends crucially on interfacial conditions. Thus, these additional elements have to be incorporated along with a complete hydrodynamic description of forces.

In the biological context, a key prerequisite to understanding how viruses, e.g. SARS-CoV-2, replicate and spread further involves investigating how they are transported to the cell membrane—eluding the elaborate defense mechanisms of the host—and stick to receptors atop the cell membrane. The interactions of viruses with host cells are notably complex and they can experience a range of repulsive physical forces due to, e.g., shape or chemistry of the cell membrane; a purely passive particle would thus be slow to penetrate these barriers. What strategies these pathogens use to overcome significant repulsive forces, which would otherwise prevent a passive particle from attaching to the cell membrane, is still not well understood. A deeper exploration of these biophysical ideas will not only improve our fundamental understanding of transport at cellular scales but also open up avenues for design of new therapeutic strategies and precise manipulation of cargo uptake by a cell, be it for nutrition, signaling or pathogen transport.

7.3 Closing remarks

A fundamental understanding of inertial forces on particles is essential to systematically manipulate fluid-borne objects in inertial microfluidics. It is somewhat surprising that relatively little is known about the motion of microparticles in the general case of unsteady spatially non-uniform flows. While recent work [73] has shown that the effect of finite particle inertia can be accounted for by a regular asymptotic expansion in the particle Reynolds number in the case of a steady, unidirectional Poiseuille flow, for Saffman-like lift

forces one must employ a singular perturbation expansion in Reynolds number [145]. Both these effects have very different origins, and scale differently with Reynolds number.

This situation is further complicated by the presence of boundaries [70, 73] and the introduction of unsteadiness [56, 92] and/or spatially non-uniform flows, for which no systematic theory existed before. Many microfluidic applications rely on vortical or unsteady flow actuation parts, in addition to an imposed transport flow, in order to manipulate microparticles; a fundamental understanding of inertial forces is crucial for the design of practical applications. This work, therefore, represents a significant advancement to the field of inertial microfluidics, since we have, for the first time, developed a generally applicable theory of particle dynamics which accounts for, (i) unsteadiness and spatial flow variation, (ii) particle inertia, and (iii) interaction with boundaries.

A specialization of the general theory to oscillatory flows immediately results in the prediction of a previously unrecognized, strong flow curvature induced attractive inertial force acting even on neutrally buoyant particles, accounting for many previously unexplained experimental observations. As a consequence of the separation of time scales between oscillatory and steady flow components, the particle motion on oscillatory time scales becomes rectified into a steady (time-averaged) motion on longer time-scales. This allowed for the development of a field theory of particle motion in streaming flows (analogous to descriptions of Lagrangian fluid motion in such flows), significantly reducing computational effort. The versatility and generality of the reciprocal-theorem-based theory has made it immediately useful in the design and analysis of practical microfluidics applications relying on microbubble streaming. We expect that this work will, through both its fundamental and practical aspects, benefit not only the fluid dynamics community but also provide insights to researchers in bioengineering and biophysics.

Appendix A

A simple, general criterion for onset of disclination disorder on curved surfaces

Determining the positions of lattice defects on bounded elastic surfaces with Gaussian curvature is a non-trivial task of mechanical energy optimization. In this Appendix[1], we introduce a simple way to predict the onset of disclination disorder from the shape of the surface. The criterion fixes the value of a weighted integral Gaussian curvature to a universal constant and proves accurate across a great variety of shapes. It provides improved understanding of the limitations to crystalline order in many natural and engineering contexts, such as the assembly of viral capsids.

A.1 Introduction

Crystalline domain systems with intrinsic curvature whose structure is governed by the minimization of an interaction energy are commonly found in nature [16, 51, 80, 105, 154, 175]. Unlike in flat 2D space where interacting particles can pack in triangular lattices, finite Gaussian curvature K_G introduces geometric frustration. This concept is quantified by the Euler theorem, requiring a total topological charge on the lattice of $Q = \sum_{i=1}^{V} q_i = 6\chi$, where $q_i = 6 - c_i$ are defect charges using c_i for the coordination number of the ith vertex, and the Euler characteristic χ (cf. Fig. A.1(a)).

While the theorem fixes the charge, the positioning of these defects co-determines the elastic energy of the shell [117], and finding minimal-energy configurations in general scenarios is a formidable task of considerable recent interest [21, 32, 60, 114, 127, 164]. Much work has focused on closed shells such as virus capsids ($\chi = 2$) [29], but to understand their *assembly* an even more fundamental problem must be investigated: the aggregation of capsid protein units often occurs *en masse* [129, 130], with one or more open-boundary shell fragments forming on an underlying RNA molecule or nucleocapsid as a scaffold [66, 120]. These scaffolds have manifold shapes, leading to e.g. the helicoid capsids of SARS-CoV or the conical HIV capsid (Fig. A.1(c)). To understand the capsid assembly, one first needs to describe the equilibrium structure of a single shell fragment (a patch or cap on the scaffold with $\chi = 1$). Whether a patch takes on its desired

[1] This Appendix is adapted from Agarwal and Hilgenfeldt [2]

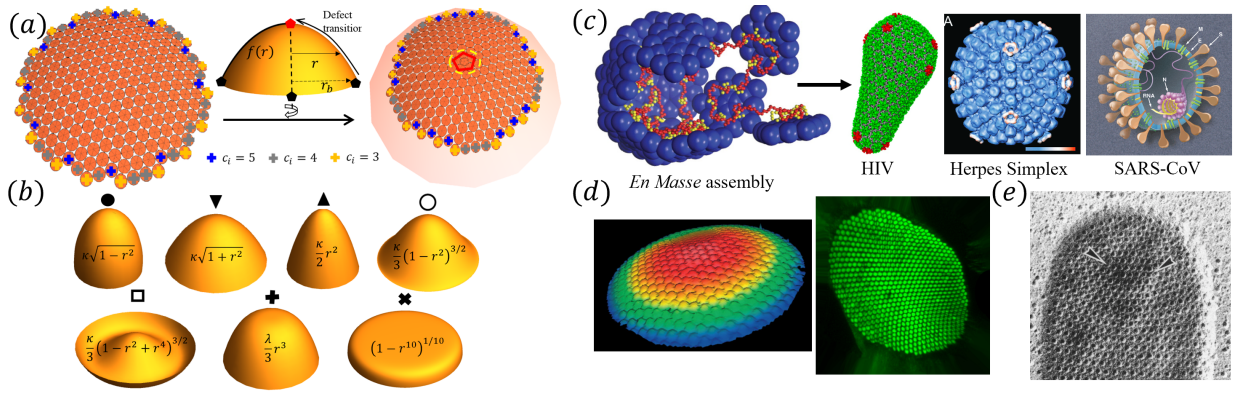

Figure A.1: (a) A single disclination defect at the apex of a cap becomes energetically favorable for large enough central curvature κ and/or cap extent r_b; (b) Sample families of axisymmetric cap shapes with their parametrizations $f(r)$; the first five have non-zero κ. Symbols are used for plotting in later figures; (c) Caps can self-assemble *en masse* to form a viral capsid [130] with various shapes [63, 64, 71]; (d) perfect crystalline order in curved microlens arrays [33] and the *Drosophila* eye [53]; (e) near-perfect order in the S-layer of the archaebacterium *T. tenax*—arrows indicate disclinations [106]. All figures reproduced with permission.

equilibrum size and shape, or whether assembly can be disrupted [104] depends on its mechanical energy, and thus crucially on defect positioning [62]. The elementary question on shape and assembly of the structure then becomes whether a ground-state crystalline patch on a given scaffold is defect-free in its interior or not. In a different context, the same question of elementary regularity can be asked of insect eyes or microlens arrays (Fig. A.1(d)), where crystalline order and Gaussian curvature are simultaneously desired for proper optical function [33, 53].

Our task is thus to predict the onset of the first topological charge in the interior of caps of general axisymmetric shape (Fig. A.1(a)(b)). While the Euler theorem allows for a distribution of dislocations (defects of positional disorder) that distinctly affect shell mechanics [12, 13], their occurrence requires extra compensating defect charges. In cases of large defect core energies this is prohibitively expensive [23, 25] and indeed even in large capsids, many metazoan epithelia [144], and ordered cell membranes [106] (Fig. A.1(e)) the only generic defects are those of orientational disorder, i.e., *disclinations*. We will thus focus on a single disclination as the onset of crystalline disorder [117]. As our cap geometry is prescribed e.g. by a scaffold, we will not consider shape changes by buckling [87, 152] or other instabilities [112].

Open caps necessitate a net charge $Q = 6$. On nearly flat surfaces, the cap boundary can accommodate these charges without distortion or energy cost (see Fig. A.1(a)). For large enough curvature, it becomes favorable for at least one defect to migrate away from the boundary. This transition has been analyzed specifically for spherical caps and paraboloids [12, 13, 60, 86], including numerical approaches to this global optimization task in a class of problems considered NP hard [60].

It is desirable to formulate general intuitive criteria for this prototypical transition: what constitutes

"large enough curvature"? Anecdotally, it has been suggested that defects migrate to positions of large local K_G [165], but counterexamples to this rule are easily found. Recent literature [75] instead proposes that the integrated Gaussian curvature $\Omega = \int K_G \mathrm{d}A/(\pi/3)$ needs to exceed a critical value for defect migration. However, significantly different values have been proposed for various experimental [75] and numerical systems [13, 60, 86], casting doubt on the generality and accuracy of this criterion.

A.2 Theoretical Formalism

Here, we develop a new, physically motivated criterion that proves quantitatively accurate across large classes of shapes. We model defects as isolated singularities within a continuum linear elastic theory framework on smooth bounded surfaces with an underlying triangulated crystal lattice at zero temperature [24, 25, 116]. We develop a formalism for elastic energy originating from [25], closely modeled on [60] and [23], of which we will only detail our variations and improvements (see Section A.5 for complete derivations). The surfaces of revolution are parametrized by $Z = Rf(r)$ with a common length scale normalized to $R = 1$. Generic surfaces have finite center curvature ($f''(0) \equiv \kappa \neq 0$), although we will also consider surfaces of higher-order flatness below. Surfaces have finite extent $0 \leq r \leq r_b \leq 1$; while we discuss shape families both intrinsically compact (e.g. spheroids) and unbounded (e.g. hyperboloids), we only consider "cap" shapes with unique Z values. The determinant g of the metric tensor, Gaussian curvature K_G, and its integral Ω are then

$$\sqrt{g} = r\sqrt{1 + f'(r)^2}, \quad K_G = \frac{f'(r)f''(r)}{r(1 + f'(r)^2)^2}, \tag{A.1a}$$

$$\Omega = 6\left(1 - 1/\sqrt{1 + f'(r_b)^2}\right). \tag{A.1b}$$

With the free energy of the defect-free lattice and the defect core energy fixed, any minimization of energy is governed by F_{el}, the elastic energy of defect-surface interaction. Focusing on stress-free boundaries, the difference of F_{el} between configurations with defects at the boundary ($r_D = r_b$) and one defect at the apex ($r_D = 0$) is a function of the traces of the stress tensor Γ,

$$\Delta F_{el}(r_b) \equiv F_{el}(0) - F_{el}(r_b) = \pi \int_0^{r_b} \left(\Gamma^2(r, 0) - \Gamma^2(r, r_b)\right) \sqrt{g}\, \mathrm{d}r, \tag{A.2}$$

where $\Gamma(r, r_D)$ has four contributions

$$\Gamma(r, r_D) = -\Gamma_D(r, r_D) - \Gamma_S(r) + U_D(r_D) + U_K, \tag{A.3}$$

given by

$$\Gamma_D(r,0) = -\frac{q}{6}\log\varrho(r), \qquad \Gamma_D(r,r_b) = 0, \tag{A.4a}$$

$$\Gamma_S(r) = \log\left(\varrho(r) r_b/r\right), \tag{A.4b}$$

$$\varrho(r) = \exp\left(-\int_r^{r_b} \frac{\sqrt{1+f'(r_1)^2}}{r_1}\mathrm{d}r_1\right), \tag{A.4c}$$

representing exact functionals, though the integral in (A.4c) may not have closed form. Here we have used integration by parts to simplify (A.4b) further from [60] (cf. Section A.5). Energies have been made dimensionless by the Young's modulus for the planar crystal, and we will use $q = +1$ (single disclination) in the following. $\varrho(r)$ is the conformal radius of a map from the surface onto the unit disk (see Section A.5 for details). (A.4a) represents the contribution of the disclination while (A.4b) captures the screening effect of Gaussian curvature. The generic shape of these functions is illustrated in Fig. A.2.

Balancing Γ_D and Γ_S represents partial defect-charge compensation by local Gaussian curvature. Further compensation is effected by U_D and U_K, which are determined by the boundary conditions through integration of Γ_D, Γ_S. In our radially isotropic case with stress-free boundaries [60], $U_D(0)$ and U_K are the straight averages

$$U_D(0) = \frac{1}{A}\int \Gamma_D(r,0)\,\mathrm{d}A, \;\; U_K = \frac{1}{A}\int \Gamma_S(r)\,\mathrm{d}A, \tag{A.5}$$

with the surface area $A = 2\pi\int\sqrt{g}\,\mathrm{d}r$. We define the critical radius $r_b = r_c$ as the extent (or cap coverage) at which a center disclination becomes favorable, i.e., $\Delta F_{el}(r_c) = 0$. Using (A.3), (A.4) and (A.5) in (A.2) yields

$$\begin{aligned}\Delta F_{el}(r_c) \equiv &\int_0^{r_c} \Gamma_D(r,0)(\Gamma_D(r,0) + 2\Gamma_S(r))\sqrt{g}\,\mathrm{d}r \\ &- U_D(0)(U_D(0) + 2U_K)A = 0\end{aligned} \tag{A.6}$$

as our rigorous criterion for transition of a disclination defect from a boundary position to the apex. Note that (A.6) follows directly from the covariant formalism of [25], which has proved successful and accurate in many contexts [23, 60, 61], but avoids general nonlinearities of surface deformations [85]. A closer discussion in Section A.5 demonstrates its accuracy for our case. The above examples from biology and technology all consist of a large enough number of lattice units, where continuum theory of defective surfaces has proved very accurate [26, 149].

The numerical solution of (A.6) is a rather opaque procedure and it is desirable to find an approximate criterion for the location of the transition that directly relates to surface shape. We compare two approaches: (1) a local small slope approximation used previously e.g. in [13], and (2) a non-local approximation leading

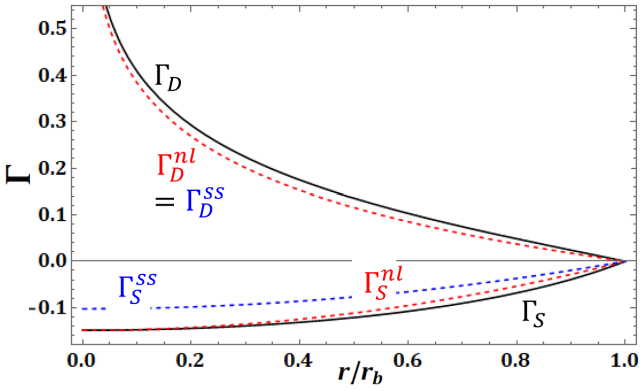

Figure A.2: Isotropic stress terms for an oblate spheroid ($\kappa = 0.8$). Black lines: rigorous covariant expressions; blue dashed: small-slope approximation; red dashed: non-local approach

to a new, more accurate and widely applicable criterion for transition.

In the small-slope approach, the functions defined above are locally Taylor expanded around $r = 0$ to leading order, requiring both $r \ll 1$ and $r_b \ll 1$, so that

$$\Gamma_S^{ss}(r) = \Gamma_S^{ss}(0)\left(1 - r^2/r_b^2\right), \tag{A.7a}$$

$$\Gamma_D^{ss}(r,0) = -\frac{1}{6}\log\left(r/r_b\right), \quad \sqrt{g^{ss}} = r, \tag{A.7b}$$

where $\Gamma_S^{ss}(0) = -\frac{1}{4}\kappa^2 r_b^2$ is the small-slope expansion of the full $\Gamma_S(0)$. Inserting into (A.5) and (A.6) gives a straightforward polynomial equation in κ and r_c, whose solution yields a criterion for critical extent as [13]

$$r_c = \sqrt{2/3}/\kappa \quad \text{or} \quad \Omega^{ss} = 3\kappa^2 r_c^2 = 2\,. \tag{A.8}$$

This formalism thus suggests that the transitional surface shape is indeed given by a universal (leading-order) value of integrated Gaussian curvature. However, different studies have determined values of this quantity that differ by more than a factor of two [13, 60, 75] depending on the surface considered.

An inherent flaw of the small-slope approximation is apparent when comparing the function Γ_S^{ss} to its exact version: not even the value at the expansion point, $\Gamma_S(0)$, is accurately reproduced (see Fig. A.2, which shows a representative case). We remedy this problem by requiring this matching to hold, replacing the local quantity $\Gamma_S^{ss}(0)$ by the exact value, so that (A.7a) is modified to

$$\Gamma_S^{nl}(r) = \Gamma_S(0)\left(1 - r^2/r_b^2\right), \tag{A.9}$$

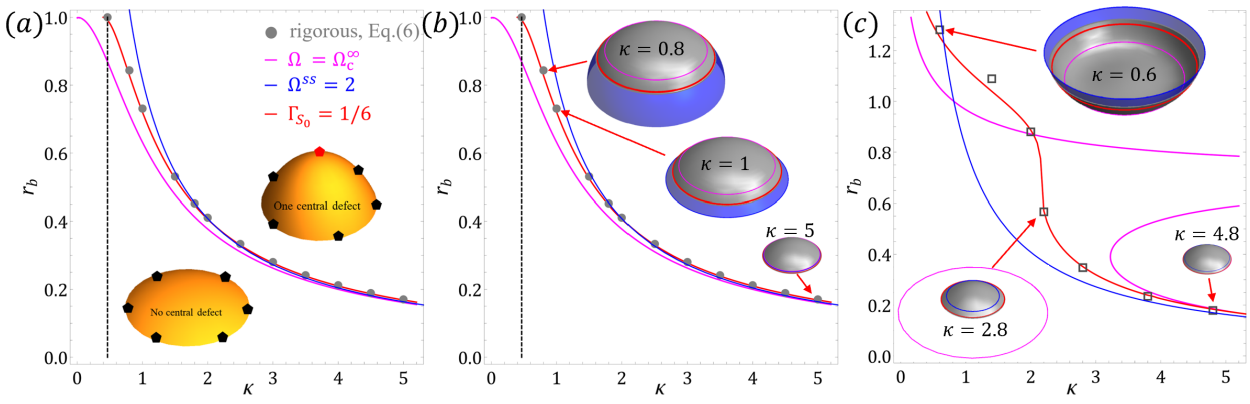

Figure A.3: Cap extent at transition as a function of κ. Gray squares are numerically obtained critical points $r_c(\kappa)$ from (A.6); blue lines are the small-slope criterion (A.8); magenta lines depict constant $\Omega = \Omega_c^\infty$. Red lines are given by the criterion $\Gamma_{S_0} = 1/6$ and are in excellent agreement with the rigorous critical points. (a) spheroids; the dashed vertical black line marks the minimal $\kappa_{c,min}$ for transitions; (b) spheroidal shapes at transition—gray caps show the rigorously computed extent, shapes determined from the approximate criteria are blue and magenta; red lines show the extent predicted from $\Gamma_{S_0} = 1/6$; (c) transition lines for the $f(r) = \frac{\kappa}{3}(1 - r^2 + r^4)^{3/2}$ "sombrero": as κ is increased along the transition line, the boundary slope s_b of this surface changes sign, leading to the sharp drop in r_c at $\kappa \approx 2$. The $\Omega = const.$ criterion obtains more than one root for $\kappa \gtrsim 3$.

with the rigorous expression

$$\Gamma_S(0) \equiv \int_0^{r_b} K_G(r) \log \varrho(r) \sqrt{g}\, \mathrm{d}r\,, \tag{A.10}$$

i.e., the trace of the full background stress tensor at the apex, a non-local quantity which represents an integrated Gaussian curvature *weighted* by the $\log \varrho$ singularity characteristic of the Green's function of the problem (see Section A.5), and thus of the local stress due to the defect Γ_D. For now, we leave the other approximations unchanged, $\Gamma_D^{nl} = \Gamma_D^{ss}$ and $\sqrt{g}^{nl} = \sqrt{g}^{ss}$.

When using (A.7b), (A.9) and (A.5) in the rigorous covariant expression (A.6), the integration is again straightforward and results in a simple prediction for $\Gamma_S(0)$:

$$\Gamma_{S_0} \equiv -\Gamma_S(0) = 1/6 \tag{A.11}$$

The LHS from (A.10) is an implicit equation in the cap extent r_c and the shape parameters (e.g. κ). The new criterion (A.11) is as conceptually simple as (A.8), but recognizes that the Gaussian curvature in each point contributes to stress relief of a central disclination with different weight.

A.3 Results and Discussion

We now examine how this simple condition on Γ_{S_0} performs. Going beyond evaluations for individual surface shapes (cf. [13, 86], [60]), we determine the location of the disclination transition in entire surface families (see Fig A.1(b)) with various distributions of curvature.

In the family of spheroids, $f(r) = \kappa\sqrt{1-r^2}$, prolate ($\kappa > 1$) shapes have a Gaussian curvature maximum at the apex, while oblate ($\kappa < 1$) spheroids have maximum K_G at the boundary. Figure A.3(a) plots the critical values $r_b = r_c$ as a function of κ. The symbols result from numerical evaluation of the rigorous covariant criterion (A.6) and show that both prolate and oblate shapes display disclination migration as long as $\kappa > \kappa_{c,min} \approx 0.465$. Thus, maximum local curvature at the (apex) disclination position is not sufficient to determine that position. For a spherical cap ($\kappa = 1$), we note that our results agree with the findings of [86], and (A.6) results in $r_c \approx 0.73$.

Plotting the small-slope formula (A.8) as an $r_c(\kappa)$ contour in Fig. A.3(a) shows that it is relatively accurate at large κ, but exhibits strong deviations for $\kappa \lesssim 1$, failing to predict even the existence of a transition for the most oblate shapes. Testing the hypothesis of constant integrated Gaussian curvature, we also use (A.1b) to plot a contour $\Omega = \Omega_c^\infty \approx 1.35$, a value obtained by matching to the small-slope value as $\kappa \to \infty$. Again, significant errors are present for smaller $\kappa \lesssim 2$, this time underestimating r_c so that the true transition shape requires "overcharging" of the surface as observed in previous studies [75, 86]. Clearly, Ω is not a constant at the transition of disclination migration (at $\kappa_{c,min}$, Ω_c^∞ is about four times smaller than Ω at the true transition point).

By contrast, the new indicator for critical shapes $\Gamma_{S_0} = 1/6$ derived above yields a transition curve in excellent agreement with the rigorous results for all spheroidal caps, cf. Fig. A.3(a,b). The Ω and Ω^{ss} criteria can fail much more severely for surfaces with strong variation of K_G, such as the family of "sombrero" shapes depicted on the lower left of Fig. A.1b. Yet, the rigorous transition is very well captured by the Γ_{S_0} criterion, see Fig. A.3(c).

In all cases, the criteria based on Ω or Ω^{ss} perform poorly for $\kappa \sim 1$. We note that in applications in nature and technology, these cases are the most practically relevant: Fig. A.3(b) shows that transition shapes for large κ are so small that they are nearly flat caps, while $\kappa \sim 1$ shapes are "bulgy". These are the shapes that non-trivially reconcile significant curvature and crystalline order, such as in an insect eye that needs to bulge (for field of view) while having ordered facets (for accurate processing of the visual information). These are also caps of a size ($r_c \sim 1$) typically required to close a virus capsid assembly with the minimum number of defects [29].

These findings hold true for all the shape families in Fig. A.1(b), designed to explore manifold cap

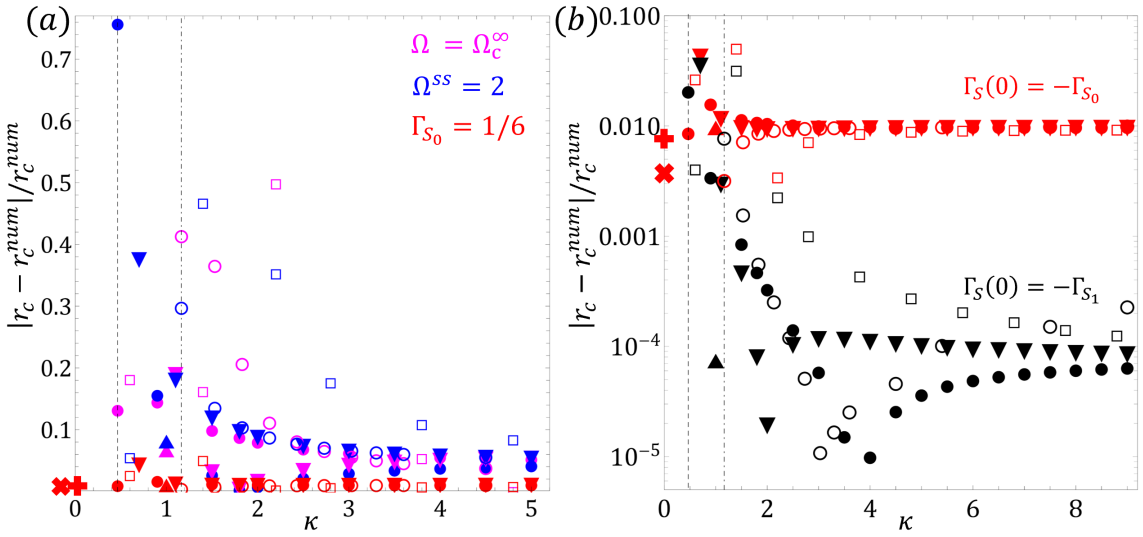

Figure A.4: Relative errors in $r_c(\kappa)$ using different transition predictors (see Fig. A.1(b) for a key to symbols). Dashed and dot-dashed vertical lines indicate limiting $\kappa_{c,min}$ for spheroids (filled circles) and "bell" surfaces (open circles), respectively. (a) Blue symbols use (A.8), magenta use constant Ω, red symbols use $\Gamma_{S_0} = 1/6$. (b) Red symbols: same as (a) on a log scale; black symbols: improved transition criterion using Γ_{S_1}.

morphologies imposed by various scaffold shapes. Figure A.4 quantifies the relative errors of $r_c(\kappa)$ for the three different criteria. Regardless of whether the parametrization allows for infinite caps (e.g. hyperboloids) or for sign changes of Gaussian curvature, the criterion of $\Gamma_{S_0} = 1/6$ uniformly outperforms those based on integrated K_G, with most errors below 1%. We note that for a paraboloid (upward triangles at $\kappa = 1$ in Fig. A.4), we find $r_c \approx 0.856$, while [60] obtained $r_c \approx 1.5$ as a consequence of neglecting $U_D(0)$ in the energy evaluation.

It is apparent from Figs. A.3 and A.4 that the transition positions (and errors) have a common asymptote for $\kappa \to \infty$. By expanding (A.11) for small r_c and large κ, we obtain the asymptotic form of the transition line for any surface of revolution with large apex curvature:

$$r_c(\kappa) \approx \frac{0.848}{\kappa} - \frac{0.146}{\kappa^3} + \frac{0.02}{\kappa^5} + \mathcal{O}\left(\frac{1}{\kappa^7}\right). \tag{A.12}$$

Note that the leading order of this equation is not equivalent to the small-slope result $r_c = \sqrt{2/3}/\kappa_c \approx 0.816/\kappa_c$ from (A.8). The new criterion improves even this leading order, and provides higher-order corrections. Perhaps surprisingly, the Γ_{S_0} criterion remains as accurate for surfaces with $\kappa = 0$ that do not share the asymptote (A.12). Two examples (the last two shapes in Fig. A.1(b)) are indicated in Fig. A.4 by the $+$ and $\times$ shapes, demonstrating the non-perturbative character of (A.11).

The criterion based on weighted integrated Gaussian curvature is not only more accurate, but more

systematic: in Fig. A.4(b), we show that the next-order expansion Γ_{S_1} of $\Gamma_S(0)$ provides a further dramatic improvement of relative errors across all shapes, particularly for larger κ. For these results, the non-local computation of $\Gamma_S(0)$ was maintained, while further terms of relative order $(r/r_b)^2$ were included in (A.9) and determined by enforcing a match to derivatives at $r = r_b$. Explicitly, this leads to

$$\Gamma_D^{nl}(r,0) = \Gamma_D^{ss}(r,0) - \frac{\left(1-\sqrt{1+s_b^2}\right)}{12}\left(1-\frac{r^2}{r_b^2}\right), \tag{A.13a}$$

$$\sqrt{g}^{nl}(r) = r + \left[r_b\sqrt{1+s_b^2} - r_b\right](r^3/r_b^3), \tag{A.13b}$$

defining the slope at the boundary as $s_b \equiv f'(r_b)$. Inserting into (A.6) and integrating results in

$$\Gamma_{S_1} = -\Gamma_S(0) = \tag{A.14}$$
$$\frac{70 + 2s_b^4 + 74\sqrt{1+s_b^2} + s_b^2\left(41+12\sqrt{1+s_b^2}\right)}{48\left(8+10\sqrt{1+s_b^2}+s_b^2\left(5+\sqrt{1+s_b^2}\right)\right)}$$

$$\approx 1/6 + s_b^2/432 + \dots . \tag{A.15}$$

We compare the Γ_{S_0} and Γ_{S_1} criteria in Fig A.4(b). The $\mathcal{O}(s_b^2)$ term in (A.15) has a very small prefactor, making the difference between Γ_{S_0} and Γ_{S_1} slight even for moderate s_b. The transition shape of surfaces with large κ is such that $s_b^2 \approx \kappa^2 r_b^2 \to 0.848$, see (A.12), which allows quantification of the second term of (A.15) in that limit. We obtain $s_b^2/432 \to 0.0099\ldots$, explaining the magnitude of the universal error asymptote of Γ_{S_0} as $\kappa \to \infty$.

A.4 Conclusions

The transition criterion introduced here argues that the primary determinant of the onset of disclination disorder on open surfaces is neither the local Gaussian curvature nor its straight integral Ω, but that the values of K_G contribute proportional to the local isotropic disclination stress (cf. (A.4a) and (A.10)). The quantity Γ_{S_0} is as easy to calculate as Ω and has a universal value at transition for all shape families investigated here. It is an accurate predictor particularly for surfaces of moderate central curvature that represent practically relevant, significantly "bulging" shapes at the edge of maintaining crystalline order. In the context of virus capsid assembly, to understand when the energetic changes associated with disclinations occur, and how to modify them through the presence of drugs [79, 156, 174], is a powerful therapeutic tool. Further work will be devoted to generalizing this criterion to anisotropic surfaces and to the prediction of

the first- or second-order character of the transitions.

A.5 Additional Information

A.5.1 Exact covariant formalism

One way to compute stress on curved elastic surfaces is to use the Airy stress function χ. It solves the following inhomogeneous biharmonic equation [23, 60]:

$$\Delta^2 \chi(\mathbf{x}, \mathbf{x}_D) = Y_0 q_T(\mathbf{x}, \mathbf{x}_D), \tag{A.16}$$

where $q_T(\mathbf{x}, \mathbf{x}_D) = \frac{\pi}{3}\delta(\mathbf{x}, \mathbf{x}_D) - K_G(\mathbf{x})$ represents both the singular contributions of disclinations and the continuous contribution of surface shape (Gaussian curvature); Y_0 is the 2D Young's modulus of the surface. We impose no-stress boundary conditions on the domain $\mathbb{P}$:

$$\chi(\mathbf{x}, \mathbf{x}_D) = 0, \quad \mathbf{x} \in \partial\mathbb{P}, \quad \nu_i \nabla^i \chi(\mathbf{x}, \mathbf{x}_D) = 0, \quad \mathbf{x} \in \partial\mathbb{P} \tag{A.17}$$

with normal ν_i. The solution of (A.16) will then be

$$\chi(\mathbf{x}, \mathbf{x}_D) = \int \mathrm{d}\mathbf{y}\, G_L(\mathbf{x}, \mathbf{y}) \Gamma(\mathbf{y}, \mathbf{x}_D), \tag{A.18}$$

where $G_L(\mathbf{x}, \mathbf{y})$ is the Green's function of the covariant Laplace operator on $\mathbb{P}$ with Dirichlet boundary conditions

$$\Delta G_L(\mathbf{x}, .) = \delta(\mathbf{x}, .), \quad \mathbf{x} \in \mathbb{P}, \quad G_L(\mathbf{x}, .) = 0, \quad \mathbf{x} \in \partial\mathbb{P}, \tag{A.19}$$

and $\Gamma(\mathbf{x}, \mathbf{x}_D) = \Delta\chi(\mathbf{x}, \mathbf{x}_D)$ is the solution of the Poisson problem

$$\Delta\Gamma(\mathbf{x}, \mathbf{x}_D) = Y_0 q_T(\mathbf{x}, \mathbf{x}_D)\,. \tag{A.20}$$

This solution can be expressed formally as

$$\Gamma(\mathbf{x}, \mathbf{x}_D) = Y_0 \int q_T(\mathbf{y}, \mathbf{y}_D) G_L(\mathbf{x}, \mathbf{y}) \mathrm{d}\mathbf{y} = -\Gamma_D(\mathbf{x}, \mathbf{x}_D) - \Gamma_S(\mathbf{x}) + U(\mathbf{x}, \mathbf{x}_D), \tag{A.21}$$

where

$$\Gamma_D(\mathbf{x}, \mathbf{x}_D) = -\frac{\pi}{3} Y_0 G_L(\mathbf{x}, \mathbf{x}_D), \quad \Gamma_S(\mathbf{x}) = Y_0 \int K_G(\mathbf{y}) G_L(\mathbf{x}, \mathbf{y}) \mathrm{d}\mathbf{y}, \tag{A.22}$$

and $U(\mathbf{x}, \mathbf{x}_D)$ is a harmonic function on $\mathbb{P}$ that enforces the Neumann boundary conditions. The first term of (A.21) represents the bare contribution of disclinations while the second term captures the screening effect of Gaussian curvature. In this Appendix, we restrict ourselves to allowing only one disclination to migrate from the boundary to the apex of the manifold. For symmetric Γ_S and Γ_D, i.e. isotropic surface and defects decorated at centre or boundary, the harmonic function can be computed by directly applying the boundary condition (A.17) in (A.21) and this results in

$$U = \frac{1}{A} \int \left(\Gamma_D(\mathbf{x}, \mathbf{x}_D) + \Gamma_S(\mathbf{x}) \right) \mathrm{d}\mathbf{x}, \tag{A.23}$$

where the surface area $A = \int \mathrm{d}\mathbf{x}$. The elastic energy for a stress-free boundary can be expressed only in terms of the isotropic stress tensor Γ as

$$F_{el}(\mathbf{x}_D) = \frac{1}{2Y_0} \int \Gamma^2(\mathbf{x}, \mathbf{x}_D) \, \mathrm{d}\mathbf{x}, \tag{A.24}$$

The Green's function satisfying (A.19) is computed explicitly by conformally mapping the surface $\mathbb{P}$ onto the unit disk of the complex plane where the Green's function is known:

$$G_L(\mathbf{x}, \mathbf{y}) = \frac{1}{2\pi} \log \left| \frac{z(\mathbf{x}) - z(\mathbf{y})}{1 - z(\mathbf{x}) \overline{z(\mathbf{y})}} \right|, \tag{A.25}$$

where $z(\mathbf{x}) = \varrho e^{i\phi}$, a point in the unit disk, is the image of a point on the surface $\mathbb{P}$ under the conformal mapping. The Green's function vanishes when the disclination is located at the boundary. For a surface $X(r, \phi)$ with first fundamental form $E = \partial X/\partial r \cdot \partial X/\partial r$, $F = \partial X/\partial r \cdot \partial X/\partial \phi$ and $G = \partial X/\partial \phi \cdot \partial X/\partial \phi$, the metric of the surface is

$$\mathrm{d}s^2 = E \mathrm{d}r^2 + 2F \mathrm{d}r \mathrm{d}\phi + G \mathrm{d}\phi^2 \,, \tag{A.26}$$

whereas the unit disk has the metric

$$\mathrm{d}s^2 = w(z) \left(\mathrm{d}\varrho^2 + \varrho^2 \mathrm{d}\phi^2 \right) . \tag{A.27}$$

where $w(z)$ is a positive conformal weight. The remaining task is now to find the conformal factor $w(z)$ and the conformal radius $\varrho(r)$ by equating the two metrics; these can be explicitly obtained for many rotationally

symmetric surfaces but in general, may not be analytically computable.

Taking the two image points on the unit disk as $z(r,\phi) = \varrho_x(r)e^{i\phi}$ and $\zeta(r',\phi') = \varrho_y(r')e^{i\phi'}$, the contribution due to the background Gaussian curvature is split into two parts $\Gamma_S(\mathbf{x}) = \Gamma_{S,1}(\mathbf{x}) - \Gamma_{S,2}(\mathbf{x})$, where

$$\Gamma_{S,1}(\mathbf{x}) = \frac{Y_0}{2\pi}\int \mathrm{d}\phi'\,\mathrm{d}r'\,\sqrt{g}K(r')\log|z-\zeta|, \quad \Gamma_{S,2}(\mathbf{x}) = \frac{Y_0}{2\pi}\int \mathrm{d}\phi'\,\mathrm{d}r'\,\sqrt{g}K(r')\log|1-z\bar{\zeta}|, \tag{A.28}$$

are evaluated analytically for the specific surfaces considered in this Appendix.

For rotationally symmetric surfaces parametrized by $X = r\cos\phi$, $Y = r\sin\phi$, $Z = f(r)$ with the first fundamental form $E = 1 + f'(r)^2$, $F = 0$, and $G = r^2$, the conformal distance ϱ (on the unit disk) can be obtained by equating (A.26) and (A.27), so that one obtains

$$w(\varrho) = \frac{r^2}{\varrho^2}, \quad \frac{d\varrho}{dr} = \mp\frac{\sqrt{1+f'(r)^2}}{r}\varrho. \tag{A.29}$$

This last ODE may be solved analytically with boundary conditions $\varrho(0) = 0$ and $\varrho(r_b) = 1$, which yields

$$\varrho(r) = \exp\left(-\int_r^{r_b}\sqrt{E/G}\,\mathrm{d}r_1\right) = \exp\left(-\int_r^{r_b}\frac{\sqrt{1+f'(r_1)^2}}{r_1}\,dr_1\right). \tag{A.30}$$

Note that in the small-slope limit, i.e. $f'(r_b) \ll 1$, the conformal distance $\varrho(r) = r/r_b$ which physically means that the manifold is a flat disk in this limit. Γ_S can be further simplified using the expansions

$$\log|z-\zeta| = \log\varrho_> - \sum_{n=1}^{\infty}\frac{1}{n}\left(\frac{\varrho_<}{\varrho_>}\right)^n\cos n(\phi-\phi'), \quad \log|1-z\bar{\zeta}| = -\sum_{n=1}^{\infty}\frac{1}{n}\left(\varrho\varrho'\right)^n\cos n(\phi-\phi') \tag{A.31}$$

where $\varrho_>(\varrho_<)$ represents the largest (smallest) modulus between z and ζ. If K_G and $\sqrt{g}$ are azimuthally symmetric then all the angular dependences in (A.5.1) vanish so that we have

$$\Gamma_{S,1}(r) = Y_0\log\varrho(r)\int_0^r\frac{f'(r_1)f''(r_1)}{(1+f'(r_1)^2)^{3/2}}\mathrm{d}r_1 + Y_0\int_r^{r_b}\log\varrho(r_1)\frac{f'(r_1)f''(r_1)}{(1+f'(r_1)^2)^{3/2}}\mathrm{d}r_1, \quad \Gamma_{S,2}(r) = 0. \tag{A.32}$$

The first integral in (A.32) is the integrated Gaussian curvature and can be analytically executed using the fact that $f'(0) = 0$ (since by symmetry the slope at the apex is zero), while the second one may be integrated

by parts to obtain

$$\begin{aligned}\Gamma_{S,1}(r) =& Y_0 \log\varrho(r)\left(1-\frac{1}{\sqrt{1+f'(r)^2}}\right)+Y_0\left[\log\varrho(r_1)\frac{-1}{\sqrt{1+f'(r_1)^2}}\right]_r^{r_b}-Y_0\int_r^{r_b}\frac{1}{\varrho(r_1)}\frac{d\varrho(r_1)}{dr_1}\frac{-1}{\sqrt{1+f'(r_1)^2}}\mathrm{d}r_1\\ =& Y_0\log\varrho(r)+Y_0\int_r^{r_b}\frac{1}{r_1}\mathrm{d}r_1 = Y_0\log\varrho(r)+Y_0\log\left(\frac{r_b}{r}\right)=Y_0\log\left(\varrho(r)\frac{r_b}{r}\right),\end{aligned} \tag{A.33}$$

where we have used (A.29) and the fact that $\log\varrho(r_b)=\log 1=0$. It is also evident that $\Gamma_S(0)$ is just the second integral in (A.32) so that

$$\Gamma_S(0)=Y_0\int_0^{r_b}\log\varrho(r_1)\frac{f'(r_1)f''(r_1)}{(1+f'(r_1)^2)^{3/2}}\mathrm{d}r_1=Y_0\left[\int_0^{r_b}\log r\frac{f'(r)f''(r)}{\sqrt{1+f'(r)^2}}\mathrm{d}r+\log r_b\left(1-\sqrt{1+f'(r_b)^2}\right)\right] \tag{A.34}$$

is a weighted integrated Gaussian curvature, expressed in terms of the parametrization $f(r)$. Additionally, for the symmetric case of a disclination positioned at the center, we have

$$\Gamma_D(r)=-\frac{Y_0}{6}\log\varrho(r) \tag{A.35}$$

which can be readily seen by setting $\mathbf{x}_D=0$ in (A.22) and (A.25). This demonstrates, for the normalization $Y_0=1$, the expressions for Γ_S and Γ_D in the main text.

A.5.2 Additional Transition shapes

We present additional evidence on the general applicability of the transition criterion $\Gamma_{S_0}=1/6$ by analyzing other shape families. In Figure A.5, we show how the different transition criteria perform for (a) "bell"-shapes $f(r)=\frac{\kappa}{3}(1-r^2)^{3/2}$ and (b) hyperboloids $f(r)=\kappa\sqrt{(1+r^2)}$. The former are an example of shapes with regions of both positive and negative Gaussian curvature occurring simultaneously. The latter represent a type of surface that is not restricted to $r_b\leq 1$, as it is unbounded. In contrast with the findings of the main text, the small-slope constant Ω^{ss} criterion here tends to underestimate r_c for given κ, while the constant Ω criterion tends to produce too large values for r_c. The deviations are again particularly strong for $\kappa\sim 1$, and for bell-shaped surfaces, $\Omega=const.$ unphysically predicts no r_c roots or double roots for some values of κ. Our $\Gamma_{S_0}=1/6$ criterion, on the other hand, performs exceedingly well for these shape families, as for all others that were tested.

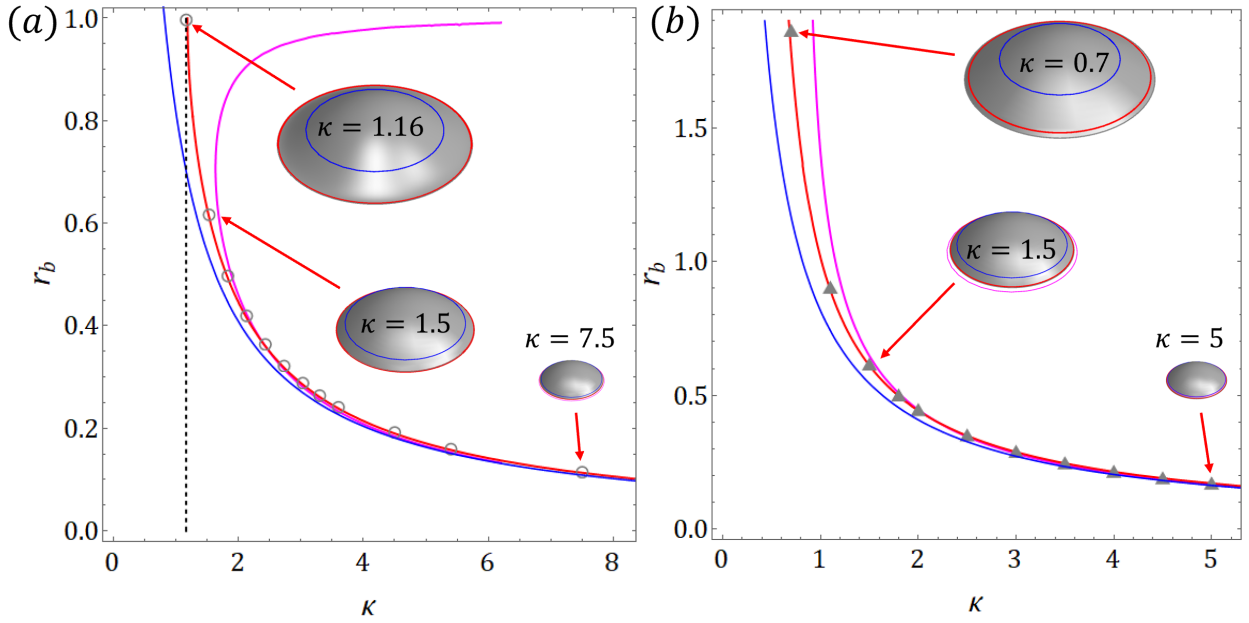

Figure A.5: Visualization of shapes at transition for (a) "bell-shaped" surfaces $f(r) = \frac{\kappa}{3}(1-r^2)^{3/2}$ and (b) hyperboloids $f(r) = \kappa\sqrt{(1+r^2)}$. Gray symbols are numerically obtained critical points from the rigorous covariant formalism; the solid blue line is the small-slope criterion $\Omega^{ss} = 2$; the solid magenta line is a line of constant $\Omega = \Omega_{c,\infty}$ and the solid red line is the non-local criterion $\Gamma_{S_0} = 1/6$. The dashed vertical black line indicates the minimal $\kappa_{c,min}$ for which transitions are observed. Gray caps illustrate the exact extent of caps for the κ values indicated, while the transition shapes determined from the approximate criteria are shown in blue and magenta; red lines indicate the extent predicted from $\Gamma_{S_0} = 1/6$

A.5.3 Comparison between continuum elasticity theories

The continuum mechanics formalism of Li, Zandi and Travesset [85] begins by describing the surface in question as a deformation from a flat or piecewise flat reference state, using the fully general, nonlinear elastic deformation tensor. This formalism quickly leads to analytically intractable results. Therefore, [85] proceeds to linearize the formalism in the limit of small $\eta = K_G - \overline{K}$ ($= -q_T$ in our nomenclature), an expansion particularly appropriate for our quantification of the disclination transition, as it reflects the compensation of curvature and defect placement at the heart of our work. A systematic leading-order expansion in η results in a linear elastic approach called the Incompatibility Framework (IF), that was shown in [85] to be in very good agreement with the full (numerical) discrete approach. The covariant Lagrangian Framework (LF) employed in the present work is a further approximation to IF that, for spherical surfaces, was already shown to be in excellent agreement with IF [85]. We demonstrate in the following that the use of LF is also appropriate in the present work, and that this is in particular true for shapes close to the disclination transition.

The elastic energy functionals of the IF and LF formalisms differ in two ways: (i) they are described by differing isotropic stress functions Γ, and (ii) the IF formalism of [85] contains an additional integral term beyond (A.24) for a no-stress boundary. However, this additional integral term is found to be of higher order in η for a defect-free surface, and to be explicitly zero for a surface with a central defect (following from $\sqrt{g}(0) = 0$). Thus, it can be neglected in all cases of interest in the present work and the energy functional is (A.24), where in IF the function $\Gamma = \Gamma^{LF}$ of the main text is replaced by $\Gamma^{IF} \equiv \Gamma^{LF} + \Gamma^{\epsilon}$. Thus, we have

$$F_{el}^{IF}(r_D) = \frac{1}{2Y_0}\int (\Gamma^{LF} + \Gamma^{\epsilon})^2 \mathrm{d}A \approx \frac{1}{2Y_0}\int ((\Gamma^{LF})^2 + 2\Gamma^{\epsilon}\Gamma^{LF})\mathrm{d}A \tag{A.36}$$

where the first term is what is already in the main text while the second term represents a correction which we will show is small in the context of present work (this then also shows that the neglecting of $\mathcal{O}((\Gamma^{\epsilon})^2)$ terms is consistent).

Now, the isotropic stresses Γ^{IF} and Γ^{LF} satisfy [85]

$$\Delta\Gamma^{IF} + 2K_G\Gamma^{IF} + (1+\nu_p)g^{rr}\nabla_r K_G \int_0^r \Gamma^{IF}\,\mathrm{d}A = Y_0 q_T, \quad \Delta\Gamma^{LF} = Y_0 q_T. \tag{A.37}$$

Substituting $\Gamma^{IF} = \Gamma^{LF} + \Gamma^{\epsilon}$, we subtract the two equations, obtaining

$$\Delta\Gamma^{\epsilon} + 2K_G\Gamma^{\epsilon} + (1+\nu_p)g^{rr}\nabla_r K_G \int_0^r \Gamma^{\epsilon}\,\mathrm{d}A = -2K_G\Gamma^{LF} - (1+\nu_p)g^{rr}\nabla_r K_G \int_0^r \Gamma^{LF}\,\mathrm{d}A \tag{A.38}$$

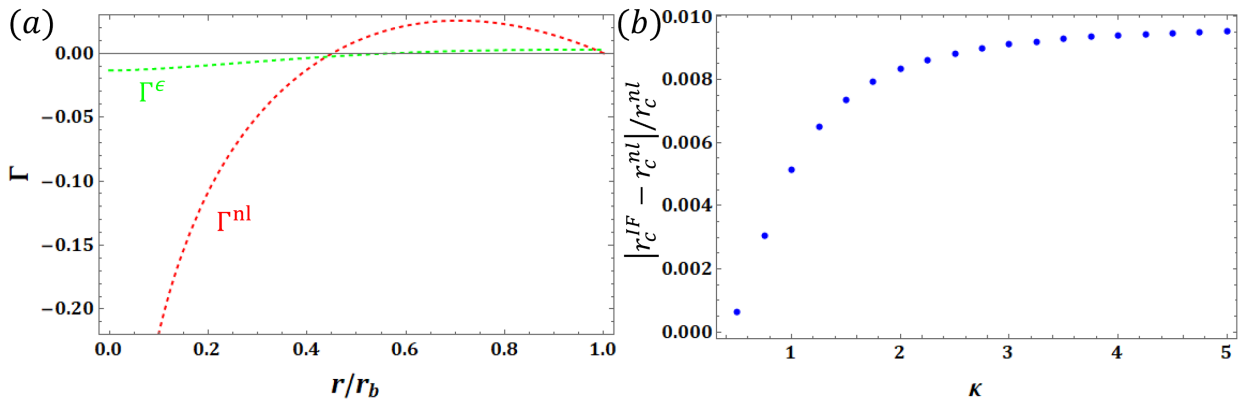

Figure A.6: (a) Γ^{ϵ}, Γ^{nl} for a prolate spheroid around transition; (b) Relative error between the critical cap extents obtained using the two formalisms is at most $\sim 1\%$ even for extremely prolate shapes

We have shown that the non-local Γ^{nl} is an accurate representation of Γ^{LF} around transition in the main text, i.e.

$$\Gamma^{LF} \approx \Gamma^{nl} \equiv \frac{1}{12} + \frac{1}{6}\log(r/r_b) + \frac{\Gamma_{S_0}}{2} - \Gamma_{S_0}\left(1 - \frac{r^2}{r_b^2}\right). \tag{A.39}$$

A few general observations are in order: Γ^{LF} for a disclination at the origin has a $\log(r)$ singularity, which a comparison of limiting terms shows is compensated in (A.38) by a much weaker $\Gamma^{\epsilon} \sim r^2\log(r)$, so that Γ^{ϵ} is negligible near the origin. Away from such a singularity, however, it is evident that $|\Gamma^{LF}| < 1/6 \ll 1$ around transition (since $\Gamma_{S_0} = -1/6$) and the dominant contribution to Γ^{ϵ} will be $\mathcal{O}(r_b^2 K_G \Gamma_{LF})$ compared with $\mathcal{O}(r_b^2 K_G)$ for Γ^{LF}. Therefore, the correction Γ^{ϵ} to Γ^{LF} is small everywhere for shapes around the disclination transition.

We exemplify this for the shape family of spheroids by analytically solving (A.38) using a small-slope approximation for the covariant Laplacian and replace $K \approx \kappa^2$, subject to a stress-free boundary such that $\int_0^{r_b}\Gamma^{\epsilon}\mathrm{d}A = 0$. The resulting solution for Γ^{ϵ} reads

$$\begin{aligned}\Gamma^{\epsilon} =& \frac{1}{2}\Gamma_{S_0}\left(1 + \frac{4}{\kappa^2 r_b^2} - \frac{2r^2}{r_b^2} - \frac{4J_0\left(\sqrt{2}\kappa r\right)}{\kappa^2 r_b^2\, {}_0\tilde{F}_1\left(;2;-\frac{1}{2}\kappa^2 r_b^2\right)}\right)\\ &+ \frac{1}{12}\left(-\frac{\sqrt{2}\pi J_0\left(\sqrt{2}\kappa r\right) G^{2,1}_{2,4}\left(\frac{\kappa^2 r_b^2}{2}\middle|\begin{matrix}1, \frac{1}{2}\\ 1, 1, 0, \frac{1}{2}\end{matrix}\right)}{\kappa r_b J_1\left(\sqrt{2}\kappa r_b\right)} + \pi Y_0\left(\sqrt{2}\kappa r\right) - 2\log\left(\frac{r}{r_b}\right) - 1\right),\end{aligned} \tag{A.40}$$

where J_n and Y_n are the Bessel functions of the first and second kinds respectively, ${}_0\tilde{F}_1$ is the Regularized Hypergeometric function and $G^{m,n}_{p,q}$ is the MeijerG function. Near the origin, $\Gamma^{\epsilon} \sim r^2\log(r)$ and is not

singular whereas $\Gamma^{nl} \sim \Gamma^{LF} \sim \log(r)$, as shown in Fig. A.6(a).

Inserting (A.40) into (A.36), we numerically find the critical cap extent such that $F_{el}^{IF}(0) = F_{el}^{IF}(r_c)$ and compare the relative error with the roots obtained from our $\Gamma_{S_0} = -1/6$ criterion in the main text for the shape family of spheroids in Fig A.6(b). The relative errors between the critical r_c's indeed prove small (the numerical closeness of the errors to Fig. 4b of the main text is coincidental—the errors have the opposite sign relative to the rigorous LF values), and these conclusions are valid, by the general arguments above, for the entire class of stress-free rotationally symmetric surfaces. Therefore, the LF formalism is an accurate description of deformations around transition within the assumption of linear elasticity.

Appendix B

Predicting the Characteristics of Defect Transitions on Curved Surfaces

The energetically optimal position of lattice defects on intrinsically curved surfaces is a complex function of shape parameters. For open surfaces, a simple condition predicts the critical size for which a central disclination yields lower energy than a boundary disclination. In practice, this transition is modified by activation energies or more favorable intermediate defect positions. Here[1] it is shown that these transition characteristics (continuous or discontinuous, first or second order) can also be inferred from analytical, general criteria evaluated from the surface shape. A universal scale of activation energy is found, and the criterion is generalized to predict transition order as symmetries such as that of the shape are broken. The results give practical insight into structural transitions to disorder in many cellular materials of technological and biological importance.

B.1 Introduction

A plethora of mechanical systems in nature and technological applications consist of interconnected units that form a thin shell or surface [16, 51, 80, 105, 116, 144, 154]. The shape of these manifolds informs their function, and often intrinsic (Gaussian) curvature K_G is required. Closed surfaces like viral capsids [87, 152] or molecular cages [31] have received much attention, but maybe even more common are open surfaces with a boundary, whether they are curved arrangements of microlenses [33], the faceted eyes of insects [78], or topographically warped sheets of graphene or other metamaterials [126, 128, 153, 171]. Capsids only become closed surfaces through assembly from open-surface states [129, 130], and strategies to disrupt the assembly through, e.g. elastic frustration [104], can be a powerful therapeutic tool [79] which therefore need to be understood in detail. As is well known, non-zero K_G on a lattice manifold is incompatible with a defect-free lattice; Euler's theorem applied to lattices translates into a statement about the topological charge Q, which

[1] This Appendix is adapted from Agarwal and Hilgenfeldt [3]

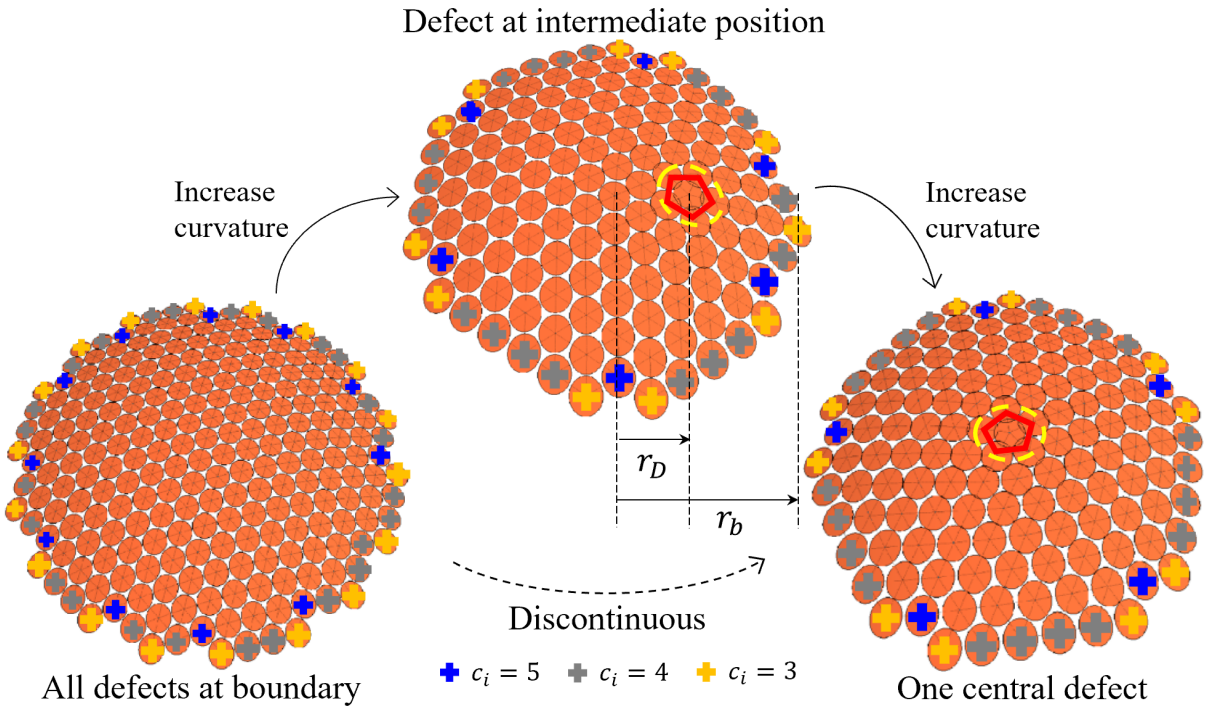

Figure B.1: The elastic ground state of a weakly curved surface has all defects decorated at the boundary; upon increasing curvature or extent r_b, a disclination at the central apex eventually becomes favorable. This state is reached either continuously via intermediate defect positions r_D (upper), or discontinuously (lower). The path taken can be predicted by properties of surface shape, such as the apical curvature or degree of rotational asymmetry.

on a triangulated lattice must be equal to

$$Q = \sum_{i=1}^{V} q_i = 6\chi, \tag{B.1}$$

where $q_i = 6 - c_i$ is the departure of the coordination number c_i of the ith vertex from the ideal coordination number of a planar triangular lattice, and χ is the Euler characteristic. The most ubiquitous example of this is the presence of (a minimum of) 12 five-fold disclination defects on a soccer ball (with $\chi = 2$). Considerable work in the past years has focused not on the requirement of the total charge of defects, but on their positioning on the manifold [12, 13, 21, 25, 27, 60, 84, 86, 165]. This is particularly relevant for open surfaces, as here the magnitude of curvature controls the number of relevant defects visible on the bulk of the manifold: while Euler's theorem with $\chi = 1$ still requires at least 6 disclinations, in a surface of small curvature they can be accommodated by the lattice at the boundary with minimal elastic energy penalty, so that the bulk of the surface remains defect-free. Only for sufficiently large curvature does it become

energetically favorable for a single disclination to leave the boundary and migrate to the bulk (cf. Fig. B.1). By extension, surfaces of varying Gaussian curvature have been shown to be preferentially populated by different numbers of defects [22, 25, 75].

For practical applications, it is highly desirable to have a unified description of this transition from a regular open surface to one with minimal disclination disorder. While local or integral Gaussian curvature can hint at preferred defect positions [13, 75], very recently a general criterion was found that is applicable for a great variety of open-cap shape families: rather than a particular local value of K_G or the value of the integrated Gaussian curvature over the entire surface, a particular *weighted integral* of K_G needs to exceed a universal threshold in order for the defect migration to be energetically favorable [2]. For a certain surface shape, this translates to a critical size (cap extent) beyond which the elastic energy for the surface with a disclination at the apex of the cap is lower than that for the surface with all defects at the boundary (cf. Fig. B.1).

However, what kind of transition is observed in practice upon increasing cap size depends not only on which configuration yields lower energy, but on the shape of the energy landscape: a transition may proceed continuously through intermediate defect positions representing energy minima, or discontinuously because an activation energy (energy barrier) needs to be overcome. These different *characteristics* of transition are illustrated in Fig. B.1, and have previously been studied numerically for the special case of spherical shells [84, 86], where an analogy to first- and second-order phase transitions has been made. The possibility of symmetry-breaking ground states in continuous transitions is significant, as this alters the predictions of observable defect patterns. Conversely, a discontinuous transition ensures that symmetric defect positioning is the only realizable option. In the context of invertebrate eyes, asymmetric placement of defects would disrupt optical regularity [58]. While many atomistic simulations allow for asymmetric equilibrium shell shapes, e.g., *en masse* assembly of virus capsids [63, 65, 123] or, more generally, protein cages [122], often the initial building block sub-units themselves are assumed to be symmetric.

In the present work, we show that these transition characteristics can be reliably extracted for general shapes, via simple criteria involving the shape of the surfaces. Our present findings are applicable to a great variety of shapes and reveal universal properties of the energy landscape around transition.

In Sec. B.2 we sketch our rigorous theoretical framework for quantifying elastic energy on surfaces of revolution, and review results on the location of the transition in parameter space. Section B.3 derives simple analytical criteria to determine the continuous or discontinuous character of transitions, reveals universal properties in the energetic structure of states surrounding these transitions, and discusses how these energy landscapes shift when breaking the continuous rotational symmetry of the manifold's mechanical properties.

Section B.4 provides discussion and conclusions.

B.2 Theoretical background

In this study, we explore single disclination transition characteristics on a large set of bounded surfaces of revolution (unless stated otherwise) using linear elastic continuum theory. The surface geometry is imposed, i.e, we disregard deformation degrees of freedom of the surface, whether elastic or through buckling, though these may play a role in other contexts [87, 112, 152]. We focus on the transition from an energetically favorable defect-free surface (more precisely, all disclinations are located at the boundary) to one with a single disclination in the bulk. While the presence of dislocations can strongly affect such transitions [12, 13], for large defect core energies dislocation distributions are prohibitively expensive energetically, while the single disclination provides a well-defined energy penalty scaling with the size of the surface [149]. Going beyond previous work [2], we shall allow the disclination to occupy an arbitrary position on the surface in order to probe the energy landscape.

B.2.1 Full covariant formalism

We follow the covariant formalism of [25, 60] with stress-free boundary conditions. The great accuracy of this approach for the present type of problem, and its relation to other formalisms detailed in [85], have been discussed in [2]. The elastic energy for an arbitrary disclination position $\mathbf{x}_D$ on a manifold $\mathbb{P}$ reads

$$F_{\mathrm{el}}(\mathbf{x}_D) = \frac{1}{2Y}\int \Gamma^2(\mathbf{x},\mathbf{x}_D)\mathrm{d}\mathbf{x}, \tag{B.2}$$

where the isotropic stress Γ can be decomposed as

$$\Gamma(\mathbf{x},\mathbf{x}_D) = -\Gamma_D(\mathbf{x},\mathbf{x}_D) - \Gamma_s(\mathbf{x}) + U(\mathbf{x},\mathbf{x}_D), \tag{B.3}$$

and

$$\Gamma_D(\mathbf{x},\mathbf{x}_D) = -\frac{\pi}{3}YG_L(\mathbf{x},\mathbf{x}_D), \tag{B.4a}$$

$$\Gamma_S(\mathbf{x}) = Y\int K_G(\mathbf{y})G_L(\mathbf{x},\mathbf{y})\mathrm{d}\mathbf{y}, \tag{B.4b}$$

where

$$G_L(\mathbf{x};\mathbf{x}_D) = \frac{1}{2\pi}\log\left|\frac{z(\mathbf{x})-z(\mathbf{x}_D)}{1-z(\mathbf{x})\overline{z(\mathbf{x}_D)}}\right| \tag{B.5}$$

is the Green's function of the covariant Laplace operator on $\mathbb{P}$ and $z(\mathbf{x}) = \varrho(r)e^{i\phi}$ is a point on the unit disk on the complex plane while $\varrho(r)$ is the conformal radius of a map from the surface onto the unit disk. Here, (B.4a) is the contribution due to a disclination positioned arbitrarily at $\mathbf{x}_D$ while (B.4b) captures the screening effect of Gaussian curvature $K_G(\mathbf{x})$. The harmonic term $U(\mathbf{x}, \mathbf{x}_D)$ is determined by the boundary conditions at the rim of the surface; the sum of these three contributions is a fine balance of different effects. Balancing Γ_D and Γ_S represents a form of local curvature argument, where local Gaussian curvature compensates for a defect charge, while $U(\mathbf{x}, \mathbf{x}_D)$ introduces non-trivial boundary-dependent modifications. Going beyond [60], in the present work we perform the explicit computation of the harmonic function U on the manifold $\mathbb{P}$ for arbitrary positioning of a disclination; one finds

$$U(\mathbf{x}, \mathbf{x}_D) = -Y \int \mathrm{d}\mathbf{y} H(\mathbf{x}, \mathbf{y}) \left(\frac{\pi}{3} \delta(\mathbf{y}, \mathbf{x}_D) - K_G(\mathbf{y}) \right), \tag{B.6}$$

where the harmonic kernel $H(\mathbf{x})$ is given by [150]:

$$H(\mathbf{x}, \mathbf{y}) = -\frac{1}{2\pi} f_0(\varrho_y) - \sum_{n \geq 1} \frac{1}{\pi} \varrho_x^n \varrho_y^n \cos n(\phi_y - \phi_x) f_n(\varrho_y) \tag{B.7}$$

This formalism relies on being able to explicitly find a conformal mapping from $\mathbb{P}$ onto the unit disk where points $\mathbf{x}, \mathbf{y}$ on the surface are mapped to complex numbers with moduli ϱ_x, ϱ_y and arguments ϕ_x, ϕ_y, respectively (see Section B.5 for details and the functional forms of ϱ, f_n). The first term of (B.7) is a radially symmetric contribution due to the boundary conditions while the infinite sum acknowledges asymmetry introduced by, e.g., an intermediate position of the disclination. Accordingly, (B.6) can now be split into two terms: $U(\mathbf{x}, \mathbf{x}_D) = U_K(\mathbf{x}) + U_D(\mathbf{x}, \mathbf{x}_D)$, corresponding to the boundary contributions due to Gaussian curvature and the non-trivial disclination singularity, respectively, viz.

$$U_K(\mathbf{x}) = Y \int \mathrm{d}\mathbf{y} H(\mathbf{x}, \mathbf{y}) K_G(\mathbf{y}), \tag{B.8a}$$

$$U_D(\mathbf{x}, \mathbf{x}_D) = \frac{f_0(\varrho_D)}{6} + \sum_{n \geq 1} \frac{(\varrho \varrho_D)^n}{3} f_n(\varrho_D) \cos n(\phi - \phi_D). \tag{B.8b}$$

U_K is a constant on surfaces of revolution, while $U_D(\mathbf{x}, \mathbf{x}_D)$, which was not taken into account in earlier work [60], has to be computed with the series truncated at a large but finite n; in general both computations are executed numerically. Note that the infinite sum of (B.8b) vanishes for a disclination at the boundary (where $f_{n \geq 1} = 0$) as well as for a disclination at the center (where $\varrho_D = 0$). For intermediate positions, as considered here, this term is generally non-zero.

Taking (B.2) together with (B.3) we have derived a rigorous covariant expression for the total energy that can be evaluated for arbitrary positions of the disclination. This reads

$$F_{\mathrm{el}}(\mathbf{x}_D) = \frac{1}{2Y} \int \left[(U_D - \Gamma_D) + (U_K - \Gamma_S) \right]^2 \mathrm{d}\mathbf{x} \,, \tag{B.9}$$

indicating that the energy penalty can be interpreted as a combination of mismatches between topological charges and harmonic contributions from disclinations and Gaussian curvature.

The difference of F_{el} for a configuration with one defect at arbitrary $\mathbf{x}_D$ and F_{el} for a configuration with only boundary defects (defect position $\mathbf{x}_D = \mathbf{x}_b$) is more explicitly

$$\Delta F_{\mathrm{el}}(\mathbf{x}_D) = \frac{1}{2Y} \int (U_D - \Gamma_D) \left[(U_D - \Gamma_D) + 2(U_K - \Gamma_S) \right] \mathrm{d}\mathbf{x}, \tag{B.10}$$

because only U_D and Γ_D depend on $\mathbf{x}_D$. Equation (B.10) is the generalization of the results of [2] to arbitrary disclination position $\mathbf{x}_D$. For the portion of the present work that considers radially symmetric surfaces, we can write $\Delta F_{\mathrm{el}}(r_D)$. In the following, we scale out the (constant) material modulus, setting $Y = 1$.

B.2.2 Critical cap extent

The formalism above simplifies if the defect position is the apex of an axisymmetric cap surface ($\mathbf{x}_D = 0$), which eliminates all angular dependences and makes U_D and U_K straight surface averages of Γ_D and Γ_S, respectively. For a given surface shape, a critical cap radius $r_b = r_c$ can then be defined as the extent of the surface for which $\Delta F_{\mathrm{el}}(0) = 0$ according to (B.10). In [2] it was shown that, rather than numerically evaluating (B.10), a simple criterion predicts r_c with great accuracy, namely,

$$\Gamma_S(0) \equiv \int_0^{r_c} K_G(r) \log \varrho(r) \sqrt{g} \, \mathrm{d}r = -\Gamma_{S_0} \,, \tag{B.11}$$

where $\Gamma_{S_0} \equiv 1/6$ is a universal constant. Thus, the Gaussian curvature weighted with the characteristic singularity $\log \varrho(r)$ of the defect stress governs the transition in parameter space. Eq. (B.11) yields $r_b = r_c$ as a function of shape parameters of the surface. In deriving this analytical criterion, an approximation was pursued that uses direct leading-order Taylor expansions of $\Gamma_D(r)$ and $g(r)$ around $r = 0$, i.e., the small-slope approximations

$$\Gamma_D^{ss}(r, 0) = -\frac{1}{6} \log (r/r_b) \,, \quad \sqrt{g}^{ss} = r, \tag{B.12}$$

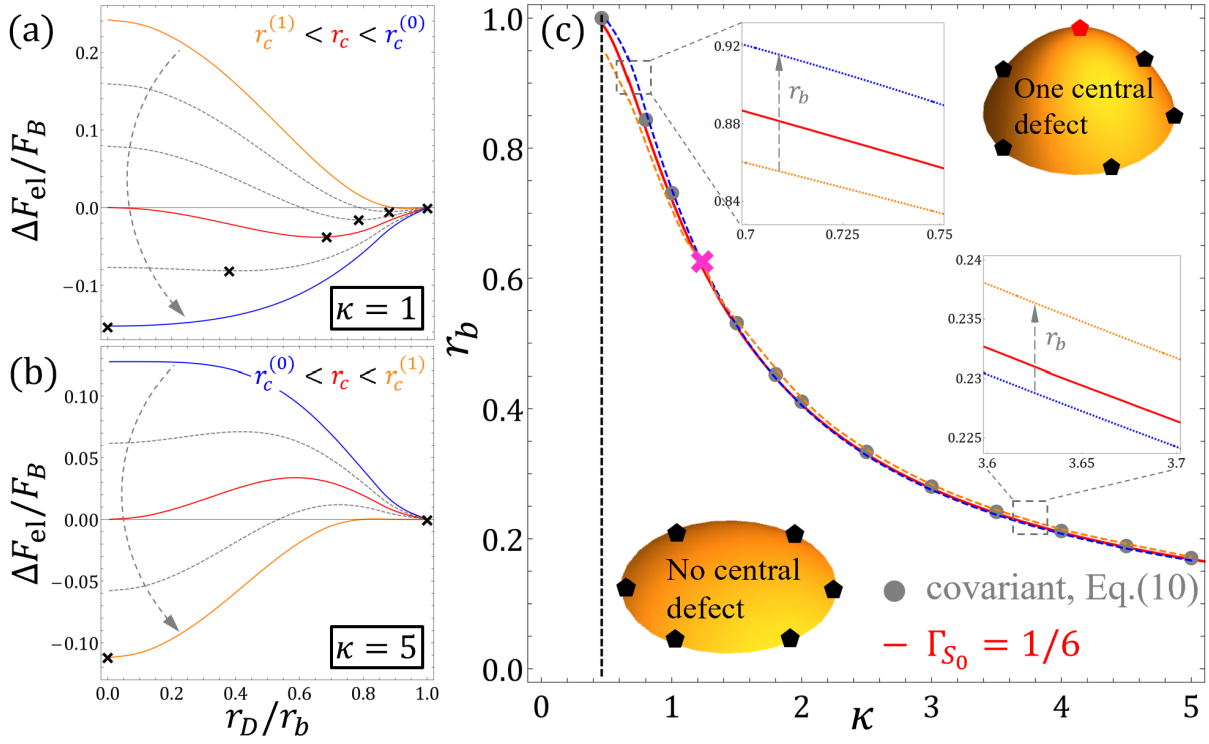

Figure B.2: Normalized energy difference $\Delta F_{\rm el}/F_B$ as a function of normalized defect position r_D/r_b (varying cap extent r_b) resulting from the full covariant formalism for (a) Sphere ($\kappa = 1$): the defect moves continuously from the boundary to the apex as r_b is increased (the optimum intermediate positions are marked by crosses) — it starts migrating at $r_b = r_c^{(1)}$ (orange curve) and reaches the center at $r_b = r_c^{(0)}$ (blue curve) (cf. [84, 86]); (b) Prolate spheroid ($\kappa = 5$): the defect migration is discontinuous and occurs abruptly once $r_b \geq r_c^{(1)}$ (orange curve). (c) Red curve is the boundary marking transition in the shape family of spheroids reproduced from [2], while gray dots are numerically obtained roots using (B.10). The orange-dashed $r_c^{(1)}$ and blue-dashed $r_c^{(0)}$ curves flanking the nominal red transition curve intersect it at a higher-order critical point $\kappa_h \approx 1.3$ (indicated by the magenta cross) and switch numerical order. Insets show a close-up of the curves for two distinct regimes of κ, on either side of the higher-order critical point.

but uses a non-local approximation for $\Gamma_S(r)$ that matches the values of this function at $r = 0$ and the boundary position $r = r_b$, i.e.,

$$\Gamma_S^{nl}(r) = \Gamma_S(0)\left(1 - r^2/r_b^2\right), \tag{B.13}$$

where $\Gamma_S(0)$ is explicitly given by the integral in (B.11), rather than using the small-slope expansion

$$\Gamma_S^{ss}(r) = -\frac{1}{4}K_G(0)r_b^2\left(1 - r^2/r_b^2\right). \tag{B.14}$$

While the use of (B.11) allows for accurate prediction of the transition in parameter space, superior to the small-slope approximation [2], in this work we shall show that in order to predict the characteristics of the transition a further improvement in analytical theory is needed.

B.3 Characteristics of the Transition

We parametrize general surfaces of revolution as $z = Z/L_r = f(r)$ with a radial length scale L_r, e.g. the equatorial radius of a spheroid. The dimensionless center curvature $f''(0) \equiv \kappa$ then represents a ratio of axial to radial length scales and is our primary parameter to vary shape within a shape family. For example, $f = \kappa\sqrt{1 \pm r^2}$ describes spheroids $(-)$ and hyperboloids $(+)$ of various aspect ratio. We investigated many different shape families [2], but confine ourselves to cap shapes with unique $z(r)$. For central defects ($r_D = 0$) on spheroids, Fig. B.2c shows that the approximation (B.11) (red line) predicts the transition to a central defect extremely accurately, compared with the numerical computation of $\Delta F_{\rm el}(0) = 0$ from (B.10) (symbols). Caps of extent $r_b > r_c(\kappa)$ have lower energy with the disclination at the apex, while smaller caps have lower energy with all defects at the boundary. As pointed out above, this picture is complicated by the possibility of energy barriers or energy minima for intermediate disclination positions $0 < r_D < r_b$.

B.3.1 Covariant formalism—effect of shape on secondary transition characteristics

The example of spheroids illustrates both of these characteristics of continuous and discontinuous transitions: Fig. B.2a plots the full covariant $\Delta F_{\rm el}$ vs. defect position r_D/r_b for spherical caps ($\kappa = 1$), varying the cap extent r_b through the critical value r_c. Here and in the following, we normalize energy differences by an elastic background energy scale

$$F_B \equiv \pi\kappa^4 r_b^6/384, \tag{B.15}$$

whose value is obtained by inserting the small-slope (B.14) and $U_K = (1/A)\int \Gamma_S^{ss} dA = -(1/8)K_G(0)r_b^2$ into (B.2) for a defect free surface, i.e. $\Gamma_D = U_D = 0$, and noting $K_G(0) = \kappa^2$.

The red line in Fig. B.2a (for $r_b = r_c$) shows that, while $\Delta F_{\rm el}(0) = 0$, the energy is even lower for an intermediate defect position. Increasing r_b smoothly moves this optimum disclination position from the boundary to the apex (crosses). This process begins at $r_b = r_c^{(1)} < r_c$ determined by $\Delta F'_{\rm el}(r_D = r_b) = 0$ (orange curve) and ends at $r_b = r_c^{(0)} > r_c$ determined by $\Delta F'_{\rm el}(r_D = 0) = 0$ (blue curve). Outside of this interval of r_b values, $\Delta F_{\rm el}(r_D)$ is monotonic. These results are consistent with predictions from the covariant formalism and numerical simulations of [84, 86] — spherical caps show a "second-order" disorder transition, with defect positions adjusting continuously.

By contrast, Fig. B.2b displays the energy landscapes for a prolate spheroid of $\kappa = 5$. At $r_b = r_c$, the critical energy curve now shows a maximum, and this remains true for all r_b in an interval $r_c^{(0)} < r_b < r_c^{(1)}$, where the $r_c^{(i)}$ are defined as above, but have switched numerical order. As a result, upon increasing r_b, an energy barrier prevents the disclination at the boundary from moving until $r_b > r_c^{(1)} > r_c$, when the defect abruptly jumps to the apex. This discontinuous transition thus requires a larger cap extent than r_c or equivalently "overcharging" beyond the $q = 1$ single disclination [13]. In Fig. B.2c, we plot the κ-dependent values of $r_c^{(0)}$ (blue-dashed) and $r_c^{(1)}$ (orange-dashed) for the entire family of spheroidal caps. They flank the red line of the nominal transition criterion $\Delta F_{\rm el}(0) = 0$ closely and intersect it at a higher-order critical point where $r_c^{(0)}$ and $r_c^{(1)}$ switch order and, therefore, continuous transitions become discontinuous. The range of cap sizes over which the transition character manifests itself (for a given κ) is relatively small, as illustrated in the two insets of Fig. B.2(c).

Can we observe such features more generally, going beyond spheroids? In Fig. B.3, we take a closer look at the shape and scale of the energy landscape at critical extent $r_b = r_c$ for four different shape families, varying $\kappa = f''(0)$ for the first three and the fourth apical derivative $\lambda = f^{(4)}(0)$ (keeping κ fixed) for the last one. Figure B.3a again illustrates the transition from continuous to discontinuous in spheroids, and pinpoints the higher-order critical point at $\kappa \approx 1.3$. Hyperboloids (a shape family with potentially infinite cap extent, Fig. B.3b) and a family of "bell-shaped" surfaces whose Gaussian curvature changes sign on the surface (Fig. B.3c), by contrast, never show continuous transitions. For large κ, however, the normalized energy difference $\Delta F_{\rm el}/F_B$ for all shapes approaches a common energy barrier. Figure B.3d shows that the transition character can be changed at constant κ by changing the value of the fourth apical derivative λ.

This is an indication that higher apical derivatives of the surface shape play a central role here. Indeed, when solving this problem for the unique surface without higher derivatives (the paraboloid), the result accurately depicts the common asymptotic shape of the energy landscape (solid lines in Fig. B.3).

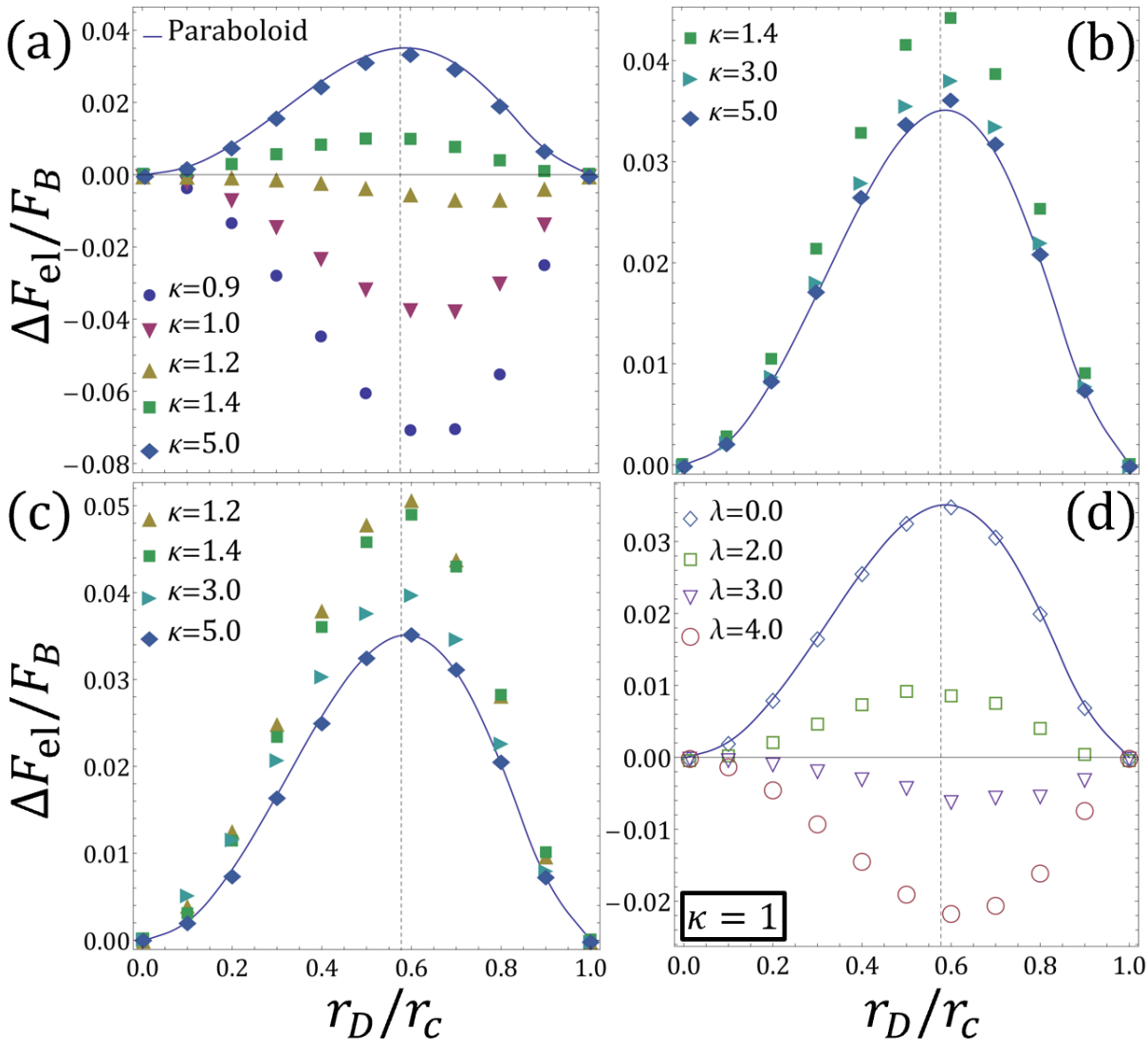

Figure B.3: Normalized energy difference $\Delta F_{\rm el}/F_B$ at transition ($r_b = r_c$) as a function of normalized defect position r_D/r_c (varying κ) for (a) Spheroid: $f(r) = \kappa\sqrt{1-r^2}$, (b) Hyperboloid: $f(r) = \kappa\sqrt{1+r^2}$, (c) "Bell-shaped" cap: $f(r) = \kappa/3(1-r^2)^{3/2}$ and (varying λ) for (d) a prototypical higher-order surface: $f(r) = \kappa r^2/2 + \lambda r^4/24$; the character of the transition is continuous for $\lambda/\kappa \gtrsim 3$. The large κ asymptote for all shapes has a common energy barrier – identical to that of a Paraboloid (indicated by solid curves). The location of the intermediate extremum is obtained by solving (B.20) and is approximately $r_{D,m} = r_c/\sqrt{3}$ (indicated by dashed vertical lines).

The numerical integration of (B.10) yields these results, but gives little physical insight. When do we expect continuous vs. discontinuous transitions? Is the scale of the energy landscape (a few percent of the normalization value F_B) indeed universal, as suggested by these examples? Exactly which features of the surface are determinants of the transition character? To answer these questions, we turn to analytical approximations.

B.3.2 Analytical theory: non-local approximation

As detailed in section B.2.2, the accurate prediction of the transition line in Fig. B.2c was not possible with a small-slope Taylor expansion, but needed the non-local improvement (B.13) [2]. Using either Γ_S^{ss} or Γ_S^{nl}, and the resulting changes in U_K, while maintaining the approximations (B.12), $\Delta F_{\mathrm{el}}(r_D)$ becomes analytically tractable. Consistent with previous work [84, 86], Figure B.4a reproduces the continuous structure of the transition for r_b around r_c for spherical caps according to the rigorous numerical computation of the covariant theory, whereas the small-slope approximation in Figure B.4b predicts a first-order transition. Intriguingly, the non-local approximation in Figure B.4c likewise does not produce any secondary characteristics at all — the energy difference at transition is flat, and monotonic at every other value of r_b. Thus, even though the non-local approximation reproduces the spread of energy values more accurately than the small-slope model, it does not probe the shape properties of the surface that are responsible for the order of the transition.

We now describe a minimal model that captures the dominant effects of the secondary transition character. Noting that a more accurate representation of the intrinsic isotropic stress $\Gamma_S(r)$ was crucial for predicting the transition location, we improve further on the approximation (B.13): in addition to matching the function value and first derivative at $r = 0$ and function value at $r = r_b$, we now require a match of the second derivative at the apex. By symmetry, this requires a fourth-order polynomial in r, namely,

$$\begin{aligned}\Gamma_S^{nl}(r) = &-\frac{\Gamma_S''(0) r_b^2}{2}\left(1-\frac{r^2}{r_b^2}\right)\\ &+\left(\Gamma_S(0)+\frac{\Gamma_S''(0) r_b^2}{2}\right)\left(1-\frac{r^4}{r_b^4}\right),\end{aligned} \tag{B.16}$$

with the full rigorous expressions

$$\Gamma_S(0) \equiv \int_0^{r_b} K_G(r)\log\varrho(r)\sqrt{g}\,\mathrm{d}r,\ \Gamma_S''(0) = \frac{K_G(0)}{2} = \frac{\kappa^2}{2}\,. \tag{B.17}$$

We use (B.4a) and (B.5) for arbitrary defect position $\mathbf{x}_D$ but employ the small-slope $\varrho^{ss}(r) = r/r_b$ and $\sqrt{g}^{ss} = r$. Inserting these into (B.10) and (B.8), the energy integral can be executed analytically (see

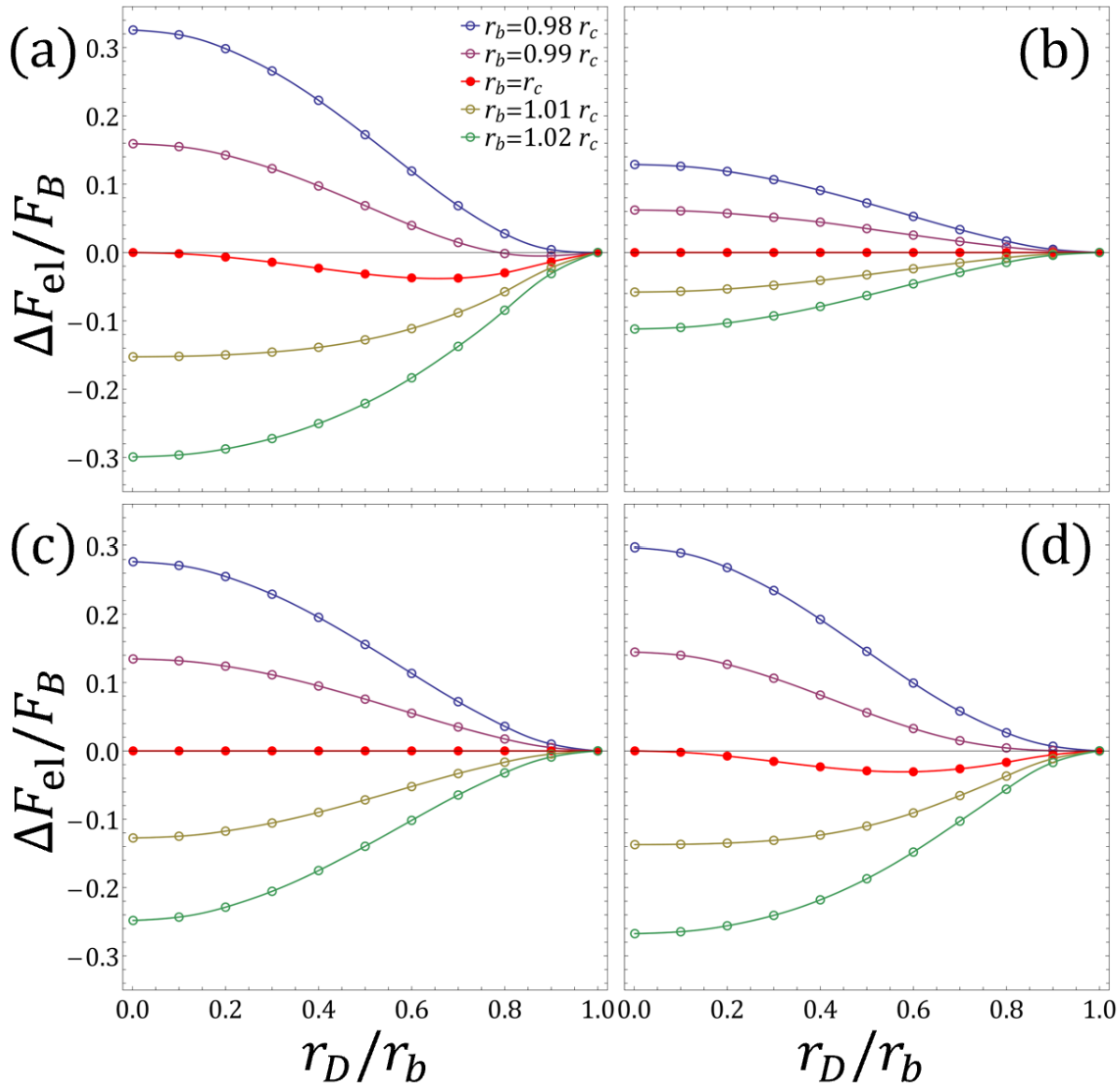

Figure B.4: Normalized energy difference $\Delta F_{\rm el}/F_B$ for a sphere ($\kappa = 1$), comparing different approaches (varying r_b around r_c): (a) full covariant Eq. (B.10) (numerical) (cf. [84, 86]), (b) small-slope (cf. [13, 86]), (c) non-local formalism from [2], (d) non-local formalism of Eq. (B.18). Only the latter, non-local analytical approach captures the characteristics of the transition.

Section B.5 for details) and results in the following closed form expression:

$$\Delta F_{\mathrm{el}}(r_D) = \frac{\pi r_b^2}{864}\left(1-\frac{r_D^2}{r_b^2}\right)^2\left[3+8\left(2+\frac{r_D^2}{r_b^2}\right)\Gamma_S(0) - \left(1-4\frac{r_D^2}{r_b^2}\right)\frac{\kappa^2 r_b^2}{2}\right]. \tag{B.18}$$

The transition threshold is defined as the extent r_b at which $\Delta F_{\mathrm{el}}(0) = 0$ and (B.18) results in

$$\Gamma_S(0) = -3/16 + \kappa^2 r_c^2/32 \tag{B.19}$$

as the transition criterion within this level of approximation. The extremum of the energy landscape is obtained from

$$\Delta F'_{\mathrm{el}}(r_D) = \frac{\pi r_D}{72}\left(\frac{r_D^2}{r_b^2}-1\right)\left[1+4\left(1+\frac{r_D^2}{r_b^2}\right)\Gamma_S(0) - \left(1-2\frac{r_D^2}{r_b^2}\right)\frac{\kappa^2}{2}r_b^2\right] \tag{B.20}$$

by setting $\Delta F'_{\mathrm{el}}(r_D)|_{r_b=r_c} = 0$. Inserting the transition criterion (B.19) leads to a straightforward non-trivial solution for the position of the minimum or maximum of the energy landscape $r_{D,m} = r_c/\sqrt{3}$. This result is indicated by dashed vertical lines in Fig. B.3 and in good agreement for the vast majority of shapes. Inserting $r_{D,m}$ together with (B.19) into (B.18) yields the scale of the secondary structure. Normalizing by F_B, one obtains

$$\Delta F_{\mathrm{el}}^{\mathrm{sec}}/F_B = \frac{4}{81\kappa^4 r_c^4}\left(-2+3\kappa^2 r_c^2\right) \tag{B.21}$$

This rigorously shows why a small-slope formalism is incapable of predicting secondary transition structure (since $\kappa^2 r_c^2 = 2/3$ in this approximation [13]). Further analytical progress can be made by determining $r_c(\kappa)$ at transition within the present approximation. By symmetry, the large κ expansion of r_c on surfaces of revolution is $r_c = a/\kappa + b/\kappa^3 + \dots$ (cf. [2]). Inserting this into (B.19) and Taylor-expanding both sides for $\kappa \to \infty$ allows us to solve for the coefficients a, b, ..., order-wise. With the definition of $\Gamma_S(0)$, this reads

$$\begin{aligned}\Gamma_S(0) =& 1-\sqrt{1+a^2}+\log\left[\frac{\left(1+\sqrt{1+a^2}\right)}{2}\right]+\frac{b(1-\sqrt{a^2+1})}{a\kappa^2} \\ &+\frac{\left(-a^4+a^2-2\sqrt{a^2+1}+2\right)(\lambda/\kappa)}{18\sqrt{a^2+1}\kappa^2}+\dots\end{aligned} \tag{B.22}$$

Finally, expanding the RHS of (B.19) and equating with (B.22) we obtain $a \approx 0.844$, $b \approx -0.042\lambda/\kappa$. Note that a generic surface (with one dominant radial length scale) will have $\lambda = \mathcal{O}(\kappa)$ and $b = \mathcal{O}(1)$. Inserting

into a large κ expansion of (B.21), we obtain:

$$\begin{aligned}\Delta F_{\text{el}}^{sec}/F_B &= \frac{4(-2+3a^2)}{81a^4} + \frac{8(4-3a^2)b}{81a^5\kappa^2} + \dots \\ &\approx 0.0135 - 0.018\frac{\lambda}{\kappa^3} + \dots \end{aligned} \tag{B.23}$$

This suggests a universal scale for the energy barrier at transition for surfaces with large central curvature, consistent with the observations of Fig. B.3. For $\kappa \to \infty$, higher derivatives are negligible and the behavior mimics that of a paraboloid. Furthermore, the result predicts a change from an energy maximum to a minimum at transition (a higher-order critical point), only if the quantity λ/κ is positive. Note that for spheroids $\lambda/\kappa = 3 > 0$, whereas for the hyperboloids or "bell" shapes of Fig. B.3bc $\lambda/\kappa = -3 < 0$. Likewise, increasing λ from zero should lead to the development of an energy minimum and thus a continuous transition, as shown in Fig. B.3d.

The formalism outlined here also settles the question of the range of the secondary structure effects described in Sec. B.3.1 i.e., the values of $r_c^{(0)}$ and $r_c^{(1)}$. Using the defining criteria $\Delta F'_{\text{el}}(r_D = 0)|_{r_b = r_c^{(0)}} = 0$ and $\Delta F'_{\text{el}}(r_D = r_b)|_{r_b = r_c^{(1)}} = 0$ in (B.20) results in the following implicit equations:

$$\Gamma_S(0) = -\frac{1}{8} + \frac{(\kappa r_c^{(0)})^2}{16}, \quad \Gamma_S(0) = -\frac{1}{4} + \frac{(\kappa r_c^{(1)})^2}{8}, \tag{B.24}$$

respectively. As before, we insert the large κ expansion $r_c^{(i)} = a/\kappa + b/\kappa^3 + \dots$, Taylor expand and determine the respective coefficients $a, b, \dots$ to finally obtain

$$(r_c^{(1)} - r_c^{(0)})/r_c \approx 0.038 - 0.07\lambda/\kappa^3 \tag{B.25}$$

This suggests that the range of the secondary features is about 4% relative to the critical r_c for surfaces with large central curvature — again, the large κ limit universally asymptotes to that of a paraboloid. On the other hand, shapes with small κ could have larger ranges, but are not accurately described by this approach. Empirically, we see for all shape families analyzed that the range of secondary characteristics remains of this order up to the smallest κ consistent with unique $f(r)$ shapes.

All of these predictions are in complete qualitative agreement with the numerical computations, while quantitative discrepancies in $\Delta F_{\text{el}}^{\text{sec}}$ can be systematically improved upon employing higher order approximations of the type that also improve the predictive error of $r_c(\kappa)$ [2]. Matching the third derivative of the

metric $\sqrt{g}$ at $r = 0$ yields

$$\sqrt{g} = r + \frac{\kappa^2}{2} r^3. \tag{B.26}$$

With only this modification (Γ_D remains unchanged from (B.12) to permit analytical evaluation of the integrals) we go through the same steps outlined above and, while the explicit expressions are more complicated, we obtain a slightly different transition criterion $r_c \approx 0.829/\kappa - 0.039(\lambda/\kappa)/\kappa^3$ and an altered secondary energy,

$$\Delta F_{\mathrm{el}}^{\mathrm{sec}}/F_B \approx 0.052 - 0.017\frac{\lambda}{\kappa^3} + \ldots, \tag{B.27}$$

which more closely approximates the empirical universal barrier height for $\kappa \to \infty$, which is $\Delta F_{\mathrm{el}}^{\mathrm{sec}}/F_B \approx 0.034$ in the full covariant computation. Eq. (B.27) predicts that the higher-order critical point is given by $\lambda_h \approx 3\kappa_h^3$. For spheroids, this locates the transition from continuous to discontinuous behavior at $\kappa_h \approx 1$, again in good agreement with the covariant computation ($\kappa_h \approx 1.3$). The remaining quantitative discrepancies can be systematically alleviated by including higher order terms in the non-local expansions, although not all integrals may be tractable analytically.

B.3.3 Non-local vs. local approximations

The results from the previous subsection would suggest that only local information about the surface (such as κ or λ) is sufficient to predict the nature of the transition, even though we employed a non-local formalism with the full $\Gamma_S(0)$. This raises the question whether a local higher-order small-slope formalism would yield similar quantitative agreement with the full covariant formalism. In order to test this, we instead employ a local fourth-order expansion of $\Gamma_S(r)$ that reads:

$$\Gamma_S^l(r) = -\frac{\kappa^2 r_b^2}{4}\left(1 - \frac{r^2}{r_b^2}\right) + \frac{\kappa^4 r_b^4}{96}\left(3 - 4\frac{\lambda}{\kappa^3}\right)\left(1 - \frac{r^4}{r_b^4}\right), \tag{B.28}$$

where we now use the small-slope expansion for $\Gamma_S(0) = -\kappa^2 r_b^2/4 + (3 - 4\lambda/\kappa)\kappa^4 r_b^4/96 + \ldots$, retaining terms up to $\mathcal{O}(r^4)$. Together with (B.26) (Γ_D remains unmodified from (B.12)), we go through the same steps as outlined in the previous subsection, i.e. we evaluate the energy integral analytically, determine the transition criterion at this level of approximation, compute the position of the extremum and finally insert all these into $\Delta F_{\mathrm{el}}/F_B$ to obtain the scale of the normalized secondary structure, which reads

$$\Delta F_{\mathrm{el}}^{\mathrm{sec}}/F_B \approx 0.057 - 0.021\frac{\lambda}{\kappa^3} + \ldots. \tag{B.29}$$

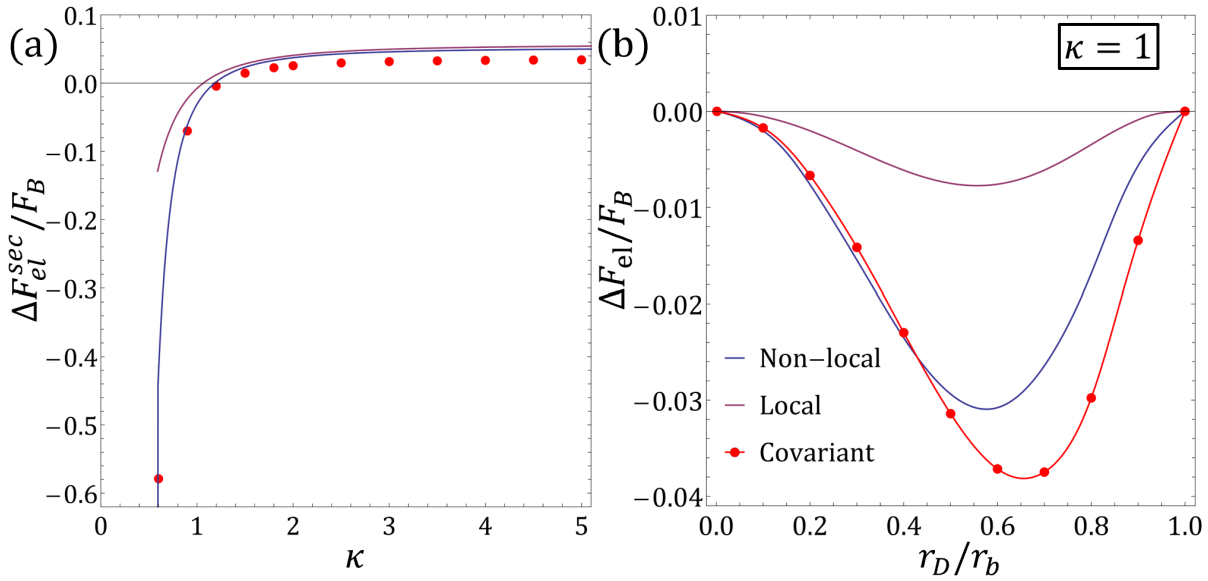

Figure B.5: (a) Scale of the normalized secondary energy structure $\Delta F_{\rm el}^{\rm sec}/F_B$ at transition: the red dots were obtained numerically by integrating the full covariant equation. While both non-local approximation (blue) and a higher order $\mathcal{O}(r^4)$ local approximation (magenta) have the same large κ asymptote, the local approach has large unphysical deviations from the covariant formalism for $\kappa \lesssim 1$. (b) Plotting the normalized energy difference $\Delta F_{\rm el}/F_B$ at transition for a sphere ($\kappa = 1$) showcases this large quantitative discrepancy in the secondary energy structure.

We plot in Fig. B.5(a) the full covariant $\Delta F_{\rm el}^{\rm sec}/F_B$ obtained by numerically integrating (B.10) (indicated by red dots) and compare the local approximation with the non-local one for the shape family of spheroids as our prototypical example. The large central curvature ($\kappa \to \infty$) limit for both converges to approximately the same asymptote with similar deviations from the covariant prediction (cf. (B.29) and (B.27)), however differences between the two become significant for surfaces with smaller values of κ that are arguably of more practical relevance [2]. Fig. B.5(b) exemplifies the significant discrepancy for the particular case of $\kappa = 1$ (sphere) — while the local approximation qualitatively captures the behavior at transition it greatly underestimates the magnitude of the energy minimum and the disagreement only gets worse for surfaces with $\kappa < 1$. Therefore, analogous to the transition criterion from our previous work [2], quantitatively describing the scale of the secondary structure around transition requires non-local information from the entire surface for shapes with $\kappa \sim \mathcal{O}(1)$.

We now turn our attention to the question of how robust this secondary-structure behavior is. In particular, the small range of cap sizes over which it occurs suggests it may be qualitatively altered by even slight deviations from the radial symmetry of the surface shape.

B.3.4 Rotational symmetry breaking

In general, the boundary of open surfaces will not obey radial symmetry; the *Drosophila* eye, for example, is well approximated by an ellipsoidal cap with an elliptical boundary [53]. While a fully covariant formalism in such a general scenario might be feasible numerically, we are not aware of any previous work that studies this role of breaking of continuous rotational symmetry. In order to estimate the magnitude of the effect of breaking boundary shape symmetry on the energy landscape, we shall utilize the small-slope approximation; as we have shown above, this does not, by itself, lead to any secondary structure of the transition (cf. Fig. B.4b). As we have furthermore shown that the energy scale of intrinsic secondary structures is bounded at least for large central curvature κ, we can give a quantitative estimate of whether symmetry breaking will change this structure.

We apply a leading-order shape perturbation to a general surface of revolution, generating an ellipse from the circular boundary by stretching/contracting perpendicular axes by an amount ϵ. Thus,

$$x = (1+\epsilon) r \cos\phi, \quad y = (1-\epsilon) r \sin\phi, \quad z = f(r) \tag{B.30}$$

with $\epsilon \ll 1$, while the metric tensor in the small-slope limit is

$$g_{ij} = \begin{bmatrix} 1+\epsilon(2+\epsilon)\cos 2\phi & -2r\epsilon \sin 2\phi \\ -2r\epsilon \sin 2\phi & r^2\left(1+\epsilon(\epsilon-2)\cos 2\phi\right) \end{bmatrix}. \tag{B.31}$$

Here, $\sqrt{g} = r(1-\epsilon^2)$ and eccentricity $e = \sqrt{1-\frac{(1-\epsilon)^2}{(1+\epsilon)^2}} = 2\sqrt{\epsilon} + \mathcal{O}(\epsilon^{3/2})$, while the small-slope Gaussian curvature is constant to $\mathcal{O}(\epsilon)$ and is given by

$$K_G(r,\phi) = \kappa^2 + \mathcal{O}\left(\epsilon^2\right) . \tag{B.32}$$

The elliptical boundary of a section cut parallel to the xy-plane is given by

$$r(\phi) = \frac{r_b(1-\epsilon^2)}{\sqrt{1+\epsilon(\epsilon-2)\cos 2\phi}} \approx r_b(1+\epsilon\cos 2\phi). \tag{B.33}$$

Breaking rotational symmetry of the surface leads to coupling of stresses in the radial and azimuthal directions. Therefore, the isotropic stresses are not as easily computed as in the previous subsections. Instead, we start by observing that the Airy stress function χ satisfies the following equation in polar coordinates

[13]:

$$\nabla_\perp^4 \chi = \frac{\pi}{3} \frac{\delta(r - r_D)\delta(\phi - \phi_D)}{\sqrt{g}} - K_G(r, \phi) \tag{B.34}$$

subject to a zero normal stress boundary condition and regularity conditions at $r = 0$. Here, $\nabla_\perp^2$ is the 2D Laplace-Beltrami operator in the small-slope limit and is given by $\nabla_\perp^2 f = \frac{1}{\sqrt{g}} \partial_i \left(\sqrt{|g|} g^{ij} \partial_j f \right)$ using the small-slope limit (B.31). Here, g^{ij} is the inverse of the metric tensor such that $g^{ij} g_{jk} = \delta^i_k$. The Airy function is related to the stress components in the usual way,

$$\sigma_{rr} = \frac{1}{r} \frac{\partial \chi}{\partial r} + \frac{1}{r^2} \frac{\partial^2 \chi}{\partial \phi^2}, \; \sigma_{r\phi} = -\frac{\partial}{\partial r} \left(\frac{1}{r} \frac{\partial \chi}{\partial \phi} \right), \; \sigma_{\phi\phi} = \frac{\partial^2 \chi}{\partial r^2}. \tag{B.35}$$

Analogous to the case of a circular boundary, we impose vanishing normal stress, i.e. $\boldsymbol{\sigma} \cdot \hat{\mathbf{n}} = 0$ on (B.34), where $\hat{\mathbf{n}} = n_r \hat{\mathbf{e}}_r + n_\phi \hat{\mathbf{e}}_\phi$ is the normal vector to the elliptical boundary. Therefore, one obtains two scalar equations:

$$\Big[\left(n_r \sigma_{rr} + n_\phi \sigma_{r\phi} \right) \hat{\mathbf{e}}_r + \left(n_r \sigma_{r\phi} + n_\phi \sigma_{\phi\phi} \right) \hat{\mathbf{e}}_\phi \Big]_{r = r_b(\phi)} = 0 \,. \tag{B.36}$$

The total in-plane elastic energy for a surface with stress-free boundary and metric g in terms of the stress components (assuming a linear constitutive relation) is given by [13, 60]:

$$F_{\text{el}} = \frac{1}{2} \int \Gamma(r, \phi)^2 dA = \frac{1}{2} \int \left(\sigma_{rr} + \sigma_{\phi\phi} \right)^2 dA, \tag{B.37}$$

where $\Gamma = \sigma_{rr} + \sigma_{\phi\phi}$ is the trace of the stress tensor.

Writing χ, and thus σ_{ij}, as a Fourier series expansion in $(\cos n\phi, \sin n\phi)$ and consistently expanding the stress components as well as $\nabla_\perp^2$ and the boundary condition in powers of ϵ, we evaluate the elastic energy up to $\mathcal{O}(\epsilon)$ (see Supplemental Information for details). Inserting the expansion $\Gamma = \Gamma_0 + \epsilon \Gamma_1$ into (B.37), the elastic energy can be cast explicitly as

$$F_{\text{el}} = \frac{1}{2} \int_0^{2\pi} \int_0^{r_b} \left(\Gamma_0^2 + 2\epsilon \Gamma_0 \Gamma_1 \right) r dr d\phi \; + \mathcal{O}(\epsilon^2). \tag{B.38}$$

In terms of Fourier components, it is evident that only the squares of the modes will contribute to the energy while the cross terms will integrate out to zero.

Systematically evaluating the $\mathcal{O}(1)$ and $\mathcal{O}(\epsilon)$ contributions to the stress tensor, we obtain an angular

correction to ΔF_{el}. The final expression reads

$$\frac{\Delta F_{\mathrm{el}}(\overline{r}_D)}{F_B} \approx \frac{2\left(2-3\kappa^2 r_b^2\right)}{3\kappa^4 r_b^4}\left(1-\overline{r}_D^2\right)^2 + \frac{4}{3}\epsilon\overline{r}_D^2\cos 2\phi_D\left(\frac{-1+2\overline{r}_D^2-3\overline{r}_D^4+2\overline{r}_D^6-4\log\overline{r}_D}{\kappa^4 r_b^4}\right), \tag{B.39}$$

where $\overline{r}_D = r_D/r_b$. The leading order is the small-slope energy expression for a symmetric cap obtained, e.g., by [13], while the next term represents the leading effect of the shape perturbation and depends, in addition to r_D, on the angular position ϕ_D of the defect.

We display in Fig. B.6, Eq. (B.39) as a function of $\overline{r}_D$ for $\epsilon = 0.05$ (eccentricity of $e \approx 0.45$) along (a) the major axis ($\phi_D = 0$) and (b) the minor axis ($\phi_D = \pi/2$). As expected, breaking the circular cross-sectional symmetry forces the system to select a preferred direction of migration of the defect, which in this situation is the minor axis: this perturbed small-slope formalism predicts a continuous variation of the defect position along $\phi = \pi/2$ until the apex position is established for a certain energy difference (here, $\Delta F_{\mathrm{el}}/F_B \approx -0.35$ as marked by the green curve in Fig. B.6(b)).

To quantify the scale of the secondary structure, we set $\Delta F_{\mathrm{el}}(0) = 0$ in (B.39) to obtain the transition criterion $r_c = \sqrt{2/3}/\kappa$ (unchanged from the rotationally symmetric situation), while the position of the maxima/minima obtained by setting $\Delta F'_{\mathrm{el}}(0) = 0$ results in $r_D \approx 0.55 r_b$, a slight but significant difference from the position for intrinsic secondary structures described in section B.3.2. Finally, inserting into (B.39) we obtain the energy scale

$$\frac{\Delta F_{\mathrm{el}}^{\mathrm{sec}}}{F_B} \approx 1.61\epsilon\cos 2\phi_D + \mathcal{O}\left(\epsilon^2\right). \tag{B.40}$$

At the critical cap extent $r_b = r_c$, the small-slope ΔF_{el} vanishes, so that the secondary energy structure is proportional to ϵ and quadrupolar in ϕ_D. Within the small-slope approximation this correction does not depend on κ when normalized by F_B. The magnitude of secondary energy maxima and minima (cf. Fig. B.6) is well described by (B.40). Having identified a universal scale of *intrinsic* secondary structure maxima in section B.3.2 as $\Delta F_{\mathrm{el}}^{\mathrm{sec}}/F_B \approx 0.034$ for moderate to large κ, we can say that symmetry breaking is likely to transform the transition character from discontinuous to continuous along the minor axis beyond a strain of $\epsilon \gg 0.02$. Quite subtle symmetry breaking is thus capable of qualitatively changing the disorder transition. We note that inclusion of the next order $\mathcal{O}(r_b^4)$ terms introduces non-trivial couplings between the shape perturbation and the secondary structure discussed in the previous subsections, leading to modification of (B.40). We know from Sec. B.3.2 that the leading term of the transition criterion r_c becomes approximately $a = 0.844$. Defining the deviation of a from the small-slope value as $\delta = a - \sqrt{2/3}$, a Taylor expansion of

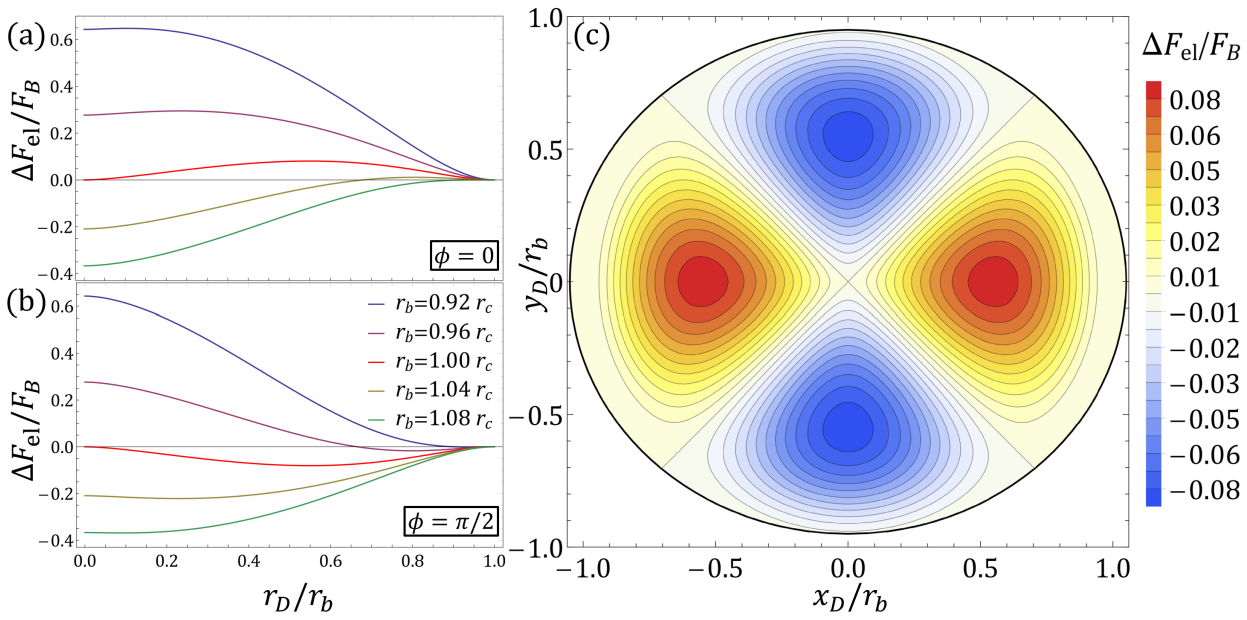

Figure B.6: Normalized energy difference $\Delta F_{\rm el}/F_B$ for an ellipsoid ($\epsilon = 0.05$); varying the cap extent r_b around transition, (a) along the major axis ($\phi = 0$), an energy maximum persists, whereas there is an energy minimum along (b) the minor axis ($\phi = \pi/2$) — thus the preferred direction of defect migration is predicted to be along the minor axis. The energy landscape is displayed in (c) showing the location of these global maxima/minima at transition, i.e. at $r_b = r_c$. Note that these plots are independent of κ since we replace r_b in (B.39) by multiples of the small-slope value $r_c = \sqrt{2/3}/\kappa$.

(B.39) in $\delta \ll 1$ alters the numerical prefactor of (B.40) to $(1.61 - 7.9\delta) \approx 1.39$. This is a small quantitative deviation that does not change the nature of the effects discussed above.

B.4 Conclusions

The present work demonstrates that simple, general criteria can be derived not just for the onset of energetically favored disclination disorder on curved open surfaces, but to predict the secondary structure of that disorder transition.

The secondary structure of the transition, i.e., whether the displacement of the disclination occurs continuously or discontinuously), is important for predictions of actual defect placement in practical applications. In particular, symmetry-breaking defect positions can be energetically favorable over well-defined ranges of parameters, such as the extent of the open surface. We have shown that these secondary effects occur over a small, quantifiable range of sizes around the onset of disorder. Similarly, the elastic energy of the surface universally changes by a well-defined amount as the defect position changes — a few percent of the total energy.

Accordingly, this secondary structure can be altered by relatively small modifications of the mechanics of

the problem. In particular, even slight anisotropy in the shape of the surface will force the optimal position of the disclination onto one of the principal axes, and will make defect displacements continuous even if they are intrinsically discontinuous.

It is noteworthy that the analytical approximations yielding results for the secondary structure of the transition require more detailed knowledge of the surface shape than those that allow for an evaluation of the onset of disorder. In particular, the fourth apical derivative of the surface shape (by symmetry the next order after the apical curvature) is a strong determinant of the transition characteristics. Likewise, our formalism makes use of the second derivative of the non-local weighted Gaussian curvature, $\Gamma''_S(0)$, as opposed to just its functional value. Our findings indicate that an increased curvature away from the apex ($\lambda > 0$) is necessary, though not sufficient, for the stabilization of intermediate defect positions (continuous transition). Intuitively, this rationalizes positions $r_D > 0$ as locally more "attractive" to defects than the origin itself. How accurately a higher-order quantity like λ can be determined in an application, and how the presence of positional disorder (dislocations) may alter the results, will be the subject of future study.

For a given shape with mobile disclinations, the current work offers easy-to-check criteria for whether the onset of disorder results in robust central defect placement (discontinuous transition) or whether a variety of configurations may be observed (continuous transition). In applications of shells with Gaussian curvature, be they viral capsids, tissue structures like insect eyes, or optical engineering systems such as microlens arrays, these insights also provide bounds on the degree of symmetry needed to maintain an ordered lattice on such surfaces.

B.5 Additional Information

B.5.1 Complete covariant formalism

We follow the covariant formalism developed by Bowick and Giomi [23], Giomi and Bowick [60] in the following. Let $\mathbb{P}$ be a smooth two-dimensional surface of a crystal lattice in $\mathbb{R}^3$. The elastic free energy of the crystal may be expressed in the form:

$$F = F_{\text{el}} + F_c + F_0, \tag{B.41}$$

where F_0 is the free energy of the defect-free monolayer, F_c is the core energy of defects and F_{el} is the elastic energy associated with defect interaction. As we will change neither the shape of the surface nor the number

of defects, any minimization is governed by $F_{\rm el}$, which can be written as

$$F_{\rm el} = \frac{Y}{2}\int \mathrm{d}\mathbf{x}\,\mathrm{d}\mathbf{y}\, G_{2L}(\mathbf{x},\mathbf{y}) q_T(\mathbf{x}) q_T(\mathbf{y}), \tag{B.42}$$

where Y is the Young's modulus for the planar crystal and $G_{2L}(\mathbf{x},\mathbf{y})$ is the Green's function for the covariant biharmonic operator on the manifold. The quantity $q_T(\mathbf{x})$ represents the effective topological charge density; in the presence of discrete $q=+1$ disclinations at $\mathbf{x}_\alpha$ it takes the form

$$q_T(\mathbf{x}) = \sum_\alpha \frac{\pi}{3}\delta(\mathbf{x},\mathbf{x}_\alpha) - K_G(\mathbf{x}), \tag{B.43}$$

where $\delta(\mathbf{x},\mathbf{x}_\alpha) = g^{-1/2}\delta(x_1 - x_{\alpha_1})\delta(x_2 - x_{\alpha_2})$ is the Dirac delta function on the manifold parametrized by $\mathbf{x} = (x_1, x_2) (= (r,\phi)$ in polar coordinates). The second term $K_G(\mathbf{x})$ is the Gaussian curvature of the surface. On a topological disk with total charge Q=+6, the minimal number of disclinations is 6. Any disclination located at the boundary will not contribute to $F_{\rm el}$, because G_{2L} vanishes there. In this work, we compare energies of configurations with all 6 disclinations at the boundary to those with one disclination located at an arbitrary $\mathbf{x}_D$. Therefore, we consider the simpler $q_T(\mathbf{x},\mathbf{x}_D) = \frac{\pi}{3}\delta(\mathbf{x},\mathbf{x}_D) - K_G(\mathbf{x})$. We begin by observing that the Airy stress function χ solves the following inhomogeneous biharmonic equation:

$$\Delta^2\chi(\mathbf{x},\mathbf{x}_D) = Y q_T(\mathbf{x},\mathbf{x}_D), \tag{B.44}$$

with no stress boundary conditions

$$\chi(\mathbf{x},\mathbf{x}_D) = 0, \quad \mathbf{x}\in\partial\mathbb{P}; \quad \nu_i\nabla^i\chi(\mathbf{x},\mathbf{x}_D) = 0, \quad \mathbf{x}\in\partial\mathbb{P}. \tag{B.45}$$

The solution of (B.44) will then be

$$\chi(\mathbf{x},\mathbf{x}_D) = \int d^2y G_L(\mathbf{x},\mathbf{y})\Gamma(\mathbf{y},\mathbf{y}_D), \tag{B.46}$$

where $G_L(\mathbf{x},\mathbf{y})$ is the Green's function of the covariant Laplace operator on $\mathbb{P}$ with Dirichlet boundary conditions

$$\Delta G_L(\mathbf{x},.) = \delta(\mathbf{x},.), \quad \mathbf{x}\in\mathbb{P}; \quad G_L(\mathbf{x},.) = 0, \quad \mathbf{x}\in\partial\mathbb{P}, \tag{B.47}$$

and $\Gamma(\mathbf{x}, \mathbf{x}_D) = \Delta\chi(\mathbf{x}, \mathbf{x}_D)$ is the solution of the Poisson problem:

$$\Delta\Gamma(\mathbf{x}, \mathbf{x}_D) = Y q_T(\mathbf{x}, \mathbf{x}_D), \tag{B.48}$$

which can be expressed formally as:

$$\Gamma(\mathbf{x}, \mathbf{x}_D) = Y \int q_T(\mathbf{y}, \mathbf{y}_D) G_L(\mathbf{x}, \mathbf{y}) d^2y = -\Gamma_D(\mathbf{x}, \mathbf{x}_D) - \Gamma_S(\mathbf{x}) + U(\mathbf{x}, \mathbf{x}_D), \tag{B.49}$$

where

$$\Gamma_D(\mathbf{x}, \mathbf{x}_D) = -\frac{Y\pi}{3} G_L(\mathbf{x}, \mathbf{x}_D), \quad \Gamma_S(\mathbf{x}) = Y \int K_G(\mathbf{y}) G_L(\mathbf{x}, \mathbf{y}) d^2y, \tag{B.50}$$

and $U(\mathbf{x}, \mathbf{x}_D)$ is a harmonic function on $\mathbb{P}$ that enforces the appB:neumann boundary conditions. The first term of (B.49) represents the bare contribution of disclinations while the second term captures the screening effect of Gaussian curvature. In this Appendix, we restrict ourselves to allowing only one disclination to migrate from the boundary to the apex of the manifold. The Green's function satisfying (B.47) can be computed explicitly by conformally mapping the surface $\mathbb{P}$ onto the unit disk of the complex plane where the Green's function is known:

$$G_L(\mathbf{x}, \mathbf{y}) = \frac{1}{2\pi} \log \left| \frac{z(\mathbf{x}) - z(\mathbf{y})}{1 - z(\mathbf{x})\overline{z(\mathbf{y})}} \right|, \tag{B.51}$$

where $z(\mathbf{x}) = \varrho e^{i\phi}$, a point in the unit disk, is the image of a point on the surface $\mathbb{P}$ under the conformal mapping. The Green's function vanishes when the disclination is located at the boundary. For a surface $X(r, \phi)$ with first fundamental form $E = \partial X/\partial r \cdot \partial X/\partial r$, $F = \partial X/\partial r \cdot \partial X/\partial \phi$ and $G = \partial X/\partial \phi \cdot \partial X/\partial \phi$, the metric of the surface will be

$$ds^2 = E dr^2 + 2F dr d\phi + G d\phi^2 \tag{B.52}$$

whereas the unit disk has the metric

$$ds^2 = w(z) \left(\varrho^2 dr^2 + \varrho^2 d\phi^2 \right) \tag{B.53}$$

where $w(z)$ is a positive conformal weight. The remaining task is now to find the conformal factor $w(z)$ and the conformal radius $\varrho(r)$ by equating the two metrics; these can be explicitly obtained for many rotationally symmetric surfaces but in general, may not be analytically computable.

Taking the two image points on the unit disk as $z(r, \phi) = \varrho_x(r) e^{i\phi}$ and $\zeta(r', \phi') = \varrho_y(r') e^{i\phi'}$, the contribution due to the background Gaussian curvature is split into two parts $\Gamma_S(\mathbf{x}) = \Gamma_{S,1}(\mathbf{x}) - \Gamma_{S,2}(\mathbf{x})$,

where

$$\Gamma_{S,1}(r,\phi) = \frac{Y}{2\pi}\int d\phi'\, dr'\, \sqrt{g}K(r')\log|z-\zeta|, \tag{B.54a}$$

$$\Gamma_{S,2}(r,\phi) = \frac{Y}{2\pi}\int d\phi'\, dr'\, \sqrt{g}K(r')\log|1-z\overline{\zeta}|, \tag{B.54b}$$

are evaluated analytically for the specific surfaces considered in this Appendix. The computation of the harmonic function on the manifold $\mathbb{P}$ is more involved and its contribution to the energy density is given by,

$$U(\mathbf{x},\mathbf{x}_D) = -Y\int d^2y H(\mathbf{x},\mathbf{y})q_T(\mathbf{y},\mathbf{y}_D), \tag{B.55}$$

where $H(\mathbf{x},\mathbf{y})$ is harmonic kernel associated with the Green's function of the weighted biharmonic operator arising from the conformal mapping of the manifold $\mathbb{P}$ onto the unit disk in the complex plane. The harmonic kernel can be written in integral form as [150]

$$H(z,\zeta) = -\int_{|\zeta|}^1 \frac{dt}{\pi t}\int_0^t ds\,\sqrt{g}k\left[\frac{\varrho^2(s)}{t^2}\zeta\overline{z}\right], \tag{B.56a}$$

$$k(z\overline{\zeta}) = \sum_{n\geq 0}\frac{(z\overline{\zeta})^n}{c_n(1)} + \sum_{n<0}\frac{(\overline{z}\zeta)^{|n|}}{c_{|n|}(1)}, \tag{B.56b}$$

$$c_n(t) = 2\int_0^t ds\,\sqrt{g}\varrho^{2n}(s). \tag{B.56c}$$

After making appropriate substitutions, one obtains

$$\begin{aligned}
H(z,\zeta) &= -\int_{|\zeta|}^1 \frac{dt}{\pi t}\int_0^t ds\,\sqrt{g}\left[\frac{1}{c_0(1)} + \sum_{n\geq 1}\frac{1}{c_n(1)}\frac{\varrho^{2n}(s)}{t^{2n}}\varrho_x^n\varrho_y^n\left(e^{in(\phi-\phi')} + e^{-in(\phi-\phi')}\right)\right] \\
&= -\int_{|\zeta|}^1 \frac{dt}{\pi t}\int_0^t ds\,\sqrt{g}\left[\frac{1}{c_0(1)} + \sum_{n\geq 1}\frac{2}{c_n(1)}\frac{\varrho^{2n}(s)}{t^{2n}}\varrho_x^n\varrho_y^n\cos n(\phi-\phi')\right] \\
&= -\int_{\varrho_y}^1 \frac{dt}{\pi t}\left[\frac{1}{2}\frac{c_0(t)}{c_0(1)} + \sum_{n\geq 1}\frac{c_n(t)}{c_n(1)}\frac{2}{t^{2n}}\varrho_x^n\varrho_y^n\cos n(\phi-\phi')\right] \\
&= -\frac{1}{2\pi}f_0(\varrho_y) - \sum_{n\geq 1}\frac{1}{\pi}\varrho_x^n\varrho_y^n\cos n(\phi-\phi')f_n(\varrho_y),
\end{aligned} \tag{B.57}$$

where

$$f_n(\varrho_y) = \int_{\varrho_y}^1 \frac{c_n(t)}{c_n(1)t^{2n+1}}dt. \tag{B.58}$$

Note that the variable s lies on the manifold $\mathbb{P}$, whereas t lies on the unit disk in $\mathbb{R}^2$. Therefore, explicitly

$$U(r,\phi,r_D,\phi_D) = -Y\int_0^{2\pi} d\phi' \int_0^{r_b} dr'\,\sqrt{g}(r')\,q_T(r',\phi',r_D,\phi_D) \left[\left(-\frac{1}{2\pi}f_0(\varrho_y) - \sum_{n\geq 1}\frac{1}{\pi}\varrho_x^n\varrho_y^n\cos n(\phi-\phi')f_n(\varrho_y)\right)\right]. \tag{B.59}$$

Here, f_0 is the azimuthally symmetric contribution while the higher order modes capture asymmetries arising due to intermediate singularity positions. ϱ is the effective topological charge density as defined according to (B.43) and Y is the material Young's modulus. We note that the isotropic contribution, i.e., due to f_0 can be shown to be the same as reported in our previous work [2] and is equivalent to $U = \frac{1}{A}\int \Gamma dA$ for rotationally symmetric surfaces with symmetric defect placement.

B.5.2 Breaking rotational symmetry

As stated in the main text, we apply a shape perturbation to a general surface of revolution, generating an ellipse from a circular boundary by stretching/contracting perpendicular axes by ϵ. Thus,

$$x = (1+\epsilon)r\cos\phi, \quad y = (1-\epsilon)r\sin\phi, \quad z = f(r) \tag{B.60}$$

with $\epsilon \ll 1$. The metric tensor in the small-slope limit is

$$g_{ij} = \begin{bmatrix} 1+\epsilon(2+\epsilon)\cos 2\phi & -2r\epsilon\sin 2\phi \\ -2r\epsilon\sin 2\phi & r^2\left(1+\epsilon(\epsilon-2)\cos 2\phi\right) \end{bmatrix}, \tag{B.61}$$

where $\sqrt{g} = r(1-\epsilon^2)$ and eccentricity $e = \sqrt{1-\frac{(1-\epsilon)^2}{(1+\epsilon)^2}} = 2\sqrt{\epsilon} + \mathcal{O}(\epsilon^{3/2})$, while the Gaussian curvature is constant to $\mathcal{O}(\epsilon)$ and is given by

$$K_G(r,\phi) = \kappa^2 + \mathcal{O}\left(\epsilon^2\right), \tag{B.62}$$

where $\kappa = f''(0)$ is the apical curvature. The elliptical boundary of a section cut parallel to the xy-plane is given by

$$r(\phi) = \frac{r_b(1-\epsilon^2)}{\sqrt{1+\epsilon(\epsilon-2)\cos 2\phi}} \approx r_b(1+\epsilon\cos 2\phi). \tag{B.63}$$

Using a regular perturbation expansion for $\chi = \chi_0 + \epsilon\chi_1$ (and consequently the stresses σ) while also expanding the Laplace-Beltrami operator for small ϵ ($\nabla_\perp^2 \approx \nabla_0^2 + \epsilon\nabla_1^2$), we solve the following biharmonic

equation for χ order-wise up to $O(\epsilon)$:

$$\frac{1}{Y}(\nabla_0^2+\epsilon\nabla_1^2)(\nabla_0^2+\epsilon\nabla_1^2)(\chi_0+\epsilon\chi_1)=\frac{\pi}{3}\frac{\delta(r-r_D)\delta(\phi-\phi_D)}{\sqrt{g}}-K_G(r,\phi). \tag{B.64}$$

The Airy stress χ relates to the stress components via the usual relations in polar coordinates:

$$\sigma_{rr}=\frac{1}{r}\frac{\partial\chi}{\partial r}+\frac{1}{r^2}\frac{\partial^2\chi}{\partial\phi^2},\quad \sigma_{r\phi}=-\frac{\partial}{\partial r}\left(\frac{1}{r}\frac{\partial\chi}{\partial\phi}\right),\quad \sigma_{\phi\phi}=\frac{\partial^2\chi}{\partial r^2}. \tag{B.65}$$

For $\epsilon\ll 1$, the normal vector components can be expanded as: $n_r=1+O(\epsilon^2)$ and $n_\phi=2\epsilon\sin 2\phi+O(\epsilon^2)$. Consistently expanding both the stress components and their arguments ($r(\phi)=r_b+\epsilon r_b\cos 2\phi$), one obtains up to $O(\epsilon)$:

$$\sigma_{rr_0}(r_b)+\epsilon\left(r_b\cos 2\phi\frac{\partial\sigma_{rr_0}}{\partial r}\bigg|_{r_b}+2\sigma_{r\phi_0}(r_b)\sin 2\phi+\sigma_{rr_1}(r_b)\right)=0 \tag{B.66a}$$

$$\sigma_{r\phi_0}(r_b)+\epsilon\left(r_b\cos 2\phi\frac{\partial\sigma_{r\phi_0}}{\partial r}\bigg|_{r_b}+2\sigma_{\phi\phi_0}(r_b)\sin 2\phi+\sigma_{r\phi_1}(r_b)\right)=0 \tag{B.66b}$$

For a stress-free boundary the elastic energy is written simply in terms of the trace of the stress tensor [60], i.e., $\Gamma(r,\phi)\approx\Gamma_0(r,\phi)+\epsilon\Gamma_1(r,\phi)=\sigma_{rr_0}+\sigma_{\phi\phi_0}+\epsilon(\sigma_{rr_1}+\sigma_{\phi\phi_1})$. Therefore, the elastic energy formally reads:

$$\begin{aligned}F_{\text{el}}&=\frac{1}{2Y}\int_0^{2\pi}\int_0^{r_b}\sqrt{g}\Gamma(r,\phi)^2drd\phi\\&=\frac{1}{2Y}\int_0^{2\pi}\int_0^{r_b}r\left(\Gamma_0(r,\phi)^2+2\epsilon\Gamma_0(r,\phi)\Gamma_1(r,\phi)\right)drd\phi+\mathcal{O}(\epsilon^2),\end{aligned} \tag{B.67}$$

which is the expression given in the main text. This energy integral is executed analytically exploiting the orthogonality of trigonometric functions.

While Azadi and Grason [13] focused on the azimuthally symmetric center or boundary placement of the defect, following work going back to Michell [109], we use a Fourier series expansion of the Airy stress function $\chi(r,\phi)=a_0(r)+\sum_{n=1}^{\infty}(a_n(r)\cos n\phi+b_n(r)\sin n\phi)$, to solve this system of equations for a general

position (r_D, ϕ_D) of the disclination. The stress components expressed in terms of this expansion read

$$\begin{aligned}\sigma_{rr} &= \frac{1}{r}\frac{\partial \chi}{\partial r} + \frac{1}{r^2}\frac{\partial^2 \chi}{\partial \phi^2} \\ &= \frac{1}{r}\left[a_0^{(1)}(r) + \sum_{n=1}^{\infty}\left\{\left(a_n^{(1)}(r) - n^2\frac{a_n(r)}{r}\right)\cos n\phi + \left(b_n^{(1)}(r) - n^2\frac{b_n(r)}{r}\right)\sin n\phi\right\}\right], \qquad \text{(B.68a)}\end{aligned}$$

$$\sigma_{r\phi} = -\frac{\partial}{\partial r}\left(\frac{1}{r}\frac{\partial \chi}{\partial \phi}\right) = \frac{1}{r}\sum_{n=1}^{\infty} n\left[\left(a_n^{(1)}(r) - \frac{a_n(r)}{r}\right)\sin n\phi - \left(b_n^{(1)}(r) - \frac{b_n(r)}{r}\right)\cos n\phi\right], \qquad \text{(B.68b)}$$

$$\sigma_{\phi\phi} = \frac{\partial^2 \chi}{\partial r^2} = a_0^{(2)}(r) + \sum_{n=1}^{\infty}\left(a_n^{(2)}(r)\cos n\phi + b_n^{(2)}(r)\sin n\phi\right). \qquad \text{(B.68c)}$$

Zeroth order solution

At $O(1)$, we employ a Fourier series expansion of the Airy stress function such that $\chi_0(r,\phi) = a_0(r) + \sum_{n=1}^{\infty} a_n(r)\cos n(\phi - \phi_D)$. The solution will be azimuthally symmetric only when the singularity is placed at the center or at the boundary of the surface [13]. This results in:

$$\frac{1}{Y}\nabla_0^4 \chi_0(r,\phi) = -\kappa^2 + \frac{\pi}{3}\frac{\delta(r - r_D)}{\pi r}\left[\frac{1}{2} + \sum_{n=1}^{\infty}\cos(n(\phi - \phi_D))\right] \qquad \text{(B.69)}$$

where $\nabla_0^2 = \frac{\partial^2}{\partial r^2} + \frac{1}{r}\frac{\partial}{\partial r} + \frac{1}{r^2}\frac{\partial^2}{\partial \phi^2}$ and subject to the radial stress component boundary condition ($\sigma_{rr_0}(r_b) = 0$, $\sigma_{r\phi_0}(r_b) = 0$). The Fourier expansion of the stress components in terms of these modes is as follows:

$$\sigma_{rr_0} = \frac{1}{r}\frac{\partial \chi}{\partial r} + \frac{1}{r^2}\frac{\partial^2 \chi}{\partial \phi^2} = \frac{1}{r}\left[a_0^{(1)}(r) + \sum_{n=1}^{\infty}\left(a_n^{(1)}(r) - n^2\frac{a_n(r)}{r}\right)\cos n(\phi - \phi_D)\right], \qquad \text{(B.70a)}$$

$$\sigma_{r\phi_0} = -\frac{\partial}{\partial r}\left(\frac{1}{r}\frac{\partial \chi}{\partial \phi}\right) = \frac{1}{r}\sum_{n=1}^{\infty} n\left(a_n^{(1)}(r) - \frac{a_n(r)}{r}\right)\sin n(\phi - \phi_D), \qquad \text{(B.70b)}$$

$$\sigma_{\phi\phi_0} = \frac{\partial^2 \chi}{\partial r^2} = a_0^{(2)}(r) + \sum_{n=1}^{\infty} a_n^{(2)}(r)\cos n(\phi - \phi_D). \qquad \text{(B.70c)}$$

The system of ODEs one thus obtains is:

$$\frac{1}{Y}\left[a_0^{(4)}(r) + \frac{2}{r}a_0^{(3)}(r) - \frac{1}{r^2}a_0^{(2)}(r) + \frac{1}{r^3}a_0^{(1)}(r)\right] = -\kappa^2 + \frac{\delta(r - r_D)}{6r} \qquad \text{(B.71a)}$$

$$a_n^{(4)}(r) + \frac{2}{r}a_n^{(3)}(r) - \frac{(1+2n^2)}{r^2}a_n^{(2)}(r) + \frac{1+2n^2}{r^3}a_n^{(1)}(r) + \frac{n^2(n^2-4)}{r^4}a_n(r) = \frac{Y\delta(r - r_D)}{3r}, \qquad \text{(B.71b)}$$

where $()'$ indicates differentiation with respect to r, along with the following system of boundary conditions

$$\frac{1}{r_b}\left[a_0^{(1)}(r_b)+\sum_{n=1}^{\infty}\left(a_n^{(1)}(r_b)-n^2\frac{a_n(r_b)}{r_b}\right)\cos n(\phi-\phi_D)\right]=0 \tag{B.72a}$$

$$\frac{1}{r_b}\left[\sum_{n=1}^{\infty}n\left(a_n^{(1)}(r_b)-\frac{a_n(r_b)}{r_b}\right)\sin n(\phi-\phi_D)\right]=0 \tag{B.72b}$$

The leading order (small-slope) Fourier amplitudes for a rotationally symmetric surface with central curvature κ in the presence of an arbitrarily positioned disclination defect is given by:

$$\begin{aligned}a_0(r)=&-\frac{Y\kappa^2r^2}{64}(r^2-2r_b^2)+\frac{Y}{24}H(r-r_D)\left(r_D^2-r^2+(r_D^2+r^2)\log\left(\frac{r}{r_D}\right)\right)\\&+\frac{Y}{48}r^2\left(1-\frac{r_D^2}{r_b^2}+2\log\left(\frac{r_D}{r_b}\right)\right),\end{aligned} \tag{B.73}$$

$$\begin{aligned}a_n(r)=&\frac{Y}{24}\frac{H(r-r_D)}{n(n^2-1)}\left[\left(\frac{r_D}{r}\right)^n\left((n+1)r^2-(n-1)r_D^2\right)+\left(\frac{r}{r_D}\right)^n\left((n-1)r^2-(n+1)r_D^2\right)\right]\\&-\frac{Y}{24}\frac{(r/r_D)^n}{n(n^2-1)}\Bigg[(n-1)r^2-(n+1)r_D^2\\&+\left(\frac{r_D}{r_b}\right)^{2n}\left(n(n-1)\left(\frac{rr_D}{r_b}\right)^2-(n^2-1)(r^2+r_D^2)+n(n+1)r_b^2\right)\Bigg],\end{aligned} \tag{B.74}$$

where H is the Heaviside function and $a_0(r)$ is the azimuthally symmetric solution reported in [13]. All the $n\neq 0$ modes go to zero when the singularity is decorated at the boundary or at the center of the surface but not otherwise.

First order solution

At $O(\epsilon)$, analogous to the zeroth order but more generally, we employ a Fourier series decomposition of the Airy stress function such that, $\chi_1(r,\phi)=c_0(r)+\sum_{n=1}^{\infty}\left(c_n(r)\cos n\phi+d_n(r)\sin n\phi\right)$. This results in

$$\frac{1}{Y}\left[\nabla_0^4\chi_1(r,\phi)+2\nabla_1^2(\nabla_0^2\chi_0(r,\phi))\right]=0 \tag{B.75}$$

where $\nabla_1^2=2\cos^2\phi\frac{\partial^2}{\partial r^2}+2\sin\phi\left(\frac{2\cos\phi}{r^2}\frac{\partial}{\partial\phi}+\frac{\sin\phi}{r}\frac{\partial}{\partial r}\right)+2\sin\phi\left(\frac{\sin\phi}{r^2}\frac{\partial^2}{\partial\phi^2}-\frac{2\cos\phi}{r}\frac{\partial^2}{\partial r\partial\phi}\right)$ and subject to the following boundary conditions:

$$r_b\cos 2\phi\frac{\partial\sigma_{rr_0}}{\partial r}\bigg|_{r_b}+\cancelto{0}{2\sigma_{r\phi_0}(r_b)}\sin 2\phi+\sigma_{rr_1}(r_b)=0, \tag{B.76a}$$

$$r_b\cos 2\phi\frac{\partial\sigma_{r\phi_0}}{\partial r}\bigg|_{r_b}+2\sigma_{\phi\phi_0}(r_b)\sin 2\phi+\sigma_{r\phi_1}(r_b)=0. \tag{B.76b}$$

Inserting the Fourier expansion, (B.75) reduces to the following system of ODEs that now have a forcing term from the previous order:

$$c_0^{(4)}(r)+\frac{2}{r}c_0^{(3)}(r)-\frac{1}{r^2}c_0^{(2)}(r)+\frac{1}{r^3}c_0^{(1)}(r)=-2\left(\frac{2r^2{a_0}^{(3)}(r)-ra_0^2(r)+a_0^1(r)}{r^3}+{a_0}^{(4)}(r)\right)$$
$$-\frac{\cos\left(2\phi_D\right)\left(3a_2'(r)+r\left(r\left(4{a_2}^{(3)}(r)+r{a_2}^{(4)}(r)\right)-3a_2''(r)\right)\right)}{r^3} \tag{B.77a}$$

$$c_n^{(4)}(r)+\frac{2}{r}c_n^{(3)}(r)-\frac{(1+2n^2)}{r^2}c_n^{(2)}(r)+\frac{1+2n^2}{r^3}c_n^{(1)}(r)+\frac{n^2(n^2-4)}{r^4}c_n(r)=$$
$$-\frac{2\cos\left(n\phi_D\right)}{r^4}\left(r\left(\left(2n^2+1\right)a_n'(r)+r\left(\left(-2n^2-1\right)a_n''(r)+r\left(2{a_n}^{(3)}(r)+r{a_n}^{(4)}(r)\right)\right)\right)\right.$$
$$\left.+\left(n^2-4\right)n^2a_n(r)\right)-\frac{\cos\left((n-2)\phi_D\right)}{r^4}\left(r\left((2(n-2)(n-1)n+3)a_{n-2}'(r)\right.\right.$$
$$\left.\left.+r\left(r\left(r{a_{n-2}}^{(4)}(r)-2(n-2){a_{n-2}}^{(3)}(r)\right)-3a_{n-2}''(r)\right)\right)-(n-2)^2n(n+2)a_{n-2}(r)\right)$$
$$-\frac{\cos\left((n+2)\phi_D\right)}{r^4}\left(r\left((3-2n(n+1)(n+2))a_{n+2}'(r)\right.\right.$$
$$\left.\left.+r\left(r\left(2(n+2){a_{n+2}}^{(3)}(r)+r{a_{n+2}}^{(4)}(r)\right)-3a_{n+2}''(r)\right)\right)+(2-n)n(n+2)^2a_{n+2}(r)\right) \tag{B.77b}$$

$$d_n^{(4)}(r)+\frac{2}{r}d_n^{(3)}(r)-\frac{(1+2n^2)}{r^2}d_n^{(2)}(r)+\frac{1+2n^2}{r^3}d_n^{(1)}(r)+\frac{n^2(n^2-4)}{r^4}d_n(r)=$$
$$-\frac{2\sin\left(n\phi_D\right)}{r^4}\left(r\left(\left(2n^2+1\right)a_n'(r)+r\left(\left(-2n^2-1\right)a_n''(r)+r\left(2{a_n}^{(3)}(r)+r{a_n}^{(4)}(r)\right)\right)\right)\right.$$
$$\left.+\left(n^2-4\right)n^2a_n(r)\right)-\frac{\sin\left((n-2)\phi_D\right)}{r^4}\left(r\left((2(n-2)(n-1)n+3)a_{n-2}'(r)\right.\right.$$
$$\left.\left.+r\left(r\left(r{a_{n-2}}^{(4)}(r)-2(n-2){a_{n-2}}^{(3)}(r)\right)-3a_{n-2}''(r)\right)\right)-(n-2)^2n(n+2)a_{n-2}(r)\right)$$
$$-\frac{\sin\left((n+2)\phi_D\right)}{r^4}\left(r\left((3-2n(n+1)(n+2))a_{n+2}'(r)\right.\right.$$
$$\left.\left.+r\left(r\left(2(n+2){a_{n+2}}^{(3)}(r)+r{a_{n+2}}^{(4)}(r)\right)-3a_{n+2}''(r)\right)\right)+(2-n)n(n+2)^2a_{n+2}(r)\right) \tag{B.77c}$$

where $n=1,2,3,4...$ These together with (B.76) are solved analytically to obtain the $\mathcal{O}(\epsilon)$ Fourier coefficients whose lengthy expressions are available upon request.

References

[1] T. Açıkalın, A. Raman, and S. V. Garimella. Two-dimensional streaming flows induced by resonating, thin beams. *The Journal of the Acoustical Society of America*, 114(4):1785–1795, 2003.

[2] S. Agarwal and S. Hilgenfeldt. Simple, general criterion for onset of disclination disorder on curved surfaces. *Phys. Rev. Lett.*, 125:078003, Aug 2020. doi: 10.1103/PhysRevLett.125.078003.

[3] S. Agarwal and S. Hilgenfeldt. Predicting the characteristics of defect transitions on curved surfaces. *Soft Matter*, 17(15):4059–4068, 2021.

[4] S. Agarwal, B. Rallabandi, and S. Hilgenfeldt. Inertial forces for particle manipulation near oscillating interfaces. *Physical Review Fluids*, 3(10):104201, 2018.

[5] S. Agarwal, Y. Bhosale, M. Gazzola, and S. Hilgenfeldt. Density contrast induced inertial forces: Quantifying an efficient tool in microfluidics and acoustofluidics. *preprint*, 2021.

[6] S. Agarwal, F. K. Chan, B. Rallabandi, M. Gazzola, and S. Hilgenfeldt. An unrecognized inertial force induced by flow curvature in microfluidics. *Proceedings of the National Academy of Sciences*, 118(29), 2021.

[7] S. Agarwal, D. Raju, and S. Hilgenfeldt. High-throughput particle sorting and focusing using microbubble streaming. *preprint*, 2021.

[8] D. Ahmed, X. Mao, J. Shi, B. K. Juluri, and T. J. Huang. A millisecond micromixer via single-bubble-based acoustic streaming. *Lab on a Chip*, 9(18):2738–2741, 2009.

[9] D. Ahmed, M. Lu, A. Nourhani, P. E. Lammert, Z. Stratton, H. S. Muddana, V. H. Crespi, and T. J. Huang. Selectively manipulable acoustic-powered microswimmers. *Scientific reports*, 5:9744, 2015.

[10] K. Ahn, C. Kerbage, T. P. Hunt, R. Westervelt, D. R. Link, and D. A. Weitz. Dielectrophoretic manipulation of drops for high-speed microfluidic sorting devices. *Applied Physics Letters*, 88(2): 024104, 2006.

[11] T. Auton, J. Hunt, and M. Prud'Homme. The force exerted on a body in inviscid unsteady non-uniform rotational flow. *Journal of Fluid Mechanics*, 197:241–257, 1988.

[12] A. Azadi and G. M. Grason. Emergent structure of multidislocation ground states in curved crystals. *Physical review letters*, 112(22):225502, 2014.

[13] A. Azadi and G. M. Grason. Neutral versus charged defect patterns in curved crystals. *Physical Review E*, 94(1):013003, 2016.

[14] D. Baresch and V. Garbin. Acoustic trapping of microbubbles in complex environments and controlled payload release. *Proceedings of the National Academy of Sciences*, 117(27):15490–15496, 2020.

[15] A. B. Basset. *A treatise on hydrodynamics: with numerous examples*, volume 2. Deighton, Bell and Company, 1888.

[16] A. Bausch, M. J. Bowick, A. Cacciuto, A. Dinsmore, M. Hsu, D. Nelson, M. Nikolaides, A. Travesset, and D. Weitz. Grain boundary scars and spherical crystallography. *Science*, 299(5613):1716–1718, 2003.

[17] Y. Bhosale, T. Parthasarathy, and M. Gazzola. Shape curvature effects in viscous streaming. *Journal of Fluid Mechanics*, 898:A13, 2020. doi: 10.1017/jfm.2020.404.

[18] V. Bjerknes. *Fields of force*. General Books, 1906.

[19] J. Blake and A. Chwang. Fundamental singularities of viscous flow. *Journal of Engineering Mathematics*, 8(1):23–29, 1974.

[20] J. R. Blake. A note on the image system for a stokeslet in a no-slip boundary. *Mathematical Proceedings of the Cambridge Philosophical Society*, 70(2):303–310, 1971. doi: 10.1017/S0305004100049902.

[21] M. Bowick, A. Cacciuto, D. R. Nelson, and A. Travesset. Crystalline order on a sphere and the generalized thomson problem. *Physical Review Letters*, 89(18):185502, 2002.

[22] M. Bowick, D. R. Nelson, and A. Travesset. Curvature-induced defect unbinding in toroidal geometries. *Physical Review E*, 69(4):041102, 2004.

[23] M. J. Bowick and L. Giomi. Two-dimensional matter: order, curvature and defects. *Advances in Physics*, 58(5):449–563, 2009.

[24] M. J. Bowick and A. Travesset. The statistical mechanics of membranes. *Physics Reports*, 344(4-6): 255–308, 2001.

[25] M. J. Bowick, D. R. Nelson, and A. Travesset. Interacting topological defects on frozen topographies. *Physical Review B*, 62(13):8738, 2000.

[26] M. J. Bowick, A. Cacciuto, D. R. Nelson, and A. Travesset. Crystalline particle packings on a sphere with long-range power-law potentials. *Physical Review B*, 73(2):024115, 2006.

[27] M. J. Bowick, L. Giomi, H. Shin, and C. K. Thomas. Bubble-raft model for a paraboloidal crystal. *Physical Review E*, 77(2):021602, 2008.

[28] H. Brenner. The slow motion of a sphere through a viscous fluid towards a plane surface. *Chemical engineering science*, 16(3-4):242–251, 1961.

[29] R. F. Bruinsma and W. S. Klug. Physics of viral shells. *Annu. Rev. Condens. Matter Phys.*, 6(1): 245–268, 2015.

[30] H. Bruus. Acoustofluidics 7: The acoustic radiation force on small particles. *Lab on a Chip*, 12(6): 1014–1021, 2012.

[31] D. Bucher, F. Frey, K. A. Sochacki, S. Kummer, J.-P. Bergeest, W. J. Godinez, H.-G. Kräusslich, K. Rohr, J. W. Taraska, U. S. Schwarz, et al. Clathrin-adaptor ratio and membrane tension regulate the flat-to-curved transition of the clathrin coat during endocytosis. *Nature communications*, 9(1): 1–13, 2018.

[32] C. J. Burke, B. L. Mbanga, Z. Wei, P. T. Spicer, and T. J. Atherton. The role of curvature anisotropy in the ordering of spheres on an ellipsoid. *Soft Matter*, 11(29):5872–5882, 2015.

[33] E. P. Chan and A. J. Crosby. Fabricating microlens arrays by surface wrinkling. *Advanced Materials*, 18(24):3238–3242, 2006.

[34] Y. Chen and S. Lee. Manipulation of biological objects using acoustic bubbles: a review. *Integrative and comparative biology*, 54(6):959–968, 2014.

[35] Y. Chen, Z. Fang, B. Merritt, D. Strack, J. Xu, and S. Lee. Onset of particle trapping and release via acoustic bubbles. *Lab on a Chip*, 16(16):3024–3032, 2016.

[36] S. Chien. Red cell deformability and its relevance to blood flow. *Annual review of physiology*, 49(1): 177–192, 1987.

[37] K. Chong, S. D. Kelly, S. Smith, and J. D. Eldredge. Inertial particle trapping in viscous streaming. *Physics of Fluids*, 25(3):033602, 2013.

[38] K. Chong, S. D. Kelly, S. T. Smith, and J. D. Eldredge. Transport of inertial particles by viscous streaming in arrays of oscillating probes. *Physical Review E*, 93(1):013109, 2016.

[39] A. J. Chung, D. R. Gossett, and D. Di Carlo. Three dimensional, sheathless, and high-throughput microparticle inertial focusing through geometry-induced secondary flows. *Small*, 9(5):685–690, 2013.

[40] S. K. Chung and S. K. Cho. On-chip manipulation of objects using mobile oscillating bubbles. *Journal of Micromechanics and Microengineering*, 18(12):125024, 2008.

[41] R. J. Clarke, S. M. Cox, P. Williams, and O. Jensen. The drag on a microcantilever oscillating near a wall. *Journal of Fluid Mechanics*, 545:397–426, 2005.

[42] W. T. Coakley and W. Nyborg. Cavitation; dynamics of gas bubbles; applications. *Ultrasound: Its applications in medicine and biology*, 3:77–159, 1978.

[43] R. Cox and H. Brenner. The lateral migration of solid particles in poiseuille flow—i theory. *Chemical Engineering Science*, 23(2):147–173, 1968.

[44] S. Danilov and M. Mironov. Mean force on a small sphere in a sound field in a viscous fluid. *The Journal of the Acoustical Society of America*, 107(1):143–153, 2000.

[45] W. R. Dean. Xvi. note on the motion of fluid in a curved pipe. *The London, Edinburgh, and Dublin Philosophical Magazine and Journal of Science*, 4(20):208–223, 1927.

[46] D. Di Carlo. Inertial microfluidics. *Lab on a Chip*, 9(21):3038–3046, 2009.

[47] D. Di Carlo, D. Irimia, R. G. Tompkins, and M. Toner. Continuous inertial focusing, ordering, and separation of particles in microchannels. *PNAS*, 104(48):18892–18897, 2007.

[48] A. Doinikov. Acoustic radiation pressure on a rigid sphere in a viscous fluid. *Proc. R. Soc. Lond. A*, 447(1931):447–466, 1994.

[49] A. Doinikov and S. Zavtrak. Interaction force between a bubble and a solid particle in a sound field. *Ultrasonics*, 34(8):807–815, 1996.

[50] A. A. Doinikov and A. Bouakaz. Effect of a distant rigid wall on microstreaming generated by an acoustically driven gas bubble. *Journal of Fluid Mechanics*, 742:425–445, 2014.

[51] W. Drenckhan, D. Weaire, and S. Cox. The demonstration of conformal maps with two-dimensional foams. *European journal of physics*, 25(3):429, 2004.

[52] J. Einarsson, F. Candelier, F. Lundell, J. Angilella, and B. Mehlig. Effect of weak fluid inertia upon jeffery orbits. *Physical Review E*, 91(4):041002, 2015.

[53] A. Fan and S. Hilgenfedt. Unpublished data.

[54] M. Farazmand and G. Haller. The maxey–riley equation: Existence, uniqueness and regularity of solutions. *Nonlinear Analysis: Real World Applications*, 22:98–106, 2015.

[55] J. Feng, P. Ganatos, and S. Weinbaum. Motion of a sphere near planar confining boundaries in a brinkman medium. *Journal of Fluid Mechanics*, 375:265–296, 1998.

[56] P. F. Fischer, G. K. Leaf, and J. M. Restrepo. Forces on particles in oscillatory boundary layers. *Journal of Fluid Mechanics*, 468:327–347, 2002.

[57] I. Fouxon and A. Leshansky. Fundamental solution of unsteady stokes equations and force on an oscillating sphere near a wall. *Physical Review E*, 98(6):063108, 2018.

[58] N. Franceschini. Pupil and pseudopupil in the compound eye of drosophila. In *Information Processing in the Visual Systems of Anthropods*, pages 75–82. Springer, 1972.

[59] M. Gazzola, P. Chatelain, W. M. Van Rees, and P. Koumoutsakos. Simulations of single and multiple swimmers with non-divergence free deforming geometries. *Journal of Computational Physics*, 230(19): 7093–7114, 2011.

[60] L. Giomi and M. Bowick. Crystalline order on riemannian manifolds with variable gaussian curvature and boundary. *Physical Review B*, 76(5):054106, 2007.

[61] L. Giomi and M. J. Bowick. Defective ground states of toroidal crystals. *Physical Review E*, 78(1): 010601, 2008.

[62] G. M. Grason. Perspective: Geometrically frustrated assemblies. *The Journal of Chemical Physics*, 145(11):110901, 2016.

[63] J. M. Grime, J. F. Dama, B. K. Ganser-Pornillos, C. L. Woodward, G. J. Jensen, M. Yeager, and G. A. Voth. Coarse-grained simulation reveals key features of hiv-1 capsid self-assembly. *Nature communications*, 7(1):1–11, 2016.

[64] K. Grünewald, P. Desai, D. C. Winkler, J. B. Heymann, D. M. Belnap, W. Baumeister, and A. C. Steven. Three-dimensional structure of herpes simplex virus from cryo-electron tomography. *Science*, 302(5649):1396–1398, 2003.

[65] M. F. Hagan. Modeling viral capsid assembly. *Advances in chemical physics*, 155:1, 2014.

[66] M. F. Hagan and R. Zandi. Recent advances in coarse-grained modeling of virus assembly. *Current opinion in virology*, 18:36, 2016.

[67] A. Hashmi, G. Yu, M. Reilly-Collette, G. Heiman, and J. Xu. Oscillating bubbles: a versatile tool for lab on a chip applications. *Lab on a Chip*, 12(21):4216–4227, 2012.

[68] T. A. Hay, M. F. Hamilton, Y. A. Ilinskii, and E. A. Zabolotskaya. Model of coupled pulsation and translation of a gas bubble and rigid particle. *The Journal of the Acoustical Society of America*, 125 (3):1331–1339, 2009.

[69] E. Hinch and L. Leal. The effect of brownian motion on the rheological properties of a suspension of non-spherical particles. *Journal of Fluid Mechanics*, 52(4):683–712, 1972.

[70] B. Ho and L. Leal. Inertial migration of rigid spheres in two-dimensional unidirectional flows. *Journal of fluid mechanics*, 65(2):365–400, 1974.

[71] K. V. Holmes and L. Enjuanes. The sars coronavirus: a postgenomic era. *Science*, 300(5624):1377–1378, 2003.

[72] J. Holtsmark, I. Johnsen, T. Sikkeland, and S. Skavlem. Boundary layer flow near a cylindrical obstacle in an oscillating, incompressible fluid. *The journal of the acoustical society of America*, 26(1):26–39, 1954.

[73] K. Hood, S. Lee, and M. Roper. Inertial migration of a rigid sphere in three-dimensional poiseuille flow. *Journal of Fluid Mechanics*, 765:452–479, 2015.

[74] S. C. Hur, H. T. K. Tse, and D. Di Carlo. Sheathless inertial cell ordering for extreme throughput flow cytometry. *Lab on a Chip*, 10(3):274–280, 2010.

[75] W. T. Irvine, V. Vitelli, and P. M. Chaikin. Pleats in crystals on curved surfaces. *Nature*, 468(7326): 947, 2010.

[76] G. B. Jeffery. The motion of ellipsoidal particles immersed in a viscous fluid. *Proceedings of the Royal Society of London. Series A, Containing papers of a mathematical and physical character*, 102(715): 161–179, 1922.

[77] S. Kim and S. J. Karrila. *Microhydrodynamics: principles and selected applications*. Courier Corporation, 2013.

[78] S. Kim, J. J. Cassidy, B. Yang, R. W. Carthew, and S. Hilgenfeldt. Hexagonal patterning of the insect compound eye: Facet area variation, defects, and disorder. *Biophysical journal*, 111(12):2735–2746, 2016.

[79] K. Klumpp and T. Crépin. Capsid proteins of enveloped viruses as antiviral drug targets. *Current opinion in virology*, 5:63–71, 2014.

[80] C. Köhler, R. Backofen, and A. Voigt. Stress induced branching of growing crystals on curved surfaces. *Physical review letters*, 116(13):135502, 2016.

[81] L. D. Landau and E. Lifshitz. *Course of Theoretical Physics Vol. 6 Fluid Mechanies*. Pergamon Press, 1959.

[82] L. G. Leal. *Laminar flow and convective transport processes*, volume 251. Elsevier, 1992.

[83] D. Lhuillier. On the equation of motion of a rigid sphere in a non uniform and accelerated inviscid fluid. incidence on two-phase flow equations. *Mechanics Research Communications*, 9(5):295–299, 1982.

[84] S. Li, P. Roy, A. Travesset, and R. Zandi. Why large icosahedral viruses need scaffolding proteins. *Proceedings of the National Academy of Sciences*, 115(43):10971–10976, 2018.

[85] S. Li, R. Zandi, and A. Travesset. Elasticity in curved topographies: Exact theories and linear approximations. *Physical Review E*, 99(6):063005, 2019.

[86] S. Li, R. Zandi, A. Travesset, and G. M. Grason. Ground states of crystalline caps: Generalized jellium on curved space. *Phys. Rev. Lett.*, 123:145501, Sep 2019. doi: 10.1103/PhysRevLett.123.145501.

[87] J. Lidmar, L. Mirny, and D. R. Nelson. Virus shapes and buckling transitions in spherical shells. *Physical Review E*, 68(5):051910, 2003.

[88] J. Lighthill. Acoustic streaming. *Journal of sound and vibration*, 61(3):391–418, 1978.

[89] R. H. Liu, J. Yang, M. Z. Pindera, M. Athavale, and P. Grodzinski. Bubble-induced acoustic micromixing. *Lab on a Chip*, 2(3):151–157, 2002.

[90] M. S. Longuet-Higgins. Mass transport in water waves. *Philosophical Transactions of the Royal Society of London. Series A, Mathematical and Physical Sciences*, 245(903):535–581, 1953.

[91] M. S. Longuet-Higgins. Viscous streaming from an oscillating spherical bubble. *Proceedings of the Royal Society of London. Series A: Mathematical, Physical and Engineering Sciences*, 454(1970):725–742, 1998.

[92] P. M. Lovalenti and J. F. Brady. The force on a sphere in a uniform flow with small-amplitude oscillations at finite reynolds number. *Journal of Fluid Mechanics*, 256:607–614, 1993.

[93] P. M. Lovalenti and J. F. Brady. The hydrodynamic force on a rigid particle undergoing arbitrary time-dependent motion at small reynolds number. *Journal of Fluid Mechanics*, 256:561–605, 1993.

[94] B. R. Lutz and D. R. Meldrum. Hydrodynamic tweezers: single-cell trapping arrays for cell dynamics. In *9th International Conference on Miniaturized Systems for Chemistry and Life Sciences, MicroTAS 2005*, pages 512–514. Transducer Research Foundation, 2005.

[95] B. R. Lutz, J. Chen, and D. T. Schwartz. Microfluidics without microfabrication. *PNAS*, 100(8): 4395–4398, 2003.

[96] B. R. Lutz, J. Chen, and D. T. Schwartz. Microscopic steady streaming eddies created around short cylinders in a channel: Flow visualization and stokes layer scaling. *Physics of Fluids*, 17(2):023601, 2005.

[97] B. R. Lutz, J. Chen, and D. T. Schwartz. Hydrodynamic tweezers: 1. noncontact trapping of single cells using steady streaming microeddies. *Analytical chemistry*, 78(15):5429–5435, 2006.

[98] A. Maali, R. Boisgard, H. Chraibi, Z. Zhang, H. Kellay, and A. Würger. Viscoelastic drag forces and crossover from no-slip to slip boundary conditions ?for flow near air-water interfaces. *Physical Review Letters*, 118:084501, 2017.

[99] A. J. Mach, J. H. Kim, A. Arshi, S. C. Hur, and D. Di Carlo. Automated cellular sample preparation using a centrifuge-on-a-chip. *Lab on a Chip*, 11(17):2827–2834, 2011.

[100] P. Marmottant and S. Hilgenfeldt. Controlled vesicle deformation and lysis by single oscillating bubbles. *Nature*, 423(6936):153–156, 2003.

[101] M. Maxey. The motion of small spherical particles in a cellular flow field. *The Physics of fluids*, 30 (7):1915–1928, 1987.

[102] M. Maxey. On the advection of spherical and non-spherical particles in a non-uniform flow. *Philosophical Transactions of the Royal Society of London. Series A: Physical and Engineering Sciences*, 333(1631):289–307, 1990.

[103] M. R. Maxey and J. J. Riley. Equation of motion for a small rigid sphere in a nonuniform flow. *The Physics of Fluids*, 26(4):883–889, 1983. doi: 10.1063/1.864230.

[104] C. I. Mendoza and D. Reguera. Shape selection and mis-assembly in viral capsid formation by elastic frustration. *eLife*, 9:e52525, 2020.

[105] G. Meng, J. Paulose, D. R. Nelson, and V. N. Manoharan. Elastic instability of a crystal growing on a curved surface. *Science*, 343(6171):634–637, 2014.

[106] P. Messner, D. Pum, M. Sára, K. Stetter, and U. Sleytr. Ultrastructure of the cell envelope of the archaebacteria thermoproteus tenax and thermoproteus neutrophilus. *Journal of bacteriology*, 166(3): 1046–1054, 1986.

[107] E. E. Michaelides. A novel way of computing the basset term in unsteady multiphase flow computations. *Physics of Fluids A: Fluid Dynamics*, 4(7):1579–1582, 1992.

[108] E. E. Michaelides. The transient equation of motion for particles, bubbles, and droplets. *Journal of fluids engineering*, 119(2):233–247, 1997.

[109] J. Michell. On the direct determination of stress in an elastic solid, with application to the theory of plates. *Proceedings of the London Mathematical Society*, 1(1):100–124, 1899.

[110] W. H. Mitchell and S. E. Spagnolie. Sedimentation of spheroidal bodies near walls in viscous fluids: glancing, reversing, tumbling and sliding. *Journal of Fluid Mechanics*, 772:600–629, 2015.

[111] E. Mograbi and E. Bar-Ziv. On the asymptotic solution of the maxey-riley equation. *Physics of Fluids*, 18(5):051704, 2006.

[112] A. Y. Morozov and R. F. Bruinsma. Assembly of viral capsids, buckling, and the asaro-grinfeld-tiller instability. *Physical Review E*, 81(4):041925, 2010.

[113] N. A. Mortensen, F. Okkels, and H. Bruus. Reexamination of hagen-poiseuille flow: Shape dependence of the hydraulic resistance in microchannels. *Physical Review E*, 71(5):057301, 2005.

[114] A. Mughal. Packing of softly repulsive particles in a spherical box—a generalised thomson problem. *Forma*, 29:13–19, 2014.

[115] A. Nadim and H. A. Stone. The motion of small particles and droplets in quadratic flows. *Studies in Applied Mathematics*, 85(1):53–73, 1991.

[116] D. R. Nelson. Defects in superfluids, superconductors and membranes. *arXiv preprint cond-mat/9502114*, 1995.

[117] D. R. Nelson. *Defects and geometry in condensed matter physics*. Cambridge University Press, 2002.

[118] W. L. Nyborg. Acoustic streaming near a boundary. *The Journal of the Acoustical Society of America*, 30(4):329–339, 1958.

[119] L. A. Ostrovsky and Y. A. Stepanyants. *Dynamics of Particles and Bubbles Under the Action of Acoustic Radiation Force*, pages 205–230. Springer, 2018. ISBN 978-3-319-68109-2. doi: 10.1007/978-3-319-68109-2_11.

[120] A. J. Pak, J. M. Grime, P. Sengupta, A. K. Chen, A. E. Durumeric, A. Srivastava, M. Yeager, J. A. Briggs, J. Lippincott-Schwartz, and G. A. Voth. Immature hiv-1 lattice assembly dynamics are regulated by scaffolding from nucleic acid and the plasma membrane. *Proceedings of the National Academy of Sciences*, 114(47):E10056–E10065, 2017.

[121] N. Pamme, J. C. Eijkel, and A. Manz. On-chip free-flow magnetophoresis: Separation and detection of mixtures of magnetic particles in continuous flow. *Journal of magnetism and magnetic materials*, 307(2):237–244, 2006.

[122] S. Panahandeh, S. Li, and R. Zandi. The equilibrium structure of self-assembled protein nano-cages. *Nanoscale*, 10(48):22802–22809, 2018.

[123] S. Panahandeh, S. Li, L. Marichal, R. Leite Rubim, G. Tresset, and R. Zandi. How a virus circumvents energy barriers to form symmetric shells. *ACS nano*, 14(3):3170–3180, 2020.

[124] I. S. Park, J. H. Shin, Y. R. Lee, and S. K. Chung. On-chip micromanipulation using a magnetically driven micromanipulator with an acoustically oscillating bubble. *Sensors and Actuators A: Physical*, 248:214–222, 2016.

[125] T. Parthasarathy, F. K. Chan, and M. Gazzola. Streaming-enhanced flow-mediated transport. *Journal of Fluid Mechanics*, 878:647–662, 2019.

[126] J. Paulose, B. G.-g. Chen, and V. Vitelli. Topological modes bound to dislocations in mechanical metamaterials. *Nature Physics*, 11(2):153–156, 2015.

[127] A. Pérez-Garrido, M. Dodgson, and M. Moore. Influence of dislocations in thomson's problem. *Physical Review B*, 56(7):3640, 1997.

[128] V. Peri, Z.-D. Song, M. Serra-Garcia, P. Engeler, R. Queiroz, X. Huang, W. Deng, Z. Liu, B. A. Bernevig, and S. D. Huber. Experimental characterization of fragile topology in an acoustic metamaterial. *Science*, 367(6479):797–800, 2020.

[129] J. D. Perlmutter and M. F. Hagan. Mechanisms of virus assembly. *Annual review of physical chemistry*, 66:217–239, 2015.

[130] J. D. Perlmutter, M. R. Perkett, and M. F. Hagan. Pathways for virus assembly around nucleic acids. *Journal of molecular biology*, 426(18):3148–3165, 2014.

[131] F. Peters, L. Lobry, and E. Lemaire. Experimental observation of lorenz chaos in the quincke rotor dynamics. *Chaos: An Interdisciplinary Journal of Nonlinear Science*, 15(1):013102, 2005.

[132] C. Pozrikidis et al. *Boundary integral and singularity methods for linearized viscous flow*. Cambridge University Press, 1992.

[133] G. E. Pradillo, H. Karani, and P. M. Vlahovska. Quincke rotor dynamics in confinement: rolling and hovering. *Soft Matter*, 15(32):6564–6570, 2019.

[134] S. G. Prasath, V. Vasan, and R. Govindarajan. Accurate solution method for the maxey–riley equation, and the effects of basset history. *Journal of Fluid Mechanics*, 868:428–460, 2019.

[135] G. Quincke. Ueber rotationen im constanten electrischen felde. *Annalen der Physik*, 295(11):417–486, 1896.

[136] D. Rabaud, P. Thibault, J.-P. Raven, O. Hugon, E. Lacot, and P. Marmottant. Manipulation of confined bubbles in a thin microchannel: Drag and acoustic bjerknes forces. *Physics of Fluids*, 23(4): 042003, 2011.

[137] D. V. Raju. Particle manipulation by attractive and repulsive forces in 2-d streaming flows. Master's thesis, University of Illinois at Urbana-Champaign, 2018.

[138] B. Rallabandi. *Quantifying microbubble streaming and its applications*. PhD thesis, University of Illinois at Urbana-Champaign, 2015.

[139] B. Rallabandi. Inertial forces in the maxey–riley equation in nonuniform flows. *Physical Review Fluids*, 6(1):L012302, 2021.

[140] B. Rallabandi, C. Wang, and S. Hilgenfeldt. Two-dimensional streaming flows driven by sessile semi-cylindrical microbubbles. *Journal of Fluid Mechanics*, 739:57–71, 2014.

[141] B. Rallabandi, S. Hilgenfeldt, and H. A. Stone. Hydrodynamic force on a sphere normal to an obstacle due to a non-uniform flow. *Journal of Fluid Mechanics*, 818:407–434, 2017.

[142] N. Riley. Steady streaming. *Annual review of fluid mechanics*, 33(1):43–65, 2001.

[143] P. Rogers and A. Neild. Selective particle trapping using an oscillating microbubble. *Lab on a Chip*, 11(21):3710–3715, 2011.

[144] D. S. Roshal, K. Azzag, E. Le Goff, S. B. Rochal, and S. Baghdiguian. crystal-like order and defects in metazoan epithelia with spherical geometry. *Scientific Reports*, 10(1):1–11, 2020.

[145] P. Saffman. The lift on a small sphere in a slow shear flow. *Journal of fluid mechanics*, 22(2):385–400, 1965.

[146] L. Schmid, D. A. Weitz, and T. Franke. Sorting drops and cells with acoustics: acoustic microfluidic fluorescence-activated cell sorter. *Lab on a Chip*, 14(19):3710–3718, 2014.

[147] J. A. Schonberg and E. Hinch. Inertial migration of a sphere in poiseuille flow. *Journal of Fluid Mechanics*, 203:517–524, 1989.

[148] M. Settnes and H. Bruus. Forces acting on a small particle in an acoustical field in a viscous fluid. *Physical Review E*, 85(1):016327, 2012.

[149] H. S. Seung and D. R. Nelson. Defects in flexible membranes with crystalline order. *Physical Review A*, 38(2):1005, 1988.

[150] S. Shimorin. The green function for the weighted biharmonic operator δ (1- z 2)- α δ, and factorization of analytic functions, and factorization of analytic functions. *Journal of Mathematical Sciences*, 87(5): 3912–3924, 1997.

[151] J. H. Shin, J. Seo, J. Hong, and S. K. Chung. Hybrid optothermal and acoustic manipulations of microbubbles for precise and on-demand handling of micro-objects. *Sensors and Actuators B: Chemical*, 246:415–420, 2017.

[152] A. Šiber. Buckling transition in icosahedral shells subjected to volume conservation constraint and pressure: Relations to virus maturation. *Physical Review E*, 73(6):061915, 2006.

[153] J. L. Silverberg, A. A. Evans, L. McLeod, R. C. Hayward, T. Hull, C. D. Santangelo, and I. Cohen. Using origami design principles to fold reprogrammable mechanical metamaterials. *science*, 345(6197): 647–650, 2014.

[154] R. Sknepnek, G. Vernizzi, and M. O. de la Cruz. Buckling of multicomponent elastic shells with line tension. *Soft Matter*, 8(3):636–644, 2012.

[155] E. Sollier, D. E. Go, J. Che, D. R. Gossett, S. O'Byrne, W. M. Weaver, N. Kummer, M. Rettig, J. Goldman, N. Nickols, et al. Size-selective collection of circulating tumor cells using vortex technology. *Lab on a Chip*, 14(1):63–77, 2014.

[156] A. C. Steven, J. F. Conway, N. Cheng, N. R. Watts, D. M. Belnap, A. Harris, S. J. Stahl, and P. T. Wingfield. Structure, assembly, and antigenicity of hepatitis b virus capsid proteins. *Advances in virus research*, 64:125–164, 2005.

[157] H. Stone, J. Brady, and P. Lovalenti. Inertial effects on the rheology of suspensions and on the motion of individual particles. *preprint*, 2001.

[158] H. A. Stone. Introduction to fluid dynamics for microfluidic flows. In *CMOS Biotechnology*, pages 5–30. Springer, 2007.

[159] G. Subramanian and D. L. Koch. Inertial effects on fibre motion in simple shear flow. *Journal of Fluid Mechanics*, 535:383–414, 2005.

[160] R. Thameem, B. Rallabandi, and S. Hilgenfeldt. Particle migration and sorting in microbubble streaming flows. *Biomicrofluidics*, 10(1):014124, 2016.

[161] R. Thameem, B. Rallabandi, and S. Hilgenfeldt. Fast inertial particle manipulation in oscillating flows. *Phys. Rev. Fluids*, 2:052001, May 2017. doi: 10.1103/PhysRevFluids.2.052001.

[162] R. Thameem, B. Rallabandi, and S. Hilgenfeldt. Fast inertial particle manipulation in oscillating flows. *Physical Review Fluids*, 2(5):052001, 2017.

[163] M. Van Hinsberg, J. ten Thije Boonkkamp, and H. J. Clercx. An efficient, second order method for the approximation of the basset history force. *Journal of Computational Physics*, 230(4):1465–1478, 2011.

[164] V. Vitelli and D. R. Nelson. Defect generation and deconfinement on corrugated topographies. *Physical Review E*, 70(5):051105, 2004.

[165] V. Vitelli, J. B. Lucks, and D. R. Nelson. Crystallography on curved surfaces. *Proceedings of the National Academy of Sciences*, 103(33):12323–12328, 2006.

[166] A. Volk, M. Rossi, B. Rallabandi, C. J. Kähler, S. Hilgenfeldt, and A. Marin. Size-dependent particle migration and trapping in three-dimensional microbubble streaming flows. *Physical Review Fluids*, 5 (11):114201, 2020.

[167] C. Wang, S. V. Jalikop, and S. Hilgenfeldt. Size-sensitive sorting of microparticles through control of flow geometry. *Applied Physics Letters*, 99(3):034101, 2011.

[168] C. Wang, S. V. Jalikop, and S. Hilgenfeldt. Efficient manipulation of microparticles in bubble streaming flows. *Biomicrofluidics*, 6(1):012801, 2012.

[169] C. Wang, B. Rallabandi, and S. Hilgenfeldt. Frequency dependence and frequency control of microbubble streaming flows. *Physics of Fluids*, 25(2):022002, 2013.

[170] M. E. Warkiani, A. K. P. Tay, B. L. Khoo, X. Xiaofeng, J. Han, and C. T. Lim. Malaria detection using inertial microfluidics. *Lab on a Chip*, 15(4):1101–1109, 2015.

[171] J. H. Warner, E. R. Margine, M. Mukai, A. W. Robertson, F. Giustino, and A. I. Kirkland. Dislocation-driven deformations in graphene. *Science*, 337(6091):209–212, 2012.

[172] Y. Xie, D. Ahmed, M. I. Lapsley, M. Lu, S. Li, and T. J. Huang. Acoustofluidic relay: sequential trapping and transporting of microparticles via acoustically excited oscillating bubbles. *Journal of laboratory automation*, 19(2):137–143, 2014.

[173] Y. Xu, A. Hashmi, G. Yu, X. Lu, H.-J. Kwon, X. Chen, and J. Xu. Microbubble array for on-chip worm processing. *Applied Physics Letters*, 102(2):023702, 2013.

[174] L. Yang and M. Lu. Small molecule inhibitors of hepatitis b virus nucleocapsid assembly: a new approach to treat chronic hbv infection. *Current medicinal chemistry*, 25(7):802–813, 2018.

[175] E. H. Yong, D. R. Nelson, and L. Mahadevan. Elastic platonic shells. *Physical review letters*, 111(17): 177801, 2013.